THE UNIVERSITY of EDINBURGH

Title	Modelling galaxies in the high redshift universe
Author	Crawford, Miller
Qualification	PhD
Year	2006

Digitisation Notes:

- Page ii missing from original
- Page vi missing from original
- Pages 132 and 194 missing from original

Modelling galaxies in the high redshift universe

MILLER CRAWFORD

Institute for Astronomy
School of Physics

University of Edinburgh
Doctor of Philosophy

August 2006

Declaration

I declare that this thesis is not substantially the same as any that I have submitted for a degree or diploma or other qualification at any other University. I further state that no part of my thesis has already been or is being concurrently submitted for any such degree, diploma or other qualification.

This thesis is the outcome of my own work except where specifically indicated in the text.

Miller Crawford
Edinburgh,
August 2006.

Acknowledgements

This thesis would double in size if I mentioned every little thing that has helped me through my PhD, so I'll do my best to keep it relatively brief!

First of all, I'd like to thank Mum, Dad and Elizabeth for endless encouragement in the last three and a half years, no matter how gloomy and self-indulgent my demeanour! I wouldn't have been able to finish without their support. Thanks also to my niece Emma Girbow, who arrived just before my final draft: coming to visit you gave me the incentive to cross that finishing line!

I'd like to thank my supervisor, Dr Eelco van Kampen, for the ideas and background work behind this thesis, cheerful encouragement in moments of despair, helpful comments and corrections and innumerable free trips to Innsbruck! Thanks must also go to my other supervisors, Prof. John Peacock and Prof. Jim Dunlop, for all their ideas, support, trips to Hawaii and often-needed encouragement. We got there in the end!

This thesis also would not have been possible without the work of Dr Gian Luigi Granato and Dr Laura Silva. I'd like to thank them for giving me a full version of *GRASIL*, providing much useful advice in its implementation and their hospitality on a visit to Padova.

Thanks also to Chris Rimes, for many useful hints and suggestions in getting to grips with the world of galaxy formation and some very useful codes, especially the merger tree creator! Thanks also to Darren Croton for providing me with the mini-Millenium simulation data.

Of course, I wouldn't have got very far without the support of my wonderful friends and colleagues. You all deserve thanks, but I'll mention a few specific ones here. Michael, Jess, Rachel Dowsett and Emma Taylor all started at the same time as me, and without the new music, pub trips, holidays, dinner parties, endless support and distractions I doubt there'd be a finished thesis

in front of me now. Olivia was always there with a friendly ear and a kind word (often crude!) whenever I felt down or stressed, and she must also take some of the credit for the finished article you're holding right now. In the last few months of writing up, a couple of games of *Worms* a day helped stave off insanity, and Tom Targett needs thanks for providing stern opposition! Coffee time and trips to the Old Bell, endless other pubs, the Meadows, flats, gardens and so on were the mainstay of PhD life: thanks to Niall, Emma Rigby, Tom Kitching, Ben, Mairi, Martin, Eric, Matt, Barney, Rita, Rachel Smith, Anita, Simon and Stuart Lynn for all the much needed distractions!

Thanks must also go to Ryan, Stuart Galbraith, Jemma, Duncan, Helen, Steve, Tom Young, Tom Davidson, Malcolm and Davey for some very amusing nights out in Edinburgh and elsewhere, and to Jenny (who perhaps also deserves a medal!) for putting a roof over my head for nearly two years.

Finally, but most importantly of all, I'd like to thank Caroline Francis from the very bottom of my heart. Without her unquestioning love and support I wouldn't be writing this now, and I owe everything to her. This is for you, Caz.

'Some scientists claim that hydrogen, because it is so plentiful, is the basic building block of the universe. I dispute that. I say there is more stupidity than hydrogen, and that is the basic building block of the universe.' - *Frank Zappa*

Abstract

This thesis describes the combination of a phenomenological model of galaxy formation with the spectrophotometric dust extinction model of Silva et al. (1998). I use N-body simulations to predict the underlying dark matter density field in a hierarchal Lambda Cold Dark Matter universe. Analytic prescriptions of gas cooling, star formation and stellar feedback describes the formation and evolution of galaxies embedded in the hierarchy of dark matter haloes. Starlight is attenuated by a two-phase medium of graphite and silicate dust grains, yielding the observed spectral energy distribution of a galaxy from the UV to the submillimetre. With this in place, the role of dust in galaxy formation can be probed and assessed in a self-consistent manner, improving on the common plane-parallel slab and tunable dust temperature approach employed in many semi-analytic models.

I first present model predictions of the local universe, demanding that an acceptable model must first perform well at $z = 0$ before being tested at high redshift. I can adequately reproduce many key local observational constraints, although a few stimulating discrepancies are present. Not only will this ground the models in reality, it will then help assess whether a 'standard' semi-analytic model can reproduce facets of the high redshift universe without recourse to new physics.

I then use the above framework to present predictions at early times, where dust is known to play an important role in influencing the observed magnitudes, colours and properties of galaxies. Two further models are introduced to assess how different parameter choices that give similar local results diverge at early times. I first concentrate on the more global, well understood facets of the high redshift universe, namely the galaxy and stellar luminosity functions. I then construct mock surveys in an attempt to account for Lyman Break Galaxies (LBGs) at $z = 3$, of which there is a comprehensive array of

high quality data available in the literature. Properties of LBGs can be adequately reproduced by the models, although there is a marked overabundance of such objects present, likely due to an underestimate of the dust extinction inherent in such objects.

I finally use the mock survey approach to study Extremely Red Objects (EROs), galaxies with $(R - K) > 5$ uncovered in deep K-band surveys, and Submillimetre Galaxies (SMGs) detected in blank field SCUBA surveys. These extreme objects tend to the bane of semi-analytic models, and I find that my model fares no different in this respect: a truncation method used to prevent the formation of overly massive galaxies at low redshift also inhibits their formation at early times. I severely underpredict the number counts of EROs and SMGs, although a few of their observational properties can be matched reasonably well. I then investigate the overlaps between distinct populations, and the fate of high redshift objects is followed through time, shedding light on relationships between evolutionary phases of galaxies.

Contents

List of Figures

List of Tables

CHAPTER 1

Introduction

1.1 Properties of galaxies in the local universe

1.1.1 The local field luminosity functions

Perhaps the most fundamental property of the galaxy population is the luminosity function (LF), commonly parametrised by the Schecter function (Schecter 1976):

$$\Phi(L) = \phi_* \left(\frac{L}{L_*}\right)^{\alpha} \exp\left(\frac{L}{L_*}\right) \frac{\mathrm{d}L}{L_*}. \tag{1.1}$$

This is based on the observation that at faint absolute magnitudes (low intrinsic luminosities), $\Phi(L)$ behaves as a power law with slope α, truncated at high luminosities around the characteristic luminosity L_*. The normalisation of the LF is given by ϕ_*.

It is simple to recast equation (1.1) in absolute magnitudes: since $L \propto 10^{-0.4M}$, we have

$$\Phi(M) = (0.4 \ \ln 10)\phi_* 10^{0.4(M_*-M)(\alpha+1)} \exp(-10^{-0.4(M_*-M)}) \mathrm{d}M. \tag{1.2}$$

In Figure 1.1, I plot the B and K band local luminosity function, as measured by a number of recent authors (see Table 1.1 for details). The B-band LF probes recent star formation, whereas the K-band LF is a good overall indicator of total stellar mass. Overplotted are derived Schecter functions for each dataset, with the best-fitting parameters again listed in Table 1.1.

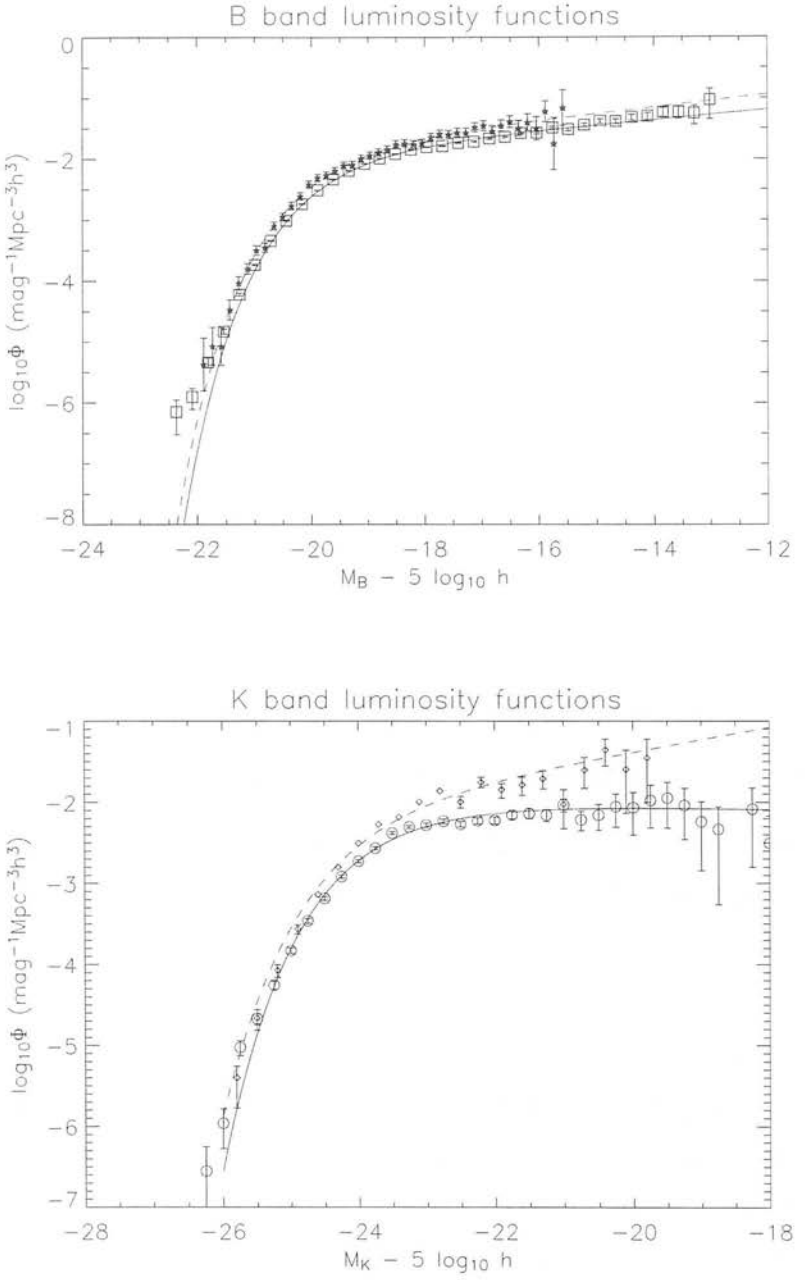

Figure 1.1: Local B and K band luminosity functions. Top panel: LFs for the 2dF Galaxy Redshift Survey (2dFGRS,squares), and the Sloan Digital Sky Survey (SDSS, stars). Overplotted are Schecter function fits to the 2dFGRS data (solid line) and the SDSS (dashed line). Bottom panel: K band LFs for the combined 2dFGRS-2MASS data (circles) and Hawaii-AAO survey (diamonds). Overplotted are Schecter function fits for the 2dF-2MASS data (solid line) and the Hawaii-AAO data (dashed line). References and parameters for the fits are given in Table 1.1.

Survey	$\phi_* h^{-3}\mathrm{Mpc}^3$	$M_* - 5\log h$	α	reference
		B band		
2dFGRS	0.0168 ± 0.0008	-19.40 ± 0.07	-1.21 ± 0.02	Norberg et al. (2002)
SDSS	0.0206 ± 0.0023	-19.51 ± 0.04	-1.26 ± 0.05	Blanton et al. (2001)
		K band		
2dFGRS-2MASS	0.0108 ± 0.0016	-23.44 ± 0.03	-0.96 ± 0.05	Cole et al. (2001)
Hawaii-AAO	0.013 ± 0.003	-23.70 ± 0.08	-1.37 ± 0.10	Huang et al. (2003)

Table 1.1: Schecter function fits derived for recent local luminosity functions

It is immediately obvious that intrinsically bright galaxies are rare objects. Nevertheless, they dominate the total luminosity of the universe, despite the large numbers of faint galaxies.

The Schecter function has had remarkable success in describing accurately the galaxy luminosity function at various wavelengths, survey depths and redshifts. However, a consensus between the parameters characterising the LF is hard to achieve. The main source of uncertainty is the faint slope α, which has wildy differing values in the various redshift surveys available. The problem is exacerbated by the difficulty in detecting intrinsically faint objects beyond the local universe, and low surface brightness objects, which can be intrinsically luminous but extrememly difficult to detect as their light is spread over a large area of sky (Bothun, Impey and Malin 1991). It does appear, however, that derived values of the faint slope are perhaps beginning to converge.

1.1.2 The Tully-Fisher relation

The Tully-Fisher relation (Tully and Fisher 1977) is an observed correlation between the mass (and hence luminosity, given a mass-to-light ratio) of a disk galaxy and its circular velocity:

$$L \propto (V_c)^{\alpha}. \tag{1.3}$$

It is easy to show that if all galaxies had the same mass-to-light ratio and surface brightness, then $\alpha = 4$. The circular velocity is derived from infra-red measurements of the rotationally-broadened 21 cm HI line. This minimises the effects of dust extinction, both within the galaxy of interest and along the line of sight in our own Milky Way. Nevertheless, results derived from galaxies with too high an inclination are prone to dust-related errors and

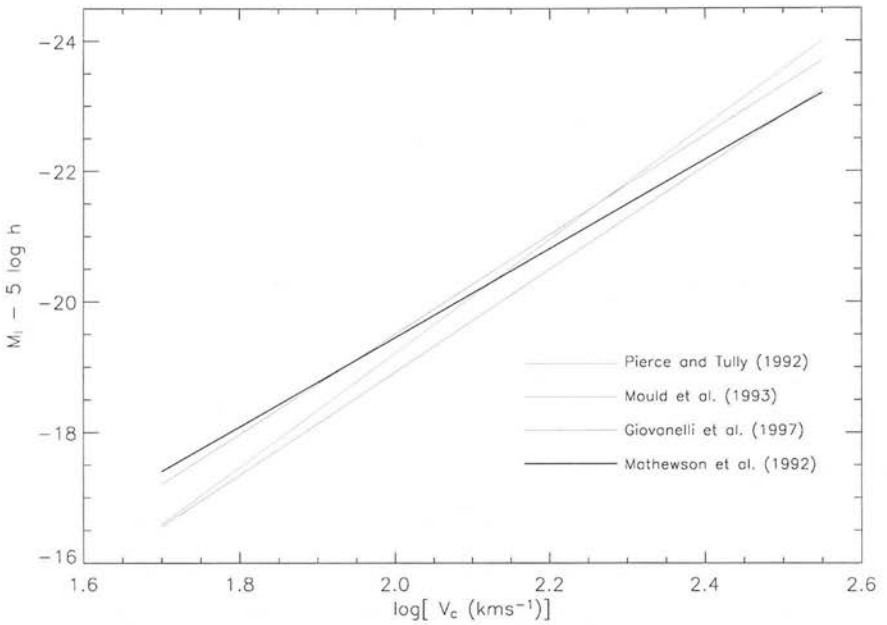

Figure 1.2: Mean I-band Tully-Fisher relations as found by four different authors

should be avoided. In addition, since the luminosity of a galaxy is derived from photometry, IR measurements give the most accurate determination of the stellar mass present. A compilation of observational estimates of the TF relation are shown in Figure 1.2. The typical scatter about the relations is ~ 0.35 mag (Giovanelli et al. 1997).

1.2 The high redshift universe

For years, observational astronomy was limited to the study of the local universe. Telescope and detector technology has improved immeasurably over the past twenty years, pushing detection limits to higher and higher redshift. The opening-up of the high redshift universe has unveiled a cornucopia of treats for both observational and theoretical astronomers, adding new species to the 'fossil record' of the universe and providing a testing ground for theories of formation and evolution.

In addition, multi-wavelength astronomy has revealed an array of previously undiscovered objects, and quite literally shed new light on the workhorse sources of observational cosmology. Objects invisible in one wave-

length can stand out like beacons in another. The high redshift universe is relatively bereft of objects visible in the optical, and studying as much of the electromagnetic spectrum as possible can reveal the internal physics and local conditions of such enigmatic sources.

1.2.1 Submillimetre emission from galaxies

The main origin for submmillimetre (submm) radiation in galaxies is thermal continuum emission from dust grains. Ultraviolet and optical light is attenuated by dust and re-emitted in the infra-red (IR), and at high redshift is shifted into the far-IR and submm regions of the electromagnetic spectrum. The spectral energy distribution (SED) of a submm source is often to be taken to be a single temperature grey-body dust distribution. At redshift z, this is given by

$$f_\nu \propto [\nu(1+z)]^{3+\beta} \left[\exp\left(\frac{h\nu(1+z)}{kT}\right) - 1\right]^{-1}. \quad (1.4)$$

Dunne et al. (2000) find that the SEDs of local submm sources are fitted well by the above, with values of $\beta = 1.3 \pm 0.2$ and $T = 36 \pm 4.9$ K.

The redshift to which a source of given flux density is visible can be calculated assuming a typical luminosity. Bright submm sources have fluxes of order $S = 8$ mJy. In Figure 1.3 I plot the 850 μm detection limits for a $L = 5 \times 10^{12}\ L_\odot$ grey-body source and a variety of dust temperatures.

The effect of the strong negative k-correction is very apparent. A typical luminous submm source at high redshift has an almost constant flux density from $z \sim 1 - 10$. Although this potentially pushes detection limits out to far higher redshift than available in other wavebands, redshifts derived from coarse, photometric measurements have very large uncertainties. Also, note the strong dependence on the assumed temperature of the dust: small changes in this can lead to drastically different output fluxes.

Unfortunately, submm observations often shed little light on the precise nature of the source, due to the featureless nature of the grey-body emission. Nevertheless, clues as to the physical conditions within the source can be gleaned under reasonable assumptions. In particular, the far infrared (FIR) luminosity is a useful tracer of the instantaneous star formation rate (SFR). Dust is produced and heated by massive O and B stars, evolving rapidly on

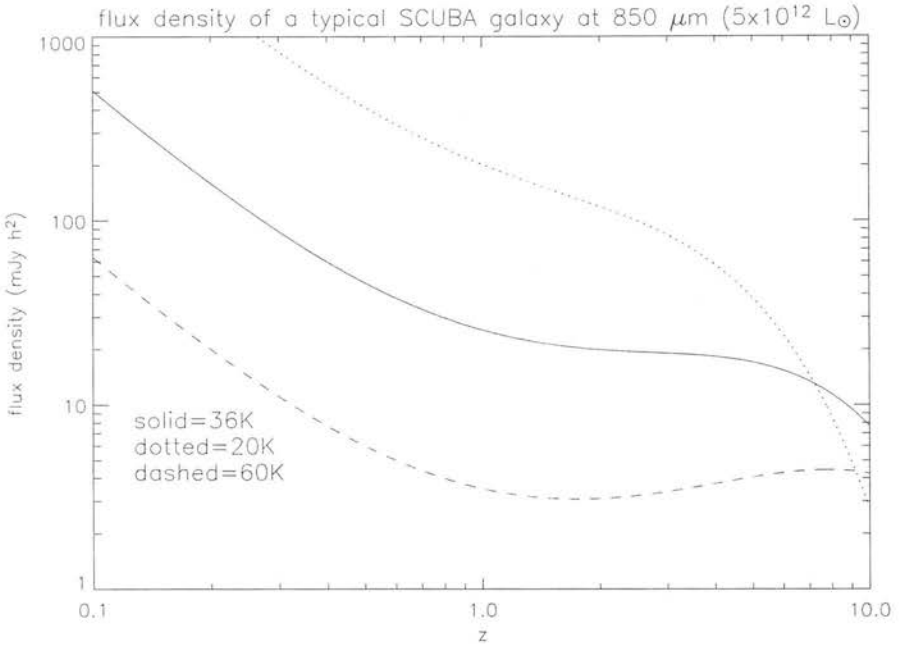

Figure 1.3: Flux density (grey-body derived) of a typical submillimetre source at 850μm in a ΛCDM cosmology ($\Omega_M = 0.3$, $\Omega_\Lambda = 0.7$) for three different dust temperatures. Solid line: $T = 36$ K, dotted line: $T = 20$ K, dashed line: $T = 60$ K. Note the very strong dependence on temperature.

timescales of $\sim 10^7$ years. Thus the FIR emission of a galaxy contains information about the present SFR.

1.2.2 Submillimetre galaxies

The advent of the Submillimetre Common-User Bolometer Array (SCUBA) comissioned on the JCMT in 1997 (Holland 1999) heralded great new developments in the study of the high redshift universe. SCUBA operated at 450 and 850μm, imaging the sky in 2.5 arcminute fields, with a spatial resolution of 14.5 arcseconds at 850 μm. Almost immediately, a new population of faint objects at sub-mJy levels was discovered (see Blain et al. 2002 for a detailed review of the literature).

These SCUBA-detected objects are generally taken to be galaxies, although there is debate as to whether they are in fact galactic in origin, perhaps cold, dusty molecular clouds (Sciama 2000, Lawrence 2001). Nevertheless, the majority view is that they are distant galaxies undergoing vigorous dust-

enshrouded star formation, either extended or confined to the central regions of a galaxy (Scott et al. 2002, Blain et al. 2002, Ivison et al. 2002, Chapman et al. 2004). However, there is the possibility that the emission arises from extensive diffuse dust in more quiescent galaxies at lower redshift (Efstathiou and Rowan-Robinson 2003, Kaviani et al. 2003). Alternatively, the emission could be due to a bright Active Galactic Nucleus (AGN), highly obscured by a surrounding dust torus.

Distinguishing between these scenarios has proved difficult with existing telescopes and instruments. A combination of factors contribute to this uncertainty. The small angular scale of the sources, coupled with the coarse resolution of existing submm instruments, limits the usefulness of observations in trying to determine the precise scale of emission regions. The extreme faintness of submm sources at other wavelengths makes detection of optical/IR/radio counterparts difficult, and there are generally many candidates to choose from within the submm instrument beamsize (Fox et al. 2002). The featureless nature of the typical dust SED holds no useful hints as to the origin of the attenuated light.

Assuming that a submm source has been detected at other wavelengths, a number of approaches can be made in trying to determine the nature of the emission. With either knowledge or reasonable assumptions of the geometry and composition of the absorbing medium, radiative transfer models (eg. Granato et al. 1994, 1996) can be used to predict the SED of a source. A small AGN would produce an SED that peaks at shorter wavelengths as compared to an extended starburst, and would be flatter in the mid-IR. Sadly, the precise geometry of a starbursting region is hard to predict, and is likely to be rather complex.

The nature of submillimetre galaxies

Assuming the high redshift galaxy population hypothesis is correct, it became clear that these so-called submillimetre galaxies (SMGs) were exceptionally luminous objects at high redshift (Hughes et al. 1998), responsible for much of the luminosity emitted by all galaxies throughout the history of the universe (Blain et al. 1999).

It is possible that SMGs are high redshift counterparts to the Ultra-Luminous Infra-Red Galaxies (ULIRGs) discovered in the IR All-Sky Survey

(*IRAS*). These galaxies have a bolometric luminosity in excess of $10^{12}L_{\odot}$ integrated over wavelengths where dust emission dominates (see Sanders and Mirabel 1996 for a review). Another class, the Hyper-Luminous Infra-Red Galaxies (HLIRGs), discovered in follow-up studies of *IRAS* detections (Rowan-Robinson et al. 1991), have bolometric luminosities of $10^{13}L_{\odot}$ and above.

Although detecting submillimetre sources is now relatively routine, asessing their significance is hard due to confusion (noise from the clustering of unresolved sources on beamsize scales) and the difficulty in assigning unique counterparts. Much of the observational efforts concentrate on regions of the sky thoroughly mapped in other wavebands in order to maximise the chances of detecting real, unambiguous SMGs.

SMG surveys

Initial indications that submillimetre-detected sources were massive, star forming systems at high redshift came from Hughes et al. (1998), from a deep submillimetre map of the Hubble Deep Field North. They found 5 bright objects in the submm, with photometric redshifts placing them all at $z > 1$, and four in the range $2 < z < 4$. Derived source counts indicated that massive amounts of star formation are taking place as early as $z > 2$, contrary to expectations at the time (Madau et al. 1996). Extended re-analysis of the field (Peacock et al. 2000, Serjeant et al. 2003a) found tentative evidence of angular clustering.

The SCUBA 8-mJy survey (Scott et al. 2002, Ivison et al. 2002, Fox et al. 2002) was the first major survey designed to identify a significant number of bright submm sources. Observations ran from 1998 to 2001 in the Lockman Hole East and Elias N2 regions of the sky, locations extensively studied at other wavelengths and relatively free of galactic cirrus. In total, 260 arcmin^2 of sky was mapped down to a flux limit of 8 mJy with a signal to noise ratio of $\sigma = 3.5$. Their best estimate of the cumulative source counts at $S_{850} > 8$ mJy is 320^{+80}_{-100} deg^{-2}. Inferred star formation rates of the sources were extremely high, ranging from a few hundred to over a thousand solar masses per year. The comoving number density of such sources was found to be $\sim 10^{-5}$ Mpc^{-3}, comparable to the number density of massive $(3-4L^*)$ ellipticals today. This suggests the possibility that SMGs could be the progenitors of the massive ellipticals we observe today. Indeed, the observed SFRs could form the mas-

sive ellipticals in a short space of time (~ 1 Gyr). If this were the case, then SMGs should be strongly clustered. High-mass luminous objects should be strongly biased towards the peaks in the density field. No conclusive detection of clustering was found, due to the small number of sources available in each region of sky. Nevertheless, the results were still consistent with the strong clustering signal detected for Extremely Red Objects (EROs) by Daddi et al. (2000) (see section 1.2.5 for a description of these galaxies).

Borys et al. (2003) performed a submillimetre survey of the Hubble Deep Field North (HDF). They detected 19 $> 4\sigma$ sources, plus an additional 15 $3.5 < \sigma < 4$ sources. They again failed to detect significant clustering, the small number of sources hampering such efforts. Multi-wavelength follow-up observations are presented in Borys et al. (2004) and Pope et al. (2005). They detect 40 SMGs in the HDF and flanking fields, and use GOODS images to show that three quarters of these have unique optical or IR counterparts. A further 18 % have more than one possible counterpart, leaving only a small fraction still unidentified at other wavelengths. Many were also identified as EROs from their IR colours.

Webb et al. (2003a) present results from the Canada-UK Deep Submillimeter Survey (CUDSS). Their number counts of SMGs with $S_{850} > 3$ mJy are consistent with other published datasets. They find tentative evidence of strong clustering for SMGs, in excess of that seen for Lyman Break Galaxies (see section 1.2.4) and comparable to the clustering as measured for EROs (see section 1.2.5).

A number of other authors have performed surveys in the submillimetre; results for SMG cumulative number counts at both bright and faint flux limits are summarised in Figure 1.4.

Physical properties of SMGs

Deep radio imaging can provide the depth and resolution necessary to examine SMGs in detail. Radio evidence suggests that SMGs are extended, chaotic objects undergoing major mergers (Ivison et al. 2002, Chapman et al. 2003b, Conscelice et al 2003), with extended regions of star formation providing the luminosity (Scott et al. 2002, Ivison et al. 2002, Stevens et al. 2003, Chapman et al 2004).

The fraction of SMGs housing an AGN is unclear at present, with estimated

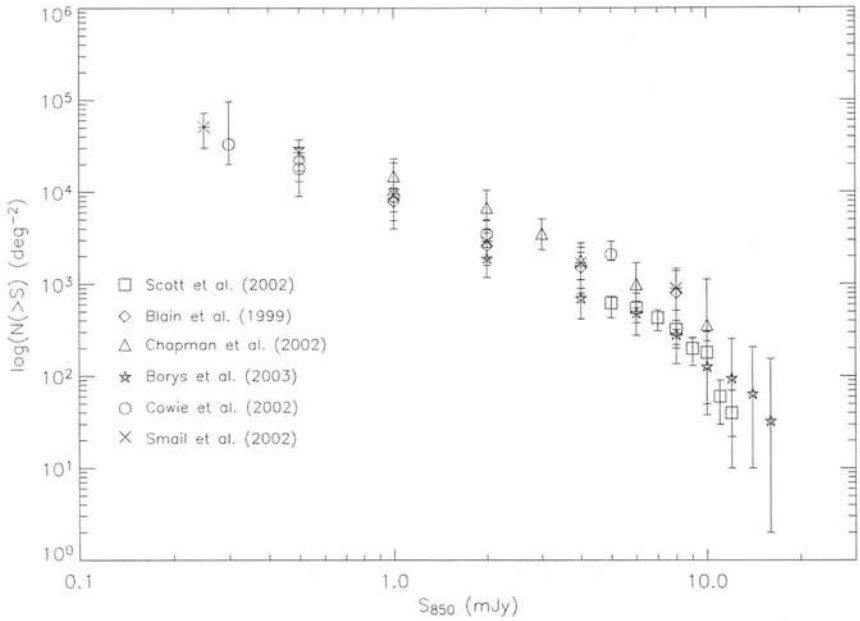

Figure 1.4: Number counts from various submillimetre surveys. Squares are from Scott et al. (2002), diamonds are from Blain et al. (1999), triangles are from Chapman et al. (2002), stars are from Borys et al. (2003), asterisks are from Cowie et al. (2002) and crosses are from Smail et al. (2002a).

fractions as low as $\sim 5\%$ (Almaini et al. 2003). More recent observations suggest a larger fraction, of order 40% (Alexander et al. 2003, Alexander 2004, Swinbank et al. 2004). Nevertheless, in most cases the AGN does not dominate the bolometric luminosity of the source, leaving intense bursts of star formation as the only plausible source of submm emission.

Both luminous radio galaxies and HLIRGs exhibit a tight correlation between their K-band luminosity and redshift (eg. Lilly and Longair 1984, Serjeant et al. 2003b). Interestingly, SMGs do not follow this relation, being fainter in K by 2 magnitudes on average with a large dispersion about the mean (Serjeant et al. 2003b). This is surprising given that HLIRGs at high redshift would have comparable submm fluxes to SMGs, and that SMGs are inferred to have luminosities similar to that of HLIRGs. Clements et al. (2004) find that SMGs are generally less luminous than radio galaxies, and display similar proprties to host galaxies of sub-μJy radio sources.

The masses of SMGs can be probed with interferometry measurements

of carbon monoxide (CO) emission (Genzel et al. 2004). Many are found to be rich in molecular gas, and give corroborating evidence of large far-IR luminosities and star formation rates. Inferred dynamical masses are of order $10^{11} M_{\odot}$, larger than Lyman break galaxies at similar redshifts.

Redshifts of SMGs are exceptionally hard to obtain due to their extreme faintness at other wavelengths, but evidence suggests that most lie at redshifts greater than unity (Chapman et al. 2003a). Indeed, the majority of those with photometric redshifts are located between redshifts 2 and 4 (Smail et al. 2000, 2002). Chapman et al. (2003a) use spectroscopic redshifts of radio counterparts to estimate a mean redshift of $z = 2.4$, and more recently, a median redshift of $z = 2.2$ in a sample of 79 SMGs with spectroscopic redshifts taken by Keck (Chapman et al. 2005).

1.2.3 SHADES

The Scuba HAlf-DEgree Survey (SHADES) will cover half a square degree of sky down to a 4σ detection limit of 8mJy at 850μm, detecting ~ 200 sources in the Subaru Deep Field South and the Lockman Hole regions of the sky (Dunlop 2005, also see `http://www.roe.ac.uk/ifa/shades/` for an overview of the survey and ongoing progress). The SCUBA observations will hopefully be supplemented by observations taken by the Balloon-borne Large Aperture Sub-millimetre Telescope (BLAST), which has been in operation from 2005 onwards. BLAST will observe the same regions of sky as SHADES at wavelengths of 250, 350 and 500 μm. This will allow source redshift estimates to within $\delta z = 0.5$.

The scientific aims of these combined surveys are threefold:

- What is the cosmic history of massive dust-enshrouded star-formation activity?
- Are SCUBA sources the progenitors of present-day massive ellipticals?
- What fraction of SCUBA sources harbour a dust-obscured AGN?

The first question can be answered by using follow-up deep far-IR photometry, which will be able to pin down the bolometric luminosities of the galaxies in the infra-red. This is where the collaboration with the BLAST experiment is crucial, as this experiment will provide the far-IR data needed to constrain

the bolometric luminosity of the detected galaxies. The BLAST survey will also provide photometric redshifts with an accuracy of $\delta z \simeq \pm 0.5$.

In determining whether the SCUBA galaxies are the progenitors of todays massive ellipticals, the clustering of the SCUBA sources must be determined. A statistically significant number of sources (with redshifts) over a large area is required to measure the clustering on scales of ~ 10 Mpc.

In order to answer the final question, follow-up observations by *Spitzer* will detect any rest-frame mid-IR emission in the sources of interest. This should be enough to determine the fraction of the SCUBA sources that are home to an active supermassive black hole, heavily extincted by the prescence of dust. van Kampen et al. (2005) outline predictions for the submillimetre population catalogued in SHADES. A number of different scenarios concerning the origin and nature of the submm sources are considered, and the clustering and redshift properties of each are analysed. The redshift distributions of bright submm sources are found to be markedly different for the models under consideration, even when smoothed with a Gaussian filter of width 0.4, comparable to the accuracy obtainable with photometric redshifts. The sky-averaged correlation function is used to measure the predicted of clustering of sources, due to the small number of sources detectable in SHADES. This method was used in the earliest galaxy redshift suveys, when small datasets were the norm. Fits to the standard correlation function $w(\theta) = (\theta/A)^{-0.8}$ and a general two-parameter power law were obtained. All the models considered exhibit sufficiently strong clustering, measurable with the final SHADES dataset. Combining clustering data with the redshift information shows marked differences between the models, implying that SHADES may be able to confirm or rule out potential formation and evolutionary scenarios for bright submillimetre galaxies.

Mortier et al. (2005) describes the progress made so far in SHADES. Reanalysis of the region already covered in the SCUBA 8-mJy Survey using the new source extraction techniques recover 13 of the 17 most significant sources originally detected. All of the recovered sources have identified counterparts in the radio. They derive a source density of 650 ± 50 deg^{-2}, more than sufficent for clustering measurements given the entire survey area. At the time of writing, around 40 percent of the survey had been completed before the catastrophic failure and retirement of SCUBA. As of October 2005, the

remainder of SHADES is being undertaken using AZTEC, the latest submillimetre detector installed on the JCMT.

1.2.4 Lyman Break Galaxies

The Lyman break is a pronounced discontinuity at 912Å in the spectrum of galaxies undergoing vigorous periods of star formation due to the hydrogen ionisation edge, heightened by absorption of UV light by local reservoirs of gas. The feature is redshifted into the optical beyond $z \sim 2$. As such, detection and non-detection of a galaxy in different filters pins down the location of the Lyman break in the galaxy spectrum, yielding a rough redshift. This technique (Steidel and Hamilton 1993) is illustrated in Figure 1.5. Care must be taken to ensure that samples are not contaminated with interlopers (both galactic and stellar). Careful colour selection criteria can help minimise the number of interlopers in a sample.

These Lyman Break Galaxies (LBGs) are generally found in the redshift range $2.5 < z < 5$ (Steidel et al. 1999, Giavalisco 2002), although candidates at $z \sim 6$ have been discovered (Stanway et al. 2004), and there is tentative evidence for detections as distant as $z \sim 10$ (Bremer et al. 2004).

The spectra of LBGs are generally similar to those of local starbursting galaxies (eg. Papovich 2001). The prescence of absorption lines suggest the prescence of metals in the LBG interstellar medium. Measured linewidths indicate the prescence of strong outflows, likely caused by supernova explosions and strong stellar winds (Pettini et al. 2001), again implying high star formation rates. Derived SFRs are in the range $10 - 100\ M_{\odot}\ \mathrm{yr}^{-1}$, although possible candidates with SFRs of order $10^3 M_{\odot}\ \mathrm{yr}^{-1}$ have been detected (Bentz et al. 2004). The metallicity of LBGs is uncertain due to the saturation of absorption lines, but can be constrained to within an order of magnitude using optical line ratios. Using this technique, ISM metallicites in the range $0.1 < Z/Z_{\odot} < 1.0$ are inferred (Pettini et al. 2001).

The stellar mass of the LBGs is generally determined by fitting the UV and optical photometry to stellar synthesis population models. Athough this technique can only constrain the mass of the starbursting population and not any older stars present, inferred masses range between $10^9 - 10^{11} M_{\odot}$, together with large quantities of dust (eg. Papovich et al. 2001, Shapley et al. 2001). This of course yields lower limits to the masses of the galaxies.

Morphologies of LBGs can be probed using HST, which can resolve the individual star forming regions even at high redshift (Steidel et al. 1996, Lotz et

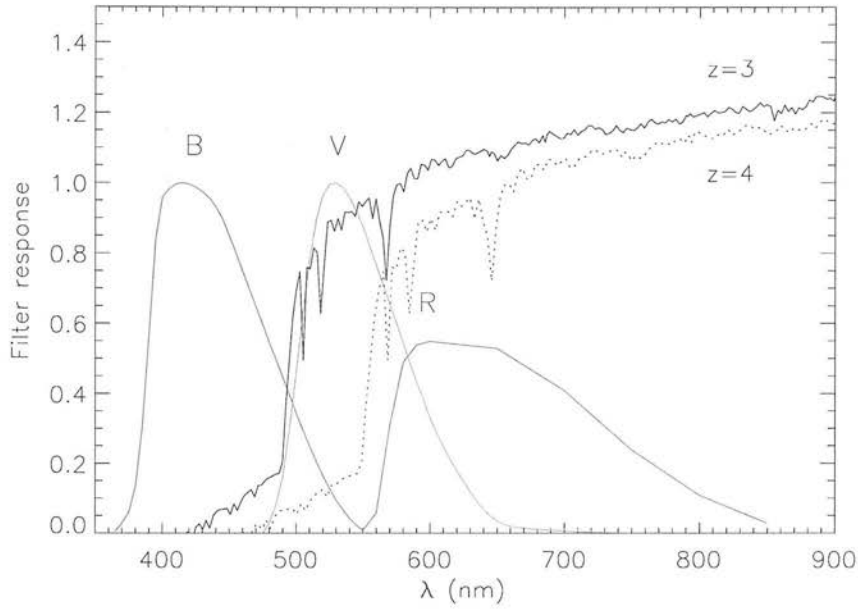

Figure 1.5: The Lyman break technique. A typical galaxy SED (in arbitary luminosity units) at z = 3 (solid line) and z = 4 (dotted line) is plotted together with the response of standard *BVR* Johnson filters. At z = 3, the galaxy is detected in *V* but not *B*, and is thus a *B*-band dropout. At z = 4, the same galaxy becomes a *V*-band dropout. Note that in reality, specialised filter sets tend to be used.

al. 2004). LBGs are in general smaller and more irregular than local galaxies with a similar B-band luminosity, with a wide range of observed morphologies.

The large number of detected LBGs and their well constrained redshifts allow fairly accurate measurements of their clustering properties. Indeed, LBGs are found to be strongly clustered (eg. Steidel et al. 1998, Giavalisco et al. 1998, Giavalisco and Dickinson 2001). However, the samples used cover small regions of sky, and results differ quite markedly from sample to sample. Nevertheless, the uncertainties tend to bias clustering estimates to lower values (the integral constraint), so it seems very likely that the LBGs are indeed strongly clustered. Thus, LBGs must be biased with respect to the overall matter distribution, being found preferentially in regions of significant overdensities. Some observations of highly concentrated regions of LBGs may indicate the earliest stages of cluster or supercluster evolution (Steidel et al. 1998).

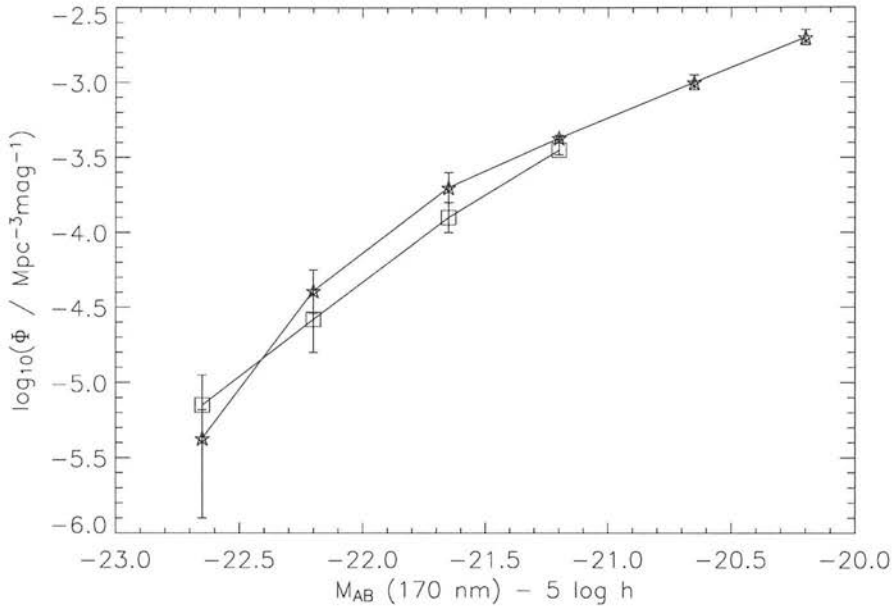

Figure 1.6: Luminosity functions of Lyman Break galaxies. Data from Steidel et al. (1999), stars are observations at z = 3 and squares are at z = 4.

Since both LBGs and SMGs appear to be star-forming systems at high redshift, it is natural to ask whether there is any overlap or correlation between the populations. Are they distinct objects with wildly differing properties, or simply from the same underlying population, uncovered by different selection techniques? Chapman et al. (2000a) present results of a SCUBA survey of known LBGs. They find that LBGs do not contribute to the bright end of the SMG population (their mean LBG flux is $S_{850} = 0.6 \pm 0.2$ mJy).

Webb et al. (2003b) find significant cross-correlation between LBGs and SMGs in the CUDSS fields. While this cannot say whether there is any specific link between the two populations, it does imply that they both trace out the same large-scale structure, an unsurprising result if both populations are the largest sites of baryonic material at high redshifts.

1.2.5 Extremely Red Objects

Extremely Red Objects (EROs) are a population of very red galaxies ($R - K > 5 - 6$) and are routinely detected in near-IR surveys (Hu and Ridgway 1994, Thompson et al. 1999, Barger et al. 1999). The precise nature of EROs

remains a point of contention. They could be old, passive ellipticals (pEROs), or strongly dust-extincted starforming or active galaxies (dsfEROs). There is evidence for a mixture of both extremes. Some have been spectroscopically confirmed as $z \sim 1$ ellipticals (Dunlop et al. 1996, Liu et al. 2000, Roche et al. 2002), and Caputi et al. (2004) find that the SEDs of some EROs are well-modelled by a single starburst at $z \sim 5$ with consequent passive evolution. Photometric and spectroscopic methods of separating the two populations yield roughly equal numbers in both classes (eg. Mannucci et al 2002, Cimatti et al. 2002).

Many authors have found ERO counterparts to submillimetre sources (Smail et al. 1999, Wehner et al. 2002, Webb et al. 2004, Pope et al. 2005), implying that at least some EROs are undergoing massive bouts of dust-obscured star formation (assuming this interpretation of the nature of SMGs holds).

EROs are highly clustered objects (Daddi et al. 2000, Roche et al. 2002), with clustering strengths of more than a magnitude higher than all galaxies down to the same magnitude limit of the ERO samples, implying that they are the progenitors of present-day massive ellipticals. Indeed, Roche et al. find the correlation length of bright EROs to be $r_o \sim 10 - 13\ h^{-1}\mathrm{Mpc}$, much higher than $r_o \sim 8\ h^{-1}\mathrm{Mpc}$, the measured value for local giant ellipticals.

1.2.6 The star formation history of the universe

What is the global history of star formation over time? When did the majority of stars in galaxies form? There are two distinct approaches to measuring the star formation history of the universe. The first, and perhaps more traditional, involves estimating the instantaneous star formation rate by observing a galaxy at a particular redshift. Particular spectral features provide the necessary relationship between flux and star formation rate, and there are a number avaliable for SFR estimation, each with its advantages and disadvantages. Observations at a range of redshifts, calibrated properly, are combined to give an overall view of the global star formation rate as a function of time. This approach was pioneered by Madau et al. (1996) and Lilly et al. (1996), and graphs of star formation as a function of redshift are often called 'Madau-Lilly plots'.

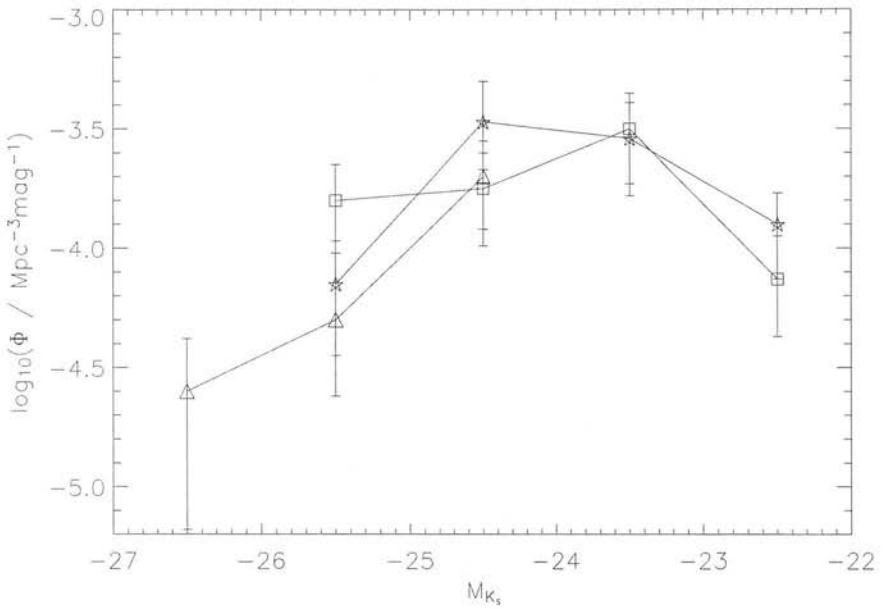

Figure 1.7: Extremely Red Object luminosity functions at different redshifts. Data from Caputi et al. (2004); stars are $z_{\rm phot}$=1.0, squares are $z_{\rm phot}$=1.5 and triangles are $z_{\rm phot}$=2.0.

Nevertheless, care must be taken when interpreting the results. Observations are invariably flux-limited; corrections for galaxies below the detection limit must be made to avoid underestimating the global star formation rate. One must also carefully consider the role of dust; if extinction is ignored the measured SFR can be biased low to its true value. See Somerville, Primack and Faber (2001) for a useful discussion on the potential pitfalls in creating and interpreting Madau plots.

Alternatively, one can examine the entire spectrum of a galaxy to infer its star formation history, as differing conditions in a galaxy (such as instantaneous SFR or metallicity) are reflected in the stellar populations created. This 'fossil record' approach (eg. Panter, Heavens and Jimenez 2003) can use local, high quality data to infer conditions at high redshift. However, intensive computational effort and sophisticated data compression techniques are required to explore the highly-degenerate parameter space and produce unique solutions.

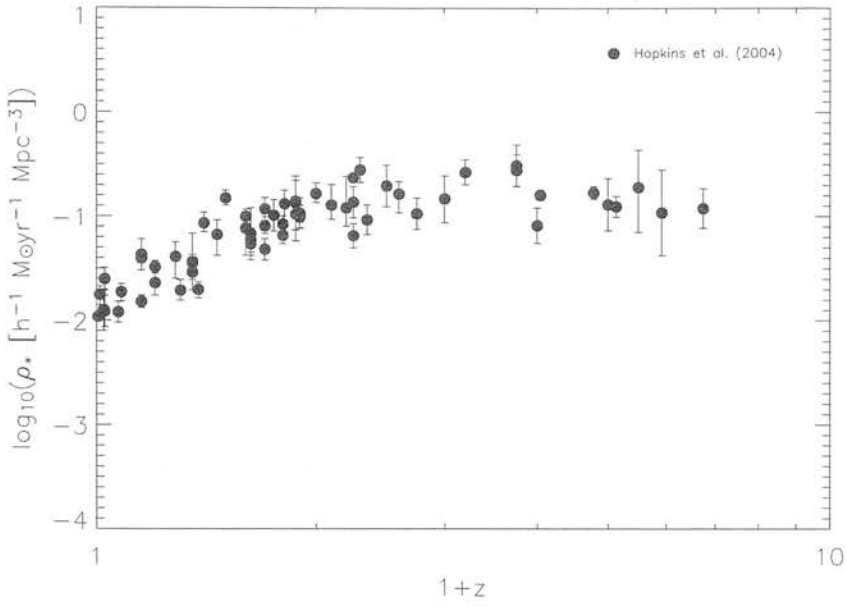

Figure 1.8: The star formation history of the universe, as compiled by Hopkins (2004). More details are available in the text.

In Figure 1.8 I plot the star formation history of the universe, as compiled by Hopkins (2004) from a variety of estimations at various redshift. All the data points are incompleteness-corrected and converted to the same ΛCDM cosmology ($\Omega_M = 0.3, \Omega_\Lambda = 0.7$). The data-points have been corrected for dust extinction assuming a uniform extinction for each observational sample. The data points to an increase in star formation out to $z \simeq 1$, then a plateau or slight decline out to $z \sim 6$. As detector technology improves (such as the imminent SCUBA2 on the JCMT) and observing high redshift sources becomes routine, it will be interesting to see where the latest SFR estimates land on the Madau-Lilly plot.

1.3 Theory of galaxy formation

1.3.1 Cosmology

How does structure in the universe arise? What is the physical origin of the matter distribution we observe in galaxy surveys? Modern Big Bang cos-

mology describes an initially dense and homogenous universe that cools and expands with passing time. In order for structure to form, there must be some departure from homogeneity at some early stage. It seems likely that initial quantum fluctuations in the density field at very early times ($< 10^{-35}$ s after the initial singularity) could provide the 'seeds' for future structure formation. Early overdensities, amplified in the inflationary stage of evolution, grow ever denser with the expansion of the universe. Study of the processes of structure formation needs an appropriate background cosmology to work in.

Friedmann equations

The Robertson-Walker (RW) metric describes the evolution of a homogenous, isotropic expanding universe (Peacock 1999):

$$c^2 d\tau^2 = c^2 dt^2 - R^2(t)\left[dr^2 + S_k^2(r) d\psi^2\right], \tag{1.5}$$

where $R(t)$ is the scale factor, r is (a time-independent) comoving distance and:

$$S_k(r) = \begin{cases} \sin r & k = 1 \\ \sinh r & k = -1 \\ r & k = 0. \end{cases} \tag{1.6}$$

Inserting the Robertson-Walker metric into the Einstein equations leads to the Friedmann equations, which describe the time-evolution of the scale factor

$$\left(\frac{\dot{R}}{R}\right)^2 = -\frac{kc^2}{R^2} + \frac{8\pi G\rho}{3}, \tag{1.7}$$

$$\ddot{R} = -\frac{4\pi G R}{3}\left(\rho + \frac{3p}{c^2}\right), \tag{1.8}$$

where ρ is the average density of the universe.

We define a dimensionless scale factor $a = R/R_0$, where R_0 is the present-day value of R. From this comes the dimensionless expansion rate

$$H = \frac{\dot{a}}{a}. \tag{1.9}$$

At small distances, this is equal to the constant of proportionality in Hubble's law for the recession velocity of galaxies $v = H_o d$.

We can now write equation (1.7) as

$$H^2 - \frac{8\pi G\rho}{3} = -\frac{kc^2}{a^2 R_o^2}. \tag{1.10}$$

Recall that for a flat universe, we have $k = 0$. It is clear that there is a critical value of the density for which this is satisfied:

$$\rho_c = \frac{3H^2}{8\pi G}. \tag{1.11}$$

A universe with $\rho > \rho_c$ will be spatially closed, and one with $\rho < \rho_c$ will be spatially open. It is convenient to define a density parameter, the ratio between density and critical density:

$$\Omega \equiv \frac{\rho}{\rho_c} = \frac{8\pi G\rho}{3H^2}. \tag{1.12}$$

There are three main components that contribute to the overall density of the universe, each with a distinct equation of state:

- non-relativistic matter (baryons+dark matter): $p_m = 0, \rho_m \propto a^{-3}$
- relativistic matter (eg neutrinos) and radiation: $p_r = \frac{1}{3}\rho_r c^2, \rho_r \propto a^{-4}$
- vacuum energy: $p_\Lambda = -\frac{1}{3}\rho_\Lambda c^2, \rho_\Lambda = \text{constant}$

The density parameter can be split up into an expression for each of the principal components of the universe at a given epoch:

$$\Omega_m(a) \equiv \frac{\rho_m}{\rho_c} = \frac{8\pi G\rho_m}{3H^2}, \tag{1.13}$$

$$\Omega_r(a) \equiv \frac{\rho_r}{\rho_c} = \frac{8\pi G\rho_r}{3H^2}, \tag{1.14}$$

$$\Omega_\Lambda(a) \equiv \frac{\rho_\Lambda}{\rho_c} = \frac{8\pi G\rho_\Lambda}{3H^2}, \tag{1.15}$$

such that $\Omega = \Omega_m + \Omega_r + \Omega_\Lambda$ is the total density of the universe. Thus the value of these parameters today is simply derived using the present Hubble constant H_o.

Introducing these into Friedmann's equation gives an expression for the evolution of the Hubble constant with the scale factor a:

$$H^2(a) = H_o^2\Big[(1-\Omega)a^{-2} + \Omega_\Lambda + \Omega_m a^{-3}. + \Omega_r a^{-4}\Big]. \tag{1.16}$$

In general, this equation must be integrated numerically, although there are simple analytic solutions for flat matter-dominated or radiation-dominated universes.

Working with the scale factor is not particularly intuitive; it is more instructive to work with observable quantities wherever possible.

Consider the light we recieve from a distant galaxy. If a particular spectral feature has rest wavelength λ, this feature will be shifted to longer wavelengths. We define redshift $z \equiv \Delta\lambda/\lambda$, where $\Delta\lambda$ is the observed shift in wavelength. By considering the path of a photon in the RW metric, it can be shown that $1 + z = R_o/R(t) = a^{-1}$. From this, we can connect the evolution of the Hubble constant to observable quantities:

$$H^2(a) = H_o^2\Big[(1-\Omega)(1+z)^2 + \Omega_\Lambda + \Omega_m(1+z)^3 + \Omega_r(1+z)^4\Big]. \tag{1.17}$$

How is the rate of change of the Hubble parameter evolving with time? We can define a dimensionless deceleration parameter

$$q \equiv -\frac{\ddot{a}a}{\dot{a}^2}. \tag{1.18}$$

This can be inserted into the second Friedmann equation, yielding

$$q = \frac{4\pi G}{3H^2}\left(\rho + \frac{3p}{c^2}\right). \tag{1.19}$$

For $q > 0$, the expansion of the universe is decelerating, and for $q < 0$ the expansion is accelerating.

How do we link this to observable quantities? Using the equations of state and density parameters for each component of the universe, we can see that

$$q(a) = \frac{\Omega_m(a)}{2} + \Omega_r(a) - \Omega_\Lambda(a). \tag{1.20}$$

High redshift supernovae light curves (eg. Perlmutter et al. 1998), considered to be standard candles, peak at dimmer apparent magnitudes than expected in an Einstein-de Sitter Universe. This can be explained by the presence of a significant cosmological constant, producing an accelerating expansion rate. In other words, we appear to inhabit a universe with $q < 0$.

1.3.2 Distances in cosmology

How far is far? There are numerous definitions of distance in cosmology, and one must take care to use the correct form in the appropriate situations. As a start, it is useful to define the *comoving radial distance*. Starting with the FW

metric, note that for photons $c^2 d\tau^2 = 0$, and that we need only consider the radial component, hence $d\psi^2 = 0$. One then integrates over redshift to give:

$$R_0 S_k(r) = \frac{c}{H_0} \int_0^z \left[\Omega_M (1+z')^3 + \Omega_R (1+z')^4 + \Omega_k (1+z')^2 + \Omega_\Lambda\right]^{-1/2} \mathrm{d}z'. \quad (1.21)$$

This has analytic solutions for matter-dominated universes, but in vacuum energy cosmologies the full numerical integral must be performed.

The *angular diameter distance* is the ratio of an object's physical size to its angular extend (in radians), and is easily derived from the comoving radial distance:

$$D_A = (1+z)^{-1} R_0 S_k(r). \quad (1.22)$$

The *luminosity distance* is a useful tool when deriving fluxes from cosmological sources. Consider the usual relation $S_\nu = L_\nu / 4\pi R_0^2 S_k^2(r)$. At large distances, photon energies are reduced by a factor $(1+z)$, as is the rate of arrival of photons. The bandwidth is reduced by a factor $(1+z)$, and the photons *observed* at frequency ν were *emitted* at frequency $\nu(1+z)$. Putting it all together, we have

$$S_\nu(\nu) = \frac{L_\nu([1+z]\nu)}{4\pi R_0^2 S_k^2(r)(1+z)}, \quad (1.23)$$

and the luminosity distance is thus given by

$$D_L = (1+z) R_0 S_k(r). \quad (1.24)$$

1.3.3 The origins of structure: linear perturbations

We live in a highly structured universe, with homogeneity only arising on the largest scales (> 100 Mpc). The cosmological framework laid out in the previous section describes a homogenous universe; any small initial perturbations in the density field are amplified by gravity. This must have occured early on in order to form the structure we observe (and indeed require to exist). Their origin is unknown, although quantum fluctuations amplified by a period of inflation is perhaps the best explanation at present. This predicts a simple Gaussian distribution for perturbations, and explains many observed properties of the cosmic microwave background.

The smooth background universe can be described as a perfect fluid. The equations of fluid motion are the Euler equation, the continuity equation and the Poisson equation:

$$\frac{\partial \mathbf{v}}{\partial t} + (\mathbf{v}.\nabla)\mathbf{v} = -\frac{\nabla p}{\rho} - \nabla\phi, \quad (1.25)$$

$$\frac{\partial \rho}{\partial t} + (\mathbf{v}.\nabla)\rho = -\rho \nabla.\mathbf{v}, \tag{1.26}$$

$$\nabla^2 \phi = 4\pi G \rho. \tag{1.27}$$

Consider some small perturbations about a homogenous background, such that $\rho = \rho_0 + \delta\rho$, $\mathbf{v} = \mathbf{v}_0 + \delta\mathbf{v}$, $p = p_0 + \delta p$ and $\Phi = \Phi_0 + \delta\Phi$. The continuity equation then becomes

$$\left(\frac{\partial}{\partial t} + (\mathbf{v}_0 + \delta\mathbf{v}).\nabla\right)(\rho_0 + \rho) = -(\rho_0 + \delta\rho)\nabla.(\mathbf{v}_0 + \delta\mathbf{v}). \tag{1.28}$$

For the case of no perturbations, $\delta = 0$ and we have the zeroth order equation $(\partial/\partial t + \mathbf{v}_0.\nabla)\rho_0 = -\rho_0 \nabla.\mathbf{v}_0$.

On expanding equation (1.28), subtracting the zeroth order equation, removing second order terms about δ and noting that ρ_0 is homegenous, we derive the linearized equation

$$\left(\frac{\partial}{\partial t} + (\mathbf{v}_0.\nabla)\right)\delta\rho = -\rho_0 \nabla.\delta\mathbf{v} - \delta\rho \nabla.\mathbf{v}_0. \tag{1.29}$$

For the Euler equation, we have

$$\left(\frac{\partial}{\partial t} + (\mathbf{v}_0 + \delta\mathbf{v}).\nabla\right)(\mathbf{v}_0 + \delta\mathbf{v}) = \frac{\nabla(p_0 + \delta p)}{\rho_0 + \delta\rho} - (\nabla\Phi_0 + \nabla\delta\Phi). \tag{1.30}$$

The zeroth order equation is $(\partial/\partial t + (\mathbf{v}_0.\nabla))\mathbf{v}_0 = -\nabla p_0/\rho_0 - \nabla\Phi_0$. Following the above procedure, we obtain the the linearized Euler equation:

$$\left(\frac{\partial}{\partial t} + (\mathbf{v}_0.\nabla)\right)\delta\mathbf{v} = -\frac{\nabla p_0}{\rho_0} - \nabla\delta\Phi - (\delta\mathbf{v}.\nabla)\mathbf{v}_0. \tag{1.31}$$

Perturbing the Poisson equation, we have

$$\nabla^2(\Phi_0 + \delta\Phi) = 4\pi G(\rho_0 + \delta\rho), \tag{1.32}$$

and the zeroth order equation is $\nabla^2\Phi_0 = 4\pi G\rho_0$. Again, following the above procedure we derive

$$\nabla^2\delta\Phi = 4\pi G\delta\rho. \tag{1.33}$$

At this point it is convenient to define the fractional density perturbation $\delta \equiv \delta\rho/\rho_0$. As $\mathbf{v}_0 = H\mathbf{x}_0$, it follows that $(\delta\mathbf{v}.\nabla)\mathbf{v}_0 = H\delta\mathbf{v}$. We now have the linearised fluid equations:

$$\frac{\partial\delta\mathbf{v}}{\partial t} + (\mathbf{v}_0.\nabla)\delta\mathbf{v} = -\frac{\nabla\delta p}{\rho_0} - \nabla\delta\Phi - H\delta\mathbf{v}, \tag{1.34}$$

$$\frac{\partial \delta}{\partial t} = \nabla . \delta \mathbf{v}, \tag{1.35}$$

$$\nabla^2 \delta\Phi = 4\pi G \rho_0 \delta. \tag{1.36}$$

We now wish to recast these equations in comoving rather than proper units; this is the easiest way to see inhomogenities growing against a uniformly expanding background. Thus, proper positions are written as $\mathbf{x}(t) = a(t)\mathbf{r}(t)$, and the peculiar velocity is $\delta\mathbf{v}(t) = a(t)\mathbf{u}(t)$. Derivatives also need to be recast in comoving coordinates: $\nabla_x = (1/a)\nabla_r$. In the following, I will omit the subscipts on ∇ for clarity, but it is important to remember that this transformation has occured.

The Euler and continuity equations thus become

$$\dot{\mathbf{u}} + 2\frac{\dot{a}}{a}\mathbf{u} = \frac{1}{a^2}\nabla\delta\Phi - \frac{1}{a^2\rho_0}\nabla\delta p, \tag{1.37}$$

$$\dot{\delta} = -\nabla . \mathbf{u}. \tag{1.38}$$

If we consider a matter-dominated universe the pressure term in equation (1.37) can be neglected. One can now use the Euler equation to eliminate the velocity in the continuity equation and derive a second order differential equation for the density field, also known as the *growth equation*. Moving to Fourier space, we expand the density perturbation in Fourier modes (assuming gaussian fluctuations) $\delta \propto \exp(-i\mathbf{k}.\mathbf{r})$. Given that each k mode evolves independently, we have

$$\ddot{\delta} + 2\frac{\dot{a}}{a}\dot{\delta} - 4\pi G\rho_0\delta = 0. \tag{1.39}$$

A linear second-order differential equation has a general solution of the form $\delta(t) = A_1 D_1(t) + A_2 D_2(t)$ where $D_1(t)$ and $D_2(t)$ are independent solutions. One of these will grow with time, and one will decay with time. We need only consider the growing solution. In the linear regime, the growth of perturbations scales as

$$\delta(t) = \delta(t_0)\frac{D_1(t)}{D_1(t_0)}, \tag{1.40}$$

where t_0 is the present day. $D_1(t)$ is generally referred to as the growth factor. For some cosmologies, it has a simple analytic solution. For example, in an Einstein de-Sitter universe ($\Omega_M = 1, \Omega_R = \Omega_\Lambda = 0$), the growth factor scales as

$D_1(t) \propto a(t)$. In a ΛCDM universe, there is no simple analytic solution, and a numerical integration must be performed:

$$D_1(t) \propto \frac{(\Omega_\Lambda a^3 + \Omega_R a + \Omega_M)^{1/2}}{a^{3/2}} \int_0^a \frac{da\ a^{3/2}}{(\Omega_\Lambda a^3 + \Omega_R a + \Omega_M)^{3/2}}. \tag{1.41}$$

Nevertheless, an accurate fitting formula is available (Carrol, Press and Turner 1992), remembering that $a \equiv (1+z)^{-1}$:

$$D_1(z) = (1+z)^{-1} \frac{5\Omega(z)}{2} \left(\Omega^{4/7}(z) - \Omega_\Lambda(z) + \left[1 + \frac{\Omega(z)}{2}\right]\left[1 + \frac{\Omega_\Lambda(z)}{70}\right] \right)^{-1}, \tag{1.42}$$

where $\Omega(z)$ is simply equation (1.12) evolving as a function of redshift.

1.3.4 Spherical collapse of overdensities

The above approach for characterising perturbations is only valid for very small values of δ. Structure in the universe is clearly non-linear, and so a different approach is required. In an Einstein de-Sitter Universe, we can proceed in an analytic fashion. The spherical collapse model considers an overdense sphere in a universe of mean density ρ and overdensity δ that will collapse under gravity to form an object of mass M. The matter outside the sphere has no effect on the dynamics of the collapse, analogous to Birkhoff's theorem in General Relativity. The evolution of such a sphere in an Einstein-de Sitter universe is governed by an equation equivalent to the Friedmann equation, and is just the standard Newtonian result for a test particle influenced by the overdense sphere (Peacock 1999, Benson 2000):

$$\frac{d^2r}{dt^2} = -\frac{GM}{r^2} = -\frac{4\pi G}{3}\rho(1+\delta)r. \tag{1.43}$$

Multiplying (1.43) by dr/dt and integrating yields

$$\frac{1}{2}\left(\frac{dr}{dt}\right)^2 - \frac{GM}{r} = E. \tag{1.44}$$

In this, E is a constant of integration, equivalent to the specific energy of the perturbation. We set to $E < 0$, in order for the perturbation to collapse. Rearranging (1.44), we get

$$\frac{r^{1/2}dr}{(GM - |E|r)^{1/2}} = \sqrt{2}\mathrm{d}t. \tag{1.45}$$

This differential equation can be tackled by letting

$$r = \frac{GM(1-\cos\theta)}{2|E|} = \frac{GM\cos^2(\theta/2)}{|E|}.$$

Differentiating this yields

$$\mathrm{d}r = \frac{GM}{|E|}\cos(\theta/2)\sin(\theta/2)\mathrm{d}\theta.$$

Applying this to equation (1.45), we have

$$\frac{GM}{|E|^{3/2}}\frac{\sin^2(\theta/2)\cos(\theta/2)\mathrm{d}\theta}{(1-\sin^2(\theta/2))^{1/2}} = \sqrt{2}\mathrm{d}t, \tag{1.46}$$

which, using the fact that $\cos^2(\theta/2) + \sin^2(\theta/2) = 1$, simplifies to

$$\frac{GM}{2|E|^{3/2}}(1-\cos(\theta))\mathrm{d}\theta = \sqrt{2}\mathrm{d}t, \tag{1.47}$$

and integrating this yields

$$\frac{GM}{(2|E|^{3/2})}(\theta - \sin(\theta)) = t - t_0. \tag{1.48}$$

From the expression for r above, we see that there is a maximium value for the radius $r_{max} = GM/|E|$, occuring at $\theta = \pi$:

$$r = \frac{r_{max}}{2}(1-\cos\theta).$$

At $t = 0$, $r = \theta = 0$ and so $t_0 = 0$. Hence, (1.48) becomes

$$\frac{GM}{(2|E|^{3/2})}(\theta - \sin\theta) = t. \tag{1.49}$$

We now wish to derive a result for the overdensity at collapse. Using $\sin\theta = \theta - \theta^3/3! + \theta^5/5! - \cdots$ and $\cos\theta = 1 - \theta^2/2! + \theta^4/4! - \cdots$, and writing $t_{max} = GM/(2|E|)^{3/2}$, we get

$$\frac{r}{r_{max}} = \frac{\theta^2}{4} - \frac{\theta^4}{48} + \cdots, \tag{1.50}$$

$$\frac{t}{t_{max}} = \frac{1}{\pi}\left(\frac{\theta^3}{6} - \frac{\theta^5}{120} + \cdots\right). \tag{1.51}$$

To first order, from (1.51) we get

$$\theta \simeq \left(\frac{6\pi t}{t_{max}}\right)^{1/3}, \tag{1.52}$$

which can be substituted into (1.51), giving

$$\theta^3 \simeq \frac{6\pi t}{t_{max}}\left[1 + \frac{1}{20}\left(\frac{6\pi t}{t_{max}}\right)^{2/3}\right], \tag{1.53}$$

and on expanding this expression

$$\theta^2 \simeq \left(\frac{6\pi t}{t_{max}}\right)^{2/3}\left[1+\frac{1}{30}\left(\frac{6\pi t}{t_{max}}\right)^{2/3}\right]. \tag{1.54}$$

If we substitute this into (1.50) and retain only terms of order $(6\pi t/t_{max})^{2/3}$ we get

$$\frac{r}{r_{max}} = \frac{1}{4}\left(\frac{6\pi t}{t_{max}}\right)^{2/3}\left(1-\frac{1}{20}\left[\frac{6\pi t}{t_{max}}\right]^{2/3}\right). \tag{1.55}$$

Now, at a sufficiently early time $t_i \gg t_{max}$ the perturbation is very small ($\delta_i \ll 1$). For a given perturbation radius r_i the mass inside the sphere is

$$M = \frac{4\pi}{3}\rho_i r_i^3. \tag{1.56}$$

As time passes and the collapse progresses, the mass inside the sphere remains constant and thus the density will rise, given by

$$\rho(t) = \frac{3}{4\pi}\frac{M}{r(t)^3}. \tag{1.57}$$

Substituting equation (1.56) and dividing by the mean density, we have

$$\frac{\rho(t)}{\rho_i} = \frac{3}{4\pi}\frac{M}{\rho_i r(t)^3},$$

and finally

$$1+\delta(t) = \frac{\rho_i}{\rho(t)}\frac{r_i^3}{r(t)^3}. \tag{1.58}$$

Eliminating r_i and $r(t)$, we derive

$$\delta(t) \simeq \frac{3}{20}\left(\frac{6\pi t}{t_{max}}\right)^{2/3}. \tag{1.59}$$

Given that in an EDS universe $a(t) \propto t^{2/3}$, it is clear that we have recovered the standard EDS result $\delta \propto a$.

Neglecting dissipative forces, the sphere will collapse to a point at $t = 2t_{max}$, and the extrapolated linear overdensity at this point is given by

$$\delta_{lin} = \frac{3}{20}(12\pi)^{2/3} \simeq 1.686. \tag{1.60}$$

Of course, collapse to a point cannot occur in practice, as substructure will lead to time-varying potentials, allowing exchange of energy between particles and introducing random motions, halting the collapse. At $t = 3t_{max}/2$ the kinetic energy of collapse is equal to half the gravitational potential energy,

and the radius of the sphere is half its maximum value. This is the condition for virialisation. If we assume that virialisation has completed at the time where collapse to a point would have occured, it can be shown that $\delta_{vir} = 18\pi^2 \simeq 178$.

For more general cosmologies, the analysis is not so simple. For open universes with no vacuum energy, Lacey and Cole (1993) derive analytic expressions for δ_{lin} and δ_{vir}, and for flat universes with a vaccum enegery, Eke et al. (1996) give numerical expressions for calculating both quantities. An approximation is given by White et al. (1993), and has a weak dependence on the matter content of the universe

$$1 + \delta_{vir} \simeq 178\Omega_M^{-0.6}. \tag{1.61}$$

Now we can define exactly what we mean by a dark matter halo: a spherical region of space where the mean overdensity is equal or greater to the value given by equation (1.61). Nevertheless, the literature usually assumes a value of $1 + \delta_{vir} \simeq 200$, taking into account the uncertainties in the precise time of virialisation.

Given a mass M and virial radius r_{vir}, other properties of a halo can easily be derived. The mean density of such a halo is just

$$\bar{\rho}(r) = \frac{3M}{4\pi G r_{200}^3}. \tag{1.62}$$

Alternatively, we can define the mean density in terms of the circular velocity $V_{200} = (GM/r_{200})^{1/2}$, yielding

$$\bar{\rho} = \frac{3V_{200}^2}{4\pi G r_{200}^2}. \tag{1.63}$$

Substituting equation (1.61) into this and noting that $\rho_c \equiv 3H(z)^2/8\pi G$ shows how the circular velocity and radius of a halo vary with redshift:

$$V_{200} = (9.4\Omega_M^{-0.3} GMH(z))^{1/3}, \tag{1.64}$$

$$r_{200} = \frac{V_{200}}{9.4\Omega_M^{-0.3} H(z)}. \tag{1.65}$$

It is clear that halo properties are not only dependent on the redshift of virialisation, but also the underlying cosmology. The behaviour of $H(z)$ is markedly different in the various cosmologies, and so haloes of a given radius and circular velocity form later in a ΛCDM universe than in an Einstein de-Sitter universe.

1.3.5 Quantifying large scale structure

The spatial dependence of fluctuations can be derived by performing a Fourier expansion of the density field. Assuming the field is periodic on a scale L, we can write

$$\delta(\mathrm{x}) = \sum \delta_k \mathrm{e}^{-i\mathbf{k}.\mathbf{x}}. \tag{1.66}$$

Periodicity forces boundary conditions on the allowed wavenumbers:

$$k_x = \frac{n2\pi}{L}, \quad n = 1, 2, \ldots$$

If we let L go to infinity, then the above sum will become an integral.

The correlation function

We define the correlation function as (Peacock 1999)

$$\xi(\mathbf{x}) \equiv \langle \delta(\mathbf{x}) \delta(\mathbf{x} + \mathbf{r}) \rangle. \tag{1.67}$$

In other words, $\xi(\mathbf{x})$ is the correlation of the density field with itself, averaged over a volume V. It describes the size of density perturbations on scales $\mathbf{r}$.

If we use equation (1.66) to expand this, let the scale become arbitarily large, thus changing the sum to an integral, we have

$$\xi(\mathbf{r}) = \frac{V}{(2\pi)^3} \int |\delta_k|^2 \mathrm{e}^{-i\mathbf{k}.\mathbf{r}} \mathrm{d}^3 k. \tag{1.68}$$

It is clear that the correlation function is just the Fourier transform of $|\delta_k^2|$, defined as the **power spectrum**.

This applies to a specific realisation of the density field, and we define the ensemble average power spectrum as

$$P(k) \equiv \langle |\delta_k|^2 \rangle. \tag{1.69}$$

We live in an isotropic universe; from the Copernican principle, the spectrum of density perturbations cannot have a preferred direction. Using spherical polar coordinates, we have

$$\xi(\mathbf{r}) = \frac{V}{(2\pi)^3} \int_0^\infty \int_0^{2\pi} \int_0^\pi |\delta_k|^2 \mathrm{e}^{-i\mathbf{k}.\mathbf{r}} k^2 \sin\ \theta \ \mathrm{d}\theta \ \mathrm{d}\phi \ \mathrm{d}k. \tag{1.70}$$

From isotropy, the angular part is trivial. We write $\mathbf{k}.\mathbf{r} = kr\ \cos\theta$, and apply de Moivre's theorem:

$$e^{-ik\cos\ \theta} = \cos\ (kr\cos\ \theta) - i\ \sin\ (kr\cos\ \theta) = \cos\ (kr\cos\ \theta),$$

as $\xi(\mathbf{r})$ is by definition a real number. Substituting $\mu = \cos\ \theta$ and performing the angular integrals yields

$$\xi(\mathbf{r}) = \frac{V}{2\pi^3}\int_0^\infty P(k)\frac{\sin\ kr}{kr}4\pi k^2 \mathrm{d}k. \tag{1.71}$$

One can also define the power spectrum in a more convenient, dimensionless form:

$$\Delta^2(k) \equiv \frac{V}{(2\pi)^3}4\pi k^3 P(k). \tag{1.72}$$

It is usual to assume that there is no preferred length scale in the power spectrum, and so the power spectrum is defined as a featureless power law

$$\langle|\delta_k|^2\rangle \propto k^n. \tag{1.73}$$

Of most application in cosmology is the scale-invariant spectrum, where $n = 1$. Inflationary theory predicts a value of n slightly different from unity, and $n = 1$ is generally assumed to be the case in cosmological simulations.

Another important cosmological definition is σ_8, the rms density variation in spheres of radius 8 $h^{-1}\ Mpc$ when filtered with a top-hat filter:

$$\sigma_8^2 = \int \Delta^2(k)\frac{dk}{k}W_k^2, \quad W_k = \frac{3}{kr}(\sin kr - kr\cos kr). \tag{1.74}$$

The value of σ_8 determines the strength of galaxy clustering in the universe.

1.3.6 Cold dark matter universes

In a Cold Dark Matter (CDM) cosmology, the majority of matter is of a non-luminous, non-baryonic nature. The presence of this unseen component is required to explain observations of the rotation curves of spiral galaxies and the dynamical masses of galaxy clusters.

The precise nature of the dark matter is uncertain. It is non-relativistic at the epoch of decoupling from the baryonic matter and radiation, and interacts

only gravitationally with baryonic matter and radiation. The DM component undergoes gravitational evolution: small structures form first, due to the low amplitude of large density fluctuations at early times. These coalesce into ever larger structures. This is the familiar hierarchal structure formation paradigm.

White and Rees (1978) present the now standard galaxy formation scenario. The dark matter collapses and virialises into haloes at early times. The baryonic gas coupled to the dark matter is shock heated to the virial temperature of the halo on formation, and is pressure supported. This temperature is hot enough to ensure that the gas is fully ionised, and the gas can thus dissipate energy. The gas cools, is no longer pressure supported and collapses to the bottom of the potential well. Stars then form from this cooled gas and a luminous protogalaxy forms at the centre of the halo. The haloes together with their embedded galaxies undergo hierarchal evolution, and experience tidal interactions and mergers throughout their lifetimes. This quick overview of the galaxy formation process involves complex and in some cases rather uncertain physical processes. It is also important to note that only disk galaxies form in this scenario; the origin of bulges and ellipticals is thought to be a result of evolutionary processes acting on discs.

Following the evolution of dark matter is relatively simple, and is by far the most understood of the myriad physical processes involved in galaxy formation. Cold dark matter is collisionless, and thus only gravity need be considered when following its evolution. There are two distinct approaches available here. Numerical techniques can be used to follow the evolution of the dark matter directly (N-body simulations, see Bertschinger et al. 1998 for a comprehensive review of the subject). Alternatively, analytic expressions for the halo mass function, merger rates and other properties of interest can be constructed (eg. Press and Schecter 1974, Bond et al. 1991, Lacey and Cole 1993, Sheth and Tormen 1999, Percival and Miller 1999).

1.3.7 Baryons

The evolution of gas coupled to the dark matter can also be studied using numerical techniques. Smoothed Particle Hydrodynamics (SPH) is a numerical method of integrating the cosmological fluid equations, first introduced

by Gingold and Monaghan (1977). Discrete identical mass particles represent fluid elements, in a similar manner to N-body codes. Indeed, SPH can easily be added to cosmological N-body codes, allowing treatment of both the baryons and dark matter without introducing any assumptions about the former. Unfortunately, interesting baryon dynamics ultimately operate on very small scales, with the collapse and fragmentation of molecular clouds of order a few parsecs across leading to star formation on sub-AU scales. It is impossible to introduce detail of this level on cosmologically significant scales. Hybrid N-body/SPH codes are generally used to study the dynamics of individual galaxy interactions and merger events. On larger scales, one needs to find a shortcut.

1.4 Semi-analytic galaxy modelling

Semi-analytical modelling (SAM) has the modest aim of providing accurate and testable properties of the matter (baryonic in paricular) content of the universe, tying together various physical processes operating on wildly different scales. The field is vast and varied, with many examples available in the literature. There are many different approaches in deriving an accurate description of the galaxy population, but there are key stages that must be included:

- The evolution of dark matter in the universe
- The evolution of the baryonic materical coupled to the dark matter
- The formation and evolution of stellar populations, with stellar feedback taken into account
- Dynamical effects on large scales, such as galaxy merging
- The output light of galaxy, dependent on stellar mass, age and metallicity.

The field of SAM has been extensively studied in the last fifteen years or so, and predictions have been made for both the local and high redshift universe. Although accurate reproductions of the $z = 0$ galaxy population are now commonplace, SAMs still tend to struggle with predicitions of many

facets of the high redshift universe.

White and Frenk (1991) were the first to explore the topic, employing the extended Press-Schechter theory outlined in Bond et al. (1991) to treat the evolution and merging of dark matter haloes in a CDM cosmology. Using the ideas of galaxy formation suggested by White and Rees (1978), they modelled the cooling of the baryonic component of haloes and its subsequent collapse to the centre of the potential, thus forming a galaxy. They employed simple scaling laws for star formation, feedback due to supernovae and chemical enrichment. Stellar populations were modelled using the Bruzual (1983) models. The luminosity density of the universe was used to tune the free parameters of the overall model.

Their model for galaxy formation managed to obtain predictions the luminosity function of galaxies and faint galaxy counts. They found that heating of primordial gas is required to stop the majority of the gas cooling in small haloes at an early epoch. Their model failed to match the observed Tully-Fisher relation for spiral galaxies.

Cole et al (1994, CAFNZ) employed a Monte Carlo technique based on the model of Cole and Kaiser (1988) to follow the merger histories of DM haloes. They studied the evolution of the embedded galaxies in a similar manner to that of White and Frenk, but utilised different relations for the star formation rate and stellar feedback, as well as different stellar population synthesis models. Their model managed to match the persent-day galaxy luminosity function (albeit with an excessively steep faint-end slope), the colour magnitude relation for galaxies, the redshift distribution and number counts of faint galaxies. Unfortunately, they too failed to match the Tully-Fisher relation, and showed a shortfall in the number of massive red galaxies. Their approach was later used to derive morphological counts of high redshift galaxies (Baugh et al. 1996a), extended to include a realistic treatment of bulges and disks (Baugh et al. 1996b), and derived properites of Lyman Break galaxies (Baugh et. al 1998).

A major refinement was presented in Cole et al. (2000), where they describe their new code GALFORM. The Monte Carlo implementation is that of

Lacey and Cole (1993), allowing dark matter haloes to have progenitors of arbitary size, not just two equal mass progenitors as in the algorithm used previously. They introduce chemical evolution of galaxies, an important improvement over their previous work. An additional bursting star formation law is introduced in merging galaxies. A first attempt was made at modelling the effects of dust extinction, using the radiative transfer models of Ferrara et al. (1999). Their model matches both the B and K band luminosity functions over at least 8 magnitudes, a significant success (albeit with little constraints available on the faint end slope). Galaxy colours match well with observational data, as do the predicted sizes for galaxy discs. Once again though, they fail to fit the Tully-Fisher relation for spirals, although the discrepancy is not so acute as in their previous studies.

GALFORM has since been used to investigate the epoch of reionisation (Benson et al. 2002a, 2002b), probe the origin of the luminosity function (Benson et al. 2003), has been compared with N-body and SPH simulations (Helly et al. 2003), given predictions of the neutral hydrogen mass function as a function of redshift (Baugh et al. 2004), the abundance of Lyman-α sources (le Delliou et al. 2005), and metal enrichment of the intracluster medium (Nagashima et al. 2005).

Granato et al. (2000) described the combination of the GALFORM code of Cole et al. (2000) with a spectrophotometric code for dust modelling, GRASIL (Silva et al. 1998, described in detail in section 2.2). The integration of the two codes allows detailed spectral energy distributions for the model galaxies produced in GALFORM to be calculated, properly taking the effects of dust into account. Again, a suite of low-resdshift predictions are well-reproduced by the model.

Kauffmann et al. (1993) implement a Monte Carlo technique based on their own extended Press-Schechter methods (Kauffmann and White 1993), giving merger trees for each dark halo, tracing its constituent parts back in time. This novel method allows a particular halo to be examined throughout history. In this way the evolution of the embedded galaxies can be followed. They followed the same prescription for gas cooling as White and Frenk (1991). They introduced a dynamical friction argument to determine the merger rates of galaxies within the DM haloes, and considered the formation of elliptical

galaxies as the result of major mergers between galaxies. Chemical enrichment was not taken into account. Fitting their free parameters to reproduce the properties of the Local Group,they managed to explain the colours, luminosities and morphologies of galaxies resident in small groups or clusters. They fail to match the Tully-Fisher relation and the luminosity density of the universe. They claimed that this was an underlying problem with the CDM cosmology rather than a shortcoming of their modelling.

Further studies looked at number counts and redshift distributions of faint galaxies (Kauffmann et al. 1994), and examined the properties of galaxies in high redshift clusters (Kauffmann et al. 1995a,1995b). Later, semi-analytic techniques were applied to N-body simulations and used to generate predictions for the local universe (Kauffmann et al 1999a) and at high redshift (Kauffmann et al. 1999b).

Somerville and Primack (1999) present an independent semi-analytic model, similar in spirit to the work detailed above. They employ Monte-Carlo realisations of merger trees using the excursion set formalism of Bond et al. (1991). They considered a variety of star formation laws, a modified treatment of gas cooling, stellar feedback inversely proportional to the escape velocity of the galactic disc, and a uniform slab treatment of interstellar dust. They manage to match both the knee of the B-band luminosity function and the zero-point of the Tully-Fisher relation, a significant success.

The 'phenomenological' model of van Kampen, Jimenez and Peacock (1999) uses N-body simulations in conjunction with a recipe designed to prevent overmerging, the erasure of substructure in dense regions due to numerical limitations in a simulation. The properties of galaxies are then calculated according to the usual semi-analytic prescriptions, applied over the lifetimes of the parent haloes. This model will be described in more detail in the next chapter.

Similar in spirit to the work by the models of Kauffmann et al. and Somerville et al. is the semi-analytic model GALICS of Hatton et al. (2003). They combine merger trees extracted from a high-resolution N-body simulation with general semi-analytic laws of galaxy formation, including a novel

treatment of galaxy merging and the resulting morphologies. As with other groups, they adequately predict many galaxy properties in the local universe, matching the optical and K band luminosity function, a reasonable fit to the Tully-Fisher relation, and for the first time in a semi-analytic model, a reasonable fit to the Faber-Jackson relation for bulges and spheroids. GALICS has been used to derive luminosity functions and correlation functions for Lyman Break galaxies (Blaziot et al. 2004) and applied to high-resolution cluster simulations (Lanzoni et al. 2005).

1.5 Semi-analytic modelling of the high redshift universe

Semi-analytic models are generally compared with data on the local universe, and have proved remarkably successful, given the approximations and simplified recipes of baryonic physics. Nevertheless, one would like a picture of galaxy formation and evolution throughout the history of the universe, and the rapid advance in telescope and detector technology is opening up the high redshift universe to detailed scrutiny.

Various groups have applied their semi-analytic models to the high redshift universe, with wildly differing results. In particular, most models fail to account for the more extreme objects known to exist at early epoch, including submillimetre galaxies and EROs (eg. Fontana et al. 2004).

In ΛCDM cosmologies, structure in the dark matter forms hierarchially, with small units combining to form ever-larger entities. One would thus expect galaxies to form in the same manner. However, this does not appear to be the case. The observational data seems to indicate that SMGs and EROs have formed the vast majority of their stars as a single masssive object, in a 'monolithic collapse'. Acommodating such large objects at early times is difficult in ΛCDM, and monolithic collapse models overpredict the abundance of massive objects at low redshift.

It might be suggested that the assumed standard ΛCDM cosmology is at fault, and that an alternative cosmology might prove more accomodating in accounting for these extreme galaxies at early times. Nevertheless, Somerville (2004) shows that this is not the case. Given the number densities, epochs and typical inferred masses of SMGs, Lyman break galaxies, EROs and

quasars, ΛCDM predicts sufficent numbers of massive enough dark matter haloes to comfortably acommodate all of these populations. In addition, semi-analytic models tend to produce enough stars globally in the early universe, failing only to predict the existence of extreme individual objects. It thus seems that there is unknown baryonic physics at play here, rather than a failing of the underlying cosmological assumptions.

Guiderdoni et al. (1998) use a simple semi-analytic technique to predict the number counts of galaxies in the far-IR and submillimetre. They manage to match the IRAS 60 μm luminosity function and cosmic infrared background. They find that faint galaxy counts in the submillimetre are strongly sensitive to the assumed evolutionary scenario, requiring a large fraction of stars to be formed in bursts at high redshift. Their model utilises only a simple uniform slab treatment of dust extinction, and do not derive the merger histories of galaxies and their parent haloes, allowing only global quantities to be predicted.

Silva (1999) present global results for the high redshift universe, using the same model as used by Granato et al. (2000). They found reasonable agreement for the evolution of the luminosity density, as long as the effects of dust obscuration are taken into account. The background radiation from 0.1 to 1000μm is well reproduced by the model. Predictions of number counts at various wavelengths are made. These match reasonably well with reality, except for the 850μm number counts, where the model produces too few objects. The discrepancy is partiularly large at the bright end, where a factor of thirty too few objects are predicted. Since the overall sub-mm background was matched well, this implies that their code creates too many under luminous sub-mm sources.

Devriendt et al. (1999) apply a simple semi-analytic prescription of galaxy formation to their STARDUST code for deriving UV-radio galaxy SEDs. They match the 15, 60, 125 and 850 μm number counts, concluding that SMGs are massive, heavily obscured galaxies undergoing extreme bursts of star formation. However, their models do not follow halo and galaxy merger trees, so the frequency of mergers and fraction of dust-obscured fraction of galaxies is a free parameter, and their success at deriving number counts is due to the considerable freedom available in tuning their model.

Another major refinement to the GALFORM+GRASIL framework is presented in Baugh et al. (2005, hereafter B05). They match both the $z = 3$ luminosity function of Lyman Break galaxies, and for the first time, the number counts of submillimetre sources. Numerous adjustments in the modelling were necessary to give this match. They invoke a 'superwind ' mode of feedback, where cold gas is expelled from a galaxy at a rate proportional to the star formation rate. Reionisation is treated by suppressing the cooling of gas in haloes with $V_c < 60\mathrm{km\ s^{-1}}$ at $z < 6$. The star formation timescale in discs is dependent on the circular velocity of the halo, rather than determined by the dynamical time of the disc. For starbursts, they employ a different dust emissivity at long wavelengths, $\epsilon_\nu \propto \nu^{1.5}$ instead of the canonical ν^2 dependence. The most crucial change, and one which has the most dramatic effect, is the use of a flat IMF $\mathrm{d}N/\mathrm{dln}m \propto m^{-x}$ with $x = 0$, in starbursts. In this case, more radiation is emitted in the UV, as more massive stars are formed. These extra massive stars eject more metals into the ISM. A flat IMF thus produces more dust, and there is more UV and optical radiation attenuated by the dust. This allows the submm number counts to be matched with relatively low star formation rates in individual objects, contrary to predictions obtained assuming a Salpeter IMF.

Somerville at al. (2001) show that the observed properties of Lyman Break galaxies can be acommodated within their semi-analytical framework, treating dust extinction as a free parameter, assuming that galaxy-galaxy mergers induce bursts of star formation, and that star formation is more efficient at high redshift. They made no attempt to account for submillimetre sources.

Kaviani et al. (2003) use the approach detailed in Kauffmann et al (1999a) to give a reasonable reproduction of the number counts of 850 μm sources, assuming that the sources are extended objects with low dust temperatures forming stars at a rate of $\sim 100\ \mathrm{M_\odot yr^{-1}}$ and that the dust temperature can be varied as a free parameter. Nevertheless, it must be noted that the latter assumption is not physically realistic. Dust grains are in radiative equilibrium between heating by incident radiation and cooling, leading to a particular temperature dependent on local conditions. Thus, large changes in dust temperature can only be achieved through corresponding large changes in the dust mass or incident radiation field.

Very recently, AGN-related feedback has invoked by numerous authors in

order to reproduce properties of the high redshift universe (eg. Granato et al. 2004, Croton et al. 2006, Bower et al. 2005). This will be examined in more detail in chapter 7.

In this thesis I describe the conjunction of a semi-analytic model combined with an accurate treatment of dust extinction, in order to produce complimentary predictions both locally and at high redshift. I will attempt to reproduce various populations at high redshift, including LBGs, SMGs and EROs. Semi-analytic models struggle to account for the presence and properties of SMGs, and semi-analytic models have yet to be tested against the known properties of EROs and related objects.

CHAPTER 2

The galaxy formation model

In this chapter, I describe the galaxy formation model used in the remainder of the thesis. The dark matter simulations are described, and a brief overview of halo identification techniques is presented. I then describe the equations governing gas cooling, star formation and associated feedback, and metal enrichment of gas. Some properties of the spectrophotometric dust code GRASIL are discussed, and integration of the two codes to give galaxy properties over a large wavelength range is detailed.

2.1 The galaxy formation model

I use the galaxy formation model of van Kampen, Rimes and Peacock (in prep.), a revised version of that described in van Kampen, Peacock and Jimenez (1999). This 'phenomenological' galaxy formation model incorporates aspects of both numerical simulations and semi-analytic modelling. Here I will summarize the main aspects of the code; I refer to Rimes (2003) for a more detailed description.

2.1.1 Dark matter simulations

Numerical methods suffer from the problem of overmerging, where small substructure is erased in dense regions. As we observe galaxies present within larger clusters, this is a significant problem that needs to be minimised. The

main cause of overmerging in numerical simulations is two-body heating (van Kampen 2000). The modelling of the dark matter as discrete particles introduces spurious interactions between pairs of particles, where in fact they should only be influenced by the overall potential of the system. Combined with poor spatial resolution, this has serious consequences for small structures, which are completely erased in dense regions (Carlberg 1994, van Kampen 1995). Using softened particles is one cure, which alters the potential of a particle such that it does not diverge as $r \rightarrow 0$. This is standard procedure in numerical simulations, but it comes at a price. van Kampen (1995) and Moore, Katz and Lake (1996) have shown that the softening can also exaberate overmerging. Softened particles are more susceptible to tidal disruption and merging, overstating the importance of these physical processes. Very high resolution simulations can circumvent this problem and resolve substructure within large galaxy clusters (eg. Moore et al. 1998, Ghigna et al. 1998). However, the high resolution can only be applied to small volumes within a cosmological simulation, so overmerging remains a problem on more global scales.

I perform simulations of a vanilla ΛCDM cosmology, with cosmological parameters as listed in table (2.1). I assume a Hubble constant of $h = 0.7$, within the error bars of the results of the Hubble Space Telescope Key Project ($h = 0.72 \pm 0.08$, Freedman et al. 2001) and recent joint analyses of WMAP and 2dF data ($h = 0.73 \pm 0.03$, see Lahav and Liddle 2006 for a review). The values of the density parameters are broadly consistent with those derived from the same WMAP-2dF constraints. The chosen normalisation of the matter density field σ_8 (see equation 1.74) is consistent with that derived from WMAP ($\sigma_8 = 0.9 \pm 0.1$, Spergel et al. 2003).

Technically, the baryon density Ω_B is a free parameter in the model, as it plays no part in the N-body simulation. Nevertheless, I chose to treat it as a fixed parameter, taking the value $\Omega_B = 0.04$, consistent with the joint WMAP-2dF estimate of $\Omega_B h^2 = 0.023 \pm 0.001$.

The simulation box contains 128^3 particles, with a box size of $50\ h^{-1}$ Mpc on a side. The particle mass is thus $4.96 \times 10^9\ h^{-1}\ M_\odot$.

An initial Gaussian random density field and velocity field is created, using the algorithm of Hoffman and Ribak (1991). Constraints on the density field can be made, such as specifiying an overdense region which will eventually

Ω_M	Ω_Λ	Ω_B	σ_8	h	n
0.3	0.7	0.04	0.93	0.7	1

Table 2.1: Cosmological parameters of the simulation boxes

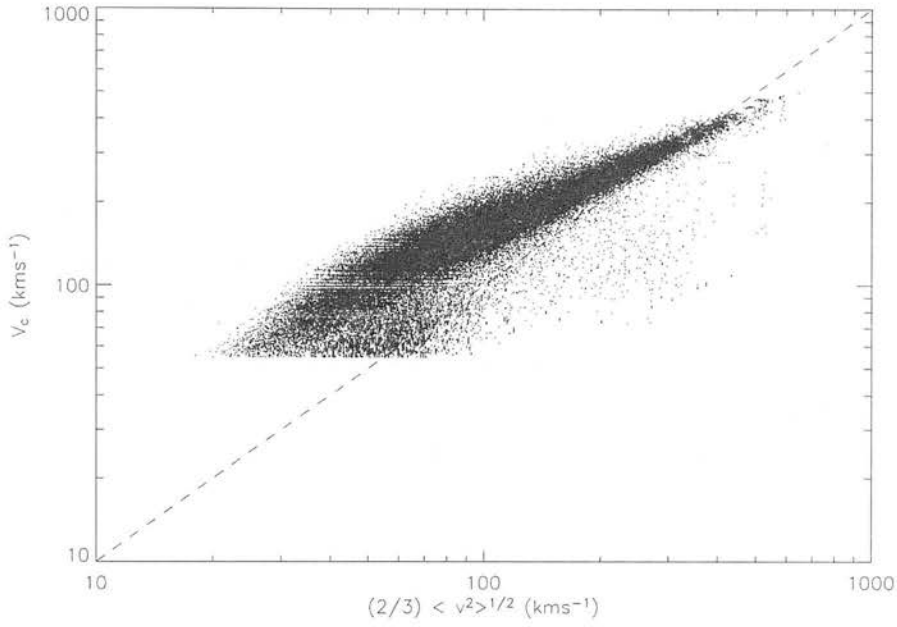

Figure 2.1: Comparison between direct measurement of the velocity dispersion of a halo and the prediction given by the spherical collapse model. See accompanying text for details.

house a cluster. I choose an unconstrained realisation to give a 'fair sample' of the universe in the box. The density fields are then displaced according to the Zeldovich approximation (Zeldovich 1970). The evolution of the dark matter is followed using the tree code of Barnes and Hut (1986), augmented by a galaxy halo formation recipe (van Kampen 1995). This is designed to prevent the problem of overmerging, discussed above.

2.1.2 Halo properties

Given a distribution of dark matter particles at a given point in time, one needs to distinguish between real, gravitationally bound structures (ie. DM haloes) and chance agglomerations of particles.

Haloes are identified using a local density percolation (also known as adaptive friends-of friends) technique (see Rimes 2003 for an in-depth discussion of the halo-finding recipe). Initial, 'parent' haloes are found by using a fixed linking length b, with $b = 0.2$ (a standard choice in these algorithms). A minimum of 10 particles is required for an overdensity to be considered a halo: this ensures dynamical stability. However, these haloes will contain substructure, which cannot be seperated out in this manner.

To identify subhaloes, regions of local overdensity are picked out using an adaptive linking length, which scales with the local density and particle mass. This seperates embedded, bound structures from their parent haloes. There are two free parameters in this method: the smoothing length s, which defines the scale on which the local density field is smoothed, and the linking parameter p, which scales the local linking length (as a fraction of the mean inter-particle distance).

Haloes form according to the spherical collapse model (Peebles 1980), and are assumed to be isothermal spheres, with a density profile

$$\rho(r) = \frac{V_c^2}{4\pi G r^2}. \tag{2.1}$$

White (1996) highlights a relationship between halo mass, circular velocity and formation redshift in the spherical collapse model

$$V_c = \left(\frac{M_{\rm halo}}{2.35 \times 10^5 \ h^{-1} M_\odot} \right)^{1/3} (1 + z_{\rm form})^{1/2} \ {\rm km \ s^{-1}}. \tag{2.2}$$

However, the circular velocity of a halo can also be directly measured from the N-body simulation. For a halo velocity dispersion $\langle v^2 \rangle$ and an isothermal profile, we have

$$V_c = \left(\frac{2}{3} \right) \langle v^2 \rangle^{1/2} \simeq \left(\frac{G M_{\rm halo}}{3 R_{\rm h}} \right), \tag{2.3}$$

where R_h is the half-mass radius. However, the velocity dispersion of a halo is a harder quantity to measure than the mass, and is more prone to numerical inaccuracies. In Figure 2.1 I plot the velocity dispersion of a halo as measured from the simulation against the spherical collapse model prediction for the circular velocity. There is a considerable scatter about the line of equality, with circular velocities being overpredicted for low velocity dispersion haloes and slightly underpredicted for the largest velocity dispersion haloes, highlighting the scatter in halo properties ignored in analytic treatments.

p	s	δV
1.0	0.5	0.25

Table 2.2: Parameters used in identifying subhaloes

In order to prevent overmerging, groups of particles are replaced with single 'halo particles' if they satisfy the virial criterion (Spitzer 1969)

$$\langle v^2 \rangle \approx 0.4 \frac{GM}{R_h}. \tag{2.4}$$

If this relation is satisfied to within some tolerance δV then the group is replaced by a single 'halo particle' softened according to the size of the original group and given the properties of the group. This will prevent the erasure of small galaxy-sized haloes by overmerging. Sufficiently large groups will not be susceptible to the numerical effects at the root of the overmerging problem, and so a maximum mass for a halo particle (200 simulation particles) is imposed. This also prevents unphysical interactions between overly large halo particles and the normal N-body particles.

In Figure 2.2 I plot the dark matter particle distribution and the virialised halo distribution in the simulation box. The classic filamentary structure of the matter distribution in a CDM universe is clearly visible.

Halo mass functions

In Figure 2.3 I plot the differential halo mass function of one of my simulation boxes with halo finding parameters given in Table 2.2. The dotted black line shows the halo mass function as found from application of a fixed-linking length percolation algorithm, the 'parent' haloes in the simulation. The parent halo mass function compares well with the analytic estimates of Press and Schecter (1974) and Sheth and Tormen (1999) and the major N-body simulations of Jenkins et al. (2001) and Croton et al. (2006). My simulation misses the high-end of the mass function simply due to the smaller box size: $50^3\ h^{-3}\ \mathrm{Mpc}^3$ as opposed to $500^3\ h^{-3}\ \mathrm{Mpc}^3$ and $3000^3\ h^{-3}\ \mathrm{Mpc}^3$ for Croton et al. and Jenkins et al. respectively. We expect the largest of these to in fact be composed of many subhaloes, and thus apply the adaptive linking-length algorithm and the virial criterion to this set of haloes. The resulting mass function is given by the solid black line. The largest haloes are clearly riddled

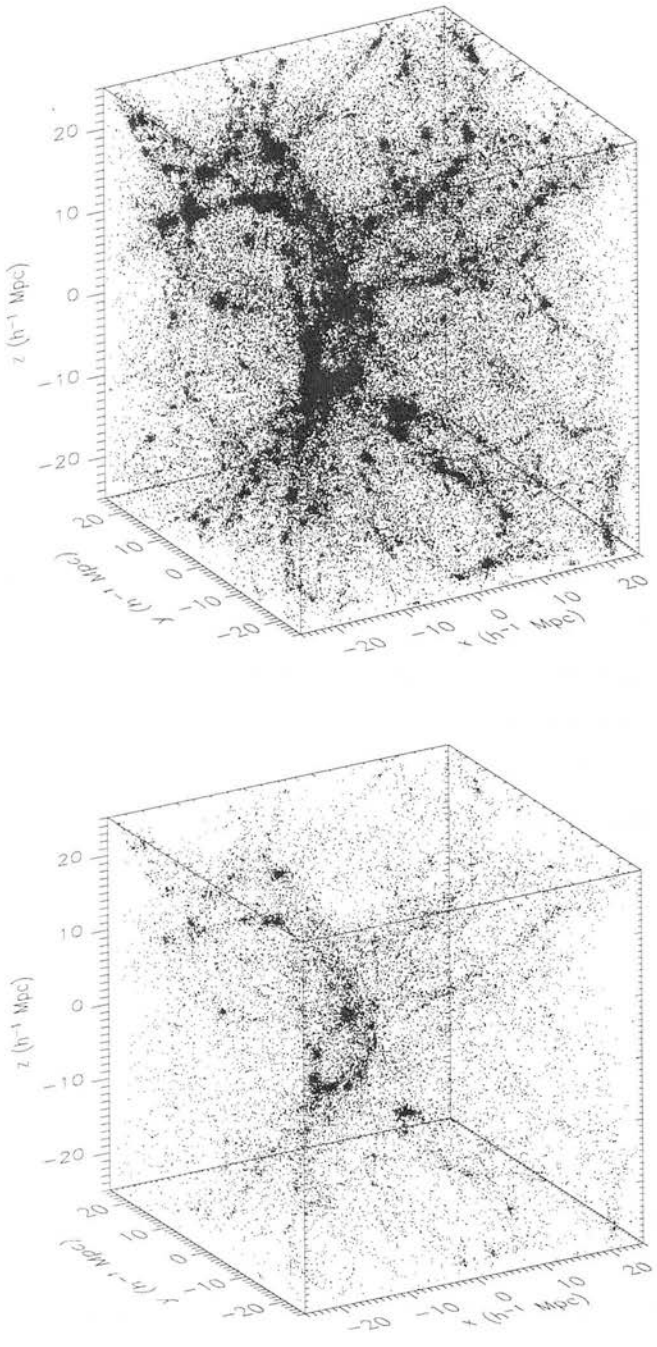

Figure 2.2: Top panel: the distribution of dark matter particles in the simulation box. Only every tenth particle is plotted for clarity. Bottom panel: the distribution of virialied subhaloes in the simulation box.

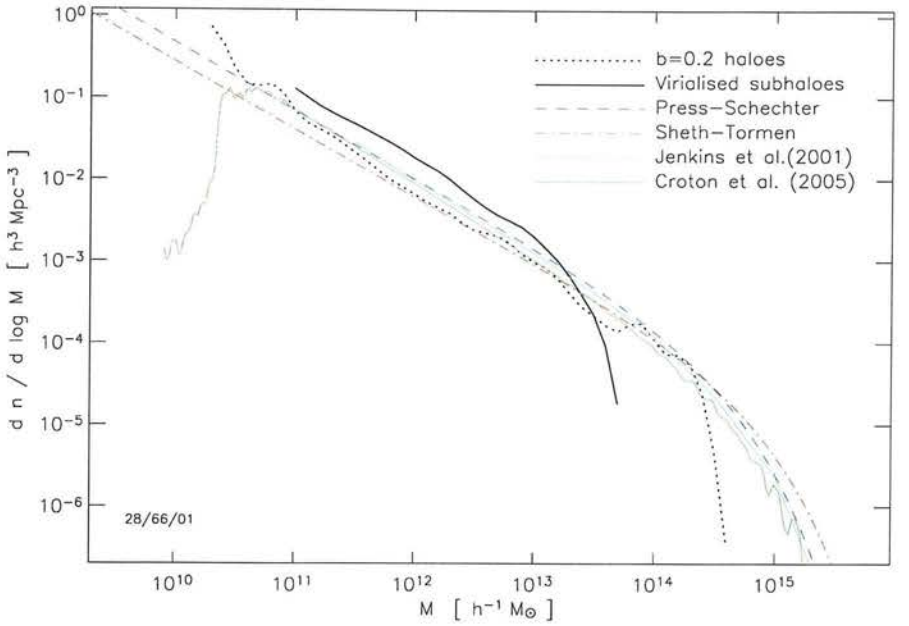

Figure 2.3: The halo mass function for the simulation box considered in this thesis, compared with analytic expressions for the mass function and examples from other major N-body simulations.

with substructure, and are resolved into smaller entities.

2.1.3 Placing galaxies in haloes

On formation, a halo contains a single galaxy. As haloes merge, the daughter galaxies can merge with each other via dynamical friction. A detailed treatment of this is not used; instead the method of Cole et al. (1994) is used. They find that a simple scaling law is consistent with more complicated hydrodynamical simulations of halo mergers involving large galaxies and their satellites (Navarro et al. 1995). Thus, galaxies merge on a timescale defined by

$$\tau_{\rm mrg} = \tau^0_{\rm mrg} \left(\frac{M_{\rm halo}}{M_{\rm gal}} \right)^{\alpha_{\rm mrg}}, \tag{2.5}$$

where $\tau^0_{\rm mrg}$ is a free parameter and is taken to be a fixed fraction of the dynamical time of the halo, defined as half the age of the universe when the halo formed.

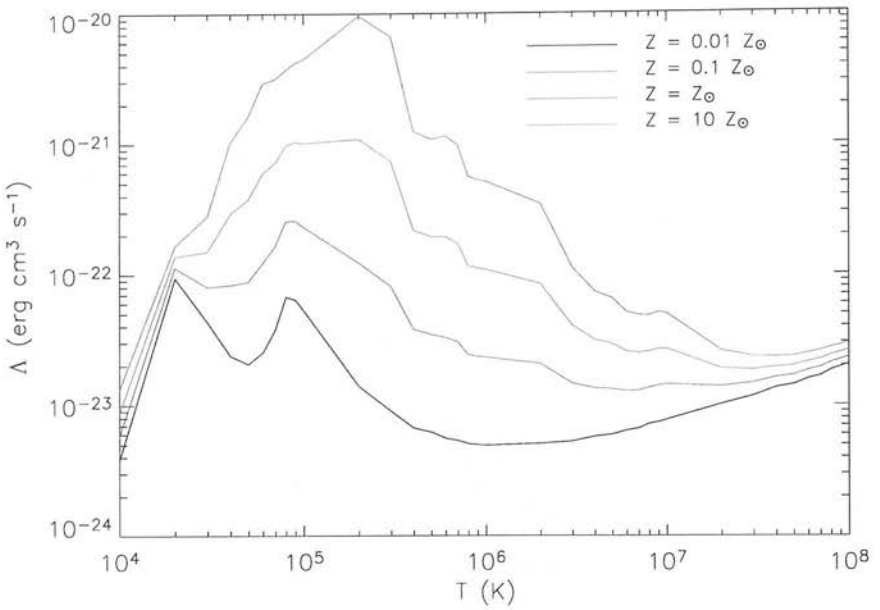

Figure 2.4: The cooling function of Sutherland and Dopita (1993) as a function of temperature and metallicity. As the metallicity of the gas increases, cooling becomes more efficent at all temperatures.

2.1.4 Baryons

Baryons are assumed to trace the dark matter. On virialisation, a halo will contain $\Omega_b M_{\rm halo}$ baryons shock-heated to the virial temperature of the halo, given by

$$T_g = \frac{\mu m_p}{2k} V_c^2. \tag{2.6}$$

This hot, ionised gas will cool radiatively (per unit volume) at a rate $n_e^2 \Lambda(T_g, Z_g)$, where n_e is the electron density and $\Lambda(T_g, Z_g)$ is the cooling function. For a given metallicity, I derive Λ by linear interpolation (or extrapolation) of the primordial and solar cooling functions of Sutherland and Dopita (1993). I plot $\Lambda(T_g, Z_g)$ for a variety of metallicities in Figure 2.4.

From the equipartition theorem, the thermal energy of the gas is $3nkT/2$, where k is the Boltzmann constant and n is the number density of particles. A cooling timescale can be defined as the time the gas takes to radiate away its thermal energy:

$$\tau_{\rm cool} n_e^2 \Lambda(T_g, Z_g) = \frac{3}{2} nkT. \tag{2.7}$$

The number density of particles can be written in terms of the local gas density, $n = \rho_g/\mu m_p$ where μ is the mean molecular mass and m_p is the proton mass. Similarly, the number density of electrons can be written as $n_e = \chi_e \rho_g/\mu m_p$, where χ_e is the number of electrons per particle. For a mixture of 77% hydrogen and 23% helium, $\mu = 0.58$ and $\chi_e = 0.52$.

Using this, the cooling function can be written as

$$\tau_{\rm cool} = \frac{3}{2}\frac{\mu m_p kT}{\rho_g(r)\chi_e^2 \Lambda(T_g, Z_g)}. \tag{2.8}$$

The gas is assumed to have an isothermal distribution, given by

$$\rho_g(r) = \frac{f_g V_c^2}{4\pi r^2 G}, \tag{2.9}$$

where V_c is the circular velocity of the halo and f_g is the fraction of the halo mass in the hot gas phase.

A cooling time can be derived by setting the cooling timescale to be equal to the halo lifetime, $\tau_{\rm cool} \equiv t_{\rm life}$. Inserting equations (2.6) and (2.9) yields an expression for the cooling radius, the region where gas can cool within the halo lifetime:

$$r_{\rm cool} = \left(\frac{f_g \Lambda(T_g, Z_g) t_{\rm life} \chi_e^2}{3\pi G \left(\mu m_p\right)^2} \right)^{1/2}. \tag{2.10}$$

Application of the virial theorem yields the mass of gas within the cooling radius:

$$m_{cool} = \frac{f_g V_c^2 r_{\rm cool}}{G}.$$

Inserting equation (2.10) into the above expression yields

$$m_{cool} = \frac{\chi_e}{\mu m_p} \frac{f_g^{3/2} V_c^2 \Lambda^{1/2} t_{\rm life}^{1/2}}{(3\pi)^{1/2} G^{3/2}}. \tag{2.11}$$

In a halo merger all of the hot gas components are amalgamated to form one reservoir heated to the virial temperature of the new halo. The most massive galaxy present is set to be the central galaxy of the new halo onto which the hot reservoir can cool and form stars. If satellite galaxies do not merge with the central galaxy, they retain their own reservoirs of cold gas and continue to form stars as before.

2.1.5 Star formation

The cold gas will form stars at a rate

$$\dot{m}_* = \frac{m_c(t, V_c)}{\tau_*(V_c)}, \tag{2.12}$$

where m_c is the amount of cold gas present in the disk. Again, in defining the star formation timescale τ_* we follow the lead of Cole et al. (1994), who find that a simple scaling law for star formation is consistent with the more detailed hydrodynamical codes of Navarro and White (1993). Hence, the star formation timescale τ_* is given by

$$\tau_*(V_c) = \tau_{*,0} \left(\frac{V_c}{300 \text{ kms}^{-1}} \right)^{\alpha_*}. \tag{2.13}$$

Feedback from supernova explosions will heat cold gas, transferring it back to the hot phase and temporarily prevent it from forming stars. The feedback is taken to be proportional to the circular velocity of the halo. Gas is reheated at a rate

$$\dot{m}_h(t, V_c) = \beta(v_c)\dot{m}_*(t, V_c), \tag{2.14}$$

where the feedback proportionality factor β is given by

$$\beta(V_c) = \left(\frac{V_c}{V_{hot}} \right)^{-\alpha_{\text{hot}}}. \tag{2.15}$$

I can now derive the stellar mass formed. From equation (2.12), we have

$$\dot{m}_*(t, V_c) = \frac{m_c}{\tau_*(V_c)} = \frac{\left[m_c^0 - (1 - \mathcal{R})m_*(t, V_c) - m_h(t, V_c)\right]}{\tau_*(V_c)}, \tag{2.16}$$

where m_c^0 is the amount of gas present to begin with, m_* is the stellar mass formed, $\mathcal{R}$ is the amount of material recycled and returned to the gaseous phase through stellar evolution and m_h is the amount of gas reheated via feedback. After integrating and substituting equation (2.14), rearranging gives the first order differential equation

$$\dot{m}_* + \frac{(1 + \beta - \mathcal{R})}{\tau_*} m_* = \frac{m_c^0}{\tau_*}, \tag{2.17}$$

where I have omitted the dependences on time and circular velocity for clarity. Over a small timestep Δt, one can solve this differential equation (by the method of integrating factors) to give the stellar mass formed:

$$m_* = \frac{m_c^0}{(1 + \beta - \mathcal{R})} \left(1 - \exp\left[\frac{-(1 + \beta - \mathcal{R})}{\tau_*} \Delta t \right] \right), \tag{2.18}$$

assuming that the gas cools instantaneously at the start of the timestep.

2.1.6 Starbursts

In the hierarchial merging scenario, small lumps of matter are continously aggregating to form large structures. Where gas-rich environments merge, it is clear that star formation will be enhanced with respect to normal, quiescent levels.

I allow starbursts to occur in two distinct scenarios:

- Starbursts from galaxy-galaxy mergers
- Starbursts from halo-halo mergers

Bursting modes of star formation allows more stars to form at earlier epochs than in a purely quiescent model. From equation (2.12) we see that star formation is more efficent in haloes with large circular velocity. At early times most haloes are small, with correspondingly low values of V_c. Without a bursting mode of star formation the observed SFRs at high redshift, as inferred from observations of SMGs and LBGs, would be very hard to acommodate in this model.

I assume that the burst can be modelled in the same manner as normal star formation, but with different star formation and cooling rates. The duration of the burst is set to the dynamical time of the new halo:

$$t_b = \tau_{\rm dyn} \equiv \frac{R_h}{\sigma_v} \approx 0.042(1+z_{\rm form})^{-1.5} h^{-1} \text{ Gyr}. \tag{2.19}$$

The bursting star formation timescale takes the same form as the quiescent mode:

$$\tau_{*,b}(V_c) = \tau_{0,*} \left(\frac{V_c}{300 \text{ kms}^{-1}} \right)^{\alpha_*}. \tag{2.20}$$

The free parameters $\tau_{0,*}$ and α_* are the same as those used in quiescent star formation. Galaxy-galaxy mergers have long been known to induce starbursts by driving material into the centres of galaxies, creating dense environments where star formation can proceed at an accelerated pace (eg. Barnes and Hernquist 1991, Mihos and Hernquist 1994, Springel and Hernquist 2005). The role of halo-halo mergers is less clear, although there is evidence that this might also enhance star formation: the numerical simulations of Evrard (1991) show that bursts of star formation occur when galaxies encounter dense regions of the intracluster medium after a halo merger, and

the simulations of Mayer et al. (2001) show that entering a dense environment can help funnel gas to the centre of the satellite, causing a burst of star formation. Entering the cluster environment also exposes galaxies to larger and more frequent interactions (eg. Moore, Lake and Katz 1998, Moore et al. 1999).

To parameterise our ignorance, I introduce two new free parameters $\xi_{\rm b,hh}$ and $\xi_{\rm b,gg}$ where the subscripts stand for bursts induced by halo-halo mergers and galaxy-galaxy mergers respectively. This simply tunes the fraction of gas allowed to form stars in a given merging event. Note that the final results are rather insensitive to the exact choices of $\xi_{\rm b,hh}$ and $\xi_{\rm b,gg}$.

In this simple model, I do not attempt to model the starburst region seperately, and assume the new stars are formed uniformly around the galaxy (in the disk in the case of a halo-halo merger or a minor galaxy-galaxy merger (defined later), and the bulge otherwise). Note that there is evidence for massive, extended starbursts occuring in SMGs (Conselice et al. 2003).

2.1.7 Star formation below the mass resolution limit

The smallest haloes present are at the mass resolution limit of the simulation. In reality, these did not just appear out of nowhere. In hierarchal clustering, these haloes must have formed from the merging of haloes below the mass resolution of the simulation. It is thus assumed that these haloes house a single stellar population, with a fixed star formation timescale. A single population with a V_c of two-thirds the value of the halo and half its age at the time of formation is used to estimate how much gas cooled in these small haloes.

These smallest haloes define a completeness limit for the results of the simulations. Although my treatment of star formation below the resolution limit predicts a star formation history and magnitude for these objects, it is clear that these results should not be taken too seriously. In any case, the impact of the sub-resolution stellar populations is expected to be small, and contribute little to the final results.

2.1.8 Truncation: curbing the excess of bright galaxies

The latest results from WMAP and 2dF imply a baryon fraction of $\Omega_B h^2 = 0.023 \pm 0.001$. This has proven to be a major hurdle in creating successful semi-analytic models. For example, Cole et al. (2000) employ a model where the hot halo gas is distributed according to the previous merging history: large haloes with complex merging histories have rarefied gas profiles, with cooling times longer than the Hubble time. This, in addition to a (then appropriate) value of $\Omega_B = 0.02$, derived a reasonable reproduction of the local universe. Yet, as Benson et al. (2003) has shown, when a value of $\Omega_B = 0.04$ is applied to the same models the cooling times in large haloes shorten drastically and a persistent excess of bright galaxies appears. Kaufmann et al. (1999) suppress cooling in haloes with circular velocities above $V_c = 350$ km s^{-1}, yet their ΛCDM simulation with $\Omega_B = 0.045$, underpredicts the abundance of L_* galaxies and overpredicts numbers of the brightest galaxies.

Despite the methods outlined in section (2.1.2), I find it necessary to invoke some form of truncation in order to prevent overcooling in large circular-velocity haloes. I strip cold gas from galaxies, prevent gas from cooling and stars forming in haloes with $V_c > 300$ kms^{-1} (chosen to match the cutoff at the bright end of the B and K band luminosity functions, section 3.1.1). While there is little physical justification for this, it is clear that such a brute force method of curbing overcooling will in some way mimic the effects of physics not implemented here, such as feedback due to AGN activity or ram pressure stripping.

2.1.9 Chemical evolution

Various processes determines the fate of metals produced by star formation. Some are permanently locked up in long-lived stars. The hot gas is enriched by metals ejected from supernovae. This can cool and form stars with an higher average metallicity.

The amount of material returned to the gas phase through stellar evolution depends on the recycle parameter $\mathcal{R}$. This is determined by the adopted , and $\mathcal{R} = 0.3$ is appropriate for a Salpeter IMF (explained in the next section). Note that I do not attempt include any time delay between star formation and the subsequent recycling of material; this is assumed to be an instantaneous

process.

A fraction of this recycled material will be metals; in this way the gas reservoirs are enriched with metals ready for the next population of stars. This is parametrised by the effective yield y.

Metals can be returned either to the hot or cold gas, and this is modelled by introducing an ejection parameter e, a fraction between 0 and 1. Usually I set $e = 0$, where all the expelled metals end up in the cold gas reservoir.

I can now write the evolution of metals in the hot and cold phase as difference equations:

$$\dot{m}_{Z,h} = m^0_{Z,h} + Z_c\ \dot{M}_{rh} - Z_h\ \dot{M}_{\rm cool} + \mathcal{R}\ e\ \dot{M}_*\ y, \tag{2.21}$$

$$\dot{m}_{Z,c} = m^0_{Z,c} - Z_c \dot{M}_{rh} - (1-\mathcal{R})\ Z_c \dot{M}_* + \mathcal{R}\ (1-e)\ y\ \dot{M}_* + Z_h\ \dot{M}_{\rm cool}. \tag{2.22}$$

I sort the star formation history of a galaxy into eleven different metallicity bins, thus giving not only the amount of stars being formed in a timestep but also their metallicity distribution.

2.1.10 Sizes of disks and bulges

As in White and Rees (1978), angular momentum is conserved as gas collapses to the centre of a halo and thus forms a thin, rotating disk. This disk is assumed to take an exponential profile

$$\Sigma_c(R) = \frac{M_c}{2\pi R_d^2} \exp\left(-\frac{R}{R_d}\right), \tag{2.23}$$

where M_c is the mass of cold gas present, and $M_c = 2\pi\Sigma_0 R_d^2$. If the disk has a flat rotation curve, then the angular momentum of the disk (assumed to be a fixed fraction $\mathscr{J}$ of the halo angular momentum) is just $2M_d R_d V_c$, and the scalelength follows as

$$R_d = \frac{\mathscr{J}\, j_{\rm disc}}{2V_c}, \tag{2.24}$$

where j_d is the specific angular momentum of the disk. $\mathscr{J}$ is another free parameter of the model, introduced to accomodate the observation that angular momentum can indeed be lost in the process of disk formation (eg. Navarro and White 1994).

Bulges form from the mergers of disks (or indeed disks plus bulges). If the ratio of masses of a satellite galaxy and the central galaxy is greater than the free parameter $f_{\rm mrg}$, then a major merger is taken to have occured and the

two disks are destroyed, forming a bulge. Gas can then subsequently cool and form a new disk around the spheroid. In minor mergers, the satellite galaxy is incorporated into the central object without disrupting the central disk.

I use a simple prescription for determining the half-mass radius of a bulge. For a virialised system, there is a simple relation between the mass and velocity dispersion of the system:

$$r_{\rm bulge} \simeq 0.4 \frac{G M_{\rm bulge}}{\langle v^2 \rangle}. \tag{2.25}$$

My model cannot predict the velocity dispersion of the bulge itself, so as a first approximation I use the velocity dispersion of the parent halo.

2.1.11 Simple stellar populations

Given the star formation history of a galaxy, how does one calculate its light output? Armed with theoretical techniques of star formation and evolution, one can calculate the luminosities and colours of a single burst of star formation (eg. Bruzual and Charlot 1993, 1999). A library of such spectra is built up by considering different initial metallicities and ages. These Simple Stellar Populations (SSPs) can be used to predict the light output of a given galaxy, as follows. Each object can be thought of as a superposition of many different SSPs, each with its own age and metallicity. Thus, the output flux of a galaxy is given by summing up spectra of the initial SSPs, weighted by the star formation rate when each SSP was born.

The luminosity of a galaxy of age t_0 is

$$L_\lambda(t_0) = \sum^{i} \int_0^{t_0} \dot{M}_*(Z_i, m, t) L_\lambda^{\rm SSP}(Z_i, t_0 - t)\, {\rm d}t, \tag{2.26}$$

where the luminosity of the SSP is given by

$$L_\lambda^{SSP}(Z, t_0 - t) = \int_{m_d}^{m_u} \frac{{\rm d}n}{{\rm d}m}\Big|_m l_\lambda(Z, m, t_0 - t)\, {\rm d}m, \tag{2.27}$$

and $l_\lambda(Z, m, t_0 - t)$ is the luminosity of a star of mass m, metallicity Z and age $t_0 - t$, Z_i and Z_f are the initial and final metallicities, m_d and m_u are the smallest and largest stellar masses in the population, ${\rm d}n/{\rm d}n|_m$ is the initial mass function evaluated at a given mass (explained below), and $\dot{M}_*(Z, m, t)$ is the star formation rate when the SSP was formed. The sum represents

the contribution from the various progenitors that have combined to form the galaxy observed at time t. Stellar populations formed in different haloes will in general have different star formation histories and metallicities.

One final subtlety remains. For a given amount of star formation in some period of time, there will be a distribution of individual stellar masses, given by the initial mass function (IMF). The colour of a star varies greatly with mass and age, and will influence the output light of the SED.

I assume that a universal IMF applies, and this is taken to be the Salpeter IMF,

$$\frac{\mathrm{d}n}{\mathrm{d}m} \propto m^{-x}, \qquad x = 2.35. \tag{2.28}$$

The lower and upper stellar mass limits are 0.1 and $120\ M_{\odot}$ respectively. Of course, there are a number of IMFs available in the literature; for reference, I plot various examples in Figure 2.5. The Scalo (1986), Miller and Scalo (1979) and the Kennicutt (1983) IMFs are all broken power laws with various indices. Baugh et al. (2005) invoke a flat ($x = 0$) IMF in starbursts to reproduce the number counts of SMGs and LBGs; I plot this here too for comparison. Far more massive stars are formed for a given amount of star formation, producing more UV and far-IR flux than for a standard power-law IMF.

Armed with the IMF, the colours and magnitudes of SSPs can be now calculated. In Figure 2.6 I plot the evolution of the broadband (Johnson) magnitudes and colours of a $1M_{\odot}$ SSP, using the models of Bruzual and Charlot (1999). Note the trend towards redder colours as the stellar age increases. Nevertheless, this highlights a degeneracy between age and metallicity; red colours are also achieved by increasing the metallicity of the SSP. In general it is not always clear which effect contributes to the colour of a given stellar population. This degeneracy plagues observations as well: is a galaxy red because of its age or metallicity? In this situation, detailed study of hydrogen and metal emission lines can help break the degeneracy (eg. Maraston and Thomas 2000).

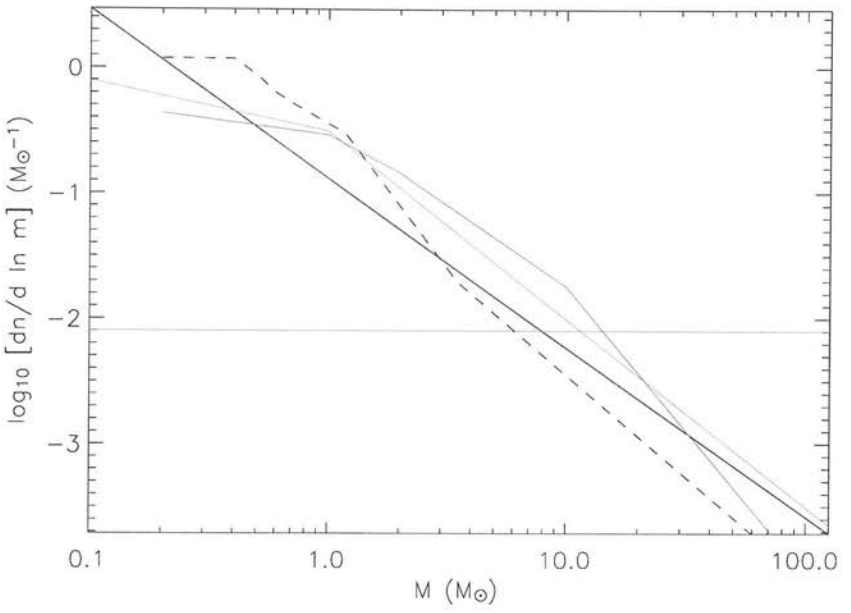

Figure 2.5: Various initial mass functions, normalised to a total mass of $1M_{\odot}$. Black curve: Salpeter (1955); green curve: Kennicutt (1983); red curve: Miller and Scalo (1979); dashed line: Scalo (1986); blue curve: Burst IMF of Baugh et al. (2005)

2.2 GRASIL

The importance of dust, especially in the high redshift universe, cannot be overstated. Without a realistic treatment of dust, the far-IR/submillimetre properties of galaxies are beyond the reach of any semi-analytic model.

GRASIL (Silva 1998, 1999) is a spectrophotometric code that calculates the effects of dust on a galaxy SED. Realistic geometries for both stars and dust are used, and dense molecular clouds, where star formation takes place, are taken into account, as well as diffuse cirrus dust. I now describe the main features of GRASIL, and detail the combining of GRASIL and my phenomenological model for galaxy formation. I will not give a comprehensive description of the dust model itself; this is available in Silva (1999, S99) for the interested reader.

Before the inclusion of dust extinction, the photometric properties of the galaxies are calculated using the synthetic stellar population models of Bertelli et al. (1994), with the effects of dusty envelopes around asymptotic

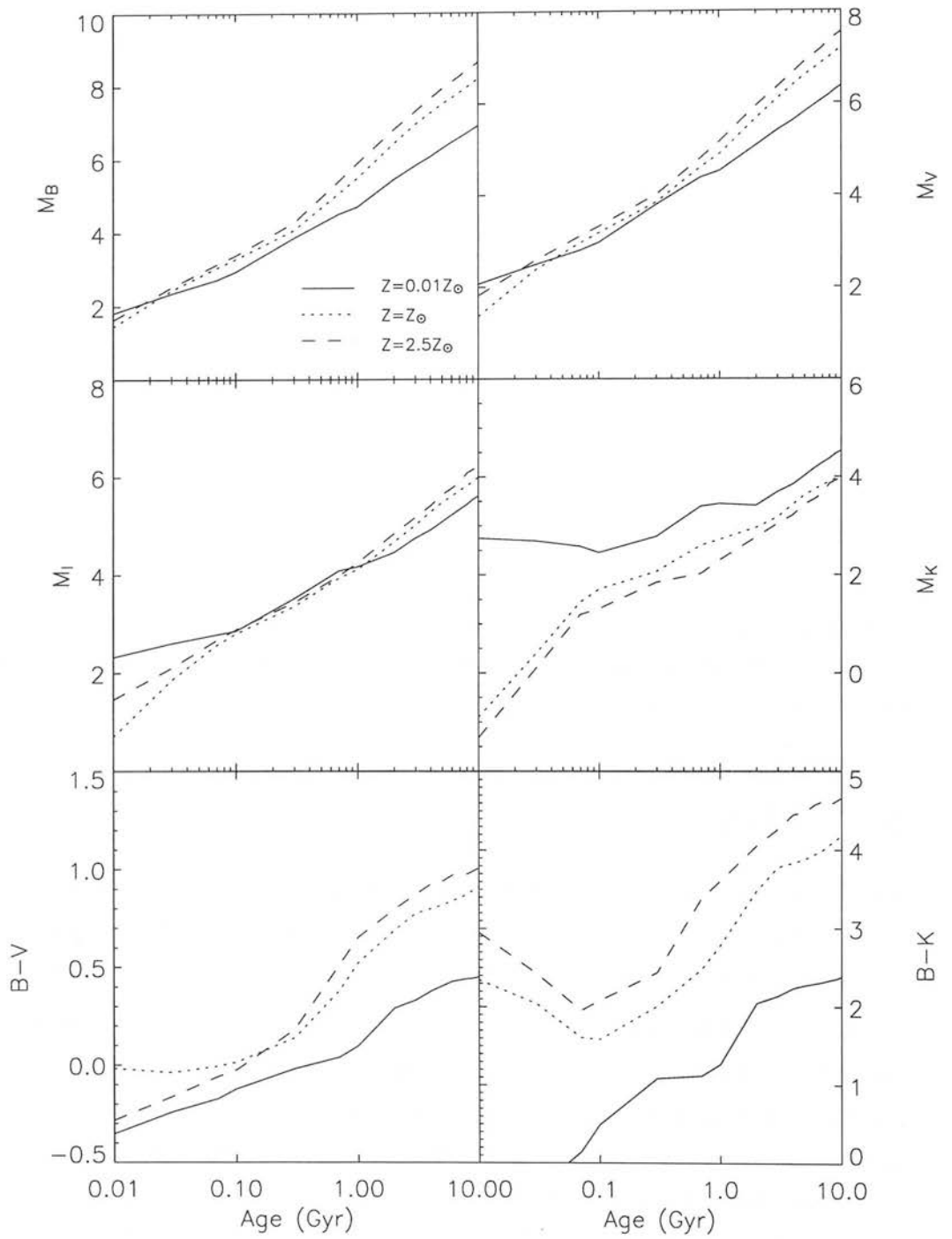

Figure 2.6: The magnitude and colour evolution of a 1 $M_{\odot}$ simple stellar population. A Salpeter IMF is assumed (see equation 2.28).Throughout, a solid line denotes an SSP with primordial metallicity, a dotted line denotes an SSP with solar metallicity and a dashed line denotes an SSP with super-solar metallicity.

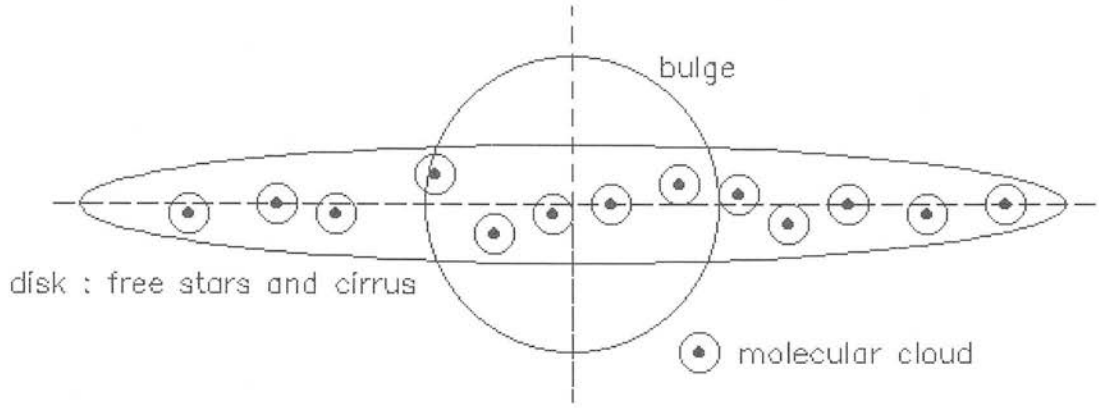

Figure 2.7: The components of a model galaxy. Based on a figure from S99

giant branch stars (AGBs) included in the calculations. A more detailed description of this particular SSP library is given in Silva (1999).

2.2.1 Galaxy geometry

A model galaxy can have both a disk and bulge component. Cold gas (and hence dust) is distributed in discrete molecular clouds and a diffuse cirrus component, as depicted in Figure 2.7.

The disk takes the form of a double exponential:

$$\rho_d = \rho_0 \exp\left(-R/R_d\right) \exp\left(-|z|/z_d\right), \tag{2.29}$$

where R_d is the scalelength of the disk and $z = r\cos\ \theta$. The bulge is given by a King profile:

$$\rho_b = \rho_0 \left[1 + \left(\frac{r}{r_c}\right)^2\right]^{-\gamma}, \tag{2.30}$$

where $\gamma = 3/2$ for stars and $\gamma = 3/4$ for dust.

Disks are truncated at $R_{gal} = 6R_d$, and bulges are truncated at the tidal radius $R_t = 10^{2.2} r_c$.

Stars, molecular clouds and diffuse gas all have the same scalelengths:

$$R_d^* = R_d^{\rm mc} = R_d^{\rm cirrus}; \quad z_d^* = z_d^{\rm mc} = z_d^{\rm cirrus}.$$

Any star formation takes place in molecular clouds. The number of molecular clouds is $N_{mc} = \delta M_g f_{mc}$, where δ is the dust to gas ratio and f_{mc} is the fraction of the gas in molecular clouds.

The initial stages of star formation are virtually invisible in the UV and optical. Stellar winds, outflows and UV flux from massive stars will destroy a molecular cloud on a timescale $\sim 10^6 - 10^7$ years (the typical lifetime of O/B stars).

Let f be the fraction of starlight re-radiated in a cloud. This parameter will decrease with time according to the age of the stars t and the parameter t_0 which sets the escape time for stars:

$$f = \begin{cases} 1 & : \quad t \leq t_0 \\ 2 - t/t_0 & : \quad t_0 < t \leq 2t_0 \\ 0 & : \quad t > 2t_0. \end{cases} \tag{2.31}$$

The parameter t_0 regulates how the UV and visible portion of the spectrum is affected by dust. The starlight locked inside a molecular cloud is modelled as a single central source.

2.2.2 The dust model

The abundance of dust is given by the dust-to-gas ratio δ, assumed to be proportional to the cold gas metallicity. For solar metallicity $Z = Z_\odot = 0.02$ we have $\delta = 1/110$, as used by Draine and Lee (1984). The dust mass of a galaxy is thus $M_{\rm dust} = k M_{\rm gas} Z_{\rm gas}$, with $k = 0.45$.

For the dust component of the interstellar medium, GRASIL takes into account the following:

- graphite grains
- silicate grains
- PAH molecules (not considered here due to the extra computational resources required)

The 2175 Å feature in the extinction curve of the Milky Way indicates the prescence of graphite grains in the interstellar medium. Prominent features in the near-IR imply the prescence of silicate grains.

The code utilises realistic size distributions of both graphite and silicate grains, set by laboratory measurements (Laor and Draine 1993). The dust mixture cross-section and absorption coefficent are given by a sum over grain radii.

Large dust grains are in thermal equilibrium with the bathing radiation field, and emit as grey bodies. Here, the emission coefficient can also be derived as a sum over grain radii. Small grains are subject to temperature fluctuations, due to the energy of incident radiation being larger than the typical energy content of the small grain. A temperature distibution for grains of a given size has to be considered in this case.

The emissivity of dust grains ϵ_ν is intimately tied to the SED of a galaxy at far-IR and beyond wavelengths. The standard dependence on frequency goes as $\epsilon_\nu \propto \nu^2$, although there have been suggestions that this is not universal, especially in starbursts. Silva et al. (1998) fit their model SED of the galaxy Arp220 (the archetypal ULIRG) using the relation $\epsilon_\nu \propto \nu^{1.6}$, and Baugh et al. (2005) find that a reasonable fit to the submilimetre number counts is achieved with $\epsilon_\nu \propto \nu^{1.5}$. Simple theoretical models do not exhibit any change in dust emissivity at long wavelengths (Draine 2003), but there is some laboratory evidence for a changing ϵ_ν for certain dust materials.

2.2.3 The equation of radiative transfer in molecular clouds

To take into account the effects of dust in optically thick molecular clouds on starlight, we must solve the equation of radiative transfer:

$$\frac{dI_\lambda}{ds} = -\alpha_\lambda I_\lambda + j_\lambda, \tag{2.32}$$

where α_λ is the absorption coefficient and j_λ is the emission coefficient.

This can be split into 2 components: $I_{\lambda,1}$, the specific intensity of radiation emitted by the central source, and $I_{\lambda,2}$, the specific intensity of radiation emitted by the dust.

For $I_{\lambda,1}$ the transfer equation is satisfied with $j_\lambda = 0$:

$$I_{\lambda,1}(r,\theta) = I_{\lambda,1}(0)\exp[-\tau_\lambda(r,\theta)], \tag{2.33}$$

where $\tau_\lambda(r,\theta)$ is the optical depth from the origin to the point (r,θ). The mean

specific intensity is given by:

$$J_\lambda = \frac{1}{4\pi} \int_{4\pi} I_\lambda \mathrm{d}\Omega. \tag{2.34}$$

For $I_{\lambda,2}$, the full transfer equation must be solved, and is given by:

$$I_{\lambda,2}(r,\theta,\beta,\phi) = \int_{(r,\theta)}^{(r_b,\theta_b)} S_\lambda(r',\theta') \exp[-\tau_\lambda(r',\theta')] \mathrm{d}\tau_\lambda. \tag{2.35}$$

The integration extends from point (r,θ) to the outer boundary of the cloud (r_b, θ_b) along the direction $(\pi - \beta, \pi + \phi)$, and τ_λ is the optical depth from (r,θ) to (r_b, θ_b). The source function is defined as $S_\lambda \equiv j_\lambda / \alpha_\lambda$.

It is assumed that the net energy transfer is dominated by radiative flux, so thermal equlibrium holds (energy input=energy output). This can be written as:

$$\int_0^\infty Q_{abs}(a,\lambda) J_\lambda \, \mathrm{d}\lambda = \int_0^\infty Q_{abs}(a,\lambda) B_\lambda(T(a)) \, \mathrm{d}\lambda, \tag{2.36}$$

where Q_{abs} is the absorption cross section. Thus, for each grain size a, T is determined by numerically integrating equation (2.36).

The lambda iteration method

There are no analytic solutions to the equation of radiative transfer above, and so it must be solved numerically. The most common way of doing this is known as the **lambda iteration method**. This involves selecting a trial value of the mean specific intensity at each point, from which a value for T and the source function S_λ are obtained. Using this an updated value of the mean specific intensity is found using the equation of radiative transfer, and the process is repeated in an iterative manner. The method proposed by Collison and Fix (1991) is used in GRASIL.

It is assumed that the local integrated flux of radiation is proportional to the change in the source function weighted by the absorption coefficent. The region of interest has N radial grid points $i = 1, 2, 3 \ldots N$.

$$F(r,\theta) \sim \frac{S(r_i,\theta) - S(r_{i+1},\theta)}{r_i - r_{i+1}}, \tag{2.37}$$

where

$$S(r,\theta) = \int_0^\infty \alpha_\lambda S_\lambda(r,\theta) \, \mathrm{d}\lambda = \int_0^\infty \alpha_\lambda J_\lambda(r,\theta) \, \mathrm{d}\lambda, \tag{2.38}$$

due to radiative equilibrium.

Hence, for the n^{th} iteration:

$$S^{(n)}(r,\theta) = \int_0^\infty \alpha_\lambda J_\lambda^{(n)}(r,\theta)\ \mathrm{d}\lambda, \tag{2.39}$$

and the calculated luminosity for the n^{th} iteration at r_i is:

$$L_i^{(n)} = \int_{4\pi} F(r_i,\theta) r_i^2\ \mathrm{d}\Omega, \tag{2.40}$$

where $F = \int\int I_\lambda \cos\theta\ \mathrm{d}\lambda\ \mathrm{d}\Omega$. Using equation (2.37) we have:

$$\frac{L_i^{(n)}}{L_i^{(n+1)}} = \frac{\int_{4\pi} S^{(n+1)}(r_i,\theta) - S^{(n+1)}(r_{i+1},\theta)\ \mathrm{d}\Omega}{\int_{4\pi} S^{(n)}(r_i,\theta) - S^{(n)}(r_{i+1},\theta)\ \mathrm{d}\Omega}. \tag{2.41}$$

To speed up the convergence to a solution, set:

$$J_\lambda^{(n+1)}(r_i,\theta) = f_i J'_\lambda(r_i,\theta), \tag{2.42}$$

$$J_\lambda^{(n)}(r_i,\theta) = J'_\lambda(r_i,\theta), \tag{2.43}$$

where f_i is a multipicative factor only dependent on the radius, J'_λ is the mean specific intensity calculated using the current source function. There is a recursion relation for the values of f_i, and this can be obtained using equations (2.41), (2.42) and (2.43):

$$f_i = f_{i+1}\left(\frac{Y_{i+1}}{Y_i}\right) + \frac{L_{cen}}{L_i^{(n)}}\left(1 - \frac{Y_{i+1}}{Y_i}\right), \tag{2.44}$$

where

$$Y_i = \int_{4\pi}\int_0^\infty \alpha_\lambda J'_\lambda(r,\theta_i)\ \mathrm{d}\lambda\ \mathrm{d}\Omega, \tag{2.45}$$

$$L_i^{(n+1)} = L_{cen}/L_i^{(n)} \quad \text{and} \tag{2.46}$$

$$f_{N-1} = L_{cen}/L_{N-1}^{(n)} \tag{2.47}$$

2.2.4 Radiative transfer through a diffuse dusty medium

Solving the full equation of radiative transfer for light passing through the diffuse dust component is unnecessary. The 'cirrus' component is optically thin in the IR and is transparent to its own photons.

Consider the cirrus component to be an infinite homogenous medium. A photon travelling through this medium will undergo a random walk due to

scattering events before ending in an absorption event. The probability of a random walk ending in an absorption event is $\epsilon_\lambda = \frac{\alpha_\lambda}{\alpha_\lambda + \sigma_\lambda}$. The mean number of free paths is $N = \epsilon_\lambda^{-1}$.

The mean effective path (rms displacement of photon after random walk) is:

$$l_* = \sqrt{N} l \qquad \Rightarrow \qquad l_* = \epsilon^{-1/2} l, \tag{2.48}$$

where l is the mean free path $l = (\alpha_\lambda + \sigma_\lambda)^{-1}$. Thus:

$$l_* = [\alpha_\lambda(\alpha_\lambda + \sigma_\lambda)]^{-1/2}. \tag{2.49}$$

One can define an effective optical depth $\tau_{\rm eff}$:

$$\tau_{\rm eff} = \sqrt{\tau_{\rm abs}(\tau_{\rm abs} + \tau_{\rm scat})}, \tag{2.50}$$

where $\tau_{\rm abs} = \alpha_\lambda L$, $\tau_{\rm scat} = \sigma_\lambda L$ and L is the size of the region.

The galaxy is divided into small volume elements V_i. Due to azimuthal symmetry the local radiation field in $V_i(r, \theta, \phi = 0)$ is calculated from the contributions from all other elements $V_k(r, \theta, \phi > 0)$. There will be contributions from both molecular cloud emission and unobscured starlight.

The specific intensity in element V_i is given by:

$$J_{\lambda,i} = \sum_k \frac{V_k(j^{mc}_{\lambda,k} + j^*_{\lambda,k}) \exp\left[-\tau_{{\rm eff},\lambda}(i,k)\right]}{r^2_{i,k}}, \tag{2.51}$$

where $\tau_{\rm eff}(i,k)$ is the effective optical depth between i and k and $r^2(i,k)$ is the volume averaged square distance from i to all points in k:

$$r^2(i,k) = \frac{\int_{\triangle\phi}\int_{\triangle\theta}\int_{\triangle r} V_k r^2 \sin\theta \; {\rm d}^2(i,k) \; {\rm d}r \; {\rm d}\theta \; {\rm d}\phi}{V_k},$$

where

$$V_k = \int_{\triangle\phi}\int_{\triangle\theta}\int_{\triangle} r^2 \sin\theta {\rm d}r \; d\theta \; {\rm d}\phi,$$

and

$$d^2(i,k) = (r\sin\theta_i - r\sin\theta\cos\phi)^2 + (-r\sin\theta\sin\phi)^2 + (r\cos\theta_i - r\cos\theta)^2.$$

We now have a total emission coefficent: $j_{\lambda,k} = j^{mc}_{\lambda,k} + j^*_{\lambda,k} + j^{\rm cirrus}_{\lambda,k}$.

Finally, the specific flux as seen by a distant observer in direction β is given by:

$$F_\lambda(\beta) = 4\pi \sum_k V_k j_{\lambda,k} \exp\left[-\tau_{eff,\lambda}(k,\beta)\right], \tag{2.52}$$

where $\tau_{\mathrm{eff},\lambda}$ is the optical depth from k to the outskirts of the galaxy along the direction β.

2.2.5 Inputs for the model

In order to calculate a full galaxy SED, the following inputs from the galaxy formation model are required:

$\Psi(t, Z)$	SF history as a function of time and metallicity
M_d	disk mass
M_b	bulge mass
$R_{1/2,d}$	disk half mass radius ($R_d = 0.595 R_{1/2,d}$)
$R_{1/2,b}$	bulge half mass radius ($R_b = 0.068 R_{1/2,b}$)
M_{gas}	mass of cold gas present
Z_{gas}	metallicity of cold gas

The output flux of a galaxy is obtained by summing SSPs of appropriate age and metallicity, weighted by the instantaneous star formation rate, using the Salpeter IMF.

2.2.6 A lookup table for submillimetre fluxes

Computing the full SED of a cosmologically significant number of galaxies requires large amounts of computational time. As an inital attempt to generate large galaxy catalogues in a short space of time, I initially considered using a lookup table to generate submillimetre fluxes for each galaxy.

In this method, a number of model galaxies with specific properties are used as standard points in a multi-dimensional array, each having a particular flux, dependent on the values of the parameters of the galaxy in question. With this, one could conceivably predict the flux of any given galaxy, simply by interpolating between the appropriate points in the array. In this particular situation, a six-dimensional lookup table was appropriate, the parameters being the mass and half-mass radius of both the bulge and disk, the cold gas mass and the cold gas metallicity. A seperate, four-dimensional array could be constructed for pure disc or bulge galaxies.

Nevertheless, this approach has many drawbacks and hidden assumptions. The most obvious is finding suitable galaxies in a simulation to construct the table from. Hand tuning, such as artificially altering the disc and

bulge radii, was generally necessary. In addition, although not an explicit free parameter in GRASIL, the present-day SFR has an enormous effect on the final SED of a galaxy, especially in the far-IR/submillimetre range. It was necessary to normalise all the galaxy 'nodes' to a particular SFR (usually 1 $M_{\odot}$ yr^{-1}) and calculate the SED based on this. Assuming that the SED is a simple function of the SFR given all other parameters, I could extract a flux for any given galaxy with an arbitary SFR. It is not at all clear that this is valid in practice. In addition, the entire star formation history of a galaxy should actually be taken into account. In effect, calculating a flux by interpolating between the galaxies assumes that the galaxy in question has an identical star formation history, which is clearly never the case. Indeed, this problem arises in the construction of the table itself. Although two galaxies may differ in only the value of one of the free parameters, they will in fact have entirely different histories. The problem is lessened in the far-IR/submillimetre region, where the flux is dominated by very recent star formation, but the optical and near-IR properties of a galaxy are dependent on stars of ages anywhere up to of order the age of the universe. It is clear that using an array of 'standard' galaxies to calculate SEDs and associated fluxes is in fact deeply flawed, and this approach was abandoned. Nevertheless, methods are available for reducing the computation time required (S99), and I detail these in the next section.

2.2.7 Speeding up the code

GRASIL is a computationally intensive code, with the workload depending on the geometry of the galaxy in question. Pure bulges are the fastest to process due to spherical symmetry, and composite disc+bulge systems need anywhere between 1 and 10 minutes, depending on the sizes of the components. The bulk of the computation is spent on calculating the optical depth between two volume elements (Silva 1999), or more precisely, calculating the line integral of diffuse gas between the volume elements $V_i(r, \theta, \phi = 0)$ and $V_k(r, \theta, \phi > 0)$, given by $\int_k^i \rho^c(s)\, \mathrm{d}s$.

Details of a useful time-saving method can be found in S99, but I summarise the main points here. In order to generate SEDs for a large sample of galaxies, the above integral is calculated only once and appropriately nor-

Geometry	computational time (s)
Bulge only ($\rho = 0$)	$\simeq 30$
Bulge only ($\rho = 1$)	$\simeq 35$
Bulge only ($\rho = 2$)	$\simeq 20$
Bulge + disk ($\rho = 0$)	$\simeq 530$
Bulge + disk ($\rho = 1$)	$\simeq 145$
Bulge + disk ($\rho = 2$)	$\simeq 75$

Table 2.3: Computational time required for the production of galaxy SEDs

malised for a set of self-similar galaxies. In practice, R_d^c/r_c must fall within a certain range for the errors introduced by applying this shortcut to be less than 25%.

I define $\omega \equiv R_d^c/r_c$ as the ratio of dust scalelength to bulge core radius, and $\kappa \equiv M_{\rm gas}/(M_{\rm stars} + M_{\rm gas})$ as the gas to total mass ratio. In the following situations, the following lower and upper limits are appropriate:

$$\omega_{\rm lo} = \begin{cases} 1 & : \quad (B/T)_B < 0.1 \\ 4 & : \quad \text{otherwise,} \end{cases} \tag{2.53}$$

$$\omega_{\rm up} = \begin{cases} 300 & : \quad \kappa < 0.01 \\ 50 & : \quad \text{otherwise.} \end{cases} \tag{2.54}$$

In practice, roughly 40 percent of spiral (ie disk + bulge) galaxies satisfy these constraints in a given simulation volume.

As mentioned above, an output SED can have the spectral resolution of the input SSPs if so desired. The extra computational time taken to generate this is negligible, so I output this complimentary SED for each galaxy.

In the following, I use $\rho = 0$ to represent a situation where no self-similar solution is possible, $\rho = 1$ denotes the production and use of a self-similar solution, and $\rho = 2$ represents the use of the self-similar solution.

From table (2.3), it is clear that using self-similar solutions for the line integral through cirrus dust greatly reduces the computational load, especially for spirals. In all, a simulation box with ~ 25000 galaxies requires $\sim 5-6 \times 10^6$ s to generate SEDs for every galaxy, or about 65 days. Spreading this workload across many machines dramatically reduces the actual time required. In practical terms, I create a 'jobfile', essentially a list of all galaxies that need to

be processed. At the beginning of each individual dust run, a flag is created indicating that the galaxy in question has been done. Then, a large number of machines can run the same code in parallel, running through the jobfile and checking for the 'done' flag until an unprocessed galaxy is found. In this way, effective balancing of workload is achieved automatically: each machine works at its own pace, doing as many jobs as it can until all are complete. This is far more efficent than giving each processor a set number of galaxies to process: in this case the more powerful or quieter machines finish their allotted jobs much faster, and then sit idle waiting for the other machines to finish. My naive parallel scheme naturally allows the faster machines to process more jobs.

2.2.8 Analysing the results

For each galaxy in a simulation box, GRASIL calculates two files containing rest frame SEDs from the far-UV to the radio: one assuming the galaxy is face on, and another where the galaxy has been assigned a random inclination. This has a particularly large effect on spiral galaxies, where the extinction can be significantly larger for edge-on disks. Each file also includes the unextincted SED, useful for quantifying the effects of dust on a particular galaxy. In Figure 2.8 I plot the SED of a typical dusty galaxy.

I use the standard UVBRIJK Johnson-Cousins set of broadband filters and Vega magnitudes throughout, unless specifically noted otherwise. The IRAS filter profiles were taken from the IRAS explanatory supplement (Beichmann 1985), the SCUBA 850μm filter profile from

`http://jach.hawaii.edu/JCMT/continuum/background/background.html`

The *Spitzer* MIPS filter profiles were taken from

`http://ssc.spitzer.caltech.edu/mips/MIPSfiltsumm.txt`

From each galaxy SED I can calcuate the rest-frame absolute magnitudes in various filters, and by redshifting the SED appropriately, can also derive an apparent magnitude or flux for that particular redshift and cosmological model (see equation 1.23).

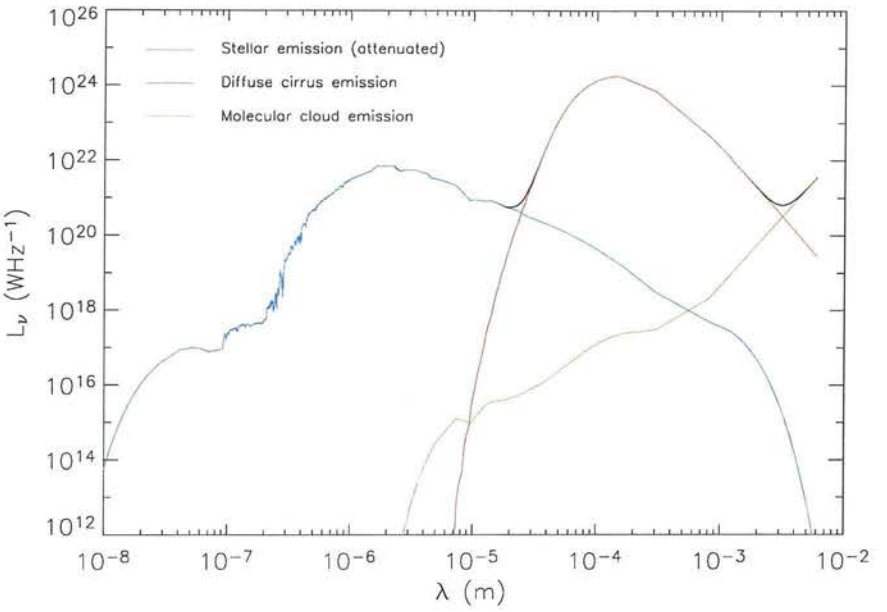

Figure 2.8: Left panel: Example galaxy SED. The various subcomponents making up the total light output are shown as different coloured lines.

CHAPTER 3

The fiducial model: properties of the local universe

In this chapter I use the galaxy formation model set out in Chapter 2 to derive various properties of the local universe. By selecting an appropriate set of free parameters I aim to derive a 'best fit' to a number of these fundamental properties. Assuming that our knowledge of local physics is reasonably correct, I derive a model that gives a reasonable reproduction to the local universe for later application at high redshift, and I present the fiducial model here.

3.1 The fiducial model

As seen in the last chapter, the galaxy formation model contains a large number of free parameters, all of which can influence the outcome of results derived from the models. Accurate treatment of dust comes with its own set of free parameters, adding to the degrees of freedom the model can potentially have. Nevertheless, these freedoms are often limited. For example, the cosmological parameters (Table 2.1) of the underlying simulation are 'hard wired' into the N-body simulation, and in any case are based on values consistent with the latest CMB analyses (eg Lahav and Liddle 2006). The density of baryonic matter is a free parameter, but cannot be varied by a significant amount without contradicting results from the above analyses.

In order to find a set of parameters for a fiducial model applicable at both low and high redshift, one should ideally calibrate the model by comparison to as much high-quality data as possible. With this in mind, I demand that my fiducial model should reproduce with reasonable accuracy some of the more fundamental properties of the local universe, of which there is a wealth of observational data available.

A large search of parameter space is necessary to find a realistic model, but is too complex to fully sample on a feasible timescale. Nevertheless, in this thesis I will on the whole not present the results of testing the free parameters, and merely report the final values I deem suitable for further study. These are given in Table 3.1. It is important to note that $\alpha_*, \alpha_{\rm hot}$ and $V_{\rm hot}$ are three different facets of one overall free parameter, and so tuning one requires an appropriate adjustment of the others (Cole et al 1994).

With the free parameters in GRASIL, I employ a different philosophy. On the whole, I choose to use the same values as S99, Granato et al. (2000) and Baugh et al. (2005). This will highlight the differences between the galaxy formation models themselves. Indeed, many of the free parameters are related to physical properties of the dust grains themselves. Altering these from their standard, laboratory derived values would be dangerous at best, and unphysical at worst. Geometrical parameters (disk scaleheight, molecular cloud mass and radius) are chosen to be consistent with observations of the Milky Way and other $L \simeq L_*$ spirals.

The best-fitting set of parameters are given in Table 3.1. I now present a variety of the model predictions and compare them with the equivalent local datasets. Unless stated otherwise, all quoted magnitudes are dust-extinction derived estimates.

3.1.1 Optical luminosity functions

In Figure 3.1 I plot the B and K band luminosity functions derived from the fiducial model. The solid line shows the dust-extincted LF, and the dotted line the dust-free estimate.

In the B band, I compare the model with LFs derived from the Two-Degree Field Redshift Survey (Norberg et al. 2002) and the Sloan Digital Sky Survey (Blanton et al. 2001). In the K band, I compare with the combined 2MASS-

Description	Parameter	Value
Fixed parameters		
Baryonic density of Universe	Ω_b	0.04
Virial criterion	δV	0.5
Recycled fraction of stellar material	$\mathcal{R}$	0.3
Mass-to-light ratio	Υ	1.0
Initial mass function	IMF	Salpeter
Free parameters		
Dynamical friction timescale (Gyr)	$\tau_{\rm mrg,0}$	$0.5 * \tau_{\rm dyn}$
Dynamical friction power law exponent	$\alpha_{\rm mrg}$	1.0
Major merger threshold	$f_{\rm mrg}$	0.3
Disk angular momentum fraction	$\jmath$	0.5
Star formation timescale (Gyr)	τ_*	2.0
Star formation scaling law	α_*	-3.0
Feedback efficency (km s^{-1})	$V_{\rm hot}$	140.0
Feedback scaling law	$\alpha_{\rm hot}$	5.5
Halo-halo merger gas fraction	$\xi_{\rm b,hh}$	0.5
Galaxy-galaxy merger gas fraction	$\xi_{\rm b,gg}$	1.0
Fraction of ejected gas returned to hot phase	e	0.0
Free parameters in GRASIL		
Typical molecular cloud mass ($M_\odot$)	$M_{\rm mc}$	10^6
Typical molecular cloud radius (pc)	$R_{\rm mc}$	15
Typical escape time for stars in clouds (Myr)	t_0	1
Fraction of gas in molecular form	f_{H_2}	0.25
Scaleheight of disks	z_d	$0.1R_d$

Table 3.1: Parameter choices in the fiducial model

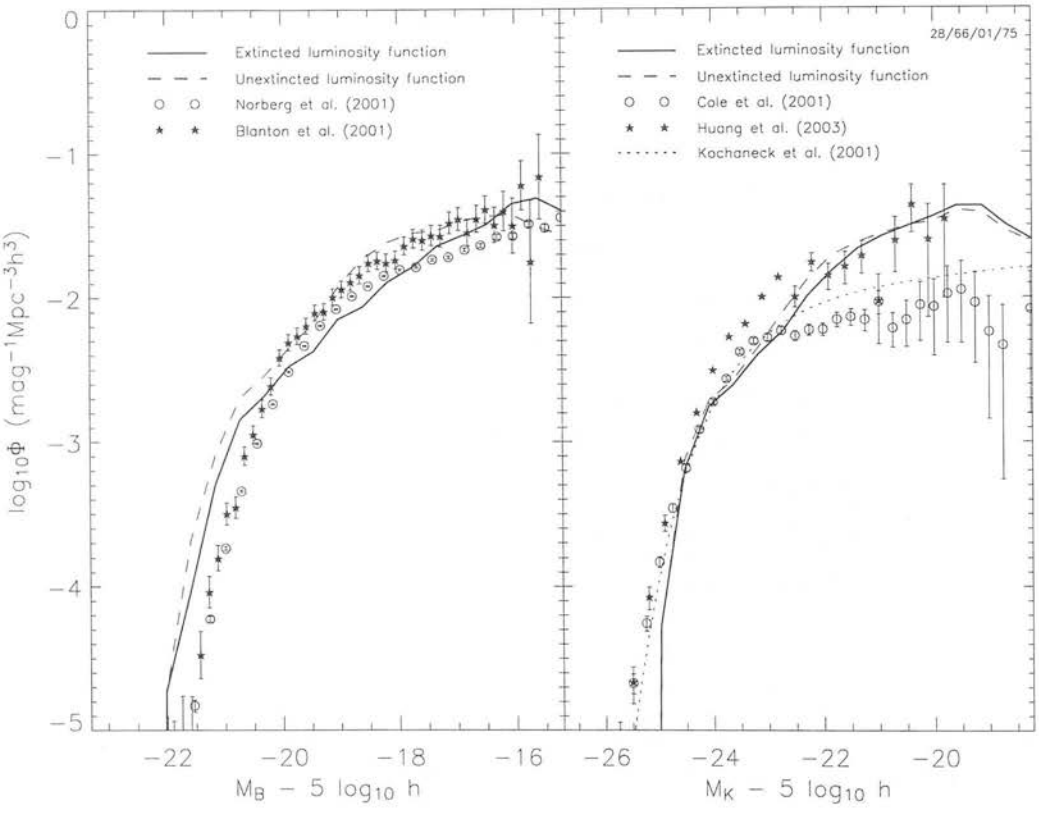

Figure 3.1: Left hand panel: the model B band luminosity function (both dust-extinguished and 'bare'), plotted together with two observational datasets. Right hand panel: the model K band luminosity function (both dust-extinguished and 'bare'), again compared with local observational estimates. See the accompanying text for more details.

2dFGRS survey (Cole et al. 2001), the Hawaii-AAO survey (Huang et al. 2003) and a Schecter function fit to a sample of 4192 galaxies in the 2MASS survey (Kochaneck et al. 2001).

In the B band, the brightest galaxies ($M_B - 5\log h \sim -20$) are roughly half a magnitude fainter when dust extinciton is included. This, in tandem with the truncation method outlined in section 2.1.9, yields a reasonable fit to the bright end of the LF, albeit still slightly overpredicting the numbers of such luminous objects. Below $M_B - 5\log h \sim -20$, the LF shows an slight underabundance of galaxies. It is interesting to note that the unextincted estimate of the LF gives a better fit to the data faintwards of M_*, implying that dust extinction is being over-estimated in these objects. This immediately suggests that the fainter galaxies perhaps house too much cold gas, leading to an overabundance of dust. Nevertheless, the slope of the faint end matches the Blanton et al. (2001) data well, implying that the choices of feedback parameter are giving the correct relative numbers of faint galaxies. The LFs are slightly affected by the choice of $\mathscr{f}$ (the fraction of halo angular momentum kept by the disk), and I find that a value of $\mathscr{f} = 0.5$ gives the best fit overall, although the differences are small. Changing the halo-halo merger and galaxy-galaxy merger free parameters has only a small effect on the LF.

In the K band the effects of dust are far less pronounced, with the brightest galaxies exhibiting negligible extinction. The brightest objects are those where truncation has come into play, stripping the gas and hence dust from the galaxies. I derive a reasonable match to the bright end of the K band LF, closely reproducing the cutoff at around $M_K - 5\log h \sim -26$. This lends credence to the idea of truncation as a necessary part of a successful semi-analytic model: although my method is rather brutal and *ad-hoc*, it is nevertheless clear that some form of curbing star formation in the brightest haloes is required.

The faint end of the K band LF matches the data reasonably well, favouring a steeper slope *a la* Huang et al. (2003) over the results of Cole et al. (2001) and Kochaneck et al. (2001). This is gratifying, as the K band LF is arguably the most fundamental measure of the galaxy population, being a useful tracer of the total stellar mass. Again, this implies that the choice of stellar feedback is approximately correct. It is interesting to note that the fainter galaxies in K are again more affected by the inclusion of dust extinction. An overabundance

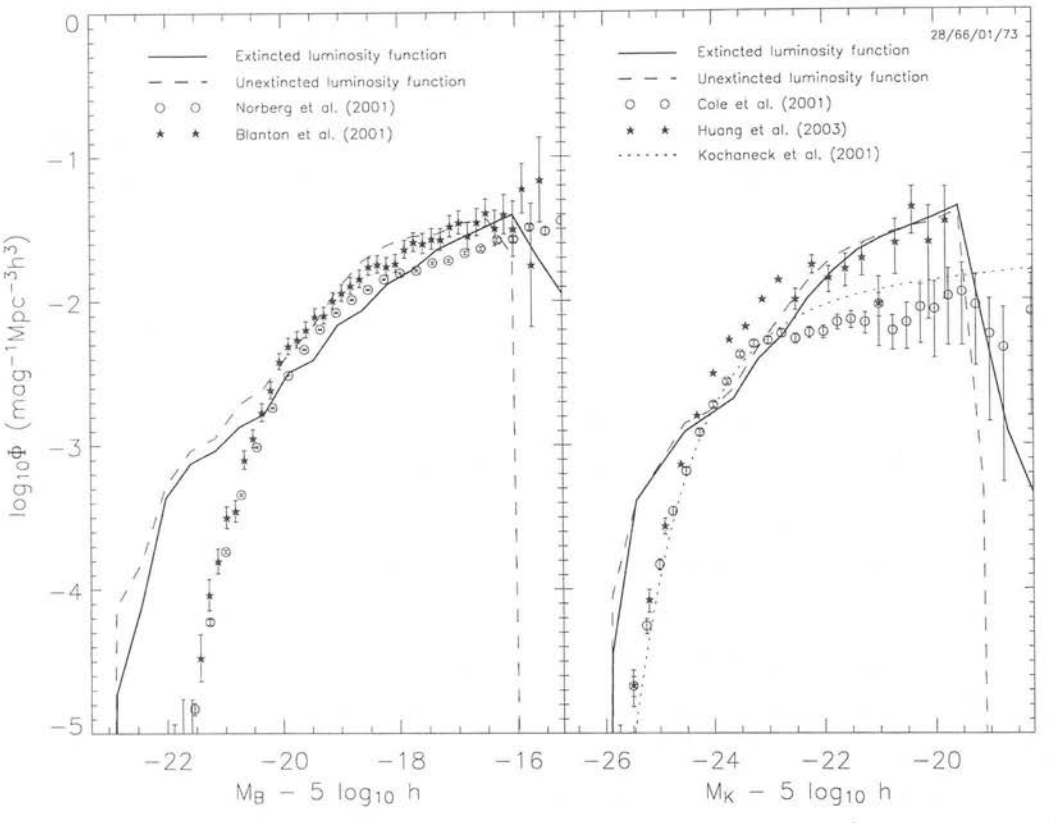

Figure 3.2: As Figure 3.1, but without truncation applied to the model galaxies. Symbols and lines as in Figure 3.1.

of cold gas in these galaxies seems the most likely explanation for this effect.

In selecting an appropriate parameter set, I have chosen the K band luminosity function as my main constraint. I argue that being a reasonably accurate tracer of the underlying stellar mass, the K band LF is a more fundamental property than either the B band LF or the I band Tully-Fisher relation. The B band LF reflects only recent cosmic history, and although the I band Tully-Fisher relation holds well for most spirals, its theoretical origin is still unknown.

The effects of truncation on the optical luminosity functions

In order to quantify the effects of truncation on the bright end of the luminosity function, I also present the results of the fiducial model without truncation. The resulting luminosity functions are plotted in Figure 3.2. The effect

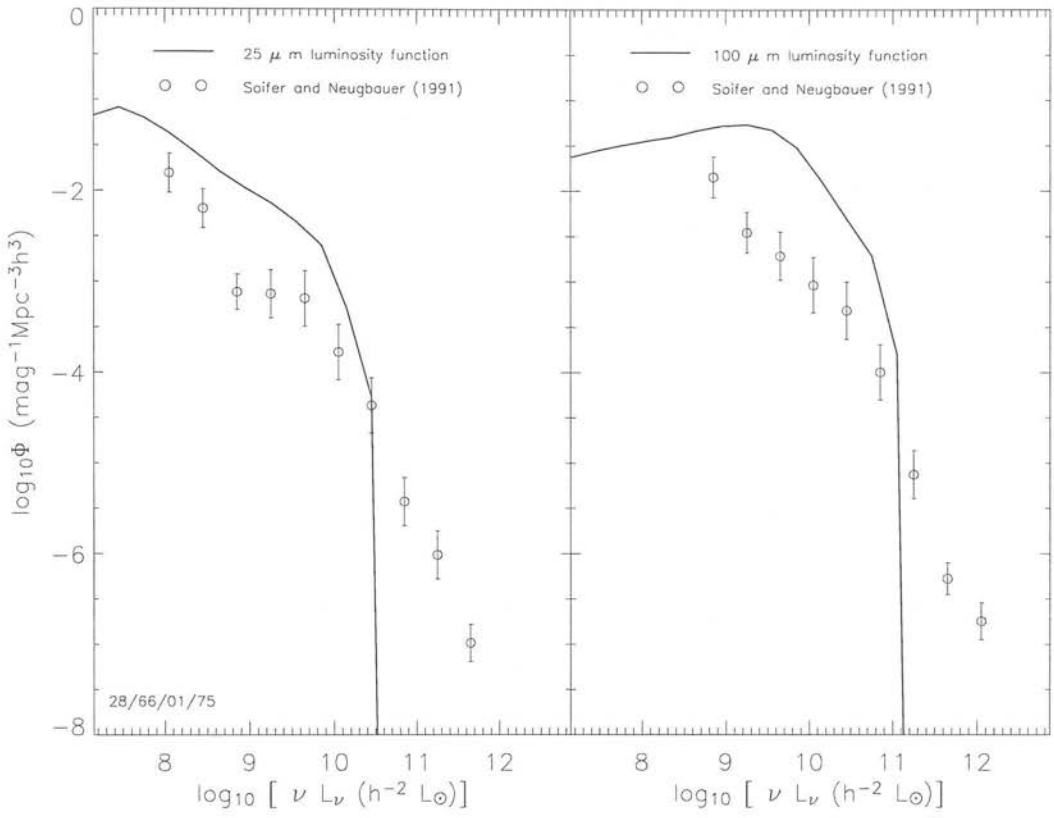

Figure 3.3: IRAS 25 and 100 μm luminosity functions, as derived for the fiducial model.

is enormous: both the B and K band LFs are degraded significantly beyond M_*. The knee of the luminosity function is lost completely, the overall shape becoming something more akin to a power law with a severe overabundance of bright galaxies, especially in B.

3.1.2 Infrared luminosity functions

As we have learnt, dust extinction is the primary source of IR radiation in galaxies. Soifer and Neugebauer (1991, SN91) use the *IRAS* Bright Galaxy Sample (Soifer et al. 1989) to compile flux-limited catalogues of local galaxies at 12, 25, 60 and 100 μm. The catalogue is complete down to 5.24 Jy at 60 microns with 313 sources, and the mean redshift is $\langle z \rangle = 0.006$. The corresponding K-corrections are therefore small.

In Figure 3.3 I compare the model LFs with those measured by SN91.

The 25 μm data shows a clear overabundance of 'average' galaxies, and a complete lack of objects bright in this waveband. As with the optical LFs, this suggests an excess of cold gas in medium-sized objects, intimately linking the deficency of B-band light and overabundance of 25 μm light. The lack of bright galaxies indicates a possible deficit of cold gas in these objects. This ties in nicely with the relative lack of dust absorption seen at the bright end of the optical LFs. The 100 μm LF highlights the same issues, with 'average' galaxies considerably brighter than expected, and a slightly less extreme cut-off at the bright end.

There are two possible explanations for the lack of extremely bright IR galaxies: either the simulation volume is too small to reliably contain such objects, or the act of truncation is preventing them from forming, stripping the cold gas from the galaxy and depriving it of a source of dust extinction. The most luminous galaxies have a space density of $\sim 10^{-7}$ mag^{-1} Mpc$^{-3}h^3$, too sparse to reliably appear in my simulation volume of 50 h^{-1} Mpc.

The effects of truncation on the IR luminosity functions

Although the absence of the most luminous IR galaxies can be explained by my small simulation volume, it is possible that truncation is partly to blame for the discrepancy at slightly lower luminosities. As in the previous section, I present the predicted IR luminosity functions when truncation is ignored. The results are plotted in Figure 3.4. The cutoff at the bright end is pushed slightly to higher luminosities. However, if truncation were removed, a possible improvement at the bright end of the IR luminosity functions would be at the expense of a considerably poorer fit in the optical regime.

3.1.3 Baryonic properties of haloes

I now examine the baryonic content of the galaxies, ie considering both the stars and cold gas. On the whole, one expects the most massive and metal rich systems to live in high circular velocity haloes: gas cools on shorter timescales in such objects, and feedback has little effect on the gas content of such a halo, allowing star formation to proceed unhindered. I show the baryonic properties of haloes in Figure 3.5. In both panels I plot the position of the Milky Way as a red star: the circular velocity of the MW is 220 km s^{-1}

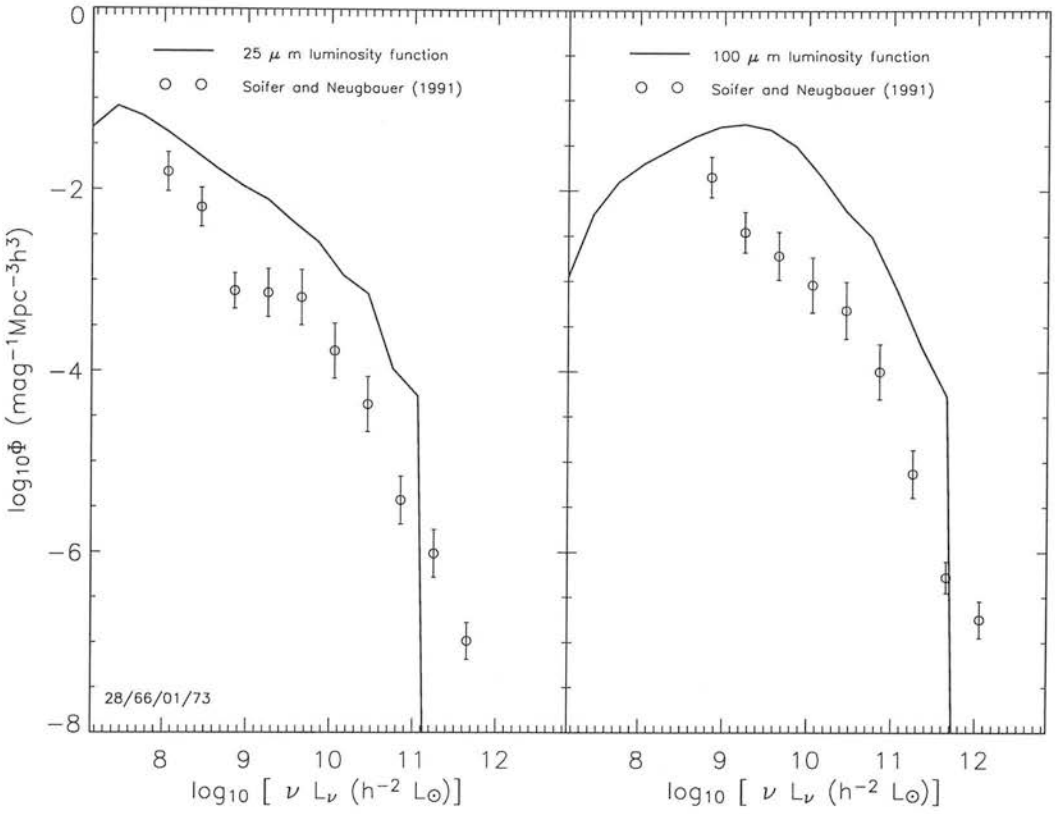

Figure 3.4: IRAS 25 and 100 μm luminosity functions, without truncation applied to the model galaxies.

(Binney and Tremaine 1987), the baryonic mass $M_{bar} = 6 \times 10^{10}\ M_{\odot}$ (Binney and Evans 2001) and the metallicity of the ISM is given by $Z_{\rm gas} = 0.016$ (Pagel 1998). The Milky Way falls well within both distributions, indicating that the galaxy formation model can predict 'average' galaxies broadly similar to the one we reside in.

3.1.4 The morphological mixture of field galaxies

The morphological mix of galaxies in the local universe is well constrained. The Stromlo-APM Redshift Survey (Loveday et al. 1996) yields the ratio E : S0 : Sabc+Irr = 13:20:67 (Baugh et al. 1996, Loveday 1996) in the local field. This is a flux-limited sample of galaxies with $b_J < 16.44$, and not directly comparable to my volume-limited simulation cubes. With this in mind, and following the lead of Hatton et al. (2003), I construct a volume-limited

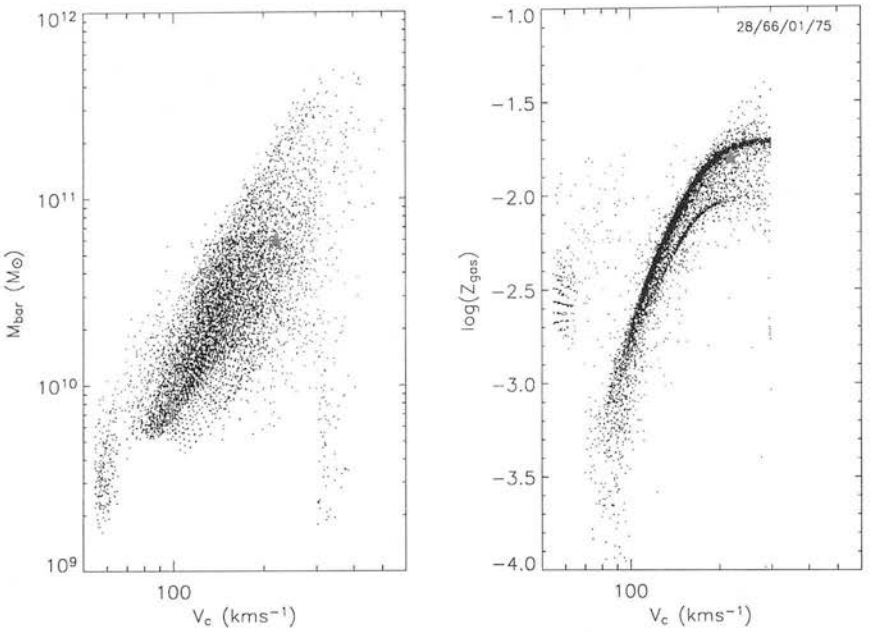

Figure 3.5: Left hand panel: baryonic mass of a galaxy as a function of halo circular velocity. Right hand panel: cold gas metallicity as a function of halo circular velocity. In both cases, the position of the Milky Way is shown as a red star.

subsample of the survey data.

The Stromlo-APM catalogue is available online at `cdsweb.u-strasbg.fr/viz-bin/VizieR-4`. From the full catalogue, I sort by morphological type and select those within the redshift range $0.0001 \leq z \leq 0.1$. For each galaxy, I calculate the absolute magnitude

$$M_B = b_J - 5\log_{10}\left(\frac{D_L}{10}\right) - k(z), \tag{3.1}$$

where I convert from b_J to Johnson B magnitudes using the conversion $B = b_J + 0.28(B-V)$, assuming a mean colour of $\langle(B-V)\rangle = 0.94$ (Norberg et al. 2002). The k-correction $k(z)$ is the mean relation found by Madgwick et al. (2002), given by

$$k_{AV}(z) = 1.9z + 2.7z^2, \tag{3.2}$$

and I assume a Hubble constant of $H_0 = 70\text{km s}^{-1}$. A final cut of all galaxies brighter than $M_B = -18.8$ is made. This volume-limited subset of the Stromlo-APM catalogue yields a morphological fraction E : S0 : Sabc+Irr = 14:19:67, with a total sample size of 801 galaxies.

In order to quantify the morphological mixture of galaxies in the fiducial model, I calculate the bulge-to-total light ratio, defined by

$$\left(\frac{B}{T}\right)_B = 10^{-0.4\Delta m_I}, \tag{3.3}$$

where $\Delta m_I \equiv m_{B,\mathrm{bulge}} - m_{B,\mathrm{total}}$ is the magnitude difference between the bulge component and the entire galaxy. With this definition in place, galaxies with $(B/T)_B \leq 0.4$ are classified as spirals, those with $0.4 < (B/T)_B < 0.6$ are classified as lenticulars and those with $(B/T)_B \geq 0.6$ are ellipticals. Of course, the eyeball classification of galaxies is in some sense a very subjective process, and is subject to uncertainties involving projection effects. Automated classification by decomposing the light profile of a galaxy can be problematic, and can give differing results depending on the functional form used for the decomposition (eg. de Jong 1995). With these caveats in mind, the boundaries described above should not be thought of as being set in stone, but will assign a reasonably accurate morphology to a given galaxy.

Applying the same $M_B < -18.8$ cut to the fiducial model yields a morphological fraction of E : S0 : Sabc/Irr = 8:8:83. Spirals are over-represented (recall that observational results suggest 14:19:67):, and both ellipticals and lenticulars are somewhat lacking. It seems that there is a lack of major merging in the simulation, relatively insensitive to the choice of f_{mrg}. I thus choose $f_{\mathrm{mrg}} = 0.3$, in common with many other semi-analytic models.

3.1.5 Gas properties of spiral galaxies

Cold gas plays a crucial part in determining the luminosity of galaxies. First and foremost, the creation of new stars requires the presence of a significant gas reservoir. Observations tend to suggest that the density of such a reservoir needs to be above a certain value before instabilities set in and molecular clouds can form. Nevertheless an attempt at modelling the so-called Kennicutt threshold (eg. Kennicutt 1989, Rimes 2003) failed to yield a reasonable match to the optical luminosity functions (too few stars formed to give an acceptable match to the K band LF), and so was left out of the fiducial model.

A second, more subtle effect concerns the influence of dust extinction. For a given amount of incident light, the observed luminosity as seen by a distant observer depends on the amount of gas present in the galaxy in question:

more gas equals more dust equals more extinction. Of course, the metallicity and geometry of the gas disk will also affect the final observed luminosity.

In Figure 3.6 I show the hydrogen gas mass-to-light ratio (calculated assuming a mixture of 77 percent H and 23 percent He, taking into account both atomic and molecular H) of spiral galaxies in the fiducial model, again defined as those where the B-band light of the bulge contributes less than forty percent of the total light. Individual points are galaxies, with the solid line showing the median of the distribution and the dashed lines the tenth and ninetieth percentiles of the distribution. For comparison, I plot two sets of observational data: that of Huchtmeier and Ritcher (1988) (squares) and Sage (1993) (circles). The former dataset measures only atomic hydrogen for faint, late-tye spirals. Nevertheless, the fraction of gas in the molecular form is low for such objects and as such should not skew the results badly. The latter dataset measures both atomic and molecular hydrogen in a bright sample of spirals of all types.

Taken as a whole, the observations predict a slow trend towards lower gas fractions in brighter objects. The data follows this overall trend, but with a far more pronounced slope than expected. Brighter than $M_B - 5\log h \leq -18$, the predictions fall within the error bars of the observations. At fainter magnitudes, the model predicts gas fractions far in excess of that observed. This result, while worrying, ties in nicely with the results of sections 3.1 and 3.2. Faint galaxies are exhibiting too much extinction, and this is intimately linked to the amount of cold gas present. The overabundance of gas in these objects neatly explains the discrepancies seen in the luminosity functions. Of course, there will be other effects at play here, but it seems likely that the cold gas issue is responsible for much of the disagreement seen earlier. Sadly, considerable tweaking of the free parameters fails to produce a better match to the above plot: even with the strong feedback parameters used in the fiducial model, significant reservoirs of cold gas remain. Rimes (2003) uses a Kennicutt threshold for star formation, which suppresses star formation in underdense regions of gas. Including a Kennicutt threshold for star formation would conceivably prevent star formation in many of these faint disks, leaving an even larger fraction of gas behind in a correspondingly fainter galaxy (however, as mentioned above, this introduced other, more severe problems into the model). There are other possible methods of removing or reheating

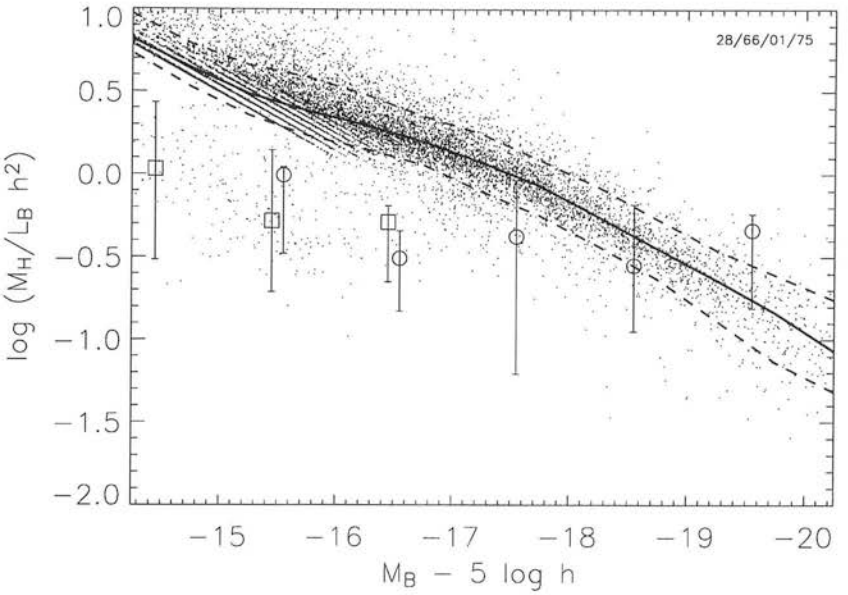

Figure 3.6: Cold gas content of all spiral galaxies brighter than M_B < -14. Squares are observations from Huchtmeier and Richter (1988) and circles are observations from Sage (1993). See the accompanying text for more details.

cold gas in galaxies: ram pressure stripping may be effective in high-density regions (eg. Abadi, Moore and Bower 1999), and Benson et al. (2003) posit a number of physical mechanisms, including thermal conduction and galactic 'superwinds'. These were introduced to help match the bright end of the K-band LF, and it is unclear how efficient these processes would be in smaller galaxies. AGN feedback may be the key ingredient missing here, and this is described more fully in chapter 6.

3.1.6 Physical properties of disks

In Figure 3.7 I plot the scalelength of a galaxy disk against its circular velocity, each point representing an individual galaxy. The Milky Way has a scalelength of $r_d = 3.5 \pm 0.5$ kpc (Binney and Tremaine 1987), and is plotted as red star. Mo, Mao and White (1998) give a simple relation for the scalelength of a thin disk, ignoring self-gravity:

$$R_d \approx 8.8h^{-1}\mathrm{kpc}\left(\frac{\lambda}{0.05}\right)\left(\frac{V_c}{250\ \mathrm{kms}^{-1}}\right)\left(\frac{H}{H_0}\right)^{-1}\left(\frac{j_d}{m_d}\right), \qquad (3.4)$$

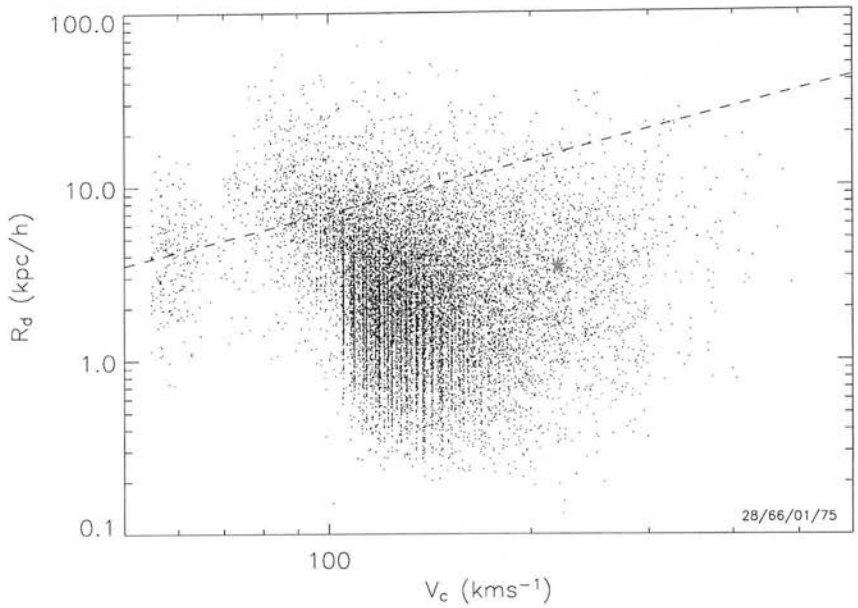

Figure 3.7: The relation between scalelengths of model disks and their circular velocity. The points represent individual spirals with $M_K < -19$ and the Milky Way is plotted as a red star. The dotted line represents the Mo, Mao and White (1998) prediction for a disk with $\lambda = 0.1$ and $j_d = m_d$ (see accompanying text for more details).

where λ is the dimensionless spin of the halo, defined by $\lambda = J|E|^{1/2}/GM^{5/2}$, V_c is the circular velocity of the halo, H is the Hubble constant at redshift z, j_d is the angular momentum of the disk (expressed as a fraction of the angular momentum of the halo, ie $J_{\rm disk} = j_d J_{\rm halo}$) and m_d is the fraction of the halo mass contained in the disk. If angular momentum is conserved, then $j_d = m_d$ and the scalelength simply depends on the spin and circular velocity of the halo (for a given formation redshift z).

For a given initial distribution of halo spins, around 10 percent will have $\lambda > 0.1$. As a comparison, I plot the prediction of equation (3.4) for $\lambda = 0.1$ and $j_d = m_d$. This line represents the ideal situation where angular momentum is conserved, and at most 10 percent of disks should have scalelengths above this line, due to a similar proportion of haloes with $\lambda > 0.1$ (Mo, Mao and White 1998). Roughly 8 percent of my disks lie above this line, assurance that my basic model for disks produces physically viable structures. Since the radius of the gas disk is assumed to be identical to that of the stellar disk,

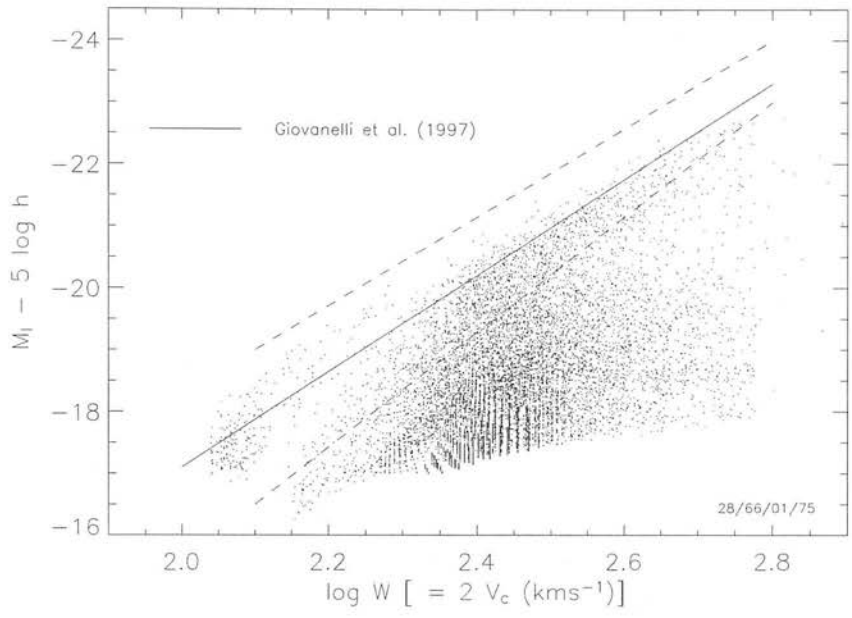

Figure 3.8: Tully-Fisher relation for model spiral galaxies $(B/T)_B < 0.4$. The solid line shows the mean relation from Giovanelli et al. (1997), and the dotted lines show the typical scatter about the mean.

it seems that roughly the correct geometry is being used when calculating dust extinction. This increases the probability that an overabundance of cold gas is to blame for the IR excess in faint galaxies.

3.1.7 Tully-Fisher relation

Matching the Tully-Fisher relation has long been a difficulty for semi-analytic models designed to reproduce the optical luminosity functions accurately (eg Cole et al. 1994, 2000). Alternatively, models tuned to match the Tully-Fisher relation invariably fail to reproduce the optical LFs (eg. Kauffmann et al. 1993).

In comparing the fiducial model to the obervational data, I select only model galaxies classified as spirals (ie. those with $(B/T)_B \leq 0.4$). Note that observations are usually corrected for inclination. With this in mind, I use the face-on magnitude for each galaxy in this section only. The velocity measure in the TF is the maximum rotational velocity of the disk. I assume that this is equal to the circular velocity of the halo, valid when ignoring the gravitational

effects of the disk. The actual observational quantity W is generally taken from Doppler-broadened 21 cm HI linewidth measurements, and hence $W \equiv 2V_c$.

In Figure 3.8 I plot the broadened linewidth W against the I band magnitude for all model spiral galaxies, represented by individual dots. The solid line is the mean TF relation found by Giovanelli et al. (1997)

$$M_I - 5\log h = -(21.00 \pm 0.02) - (7.68 \pm 0.13)(\log W - 2.5), \tag{3.5}$$

and the dotted lines are the (magnitude dependent) scatter about the mean. The majority of the spirals fall well below the observed relation, either rotating too quickly or being roughly 1-2 magnitudes too faint in I. There is a significant population of faint spirals with fast rotational velocities. The model thus shares a deficiency with many other semi-analytic models, and has failed to match the LFs and the TF simultaneously. van Kampen, Jimenez and Peacock (1999) matched both the knee of the luminosity functions and the zero-point of the Tully-Fisher relation, and this more complicated version of their galaxy formation model does not. For the purposes of this study however, I argue that it is the *total stellar mass* that is of paramount importance when studying the high redshift universe, and thus a good fit to the local K-band LF is therefore of fundamental importance.

3.1.8 Galaxy colours: the optical regime

In the top panel of Figure 3.9 I plot the colours of model galaxies ($M_K < -18$) as a function of their bulge to total light ratio. I compare the results with the observational data of Buta et al. (1994). Note that these authors use Hubble T-type as a morphological indicator. Following the lead of Baugh et al. (1996b), I convert Hubble T-type to $(B/T)_B$ using equation (5) of Simien and de Vaucouleurs (1986):

$$\langle \Delta m_I(T) \rangle = 0.8 + 0.145T + 0.0284T^2 + 0.00267T^3. \tag{3.6}$$

Each point is an individual galaxy, the solid line is the mean relation and the dashed lines are the tenth and ninetieth percentiles of the distribution. The results from Buta et al. are plotted as filled diamonds. My model predicts a large population of red ($(B-V) \sim 0.8$) spirals that are not present in the data. The mean colour trend as a function of morphology is much flatter than

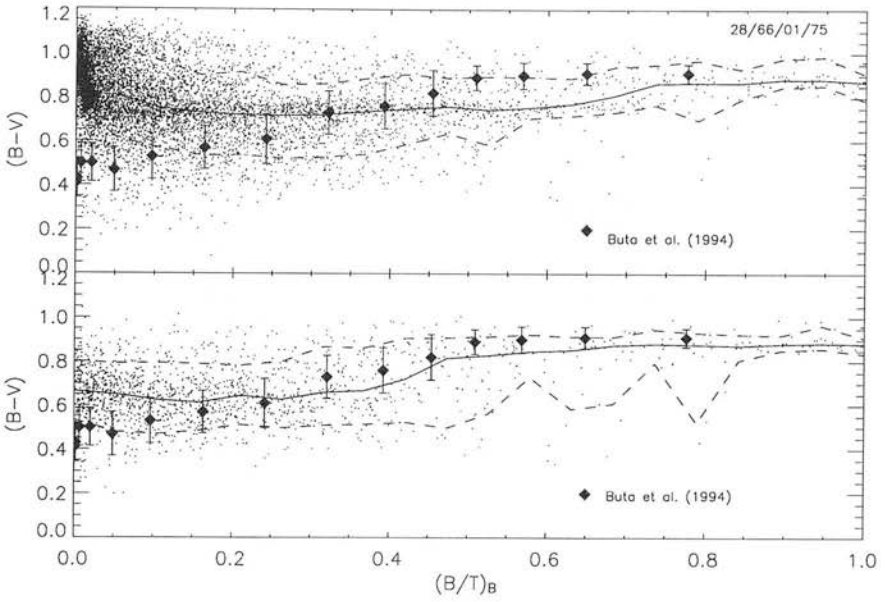

Figure 3.9: Top panel: the colour-morphology relationship for all galaxies brighter than $M_K < -19$. Bottom panel: the same, but for all galaxies brighter than $M_B < -18.8$, the same selection criteria as in section (3.3.5).

observed. However, the model lenticulars and ellipticals have colours broadly similar to the data.

In the bottom panel I plot the same colour-morphology relation, but this time only selecting those with $M_B < -18.8$, as in section (3.3.5). This will hopefully exclude some of the fainter objects near the resolution limit of our simulation, whose properties may be subject to error. In this case, the discrepancy between model and data is far less acute, although the spirals are still too red. In the case of the fainter objects, it is possible that galaxies are being mis-classified as spirals. The N-body simulations used predict that most mergers that occur are classified as minor, insensitive to reasonable variations in $f_{\rm mrg}$. The reasons for this are unclear, but a lack of major mergers is likely to be at the root of the overabundance of spirals.

It has long been known that galaxies of different morphology occupy different regions of a colour-magnitude diagram (eg Tully et al. 1982). Late type (Sabcd) and early type (E+S0) galaxies show a bimodal distribution (eg. Baldry et al. 2004), with the early types being systematically redder and more

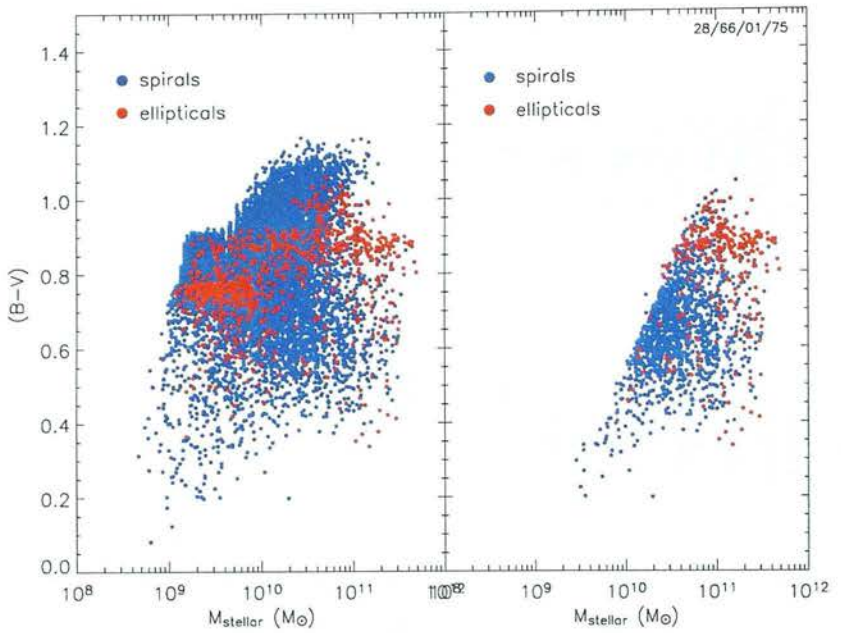

Figure 3.10: Left panel: galaxy colour as a function of stellar mass, for all galaxies brighter than $M_K < -19$. Right panel: the same but for all galaxies brighter than $M_B < -18.8$, as in section (3.3.5).

massive. This division has been present since at least $z \sim 1$ (Bell et al. 2004), and the relative numbers in each population is dependent on the local environment (Balogh et al. 2004). Such a bimodality is also present in plots of colour as a function of stellar mass, and is a common test of semi-analytic models (eg. Bower et al. 2005, Menci et al. 2005, Croton et al. 2006).

In the left-hand panel of Figure 3.10 I show the colour-mass relationship for all model galaxies brighter than $M_K < -19$. The population of small, red spirals is clearly visible, and there is no real hint of the bimodality seen in the data.

As above, I replot the colour-mass relation for all galaxies brighter than $M_B < -18.8$, shown in the right-hand panel of Figure 3.10. Again, the results appear more realistic when we consider the more massive galaxies. The ellipticals tend to be the most massive galaxies present, and their colours are reasonably accurate (cf. figure 3 of Bower et al. 2005 and figure 9 of Croton et al. 2006). The brightest spirals tend to be bluer than the ellipticals, although some are again surprisingly red. As I will show in section 3.1.10,

the model star formation history of the universe is consistent with reality. Why then is there a propensity towards overly-red galaxies in the model? Since the more massive galaxies in the simulation have reasonably consistent colours, it seems that small galaxies are forming their stars too early due to the overly-large fraction of gas present in their parent haloes, accounting for their red colours. It is possible that many small, red spirals are being spuriously flagged as disk-dominated due to deficencies in the treatment of merging.

Despite the problems highlighted here, it appears that I can reasonably match the colours of at least the brightest galaxies. This is gratifying, as it is the bright objects in the universe that the next two chapters are concerned with.

3.1.9 Galaxy colours: the IR regime

I can also characterise a set of IR colours by taking ratios of the luminosity per octave in a given waveband. I define three colours as follows:

$$\begin{aligned} 12/25 &\equiv \log\left[\frac{\nu L_\nu(12\mu\mathrm{m})}{\nu L_\nu(25\mu\mathrm{m})}\right], \\ 12/60 &\equiv \log\left[\frac{\nu L_\nu(12\mu\mathrm{m})}{\nu L_\nu(60\mu\mathrm{m})}\right], \\ 60/100 &\equiv \log\left[\frac{\nu L_\nu(60\mu\mathrm{m})}{\nu L_\nu(100\mu\mathrm{m})}\right]. \end{aligned} \tag{3.7}$$

These are chosen for ease of comparison with SN91, who present the same mean colours as a function of total IR luminosity for their sample outlined in the previous section. Their total IR luminosity is defined as a weighted sum of the luminosity per octave in the four IRAS bands:

$$L_{IR} = 0.97\nu L_\nu(12) + 0.77\nu L_\nu(25) + 0.93\nu L_\nu(60) + 0.60\nu L_\nu(100). \tag{3.8}$$

I plot the model IR colours as a function of total IR luminosity in Figure 3.11. In the following, note that their results are for a flux-limited sample of galaxies, while I plot the colours of every galaxy in my simulation cube with $M_K < -19$ and cold gas still present. Each point is an individual galaxy, with the red lines describing the mean, 10th and 90th percentiles of the distribution. Cyan circles with error bars are the data points of SN91. I match the colours of the brightest galaxies well, reproducing the correct colour trends

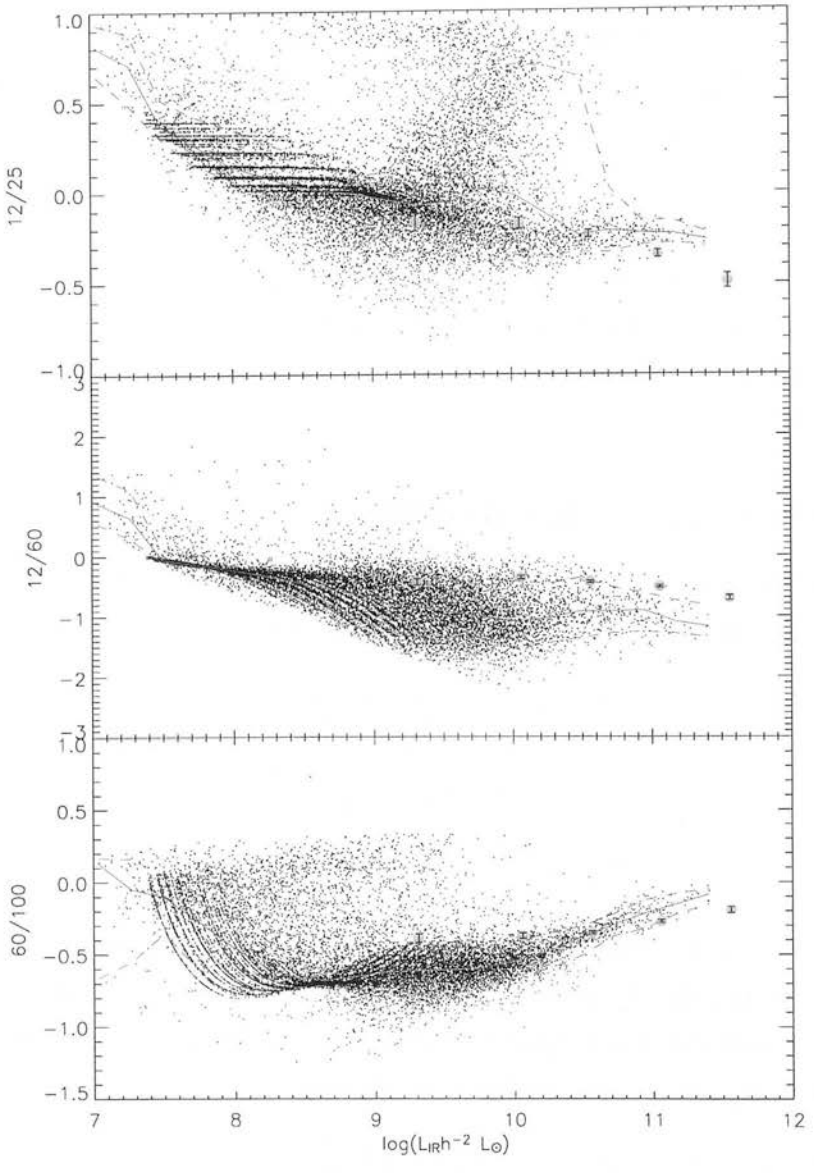

Figure 3.11: IR colours for model galaxies. In each panel, points represent individual galaxies, the solid red line is the mean of the distribution and the dotted lines are the tenth and ninetieth percentiles. Cyan circles are the relevant data points of Soifer and Neugebauer (1991), with their mean errors.

as a function of the overall luminosity. I lack galaxies at the brightest data points, again highlighting the effects of truncation and the limited survey volume.

3.1.10 Star formation history of the universe

In Figure 3.12 I show the star formation history of the universe as derived from the fiducial model. The total SFR is split into its five components: quiescent star formation in disks, quiescent star formation that now resides in bulges and ellipticals through merging, galaxy-merger driven starbursts, halo-merger driven starbursts and star formation below the resolution limit. Star formation in disks is dominant from $z \sim 6$ onwards, and sub-resolution star formation is very weak even at high redshift (vindicating my assumption that the uncertainties in such a process will have little bearing on the final results). Halo-merger driven star formation is briefly dominant at very high redshift, and galaxy merger-induced star formation has a broad peak around $z \sim 2-3$. This is an interesting result: the genesis of SMGs and LBGs is generally thought to be from merger-driven star bursts, and the model estimate for this peaks at around the same redshift range where such objects are found in reality.

For comparison, I plot a compilation of incompletness and dust corrected observational data, as taken from Hopkins (2004). The model yields a very good match to the data out to roughly $z \sim 1.5$, matching the broad slow rise in the global star formation rate. The model has a broad peak at $z \sim 2-3$, broadly consistent with the data. Even at redshifts $4-5$, the predicted SFR falls within the error bars of the data. Indeed, at this redshift objects are hard to detect, and the true value of the global star formation rate is likely to rise as more sources are unearthed. This is an encouraging result, implying that sensible application of the fiducial model at higher redshift is feasible.

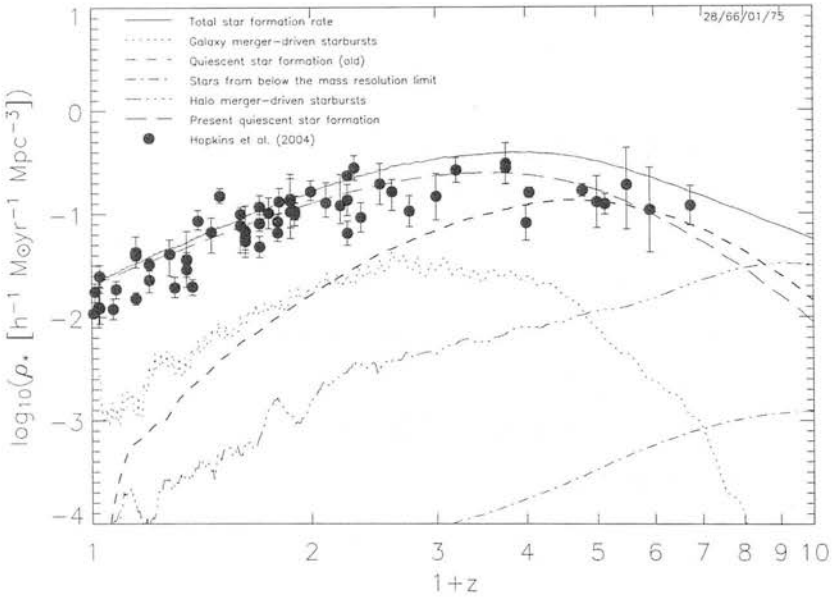

Figure 3.12: Star formation history of the universe, as derived from the fiducial model. Observational data is taken from Hopkins (2004). The solid line shows the total star formation rate in the fiducial model. The long-dashed line shows the model quiescent star formation rate, those stars that are still located in disks. The dashed line shows 'old' quiescent star formation; these stars were not formed in bursts but are now located in bulges due to morphological evolution. The dotted and dash-dot-dot-dot lines shows stars formed in galaxy-galaxy and halo-halo merger events respectively, and the dash-dotted line shows the (small) contribution to star formation from objects below the mass resolution limit.

CHAPTER 4

The high redshift universe 1: Global properties and Lyman Break Galaxies

In this chapter I use the galaxy formation model set out in chapter 2, together with the fiducial parameter set described in chapter 3 to study facets of the high redshift universe. I describe the construction of mock surveys, to best simulate real datasets and reproduce observational techniques and limitations wherever possible. I also introduce two extra models that perform well locally, to illustrate the varying properties predicted at high redshift from different parameter sets. In this chapter I concentrate on some of the more predictable, fundamental properties of the high-redshift universe: the evolution of the luminosity and stellar mass functions, and Lyman Break Galaxies (LBGs), which seem destined to make up the majority of the galaxy population seen today.

4.1 Creating mock surveys

As well as studying the properties of galaxies in their rest frame, much can be learned from creating mock surveys, analogous to those actually undertaken

at the telescope. Producing such a survey involves many subtle issues that have to be treated carefully.

Assume for a moment that computational practicalities can be ignored, and that a survey of given depth and width can easily be constructed and analysed by stacking simulation boxes. Such a survey will still be limited in terms of the clustering analyses that can be succesfully applied. Placing identical boxes side by side can induce unwanted periodicities in the data. The size of the box limits the distance over which clustering can be measured; any signal on scales larger than an individual box will be entirely artificial and should be ignored. In fact, the discontinuous nature of placing boxes side-by-side should reduce the clustering signal to zero. This issue rears its head when estimating clustering on large angular scales. At low redshift, this may not be an issue, but at high redshift the box size will severely limit the potential for simulating wide-angle surveys.

The mass resolution of the simulation fixes a minimum size of galaxy with a fully-resolvable history. As one moves to higher redshift, this limit gets closer to the sizes of the galaxies in consideration. Thus, it is clear that deep surveys at high redshift are hard to simulate without very high mass resolution in the underlying simulation.

There is little one can do about the mass resolution issue, but steps can be taken to ensure that meaningful datasets can be extracted from mock surveys. To reduce computational effort, one can take a number of boxes at discrete redshifts, forming an irregular survey volume. This is filled out by interpolating galaxy properties between these snapshots. Depending on the size and depth of the required survey, it may be necessary to stack boxes in the transverse direction as well as the radial direction.

4.1.1 Building a light cone

For my simulation box, I have 66 discrete output 'snapshots'. This is not sufficent to fully sample the density field in the radial direction. As an example, consider a mock survey with a maximum redshift $z = 4$. The comoving radial distance $R_0 S_k(r)$ is given by

$$R_0 S_k(r) = \frac{c}{H_0} \int_0^z \left[\Omega_M (1+z')^3 + \Omega_R (1+z')^4 + \Omega_k (1+z')^2 + \Omega_\Lambda\right]^{-1/2} \mathrm{d}z',$$

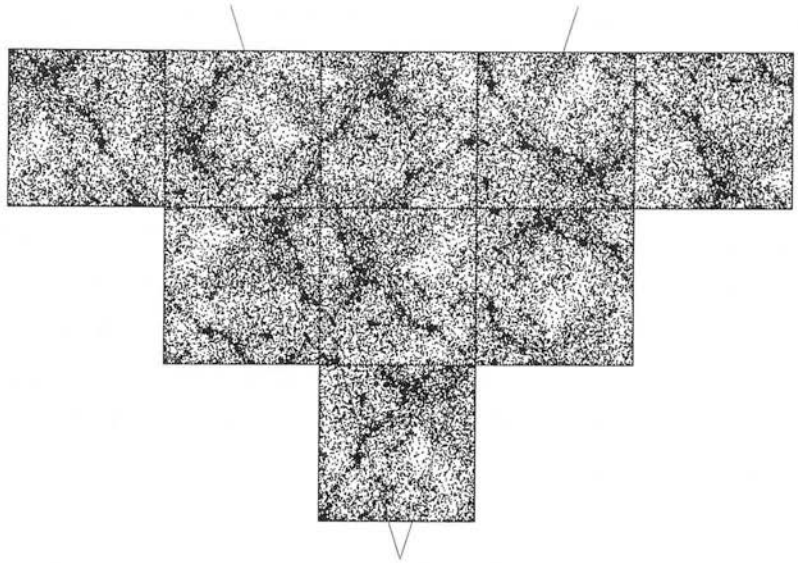

Figure 4.1: Schematic of the cone building process. Three simulation snapshots have been rotated randomly and the galaxies have been shifted *en masse* in a random manner See the accompanying text for more details.

and is $\simeq 5000h^{-1}$Mpc for $z = 4$. For a simulation box with sides $50h^{-1}$ Mpc, we need ~ 100 boxes along the line of sight, nearly a factor 2 more snapshots than are available. Thus, interpolation of galaxy properties will be necessary for the extra boxes laid down to fill in the gaps.

In practice, due to time constraints I used a subset of these snapshots at low redshift in order to reduce the computational burden. While not ideal, I am generally interested in the simulation properties before $z \sim 1$, and thus missing out a number of low z boxes should have little bearing on the results.

In order to minimise artificical clustering signals, I apply the following transformations when duplicating boxes:

- Each box is rotated randomly through multiples of 90 degrees, such that a different face is perpendicular to the line of sight each time.
- The contents of each box are shifted randomly in the x, y and z coor-

dinates, with galaxies leaving the box re-entering through the opposite face.

- The entire grid of boxes is rotated perpendicular to the line of sight by some random angle.

In Figure 4.1 I show a rough schematic of the cone building process. Three different snapshots have been tiled radially (no interpolation between snapshots has been made here), with the galaxy positions being randomly shifted by two of the three processes outlined above. Note that I have not made any cut in magnitude in this diagram, it is merely meant to illustrate the tiling and shifting process. Every second galaxy is plotted for clarity. The red lines represent a survey volume of given solid angle. As we go to higher redshift, more than one box lined up perpendicular to the line of sight is required to fill in the cone.

Given the rest-frame SED of a galaxy, what will its observed properties be when placed at a given redshift? The general expression for the apparent magnitude of a galaxy is given by

$$m = M + 5\log(D_L) + 25 + K(z) + e(z), \tag{4.1}$$

where D_L is the luminosity distance (see equation 1.23) is in Mpc, $K(z)$ is the k-correction, dependent on the shape of the SED and $e(z)$ is an evolutionary correction, taking into account the change in shape of a rest-frame galaxy SED over the time between emission and reception of the photons. As the model SEDs are derived for a specific redshift and hence age, evolutionary corrections are unnecessary here and I need only be concerned with the k-correction. At large distances the SED of a galaxy is shifted redwards, and bluer spectral features are shifted into a given bandpass of interest. This must be taken into account when deriving apparent magnitudes of sources: features observed at frequency ν_o were emitted at frequency $\nu_e = \nu_o(1+z)$. For a source with luminosity L_ν in W Hz^{-1}, the observed flux is given by (Peacock 1999):

$$S_\nu(\nu_o) = \frac{L_\nu([1+z]\nu_o)(1+z)}{4\pi D_L^2}. \tag{4.2}$$

The shifting of the SED to lower frequencies performs the k-correction, and the magnitude of the source in a given bandpass can be derived from the observed flux in the usual manner.

In the following chapter, I will focus on global predictions of the model at high redshift, namely the evolution of the K-band luminosity function and the evolution of the stellar mass function. I then present a study of Lyman Break Galaxies (see section 1.2.4) in the redshift range $2.7 < z < 3.4$. This chapter is therefore an attempt to demonstrate how the model fares with the 'less extreme' facets of the high redshift universe: LBGs seem to be reasonable analogues of the normal galaxy population seen today.

4.1.2 Alternative models

In order to assess the effect that changing free parameters has on the properties of the high redshift universe, I introduce two additional models that yield reasonable matches to the local luminosity functions.

- **Model 1**: The fiducial model outlined in chapter 1.
- **Model 2**: differs from model 1 only in star formation timescale $\tau_* = 8$ Gyr, instead of the fiducial 2 Gyr. The star formation history of the universe differs greatly from model 1, as shown in Figure (4.2). The B and K luminosity functions give slightly poorer fits to the $z = 0$ data, but are still reasonably acceptable. Also, there is a subtle difference in the treatment of merging galaxies. Baugh et al. (2005) find that matching submillimetre number counts requires a modification to the emisssivity of dust grains in bursting galaxies, and in model 3 I follow this philosophy by altering the emissivity from $\epsilon_\nu \propto \lambda^{2.0}$ to $\epsilon_\nu \propto \lambda^{1.5}$ (for $\lambda > 100$ μm) in galaxies that have undergone a merger within the last Gyr. This has no effect on the optical/near IR properties of a galaxy.
- **Model 3**: differs from model 1 in that the parameter determining the amount of time young stars spend in their parent molecular clouds is changed from $t_{\rm esc} = 1$ Myr to $t_{\rm esc} = 10$ Myr. This has a profound effect on the UV region of a galaxy SED, as far more light from young stars is masked by the surrounding dusty molecular cloud. Indeed, the very brightest stars will spend their entire life inside the cloud, diminishing the UV flux significantly. In addition, the change to the dust emisivity in recent mergers detailed above is also implemented in this model. The luminosity functions are shown in Figure (4.3) (note that the star

formation history of this model is identical to that of model 1).

4.2 Global model predictions at high redshift

4.2.1 Evolution of the K band luminosity function

Probing 'normal' galaxy evolution out to redshifts of 1 and beyond is best performed in the near-IR. In this wavelength regime, the k-corrections are insensitive to galaxy morphology (Cowie et al. 1994) and smaller than in other wavebands. K band observations are relatively unaffected by dust extinction, and are a good tracer of the underlying stellar mass (eg. Madau et al. 1998, Pozzetti et al. 2003).

Caputi et al. (2005, C05) compile a sample of 2905 galaxies with $K_s < 21.5$ selected from the Great Observations Origins Deep Survey (GOODS). They derive redshifts for each object using a variety of independent techniques, and construct rest frame luminosity functions at $z = 1.0, 1.5, 2.0$ and 2.5. they find that the LFs are well fit by the evolving Schecter function

$$\Phi(L)\mathrm{d}L = \phi_0(z)\left(\frac{L}{L^*(z)}\right)^{\alpha}\exp\left[-\frac{L}{L^*(z)}\right]\mathrm{d}\left(\frac{L}{L^*(z)}\right), \tag{4.3}$$

with the usual conversion to magnitudes $L/L_*(z) = 10^{-0.4(M-M_*(z))}$. The normalisation of the LF evolves as

$$\phi_0(z) = \phi_0(\mathrm{z}=0)\exp\left[-\left(\frac{z}{z_\phi}\right)^{k_\phi}\right], \tag{4.4}$$

and the characteristic magnitude evolves as

$$M_*(z) = M_*(\mathrm{z}=0) - \left(\frac{z}{z_M}\right)^{k_M}. \tag{4.5}$$

The fixed parameters are given by $\alpha = 1.09$ and $M_*(\mathrm{z}=0) = -24.19 \pm 0.05$ (cf. Kochanek 2001), and their best-fit values for the free parameters are summarized in Table 4.1.

I also have rest-frame K-band luminosity functions from the mini-Millenium Simulation (Croton, private communication), which uses the same galaxy formation model as Croton et al. (2005) (including their model of AGN feedback as a means of curbing the formation of bright galaxies at early times)

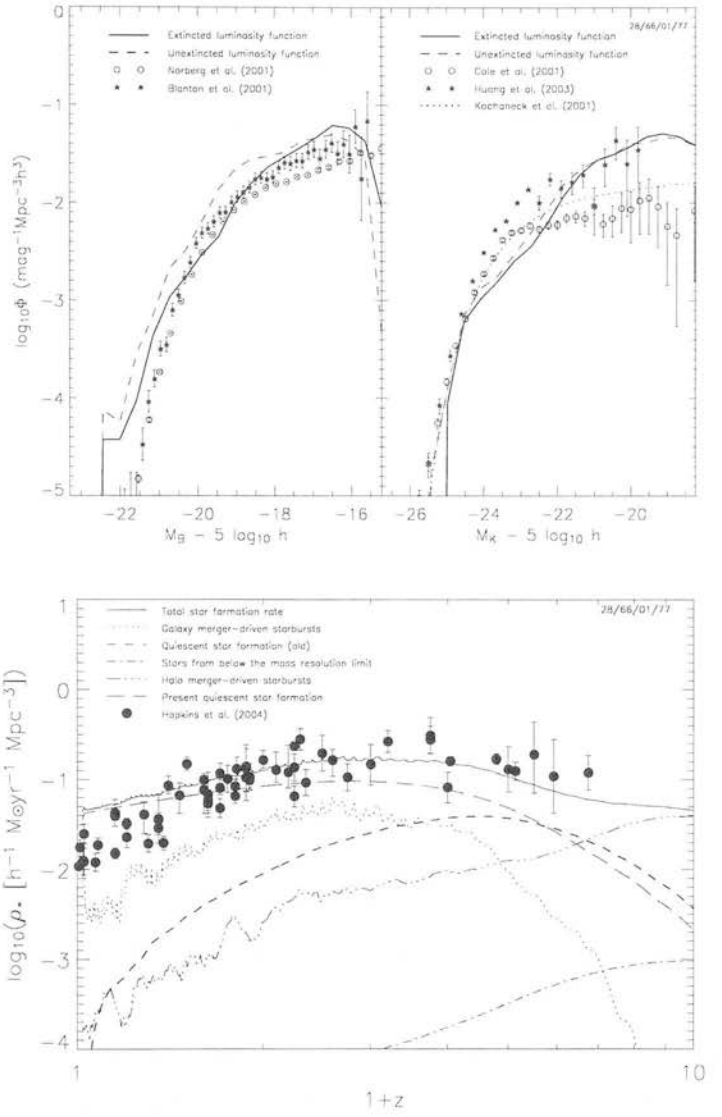

Figure 4.2: Top panel: B and K-band luminosity functions for model 2. Note the undesirable lack of L_* galaxies visible from the K-band LF. Bottom panel: Star formation history of model 2. The peak in SFR is much broader and less defined than in model 1. Note the (relative) importance of bursts at relatively high redshift.

k_ϕ	z_ϕ	k_M	z_M	$\phi_0(z=0)(\mathrm{Mpc}^{-3})$
1.67 ± 0.08	1.78 ± 0.06	0.63 ± 0.10	1.88 ± 0.10	$(3.9 \pm 0.3) \times 10^{-3}$

Table 4.1: Best fitting free parameters for LF evolution (C05)

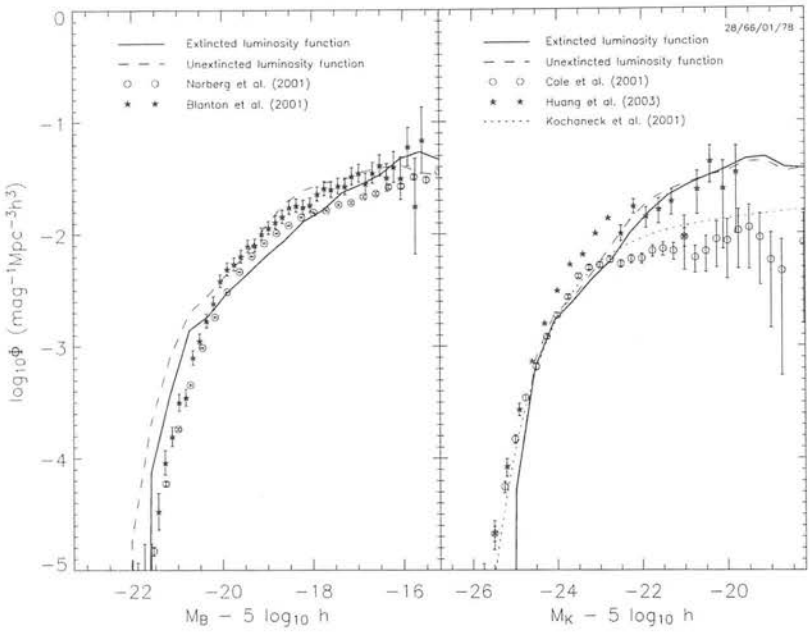

Figure 4.3: Local B and K luminosity functions for model 3. Note that the star formation history of model 3 is identical to that of model 1, and so I do not reproduce it here (see Figure 3.12).

in a box of 62.5 h^{-1} Mpc on a side, much smaller than the Millenium Simulation ($500h^{-1}$ Mpc). This box should be roughly comparable to my own, similarly sized simulation volume.

In Figure 4.4 I plot the K-band LF at $z = 1$ and 2 for model 1 (top panels) and model 2 (bottom panels) At each redshift the solid black line gives the model prediction, and the solid red line gives the mini-MS prediction. At $z = 1$ I compare the theoretical results with the results of C05, Sarracco et al. (2005) and predicitons from the K20 survey (Pozzetti et al. 2003). At $z = 2$ I again plot the relevant results of C05. Note that there is neligible difference between the K-band LFs of models 1 and 3, and so I only show the former here for brevity.

It is clear that the bright end of the LF is severely lacking in both models once we probe beyond the local universe. Indeed, the results imply a *brightening* of the characteristic luminosity as we move from $z = 0$ to 2, and little evolution beyond $z = 1$. It is important to bear in mind that the datasets probe only the bright end of the LF, and thus the faint end slope of the Schecter function

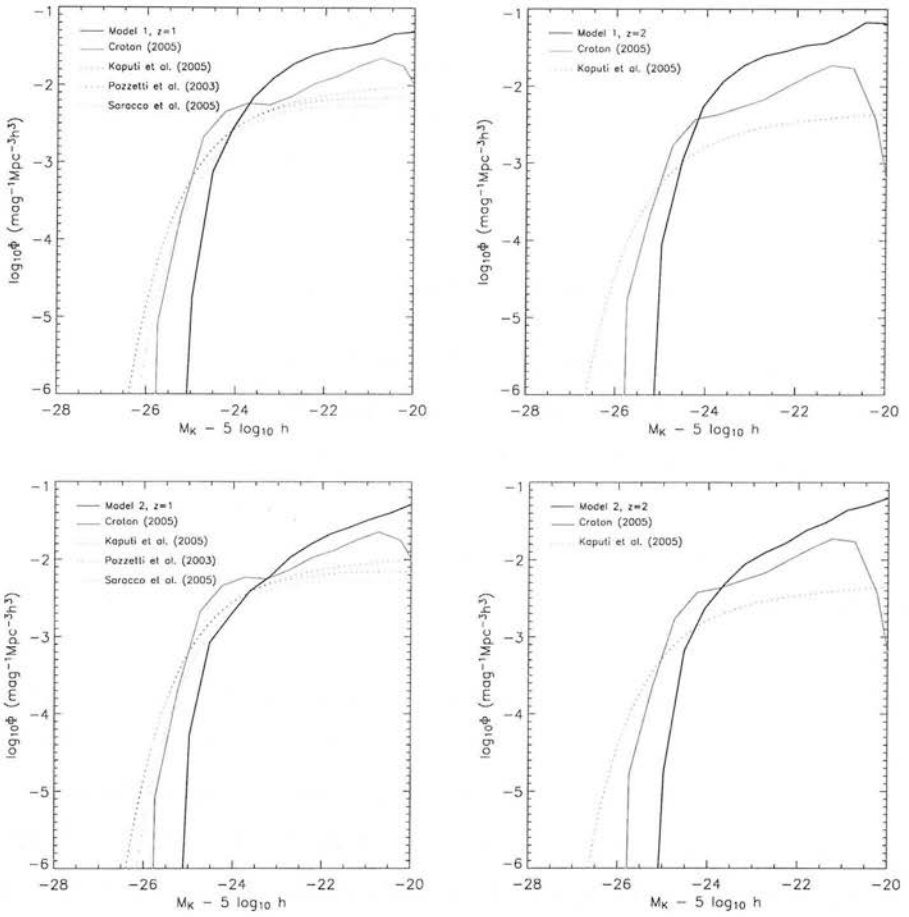

Figure 4.4: Evolution of the K-band LF for models 1 and 2. Top panels: Model 1 predictions at $z = 1$ (top-left) and $z = 2$ (top right). Bottom panels: Model 2 predicitons at $z = 1$ (bottom-left) and $z = 2$ (bottom-right). See the accompanying text for more details.

fits are subject to large uncertainties. Nevertheless, the surprising abundance of luminous galaxies at high redshift is common to all the observations, and given the plethora of massive galaxies seen at early times (SMGs, EROs to name but a few) it seems that galaxy formation has proceeded in an apparently anti-hierarchial fashion: the brightest objects are in place from early times, and faint sources appear later. Given the small difference in volume between my own simulations and the mini-Millenium simulation of Croton et al. it seems that AGN feedback gives a better match to the bright end of the LF than my own, rather brutal method of truncation. This is perhaps reassuring, given that the former should be more akin to reality.

4.2.2 Evolution of the stellar mass function

The previous section has shown that the models underpredict the number of K-luminous galaxies at high redshift. It is natural to ask whether this is due to a genuine lack of galaxies, or whether the sources are simply not *bright* enough to match the luminosity functions. Given that K-band light is a reliable tracer of the underlying stellar mass, this seems unlikely. Nevertheless, plotting the stellar mass functions at given redshifts will clarify this issue. This will only be relevant for models 1 and 2: the star formation histories of model 3 are identical to that of model 1, as the changing of dust parameters merely affects the output magnitudes of pre-existing stellar populations.

For each model, I use the full simulation outputs at redshifts $0, 1, 2$ and 3 to plot the mass function. Note that I do not attempt to match any observational criteria here (such as limiting galaxy magnitude) and simply present the mass functions at face value.

In Figure 4.5 I compare the derived mass functions (MF) of model 1 with a variety of data sets. The top-left panel compares the model prediction with the results of Bell et al. (2003), as derived from g-band detections in the SDSS Early Data Release (assuming a universal Salpeter IMF). The model matches the bright end of the MF well, although we lack the most massive galaxies (as reflected in the luminosity function, Figure 2.10). The model overpredicts the abundance of low-mass galaxies, although the faint end slope is subject to the same variations as in the LFs, and there are many uncertainties in deriving stellar masses from galaxy spectra (star formation histories, the role of dust

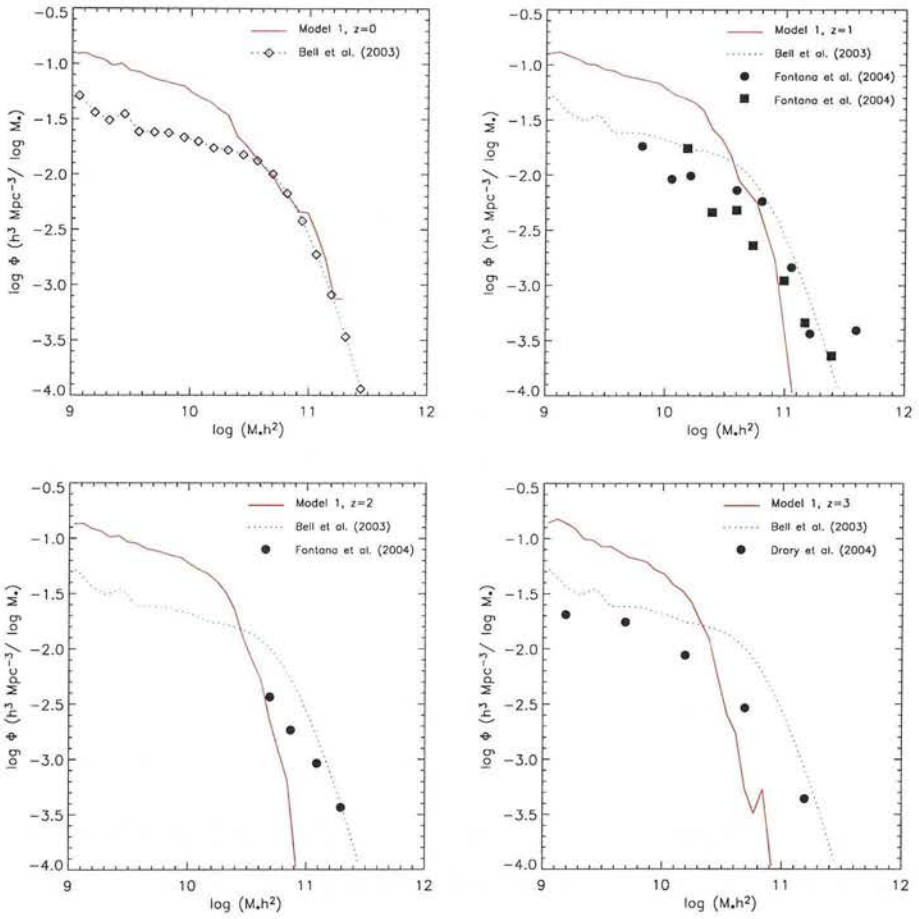

Figure 4.5: Stellar mass functions of model 1 at $z = 0, 1, 2$ and 3. In each panel the red line gives the model prediciton and the dotted blue line gives the local estimate given by Bell et al. (2003). See the accompanying text for more details.

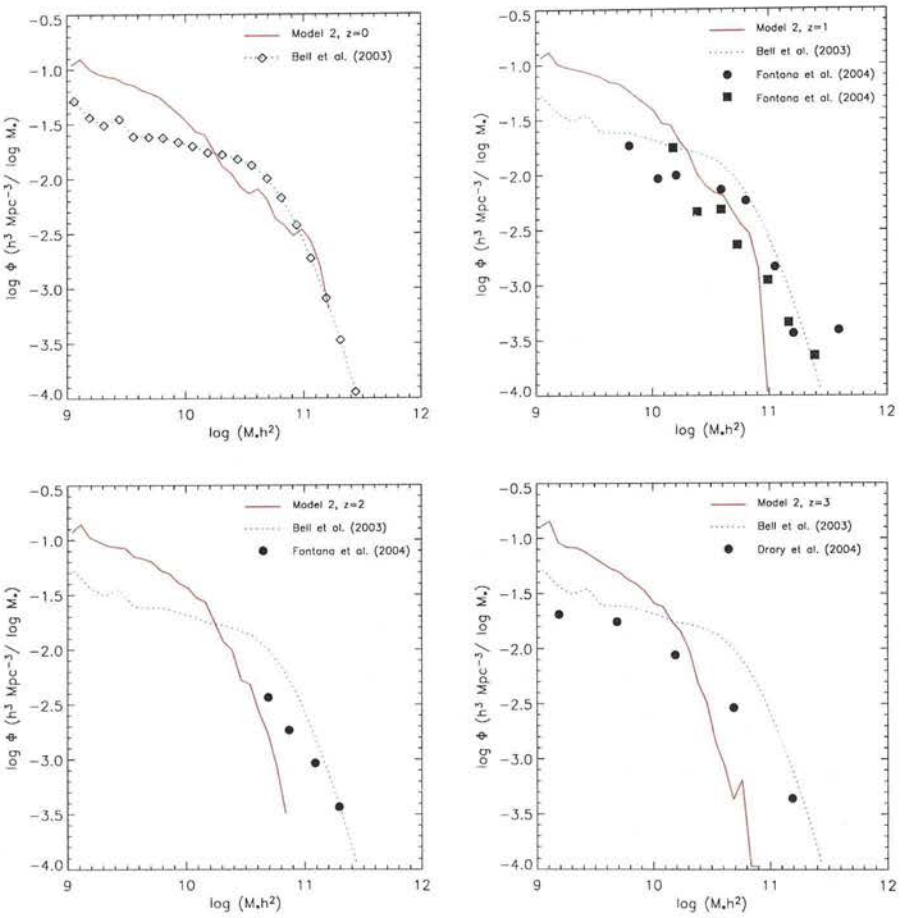

Figure 4.6: As Figure 4.5, but for model 2.

etc). We now move onto $z = 1$, and plot the model prediction against results. In all the panels I plot the local MF of Bell et al. (2003) to give an impression of the evolution of the MF with time. I also plot two results from the K20 survey (Fontana et al. 2004), MF predictions for the redshift ranges $0.7 \leq z \leq 1.0$ and $1.0 \leq z \leq 1.5$. Comparing the local estimate of Bell et al. (2003) and the data points of Fontana et al. (2004), it is apparent that the massive end of the MF has evolved little with time: the brightest galaxies we see today were already in place at $z \sim 1$. In contrast, the model prediction now shows a definite lack of massive galaxies. The discrepancy grows ever more acute as we move to $z = 2$, where I plot the $1.5 \leq z \leq 2$ MF estimate from the K20 survey. Again we see in the data that the most massive galaxies are still there even at this early time, flying in the face of simple hierarchial arguments. At $z = 3$ the massive

galaxies are *still* there, as measured by Drory et al. (2004) using mulicolour photometry of galaxies in the Fors Deep Field and the GOODS-South.

Note that the overall behaviour of model 1 is broadly similar to that of many other semi-analytic models: as Fontana et al. (2004) have shown, many of these (eg. Cole et al. 2000, Menci et al. 2002) fail to match the massive end of the MF beyond redshift zero, and predict an overabundance of less massive (faint) galaxies. Bower et al. (2005) have shown that the model of Baugh et al. (2005), tuned to reproduce the submillimetre counts by introducing a top-heavy IMF in bursts, also fails to produce sufficent massive galaxies at high redshift.

The behaviour of model 2 is broadly similar to that of model 1, and does not warrant too much discussion. The 'dip' visible at the knee of the LF is also present in the MF at $z = 0$, and systematically produces less massive galaxies at high redshifts compared to model 1. This is simply due to the longer star formation timescale: star formation is suppressed at high redshift, yielding less massive galaxies at a given time than models with a shorter SF timescale. It is possible that a model where bursting modes of star formation are more important may give a better match to the mass functions, giving more stars formed early on over and above those formed quiescently. However, investigating this possibility is deferred to future work.

4.3 Lyman break galaxies at $z \sim 3$

As alluded to in chapter 1, Lyman Break galaxies (LBGs) are one of the most important classes of galaxy in the high redshift universe. They are certainly the most extensively studied; $\sim$ 1000 examples have been discovered by a plethora of authors.

Selecting LBGs from the vast sample of galaxies at all redshifts requires use of the Lyman break technique, as discussed in section 1.2.4. In practice, one uses more stringent constraints than simple detectability through filters; to minimise interlopers a variety of criteria must be met for a galaxy to be selected as a genuine LBG. Optimised filters are often used to minimise the effects of light pollution and other unwanted atmospheric phenomena.

Steidel et al. (2003) present a summary of their previous surveys aimed at detecting LBGs in the redshift range $2.7 \leq z \leq 3.4$. They employed a set

of non-standard $U_n G\mathscr{R}$ filters to optimise detection, straddling the Lyman break feature and the near-flat continuum beyond. The filter bandpasses are presented in Figure 4.7, taken from Steidel et al. (2003). The solid and dotted lines represent the effective bandpasses before and after CCD efficiencies and atmospheric attenuation are taken into account. Note the large effects of the atmosphere on the U_n band especially, something that must be allowed for if accurate magnitudes comparable to those of ground-based surveys are desired.

Derived magnitudes are given in the AB system (Oke and Gunn 1983), defined by

$$m_{AB} = -2.5 \log f_\nu + 8.9, \tag{4.6}$$

where f_ν is in Janskys and the constant is set such that for a source with a flat spectrum $f_\nu \propto \nu^0$, $m_{AB} \equiv V$, where V is the usual Johnson filter.

They select LBGs according to the following criteria:

$$\begin{aligned} \mathscr{R} &\leq 25.5, \\ G - \mathscr{R} &\leq 1.2, \\ U_n - G &\geq G - R + 1, \\ U_n - G &\geq 1.6, \\ G - \mathscr{R} &\geq 0.0. \end{aligned} \tag{4.7}$$

This delimits a region in the $(G - \mathscr{R})$ - $(U_n - G)$ colour-colour plane that selects galaxies most likely to lie within the above redshift range. Giavalisco and Dickinson (2001) find that $\sim 3\%$ of objects selected in this manner turn out to be interlopers, the majority of these being foreground stars. Of course, my simulations will not be subject to such interlopers, and as the redshifts of all my sources are known, I can quantify the efficency of the above colour selection.

In my 'standard' lightcone, I apply the dust processing to all galaxies brighter than $M_K \leq -22.5$ as derived from the galaxy formation models before GRASIL is applied. As mentioned before, this is done in order to reduce the computational load, and should include the vast majority of objects of interest. I have a full simulation box (post-dust processing) available at $z = 3.09$ for the three models, and a study of galaxies satisfying the LBG criteria indicates that many of these probe fainter pre-dust rest frame magnitudes (for

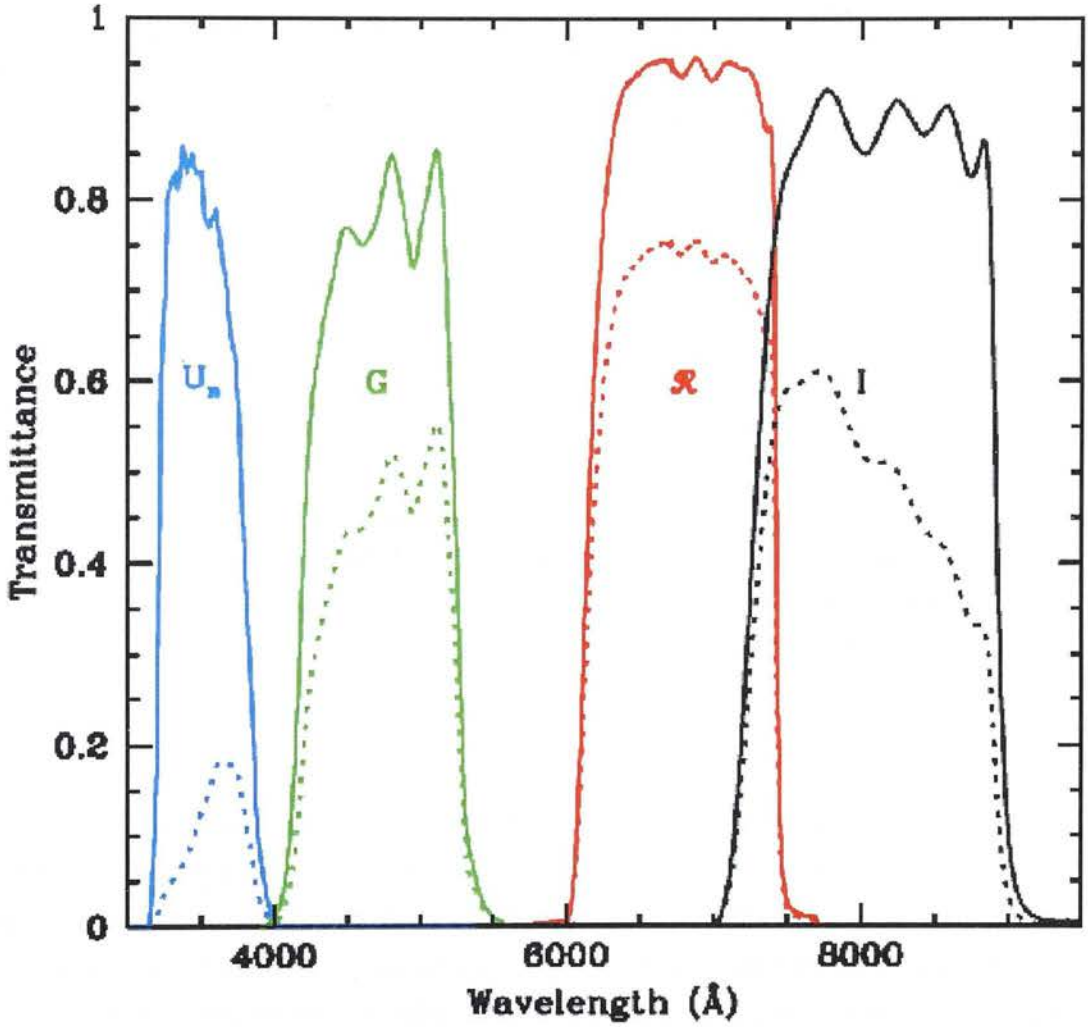

Figure 4.7: The $U_n G \mathscr{R}$ filter set as employed in LBG surveys at $z \sim 3$. The solid lines represent the 'ideal' filter profiles and the dotted lines represent the filter profiles once CCD efficency and atmospheric attenuation have been taken into account. Figure taken from Steidel et al. (2003).

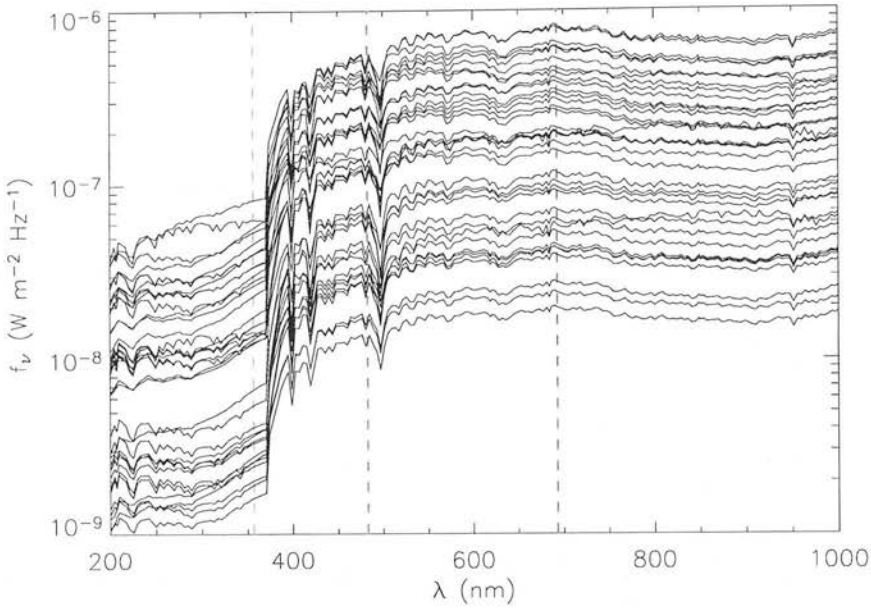

Figure 4.8: A sample $z = 3$ LBGs brighter than $\mathscr{R} = 25.5$ taken from the fiducial model. The dotted lines represent the approximate centres of the U_n (cyan), G (green) and $\mathscr{R}$ (red) filters. Note the prominence of the lyman break, straddled by the U_nG filters at this redshift

models 1 and 2 at least). With this in mind, in the simulation boxes between $2.6 < z < 3.7$ I reduce the magnitude limit for dust processing to $M_K = -20.5$. Of course, this will mean that the identification of interlopers may not be complete, in that faint galaxies at other redshifts may well inadvertently satisfy the LBG criteria. Nevertheless, the colour selection is tuned to filter out the majority of galaxies outwith the redshift range of interest, so the effect should be small.

In Figure 4.8 I show a sample of LBGs at $z = 3$ taken from model 1. The dotted lines represent the approximate centres of the $U_nG\mathscr{R}$ filter set. At this redshift the U_n and G filters straddle the Lyman break and the $\mathscr{R}$ samples the continuum beyond.

Note that in the rest of this chapter, I will be assuming a Hubble constant of $h = 0.7$ except where noted.

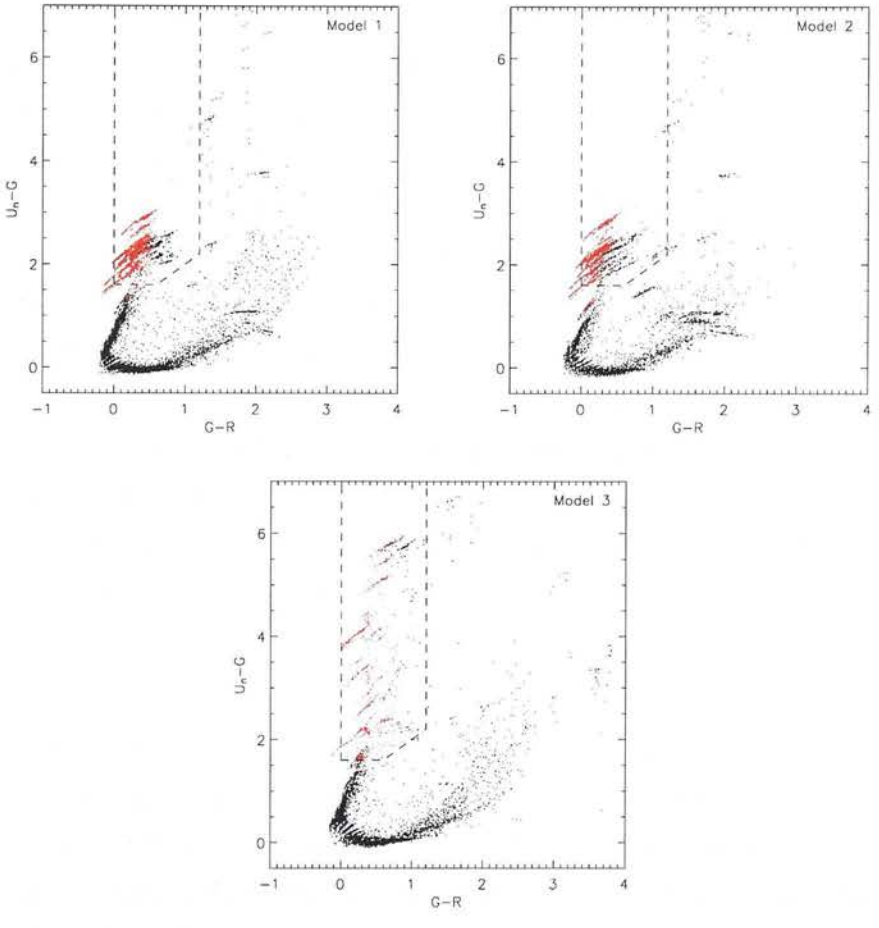

Figure 4.9: colour-colour plot of LBGs with $\mathscr{R} < 25.5$ in a mock 0.1 deg^2 survey for models 1, 2 and 3. Red dots are galaxies in the correct redshift range, and black dots lie outwith this range. The dashed trapezium denotes the region in the colour-colour plane where equations 4.8 are satisfied.

4.3.1 Testing the colour selection criteria

In Figure 4.9 I plot colour-colour plots of all galaxies brighter than $\mathscr{R} \leq 25.5$ in a mock 0.1 deg^{-2} survey for each model in turn. The red points represent galaxies within the redshift range $2.7 \leq z \leq 3.4$ ie. the optimal range for LBG selection as per equations (4.8). Black dots represent galaxies outwith this redshift range. The dashed trapezoid denotes the plane in the colour-colour plot where equations (4.8) are satisfied and hence selected as LBGs. It is clear that the colour criteria selects the majority of galaxies in the required redshift range in all cases. Only $11, 15$ and 7% of galaxies within the redshift range are missed by the cut in colour for models 1, 2 and 3 respectively. A number of galaxies are spuriously flagged as LBGs yet lie outside the redshift range. $21, 25$ and 21% of selected galaxies are interlopers in models 1, 2 and 3. Nevertheless, the literature definition of an interloper is rather less strict: either a star or a galaxy at $z < 2.3$. With this less stringent definition in mind, I find that $\sim 0.1\%$ of the detections are classed as interlopers in all cases. It is clear that model 3 is the most efficient at producing LBGs selected as per the observations, yielding the (joint) smallest fraction of interlopers and the highest fraction of positive identifications. The colour-colour plot best reproduces the steep rise in $U_n - G$ expected for sources at $z = 3$ (eg. Figure 2 of Steidel et al. 1995).

The above results show that broadband colour selection is indeed an efficent method of selecting LBGs in the correct redshift range. It is encouraging that the fiducial model produces galaxies with the correct colours at high redshift, and implies that our star formation histories and treatments of gas cooling and stellar evolution are broadly consistent with reality. Nevertheless, rest frame UV light is sensitive to the choice of parameter in the dust model, and model 3 explores one such adjustment to the model.

I now run 20 light cones spanning 1deg^2 and apply the LBG selection criteria to each mock survey. These independent realisations are all equally valid as a given survey, and as an ensemble can be used to estimate the variation from cone to cone, a first estimate of the effects of cosmic variance on scales equivalent to the angular scale of the survey.

I find mean values of $\langle N_{\rm LBG} \rangle = 32960, 24236$ and 13367 with standard deviations of $467, 305$ and 224 for models 1, 2 and 3. This yields number densities

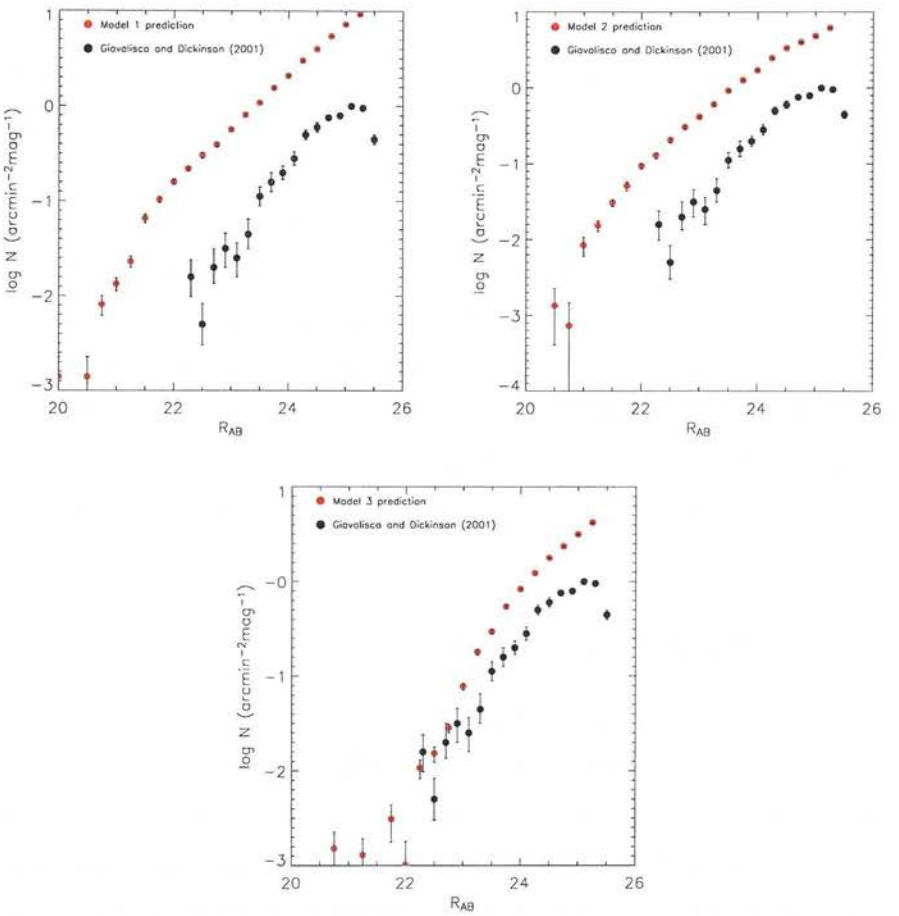

Figure 4.10: LBG number counts in models 1 (top-left), 2 (top-right) and 3 (bottom). In each panel the predicitons (red circles) are compared with the results of Giavalsco and Dickinson (2001, black circles). Models 1 and 2 dramatically overpredict the number of LBGs at all magnitudes, while model 3 fares rather better (due to the increased extinction in the UV brought about by a factor 10 increase of $t_{\rm esc}$), although still showing an overabundance of faint and very bright objects.

of $9.16, 6.73$ and 3.71 arcmin^{-2}, all in excess of the observed values: Giavalisco and Dickinson (2001) find a mean number of 1.22 ± 1.15 arcmin^{-2}, and Steidel et al. (2003) find a value of 1.72 arcmin^{-2} over a number of surveys covering different regions of the sky. Although around 20% of detections are interlopers in observational surveys, models 1 and 2 still vastly overproduce the number of LBGs compared to the real universe. The relative lack of galaxies in model 2 reflects the longer star formation timescale, leaving galaxies unable to form as many stars before $z \sim 3$. Model 3 fares rather better: the order of magnitude change in $t_{\rm esc}$ renders galaxies fainter, so a large number of sources drop out of the sample. Neverthless, there is still a factor $2-3$ discrepancy with respect to the observations. It is possible that there is still too little in the way of dust extinction present, or there may be subtle resolution effects at play. This is examined in more detail later. Note that the overabundance of LBGs implies that they do *not* contribute significantly to the bright end of the K-band LF at that epoch, given the lack of bright galaxies in K at high redshifts seen earlier. This too will be explored in more detail in due course.

4.3.2 Number counts of LBGs

In Figure 4.10 I plot the differential number counts of LBGs in 20 mock surveys. Each red circle represents the median number of galaxies in a given (observer frame) magnitude bin, and the error bars are the standard deviation in each bin. Black circles show the results of Giavalisco and Dickinson et al. (2001), a survey of 547 LBGs with photometric redshifts in the equivalent redshift range. Given the anomalous number of LBGs produced by models 1 and 2, it comes as no surprise to see a vast discrepancy between predicted results and the data. A large excess of galaxies is present in every magnitude bin, and the brightest galaxies are roughly 2 magnitudes too bright in $\mathscr{R}$. Again, model 3 does a better job at reproducing the observations, athough there is a general excess of faint sources, and a small number of extremely bright galaxies. However, the survey size of Giavalisco and Dickinson is ~ 700 arcmin^{-2}; it is possible that a larger survey volume would include comparitively rare, bright LBGs. The brightest model LBGs all lie in massive haloes, in most cases beyond the truncation limit. The lack of dust extinction allows the UV light to escape unextinguished, leaving the galaxy extremely bright in $\mathscr{R}$.

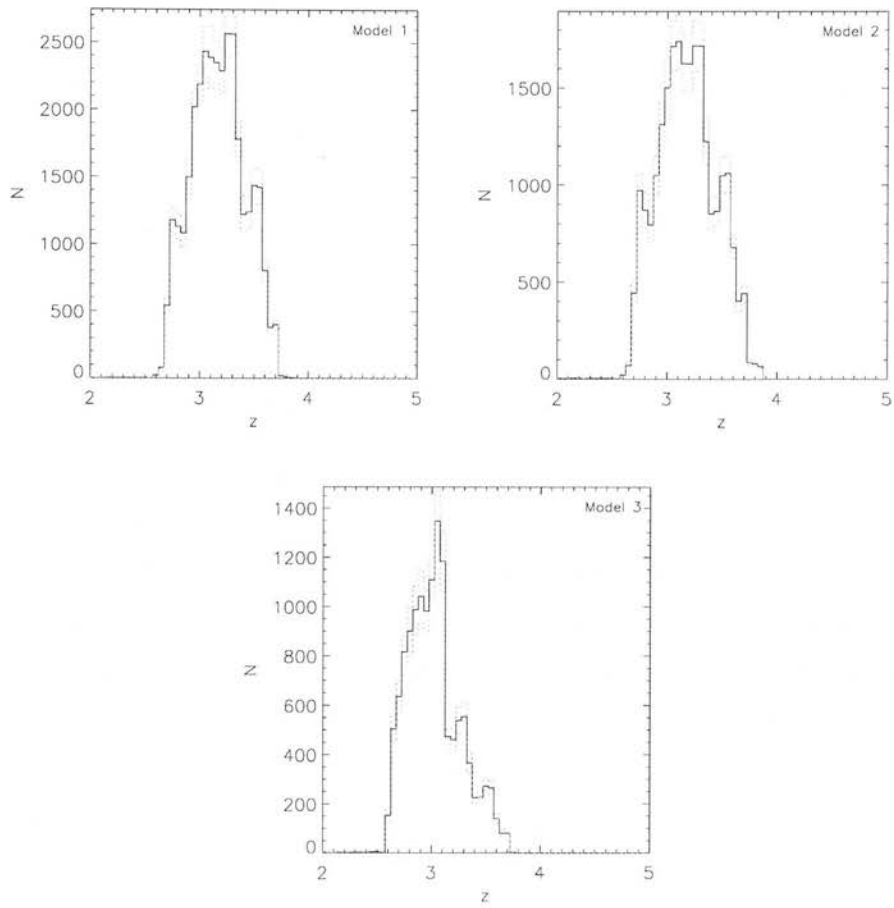

Figure 4.11: The redshift distribution of LBGs in model 1. The solid histogram shows the median number of galaxies in each redshift bin averaged over 20 mock surveys, and the dotted red and blue histograms show the standard deviation in each bin. Interlopers are preferentially located at high redshift.

4.3.3 The redshift distribution of LBGs

In Figure 4.11 I show the redshift distribution of LBGs averaged over 20 mock surveys for the three models. The solid histogram is the median number in each bin, with the red and blue dotted histograms showing the standard deviation in each bin. It is clear that the majority of selected LBGs lie within the desired $2.7 \leq z \leq 3.4$ redshift range. Interlopers are far more prevalent at high rather than low redshift. The distribution is stable from survey to survey and model to model, and peaks at around $z \sim 3.2$, very similar to the mean value of $\bar{z} = 3.04$ found by Giavalisco and Dickinson (2001). The histograms

show that the vast majority of interlopers are located at larger redshifts than the region of interest.

As each light cone is created randomly, each should be considered equally valid as a mock survey. I now select an individual light cone and explore in more detail the properties of candidate LBGs in the three models. I exclude known interlopers from the following analysis, in order to pin down the propeties of 'real' LBGs.

4.3.4 The parent dark matter haloes of LBGs

In Figure 4.12 I show the probability densities of halo mass and circular velocity of LBGs. The median halo masses and circular velocities are summarised in Table (4.2). The large standard deviations reflect the broad distribution of halo masses harbouring LBGs. In all three models LBGs are preferentially housed in relatively low circular velocity, low mass haloes of order $\sim 2-3\times10^{11}\ M_{\odot}$. In contrast with other semi-analytic results, the ΛCDM simulation of Baugh et al. (1998) predicts a mean LBG halo mass of $\sim 10^{12}M_{\odot}$ and a circular velocity $V_c \sim 200-300$ kms^{-1}. The combined N-body/semi-analytic simulation of Blaziot et al. (2003) yields $\langle M_{\rm h,LBG}\rangle \sim 4\times10^{12}M_{\odot}$. Adelberger et al. (2005) compare a sample of LBGs with N-body simulations and derive a lower median mass of $\langle M_{\rm h,LBG}\rangle \sim 7.25\times10^{11}M_{\odot}$. The median circular velocity derived by Mo, Mao and White (1999) using an analytic model of disk and star formation predicts an inferred median LBG halo mass of $\langle M_{\rm h,LBG}\rangle \sim 2\times10^{12}M_{\odot}$, assuming that LBGs are the most massive galaxies at that time and hence occupy the most massive DM haloes (this and similar schemes will be referred to as the 'massive halo model' from now on). This is an important caveat, as it is clear that there are other massive galaxy populations present at the same redshift: derived masses of SMGs and Distant Red Galaxies (DRGs, eg. Daddi et al. 2004, van Dokkum 2006) tend to be in excess of those predicted for LBGs. Clearly then, LBGs do not necessarily occupy the most massive haloes present at the time.

In support of this alternative viewpoint, Kolatt et al. (1999) assume that LBGs are formed by collisions between haloes in N-body simulations and find that LBGs can be hosted in haloes as small as $M_{\rm h,LBG} \sim 8\times10^{9}M_{\odot}$, more than two orders of magnitiude smaller than the massive halo model.

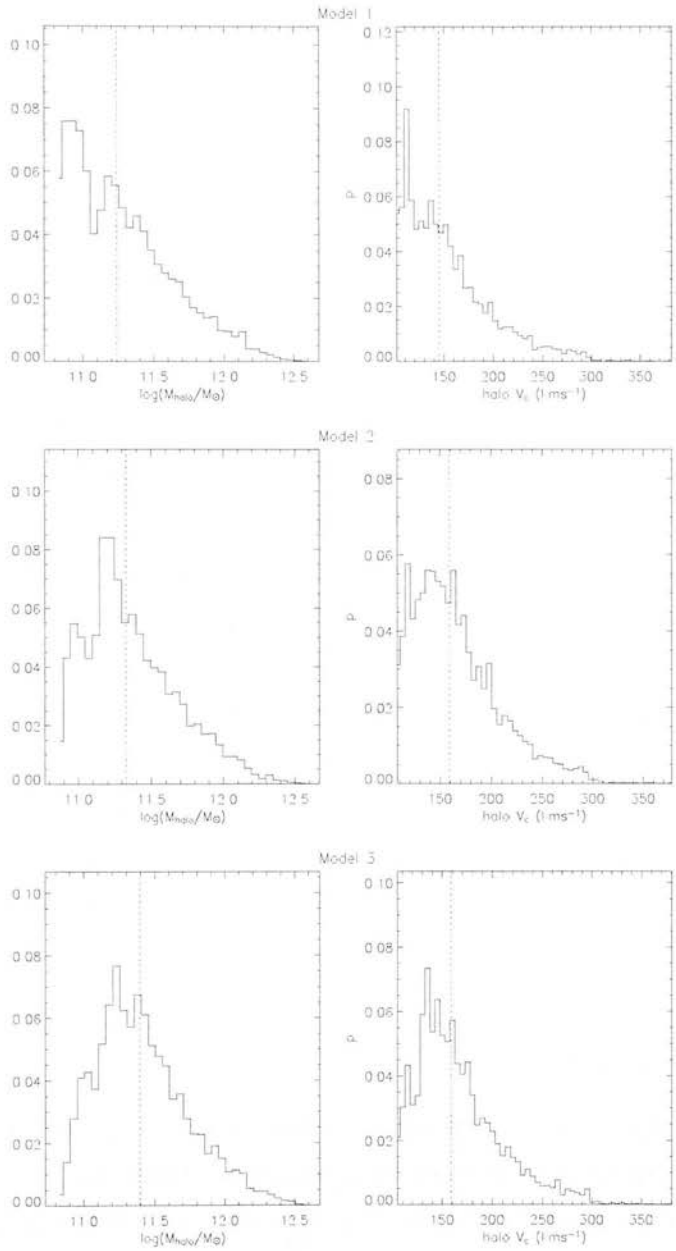

Figure 4.12: Parent halo properties of LBGs in models 1, 2 and 3. Left hand panel: halo mass probability density. Right hand panel: halo circular velocity probability density. The dotted lines denotes the median values, available in Table 4.2.

Weschsler et al. (2001) show that the collisional starburst semi-analytic model of Somerville et al. (2001) predicts clustering of LBGs comparable to that derived from the massive halo model, and the mean halo mass is $\langle M_{\rm h,LBG} \rangle \sim 2 \times 10^{11} M_{\odot}$ (Primack, Wechsler and Somerville 2003). Weatherley et al. (2005) use refined analysis of LBG rotation curves to derive the circular velocity and hence mass of the parent haloes, finding a mean value of $\langle M_{\rm h,LBG} \rangle \sim 4 \times 10^{11} M_{\odot}$.

Bringing all of the above together, it appears that there is little consensus on the properties of haloes housing LBGs, with masses in the range $10^{10} - 10^{12}$ $M_{\odot}$ deemed plausible. Results of $\sim 2 \times 10^{11} M_{\odot}$ are certainly consistent with at least the low-mass estimates, indeed almost identical to the collisional starburst model of Somerville et al. (2001). Nevertheless, we have seen that models 1 and 2 dramatically overpredict the number counts and brightness of LBGs. In model 3 many of the low-mass haloes drop out of the sample as their daughter galaxies fall below the detection limit in $\mathscr{R}$. Nevertheless, the median halo mass in model 3 is only slightly larger in model 3.

The left-hand panel of Figure 4.13 shows the number of LBGs as a function of their $\mathscr{R}$ magnitude: for models 1 (top panel) and 2 (middle panel) the majority of sources are very faint ($\mathscr{R} > 25$). In model 3, many of these vanish from the sample. The right-hand panel shows the $\mathscr{R}$ magnitude of an LBG as a function of the parent halo, each dot representing a single galaxy. We see that the majority of the faint sources are housed in low mass haloes around the $\sim 10^{11} M_{\odot}$ range.

4.3.5 Physical parameters of LBGs

I now go on to explore the individual properties of LBGs, presenting a number of different predictions for their physical characteristics and comparing this with available observational data. In this section, I ignore the interlopers and present properties only for 'true' LBGs (ie. those that satisfy the colour criteria and lie in the correct redshift range).

Stellar masses

The top panels of Figure 4.14 show the probability distribution of LBG stellar masses for models 1, 2 and 3 respectively. The black histogram gives the

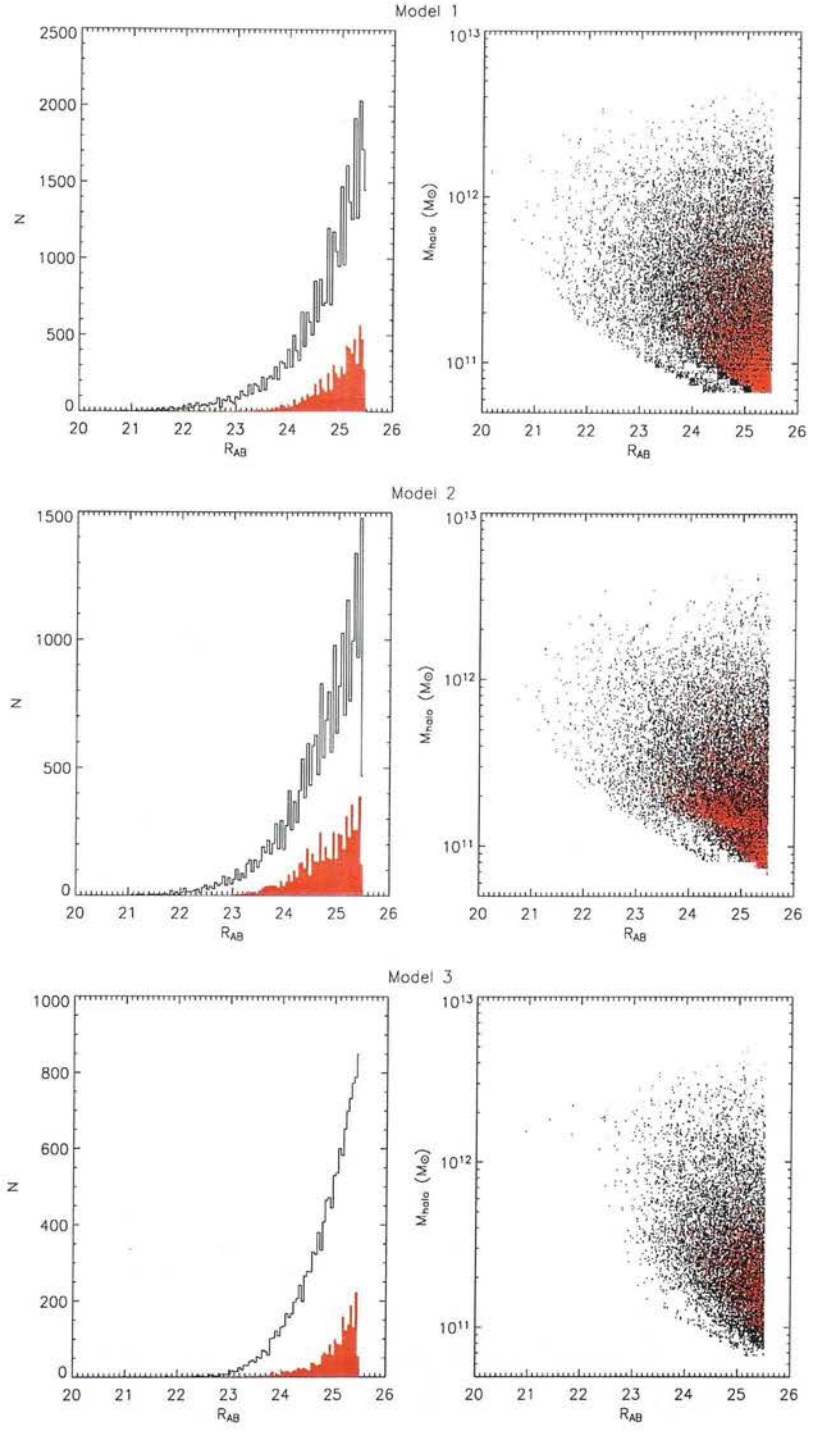

Figure 4.13: Left hand panel: The black histogram shows the number of LBGs in each magnitude bin, and the solid red histogram shows the number of interlopers (galaxies selected as LBGs but lying outside the redshift range. Right hand panel: LBG parent halo mass as a function of magnitude. Black dots are colour-selected LBGs lying within the redshift range, and red dots are interlopers. Interlopers tend to lie at the faint end of the distribution and reside in mainly low-mass haloes.

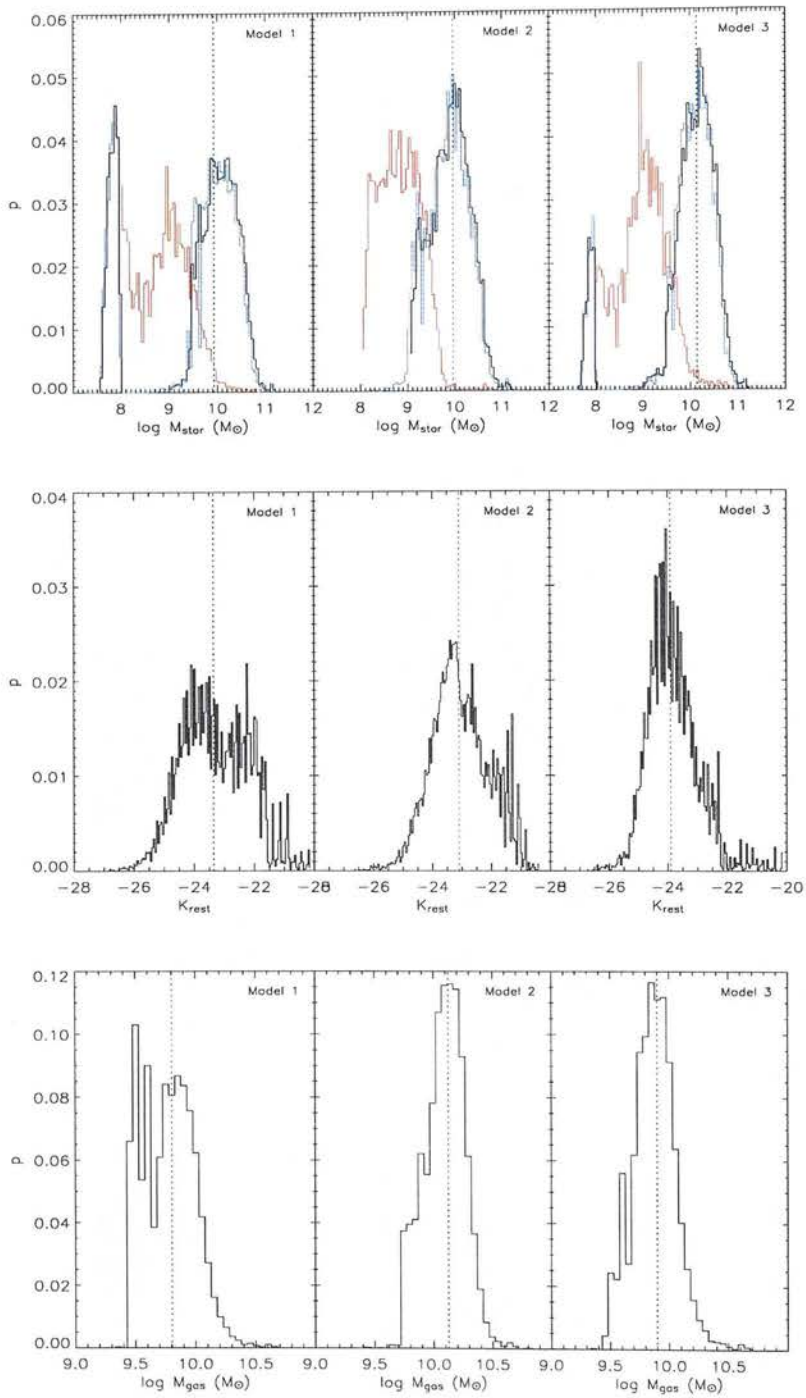

Figure 4.14: LBG properties in the three models. Top panels: the stellar mass of LBGs in models 1, 2 and 3. The black histogram gives the total mass, and the blue and red histograms give the masses of the disk and bulge components respectively. Middle panels: rest frame K-band magnitudes. Bottom panels: cold gas masses. Median values are available in Table 4.2.

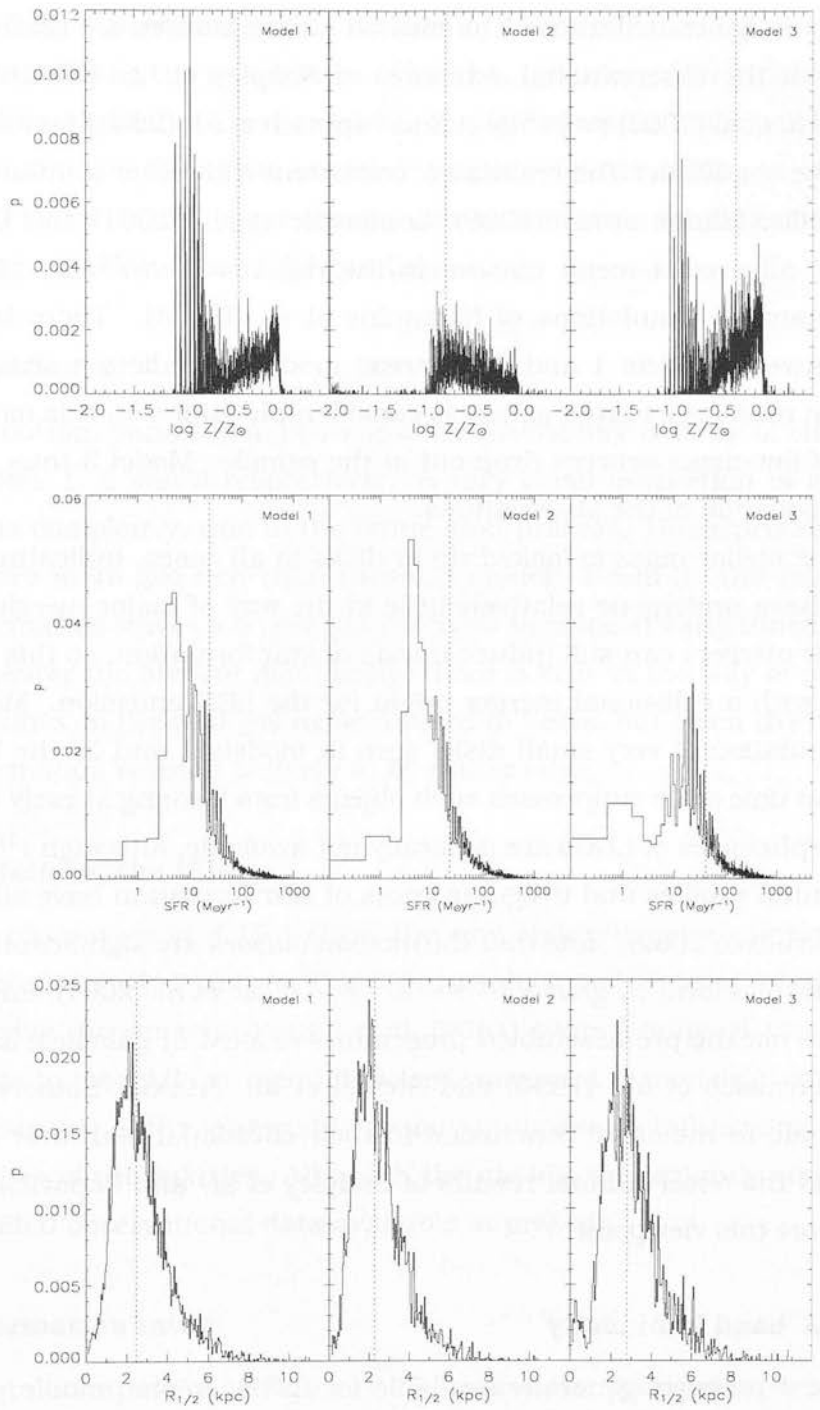

Figure 4.15: Further LBG properties in the three models. Top panels: the cold gas metallicity of LBGs in models 1, 2 and 3. Middle panels: Star formation rates (averaged over the last 100 Myr). Bottom panels: mass-weighted half-mass radii. Median values are available in Table 4.2.

total mass, the blue histogram the mass in the disk component and the red histogram the bulge contribution. The median stellar masses are reasonably consistent with the observational estimates of Shapley et al. (2001) ($2.5 \times 10^{10} M_{\odot}$), Pettini et al (2001) ($\sim 10^{10} M_{\odot}$) and Papovich et al. (2001) ($\sim 10^{10} M_{\odot}$), if a little on the small side. The results are consistent with other semi-analytic studies of LBGs: Baugh et al. (1998), Somerville et al. (2001) and Blaziot et al. (2003) all predict mean masses in the region of $\sim 10^{10} M_{\odot}$, as does the hydrodynamical simulations of Nagamine et al. (2004). There is little difference between models 1 and 2, whereas model 3 predicts a somewhat larger median mass. As a given galaxy is considerably fainter in this model, a population of low-mass sources drop out of the sample. Model 3 thus yields a better reproduction of the observations.

Most of the stellar mass is locked up in disks in all cases, indicating that the galaxies have undergone relatively little in the way of major merging. Of course, minor mergers can still induce bursts of star formation, so this is not inconsistent with a collisional merger origin for the LBG emission. Model 2 loses the population of very small disks seen in models 1 and 3: the longer star formation time scale suppresses such objects from forming at early times. Accurate morphologies of LBGs are generally not available, although $r^{1/4}$ profiles, exponential profiles and irregular knots of star formation have all been observed (Giavalisco 2002). Note that the median masses are significantly less than the mass of a local L_* galaxy ($\sim 8 \times 10^{11} M_{\odot}$) (Cole et al. 2001), impyling that LBGs *are not* the pre-assembled progenitors of local L_* galaxies, as suggested by Giavalisco et al. (1996) and Steidel et al. (1996). Somerville et al. (2001) come to the same conclusion in their collisional starburst model for LBGs, and the observational results of Shapley et al. and Papovich et al. further support this viewpoint.

Rest frame K band luminosity

Although not a property generally available for LBGs, in the middle panels of 4.14 I show the probability density of rest-frame K band magnitudes for models 1, 2 and 3 respectively. The results reinforce the earlier interpretation that LBGs do not represent *pre-assembled* progenitors of local $\sim L_*$ galaxies. Kockaneck et al. (2001) derive a local value of $M_* = -24.19$ (for $H_0 = 70$ kms^{-1}), brighter by a factor ~ 2 than the median magnitude of the LBGs (somewhat

less for model 3). Recall also that stellar populations dim as they age (see Figure 2.6), exacerbating the discrepancy. This of course does not preclude LBGs from being the progenitors of local L_* galaxies, merely that some of the mass is assembled at lower redshift. The fate of model LBGs will be examined in due course. Note that model 2 predicts fainter LBGs on average than models 1 and 3: the longer star formation timescale inhibits star formation, leading to less luminous LBG candidates.

Cold gas mass

In the bottom panels of 4.14 I show the probability density of cold gas mass in models 1, 2 and 3 respectively. A very small proportion of galaxies lack cold gas completely, due to the truncation process. Unsurprisingly, model 2 LBGs are more gas-rich than those in models 1 and 3: the relative lack of star formation leaves a larger gas reservoir in place at early times, ready to be used nearer the present day. Sadly, there is little in the way of observational constraints on the cold gas mass housed in LBGs, but given the high inferred star formation rates, it is likely to be rather large.

Metallicity of the ISM

In the top panels of 4.15 I show the probability density of cold gas metallicity in models 1, 2 and 3. The ISM metallicity of LBGs is relatively unconstrained at the moment: Pettini et al. (2001) quote a range of $0.1 < Z/Z_{\odot} < 1.0$. Galaxies in model 2 are metal-deficient compared to models 1 and 3, another manifestation of the longer star formation timescale influencing the internal properties of the galaxies. All in all, the models are certainly consistent with the limited observational data available at present.

Star formation rates

In the middle panels of Figure 4.15 I show the probability density of LBG star formation rates averaged over the last 100 Myr. A small tail of high-SFR ($> 100 M_{\odot}$ yr^{-1}) objects are present in all three of the models. Shapley et al. (2001) use stellar population models to derive rest-frame optical properties of a sample of 118 LBGs at $z \sim 3$. By varying star formation histories, the time of onset of star formation and the degree of dust extinction they derive

best-fitting models for LBGs. They find a median SFR of $\sim 90\ M_\odot\ \mathrm{yr}^{-1}$, with a very broad distribution in the range $\sim 10 - 2000\ M_\odot\ \mathrm{yr}^{-1}$. Models 1 and 2 predict mean values that are slightly lower than this estimate, whereas model 3 reproduces the observational result nicely.

Radii of LBGs

In the bottom panels of Figure 4.15 I show half-mass radii of model LBGs, a mass-weighted average over the disk and bulge half-mass radii.

The median values in each model agree well with observations: Giavalisco et al. (2001) find typical half-light radii of $2 - 3$ arcsec, translating to a physical scale of $1.54 - 2.3$ kpc in a ΛCDM universe with $H_0 = 70\ \mathrm{kms}^{-1}$. Pettini et al. (2001) also derive a value of $r_{1/2} \sim 2.5$ kpc. The median values also corresponds well with the semi-analytic results of Somerville et al. (2001) and Blaziot et al. (2003).

The magnitude of dust exctinction in LBGs

Extinction in a galaxy is often written as

$$E(B-V) = (B-V) - (B-V)_0, \tag{4.8}$$

where the subscript 0 denotes unextinguished (dust-free) magnitudes. The best fit models to the LBG sample of Shapley et al. (2001) described above yield a mean rest-frame extinction of $\langle E(B-V)\rangle = 0.155$, with values in the range $-0.05 < E(B-V) < 0.4$. The models all correspond reasonably well with the results of Shapley et al. (2001) and Steidel et al. (1999) (see their Figure 9), although one must bear in mind that the LBGs in models 1 and 2 tend to be roughly 2 magnitudes too bright. Since stars spend longer embedded in molecular clouds in model 3, dust extinction will play a more important role in determining the observed UV flux. Unsurprisingly, galaxies are redder in this model, and the median value of $E(B-V)$ is a better match to reality.

4.3.6 IR properties of LBGs

The inferred extinctions and star formation rates of LBGs imply that they should be luminous in the IR. Nevertheless, the small median submillimetre flux of LBGs (eg. Chapman et al. 2000a, Webb et al. 2003b) implies that

	z	$\langle M_{\rm star} \rangle$ ($10^{10} M_\odot$)	$\langle M_{\rm halo} \rangle$ ($10^{11} M_\odot$)	$\langle M_{\rm gas} \rangle$ ($10^{10} M_\odot$)	$\langle Z_{\rm gas} \rangle$ ($Z_\odot$)	SFR ($M_\odot$ yr^{-1})
1	3.12(0.18)	0.85(1.58)	1.72(3.43)	0.64(0.41)	0.007(0.005)	23.24/66.64
2	3.11(0.18)	0.88(1.46)	2.12(3.40)	1.33(0.59)	0.003(0.004)	22.53/61.48
3	3.01(0.17)	1.36(1.79)	2.48(3.88)	0.79(0.45)	0.010(0.005)	41.79/90.54

	$\langle r_{1/2} \rangle$ (kpc)	M_K (rest)	V_c (halo) (kms^{-1})	$E(B-V)$ (obs)	$E(B-V)$ (rest)
1	2.48(1.36)	−23.36(1.12)	145.0(43.0)	0.26(0.13)	0.13(0.12)
1	2.27(1.27)	−23.09(0.98)	159.0(41.0)	0.24(0.12)	0.12(0.07)
3	2.78(1.45)	−23.91(0.87)	159.0(42.0)	0.42(0.14)	0.17(0.07)

Table 4.2: LBG properties of the various models. In each column, the median value is given for the models, along with the standard deviation in brackets. The star formation is written as median/mean, indicating the effects of the high-SFR tail.

their IR properties are not as extreme as SMGs (examined in more detail in the next chapter).

Far-IR luminosity is often defined as the integral of an SED in the range $8-1100$ μm (eg. Chapman et al. 2004). I use this to calculate the rest-frame IR luminosity of LBGs in the three models. Medians and standard deviations as a function of $\mathscr{R}$ are given in Table 4.3. There is an obvious correlation between brightness and IR flux in all the models. The large drop in the number of LBGs in model 3 is reflected in the fainter luminosities. Clearly a population of IR-bright galaxies drop out of the LBG sample when a different value of $t_{\rm esc}$ is used. In Figure 4.16 I show the luminosity distributions for all LBGs in the three models. A large fraction have IR luminosities in excess of 10^{12} $L_\odot$, and thus would be classed locally as ULIRGs (Arp 220, the archetypal ULIRG, has $L_{\rm IR} \sim 10^{12}$ $L_\odot$). Given the lack of observational constraints on the far-IR luminosity of LBGs, it is hard to say anything concrete about the significance of the model results at this point. It is likely that if the model SMGs have submillimetre fluxes consistent with reality, then the far-IR luminosities are reasonably correct. This will be investigated in the next chapter.

4.3.7 Ages of LBGs

LBGs inhabit a universe in its infancy: the redshift range $3.4 > z > 2.7$ corresponds to a cosmic age of $\sim 1.8 - 2.4$ Gyr. But how old are the LBGs? This

model	$\mathscr{R} < 22.0$	$\mathscr{R} < 23.0$	$\mathscr{R} < 24.0$	$\mathscr{R} < 25.5$
1	3.89(2.72)	2.72(2.73)	1.14(2.16)	0.15(1.88)
2	4.11(4.01)	2.40(2.95)	1.10(2.20)	0.18(1.30)
3	1.26(1.73)	1.25(4.20)	0.95(3.20)	0.38(1.86)

Table 4.3: Model comparisons of total rest-frame IR luminosity of LBGs as a function of $\mathscr{R}$. All values are in units of $10^{12} L_{\odot}$. Standard deviations are given in brackets.

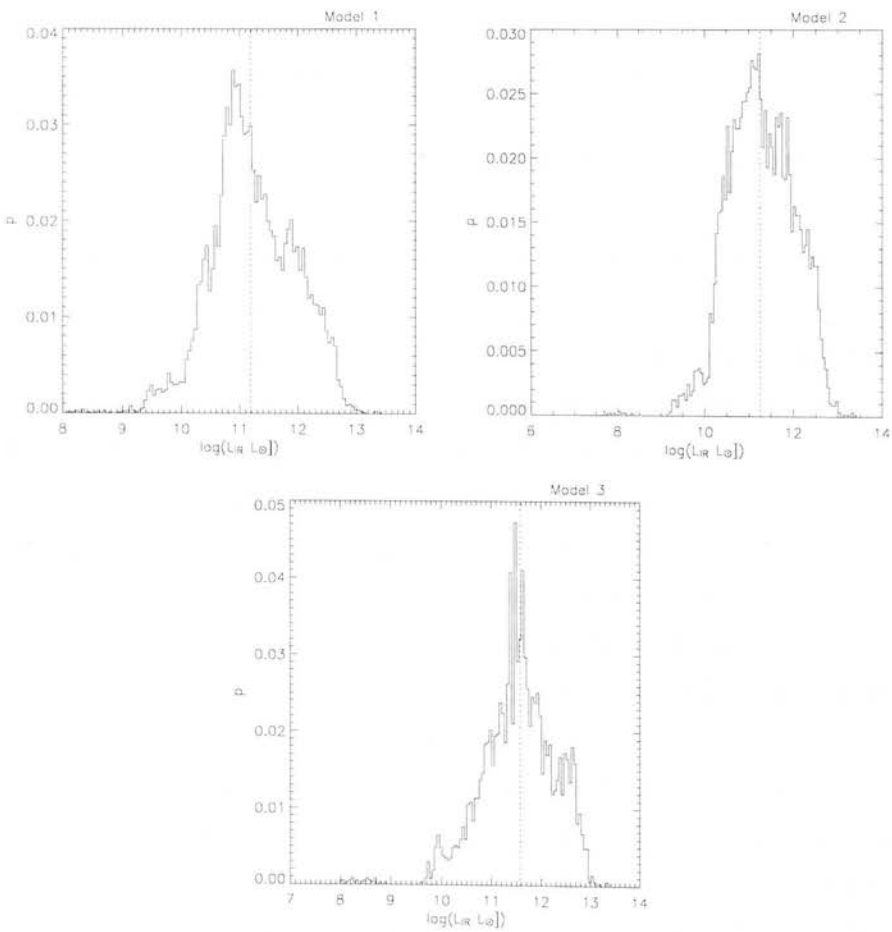

Figure 4.16: Far-IR luminosities of all LBGs in each model. The dotted line gives the median value of $L_{\rm IR}$ in each case.

model	$\mathscr{R} < 22.0$	$\mathscr{R} < 23.0$	$\mathscr{R} < 24.0$	$\mathscr{R} < 25.5$
1	1.12(0.32)	1.12(0.36)	0.97(0.47)	0.66(0.44)
2	1.25(0.26)	1.12(0.32)	1.08(0.38)	0.94(0.42)
3	1.63(0.20)	1.39(0.27)	1.15(0.36)	0.97(0.46)

Table 4.4: Median ages (in Gyr) of LBGs as a function of their $\mathscr{R}$-band magnitude for the three models. The standard deviations are given in brackets.

question has numerical implications as well as observational ones. As Blaziot et al. (2003) have pointed out, a generic problem with using N-body simulations as the basis for semi-analytic models is the limited mass resolution available. Galaxies that form in haloes at the mass resolution threshold cool gas too quickly: in reality, such a galaxy would be made up of smaller entities with longer cooling timescales and would have already formed stars. The properties (particularly luminosities) of very young galaxies are therefore likely to be affected by this limitation in resolving the merger history of galaxies.

In Table 4.4 I show the median ages of LBGs as a function of $\mathscr{R}$ in the three models. Age in this sense is defined as the time between the present day (the time at which the galaxy is observed) and the formation time of the first projentor halo of the LBG. There is a clear trend for faint galaxies having formed only recently, and their properties may be suspect.

In Figure 4.17, a variation of the bottom-left panel of Figure 4.13, I compare the number of 'young' and 'old' LBGs in model 3 as a function of $\mathscr{R}$, where the demarcation between the two regimes is taken to be 1 Gyr. It is clear that the faint galaxies are preferentially young objects, and this suggests that the properties of these galaxies are subject to numerical uncertainty and error. A simulation with significantly better mass resolution will be required to accurately pin down the faint end of the LBG population.

4.3.8 What is the fate of LBGs?

Although the simulation boxes used in making light cones only contain the brightest objects, for each model a full simulation box is available at $z = 0$. This allows objects of interest at high redshift to be followed forwards in time, and their eventual fate in the local universe ascertained. In Table 4.5 I show median values of the rest-frame K-band magnitudes and stellar masses of

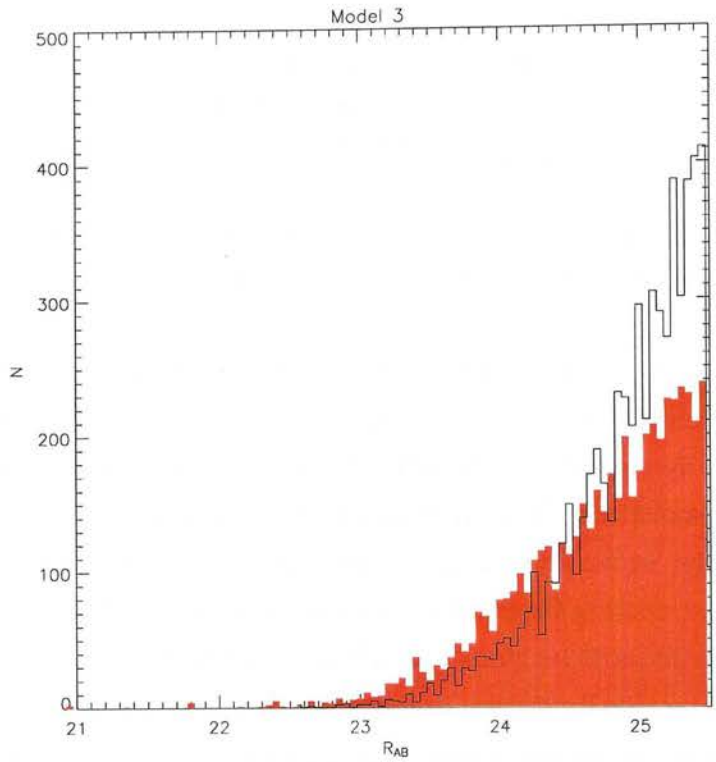

Figure 4.17: Number LBGs as a function of $\mathscr{R}$ in model 3. A variant of the bottom-left panel of Figure 4.13, the solid histogram shows the number of LBGs younger than 1 Gyr as a function of $\mathscr{R}$, whereas the solid red histogram shows the number of LBGs older than 1 Gyr as a function of $\mathscr{R}$. There are more faint, young galaxies than faint, old galaxies, and the opposite is true of the bright sources.

LBG descendants (as a function of $\mathscr{R}$) in the three models, and in 4.18 I plot the distributions of these properties for all LBGs in model 3, the most realistic.

Most LBGs do not end up in L_* galaxies, due to the large proportion of low mass LBGs identified in the models. Nevertheless, the descendants do span a large range of properties, with a small proportion numbering among the most massive galaxies at $z = 0$. There is a clear trend for bright LBGs residing in bright galaxies in the local universe, and overall LBGs in model 3 become significantly more luminous objects. The vast majority are still spiral galaxies (recall that $B/T < 0.4$ corresponds to a spiral), but given the overly-large fraction of discs at $z = 0$ in the models this is not a suprising result. Model 3 predicts a number of LBGs that have surprisingly low stellar masses at $z = 0$: these are galaxies that have since undergone little evolution.

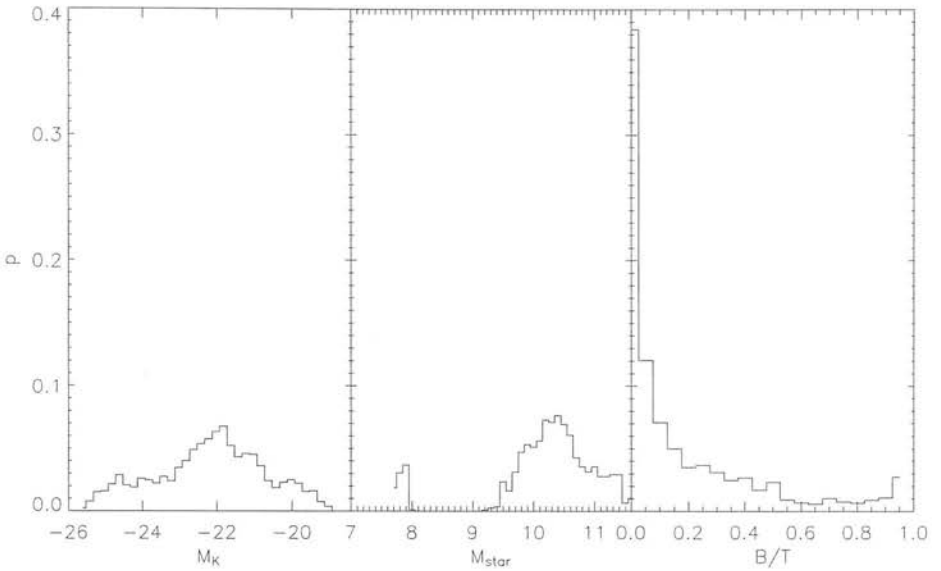

Figure 4.18: Properties of LBG descendants in model 3. Left panel: distribution of rest-frame K-band magnitude. Middle panel: distribution of stellar masses. Right panel: distribution of bulge to total light ratio, as defined as in equation 3.3.

Overall, there seems to be no preferential destination for LBGs: they span a wide range of properties at the time of observation, and they seem to now occupy the normal field population. Figure 4.19 shows some example merger trees of three LBGs taken from model 3. The dotted blue line shows the time of observation as an LBG. Galaxies 98 and 2263 have undergone rather complicated merger histories, involving many major merger events, while galaxy 40 has lived a relatively quiet existence, assembling its mass through small accretion events. It does not appear that particular events cause a galaxy to be visible as an LBG, rather just a reasonably active phase of star formation. The bottom plot shows the build-up of halo mass as a function of redshift. Much of the halo mass has already been assembled by the time of LBG observation.

4.4 Conclusions

The results of this section have shown that the galaxy formation model outlined in chapter 2 can reproduce at least some of the properties of the high

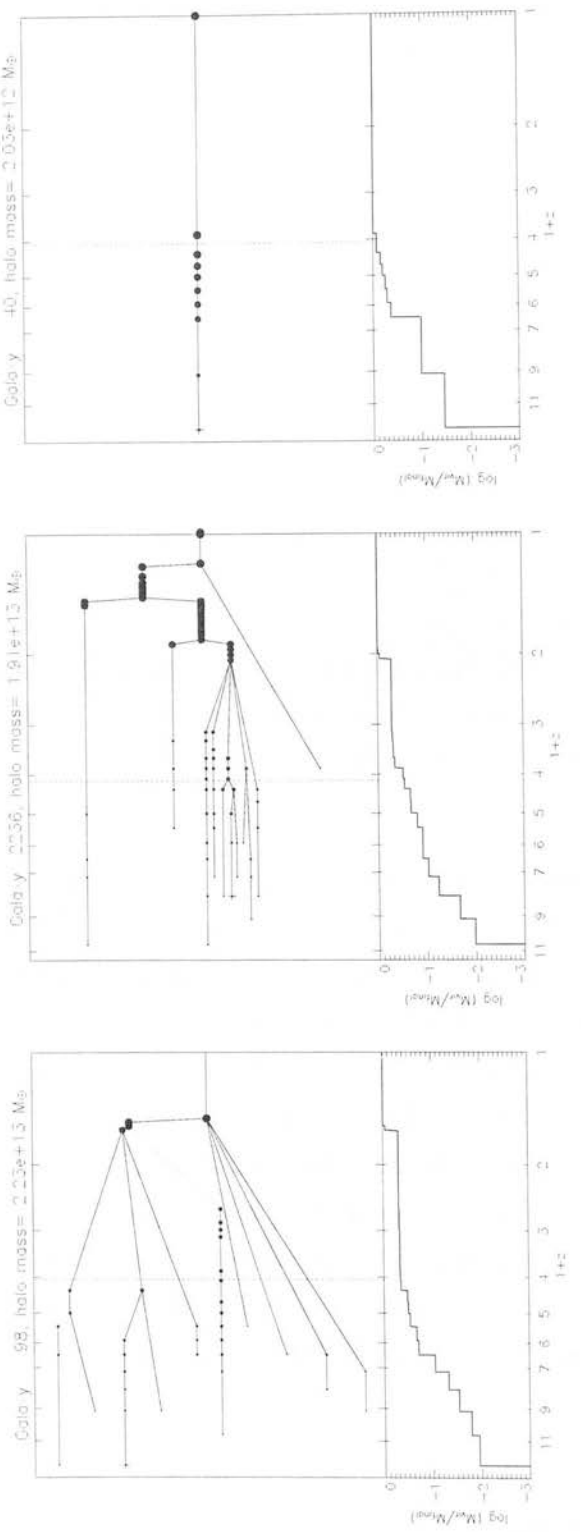

Figure 4.19: Example merger trees of LBGs in model 3. In the top panel, each circle represents a merging event, with the size of the symbol proportional to the mass of the halo. The cross shows the most massive progenitor. In the bottom panel I show the fraction of the final mass assembled in all progenitor haloes as a function of redshift.

	$\mathscr{R} < 22.0$	$\mathscr{R} < 23.0$	$\mathscr{R} < 24.0$	$\mathscr{R} < 25.5$
		Model 1		
M_K	−22.7(1.1)	−22.5(1.2)	−22.2(1.4)	−21.3(1.7)
$M_{\rm star}$ $(10^{10}M_\odot)$	4.5(8.7)	3.6(8.4)	2.9(8.4)	1.1(7.0)
		Model 2		
M_K	−22.6(1.1)	−22.4(1.2)	−22.1(1.3)	−21.5(1.5)
$M_{\rm star}$ $(10^{10}M_\odot)$	4.4(8.3)	2.6(7.8)	2.0(7.6)	1.1(6.4)
		Model 3		
M_K	−23.7(0.7)	−23.7(1.0)	−22.7(1.1)	−22.0(1.3)
$M_{\rm star}$ $(10^{10}M_\odot)$	11.1(11.1)	11.2(10.0)	4.3(9.0)	2.4(7.0)

Table 4.5: Median properties of LBG descendants at $z = 0$ in the three models. Standard deviations are given in brackets.

redshift universe. Massive and luminous galaxies are under-represented at early times, a problem common to many other semi-analytic models. A reasonably accurate reproduction of the LBG population is possible, with model 3 outperforming the others by some margin. The longer value of $t_{\rm esc}$ used in this model implies that significant amounts of dust reprocessing of starlight is necessary to match the bright end of the LBG number counts. Silva et al. (1998) find that a value of $t_{\rm esc} \sim 5$ Myr gives good fits to the properties of local spiral galaxies, and that larger values ($t_{\rm esc} \sim 20$ Myr) are appropriate for low redshift starbursts. Model 3 uses $t_{\rm esc} = 10$ Myr, perhaps implying that LBGs, although 'normal' in many ways, also share many of the characteristics of starbursts. It is clear that a truly accurate study of the LBG population will require better mass resolution, but overall the results are reasonably encouraging.

CHAPTER 5

The high redshift universe 2: Extremely Red Objects and Submillimetre Galaxies

I now go on to examine properties of more 'extreme' classes of object found in the high redshift universe, in particular the Extremely Red Objects (having colours in excess of $(R-K) > 5$ or $(I-K) > 4$) routinely detected in deep K-band surveys, and the population of bright Submillimetre Galaxies (SMGs) discovered since SCUBA went online at the JCMT. Traditionally, semi-analytic models have trouble reproducing these populations (eg. Silva et al. 1999, Fontana et al. 2004, Baugh et al. 2005), and often resort to new physics or unphysical parameterisation of dust properties in order to force reasonable matches to their properties. The aim of this chapter is to investigate whether including a self-consisent model of dust emission can help predict the presence of these extreme objects more easily, or whether the models suffer the same problems as many other groups in the field.

5.1 Extremely Red Objects

Roche et al. (2002, R02) present results for the number counts, clustering and morphologies of a sample of 158 galaxies identified as EROs with $(R-K) > 5$

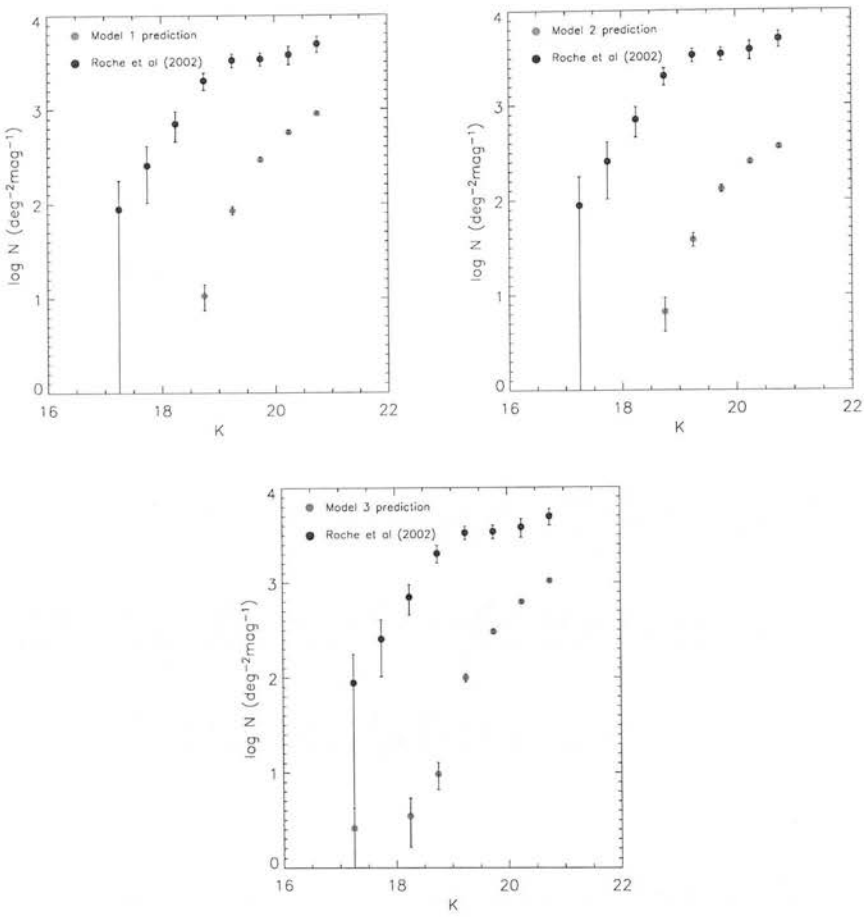

Figure 5.1: ERO number counts for models 1, 2 and 3, compared with the results of Roche et al. (2002).

and $K \leq 21.0$ within 81.5 arcmin^2 of the ELAIS N2 field. I construct 20 mock surveys of 1 deg^2 using the techniques outlined in section 4.1.2. I apply the same selection criteria for EROs as R02 and construct a table of all sources observed in the mock survey.

5.1.1 Number counts

As a first test of the models I calculate the number counts of EROs in the derived mock surveys. For each cone, I sort the galaxies into bins of magnitude equivalent to those used in R02, giving the differential number counts for EROs in each cone. I then average over the 20 cones to give a mean number in each magnitude bin. I plot the results in Figure 5.1. The red circles represent

the mean model number counts and the black circles the observed values from R02. In both cases the error bars show the $N^{1/2}$ error on the number of galaxies in each magnitude bin. It is immediately obvious that all the models vastly underpredict the number of EROs observed in reality, with model 2 yielding significantly smaller source counts than models 1 and 3. Since star formation occurs later in this model, galaxies are not able to generate significant large populations of old, red stars. Model 3 performs sonewhat better than the others: the longer value of t_{esc} has dimmed the UV flux. This is redshifted roughly into the R-band at the redshifts probed here, and thus boosts the predicted values of $(R-K)$. The marginal presence of bright EROs $(K < 19)$ in this model indicates that the extra dust extinction has allowed a number of luminous galaxies to cross the ERO colour threshold.

Roche et al. (2002) find 198 EROs brighter than $K < 21$, yielding a number density of 1.93 arcmin^{-2}. Models 1, 2 and 3 predict median number densities of $0.24, 0.11$ and 0.31 arcmin^{-2} respectively, around an order of magnitude smaller than predictions. The fraction of galaxies being classified as EROs is small: $\sim 2, 3$ and 3 % for models 1, 2 and 3 down to a limit of $K \leq 21.0$, in contrast with $\sim 14\%$ as found by R02.

It is worth emphasising that the mock surveys do not include any overdense regions, since they are constructed entirely from 'fair samples' of the universe. Given that EROs display strong clustering (Daddi et al. 2000, Roche et al. 2002), it seems likely that the mock surveys are artificically lacking in EROs over a given area simply due to the lack of overdensities, their preferential habitats. Of course, one could create a simulation with constrained initial conditions, so that a dense cluster region will form in the simulation volume. Using this to create a mock survey would then overemphasise dense regions of the universe, and would not be consistent with reality.

5.1.2 The redshift distribution of EROs

In Figure 5.2 I show the redshift distribution of EROs in models 1, 2 and 3. The solid histogram is the mean number of galaxies in each redshift bin over 20 surveys, and the blue and red dotted histograms represents the standard deviation in each bin. In all three models there is a peak in the distribution at around $z \sim 1.5$, in good agreement with the photometric redshift estimates

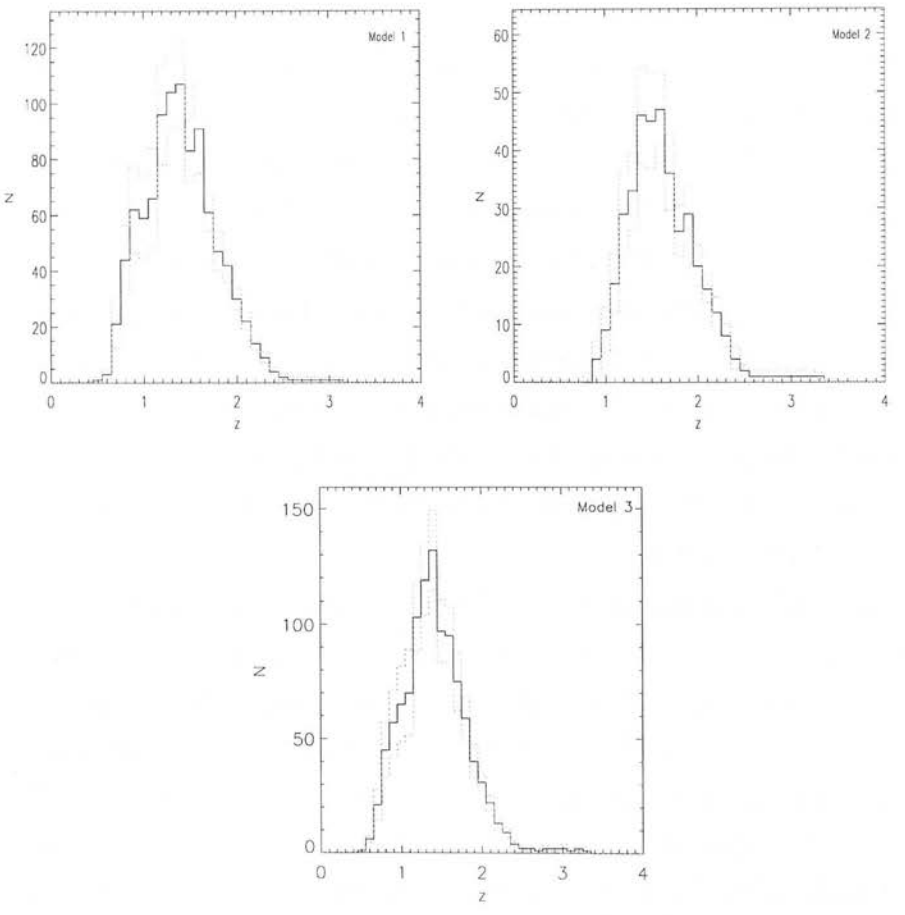

Figure 5.2: ERO redshift distribution for the three models. The black histogram gives the median number of galaxies in each redshift bin, and the red and blue histograms give the mean minus the standard deviation in each bin.

of 198 EROs given by Caputi et al. (2004). Both models also agree well with the results of Wilson et al. (2004), who find that two-thirds of all EROs lie beyond $z = 1.3$. For models 1, 2 and three this fraction is 70.4, 85.0 and 59.6 % respectively.

The models also exhibit a high redshift tail out to $z \sim 3$, agreeing with the hypothesis that the majority of EROs lie in the range $1 < z < 2$, with a small population of extreme objects at higher redshift (eg. McCarthy 2004). Gear et al. (2000) also point out that the unfavourable k-correction inhibits the detection of EROs beyond $z \sim 2.5$.

The differences in the number and redshift distributions of EROs between the models can easily be accounted for by comparing their star formation timescales. Recall that models 1 and 3 have a short star formation timescale $\tau_* = 2$ Gyr, while model 2 has the larger value $\tau_* = 8$ Gyr. Given the scaling of star formation rate with circular velocity and hence redshift (equation 2.13), we see that a longer star formation timescale leads to the suppression of star formation at early times. This is clearly visible by comparing the star formation histories of the models (Figures 3.12 and 4.2, the SFR history of model 3 is identical to that of model 1). At high redshifts, more star formation is taking place in model 1 (and 3), leaving behind more red, evoloved stars at a given later epoch. In model 2, massive galaxies (those expected to contribute to the ERO population) are less numerous and bluer.

Summing up the results of the last two sections, it seems that the models vastly underpredict the number of EROs, but those that do exist lie in the right redshift range. There are a number of possibilities for the deficit in the number counts: I have already shown that the models lack the most massive galaxies. In addition, the magnitude of dust extinction may be underestimated, or EROs may preferentially lie in overdense regions of the universe, which are absent from the light cone by design.

5.1.3 A comparison between EROs and faint K-selected galaxies

The lack of completeness in the light cones prohibits a comprehensive comparison of EROs with other K-selected galaxies within the same magnitude

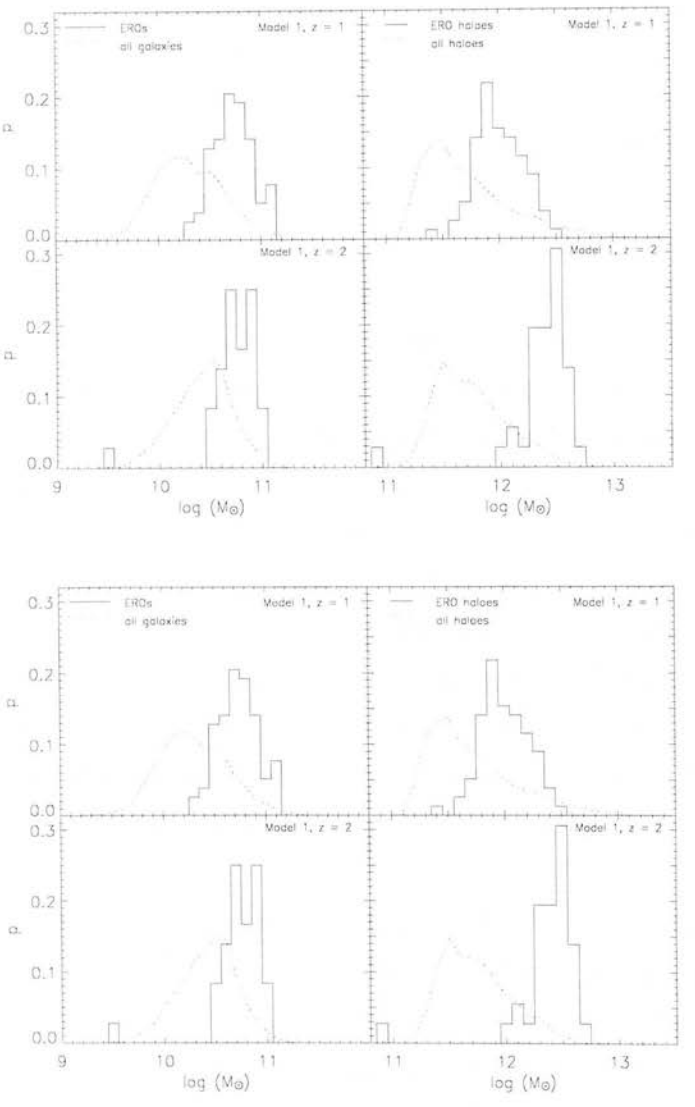

Figure 5.3: ERO stellar mass distribution compared with all galaxies brighter than the same K band limit. Upper panel: results for model 1. Lower panel: results for model 2 (eventually). See the accompanying text for more details.

limit. Nevertheless, I can use full simulation boxes at $z = 1$ and 2 to show a basic comparison between EROs and 'normal' galaxies brighter than the same limiting K-band magnitude. Figure 5.3 shows the probability density as a function of stellar mass for EROs defined as in the previous section (solid histogram) and all galaxies down to the same magnitude limit $K < 21$ (dotted histogram). Both boxes are hampered by the small number of EROs, but clear trends still emerge. The left-hand panels compare the stellar mass of EROs and 'normal' galaxies at redshifts 1 and 2. They are clearly more massive on average than 'normal' galaxies at both epochs. It is therefore not surprising to find that EROs also tend to occupy the most massive haloes at a given epoch, and this is illustrated in the right-hand panels. The effect is especially pronounced at $z = 2$, with the peak in the halo mass distribution of EROs an order of magnitude bigger than the peak in halo mass for normal galaxies down to the same magnitude limit. This bias towards high masses qualitatively agrees with the strong clustering signals observed for EROs (eg. Daddi et al. 2002, Roche et al. 2002, 2003).

5.1.4 Physical parameters of EROs

I now explore the physical properties of model EROs and compare with the data. As in the previous section, I report the results from a single 1 deg^2 mock survey for each model. The model 1 survey contains 1098 candidates, the model 2 survey contains 421 and model 3 houses 1136 sources. Despite the severe lack of EROs in all the models, it will be interesting to see if the few that are produced display similar properties to their (far more numerous) counterparts in reality.

Stellar masses

The top panels of Figure 5.4 show the distribution of stellar masses in models 1, 2 and 3 respectively. Black histograms show the total mass, blue histograms the mass locked up in disks and red histograms the mass of the bulge component. The median mass varies little between the models (see Table 5.1), lying in the region $\sim 6-7\times10^{10}\ M_{\odot}$. This is consistent with the results of Caputi et al. (2004), who find a mass range of $\sim 3\times10^{9} - 3\times10^{11}\ M_{\odot}$ in a survey of 198 EROs with $(I_{775}-K_s) > 3.92$ (analogous to $(R-K) > 5$). However,

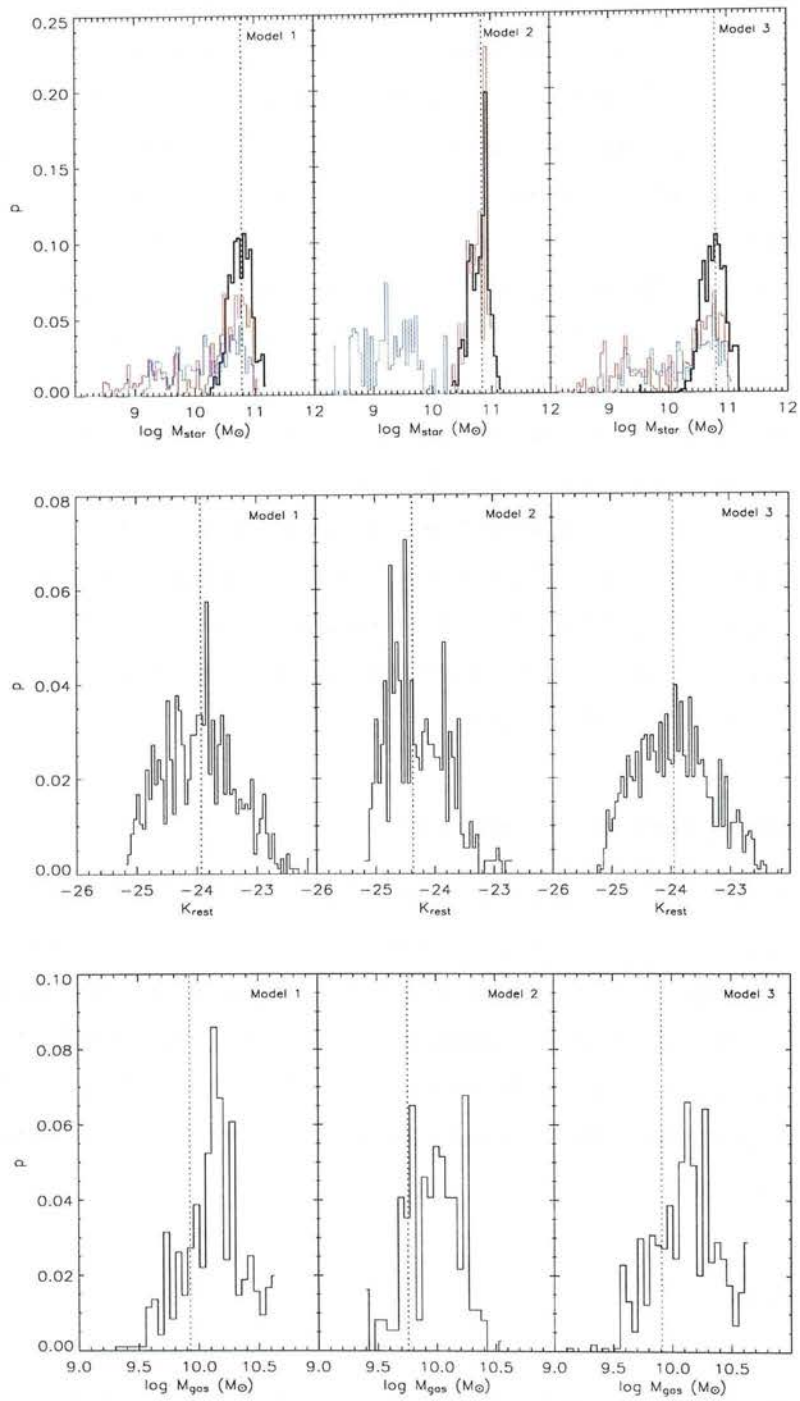

Figure 5.4: ERO properties in the three models. Top panels: the stellar mass of EROs in models 1, 2 and 3. The black histogram gives the total mass, and the blue and red histograms give the masses of the disk and bulge components respectively. Middle panels: rest frame K-band magnitudes. Bottom panels: cold gas masses. Median values are available in Table 5.1.

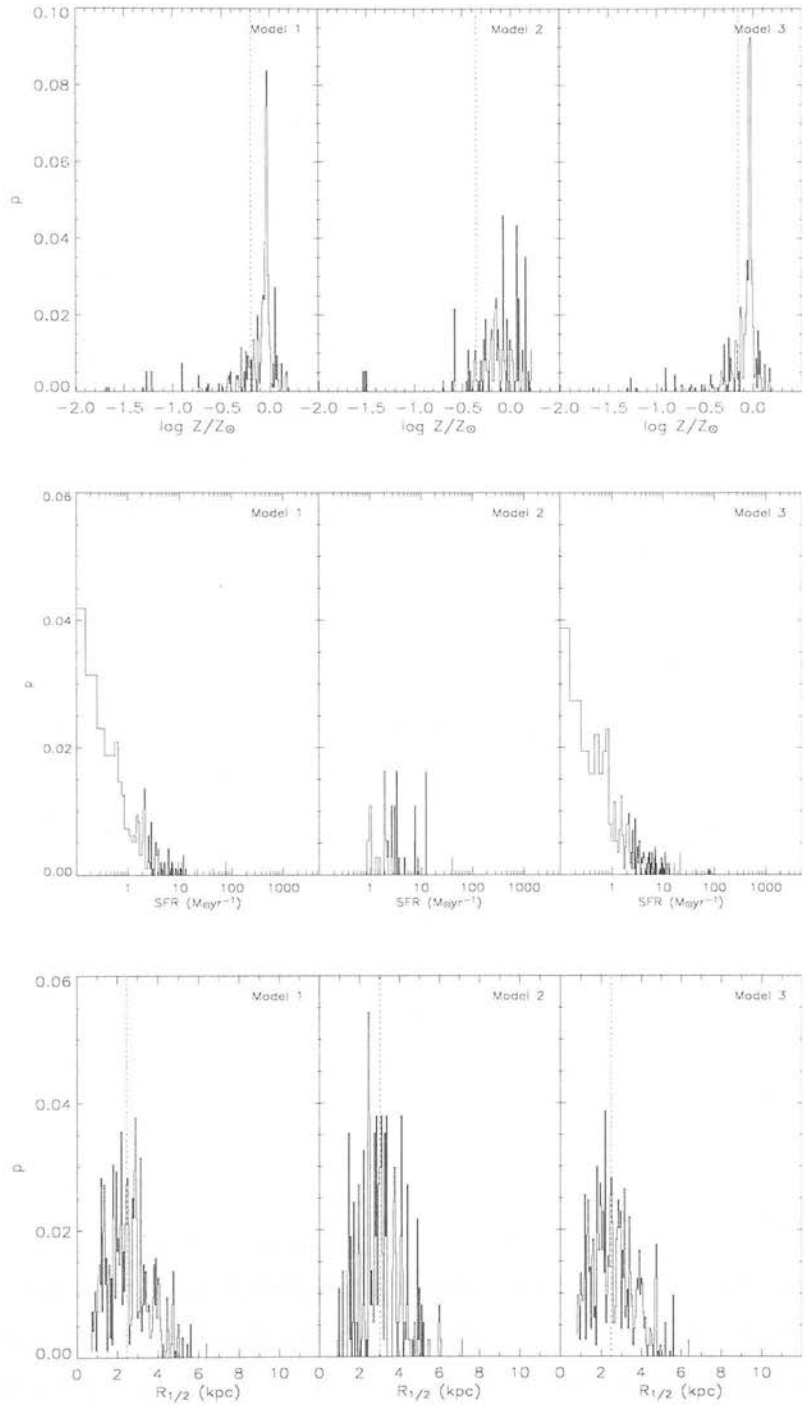

Figure 5.5: Further ERO properties in the three models. Top panels: the cold gas metallicity of EROs in models 1, 2 and 3. Middle panels: Star formation rates (averaged over the last 100 Myr). Bottom panels: mass-weighted half-mass radii. Median values are available in Table 5.1.

the models produce very few EROs with masses $> 10^{11} M_{\odot}$, in contrast to the results of a number of authors (eg. Longhetti et al. 2005, Georgakakis et al. 2006). This of course is a direct result of the lack of massive galaxies at high redshift in the models, as shown in chapter 4.

Much of the mass appears to be locked up in bulges, especially so in model 2. A common consensus between observational determinations is hard to find. Roche et al. (2002) find a $3:2$ mixture of early and late types for a subset of $K \leq 19.5$ EROs. In contrast, Yan and Thompson (2003) find that a sample of $K_s \sim 18.7$ EROs imaged by HST is dominated by disks (~ 60 %), with around 30 % classified as early type galaxies and the rest irregular or unclassifiable. Gilbank et al. (2004) find roughly equal contributions from disks and bulges in their survey, as did Cimatti et al. (2004). The model results are certainly consistent with this rather clouded picture.

Rest-frame K-band magnitudes

In the middle panels of Figure 5.4 I show the distribution of rest-frame K-band magnitudes for models 1, 2 and 3 respectively. EROs tend to be slightly brighter (albeit less numerous) in model 2. This is due to the different star formation timescales: the galaxies will be younger and hence brighter. The models display median K magnitudes similar to that of local L_* galaxies, although there is a common lack of very bright galaxies as seen by a number of authors (eg. Pozzetti et al. 2003, Longhetti et al. 2005). Again, this is reflected in the bright-end deficit in the rest-frame K-band LFs, as shown in chapter 4.

Cold gas masses

In the bottom panels of Figure 5.4 I show the distribution of cold gas masses for models 1, 2 and 3 respectively. Note that the median values (see Table 5.1) are skewed significantly by the large fraction of EROs with no gas ($43.4, 42.1$ and 36.1 % for models 1, 2 and 3). Those that do harbour cold gas tend to have significant amounts present, in excess of $10^{10} M_{\odot}$ in most cases. Although few estimates for the gas mass of EROs exist, a significant fraction are estimated to be dusty starbursts, requiring large attendant reservoirs of gas. Detection of CO emission in HR10 (the archetypal dusty ERO) by Greve, Ivision and

Papadopoulos (2003) yields a molecular gas mass of $\sim 6 \times 10^{10} M_{\odot}$, and *XMM-Newton* observations of EROs (Brusa et al. 2005) reveal the presence of large column densities of cold gas. The truncation process removes all cold gas in galaxies residing in parent haloes with $V_c > 300$ kms^{-1}, purging the gas from nearly half the EROs in a model.

Gas metallicity

In the top panels of Figure 5.5 I show the distribution of ISM metallicity for models 1, 2 and 3. Again, the median values are skewed by the significant fraction of EROs lacking gas. In the subset of EROs that do contain gas, a metallicity of roughly solar is prevalent. There is little in the way of observations to confirm or refute this, although if EROs are evolved, red systems with large stellar masses then it seems likely that the corresponding metallicites would also be high.

Star formation rates

In the middle panels of Figure 5.5 I show the distribution of star formation rates in models 1, 2 and 3 respectively. The lack of gas in many objects leads to an attendant lack of star formation. $\sim 16.4, 12.4$ and 21.9% of EROs are forming stars at rates in excess of 1 $M_{\odot}$ yr^{-1} in models 1, 2 and 3. Georgakakais et al. (2006) find a mean star formation rate of ~ 25 $M_{\odot}$ yr^{-1} for a sample of EROs with $K < 19.5$ and $(I - K) > 4$. The models clearly do not match this result.

Radii of EROs

In the bottom panels of Figure 5.5 I show the distribution of mass-weighted radii (as defined in the previous section) for EROs in models 1, 2 and 3 respectively. The median values are reasonably similar, and overall EROs tend to be large objects. Observational estimates of physical sizes are hampered by the lack of unambiguous classifications in many cases. Nevertheless, a subset of six bright EROs in the Roche et al. (2002) sample have half-light radii in the range $0.28 < r_{1/2} < 1.42$ arcseconds. For a ΛCDM cosmology with $H_0 = 70$ kms^{-1} this corresponds to radial sizes of $2.24 - 11.37$ kpc at $z = 1$ and $2.34 - 11.89$ kpc at $z = 2$. The models thus seem to be reasonably consistent

	z	$\langle M_{\rm star}\rangle$ ($10^{10}M_\odot$)	$\langle M_{\rm halo}\rangle$ ($10^{12}M_\odot$)	$\langle M_{\rm gas}\rangle$ ($10^{10}M_\odot$)	$\langle Z_{\rm gas}\rangle$ ($Z_\odot$)	SFR ($M_\odot$ yr^{-1})
1	1.40(0.38)	6.02(2.77)	2.21(1.80)	0.84(1.10)	0.012(0.009)	0.00/0.86
2	1.61(0.38)	6.89(2.44)	2.56(1.50)	0.57(0.76)	0.009(0.010)	0.00/0.69
3	1.40(0.38)	6.25(2.98)	1.97(1.75)	0.81(1.14)	0.014(0.009)	0.00/1.34

	$\langle r_{1/2}\rangle$ (kpc)	M_K (rest)	V_c (halo) (kms^{-1})	$E(B-V)$ (obs)	$E(B-V)$ (rest)	$f(z>1.3)$
1	2.46(1.01)	−23.9(0.6)	288.0(42.0)	0.11(0.37)	0.13(0.10)	0.63
2	3.02(1.09)	−24.4(0.5)	275.0(44.0)	−0.02(0.33)	0.08(0.09)	0.85
3	2.49(1.06)	−24.0(1.4)	286.0(43.0)	0.14(0.41)	0.14(0.32)	0.60

Table 5.1: ERO properties for models 1, 2 and 3. Median values are given along with the standard deviations in brackets.

with the limited observations.

5.1.5 Extinction in EROs

At least the dusty subclass EROs would be expected to display significant amounts of extinction. The model EROs have suprisingly low values of $E(B-V)$, albeit with a large scatter. Georgakakis et al. (2006) find that stellar population models with rest-frame $E(B-V) \sim 0.5$ gives good fits to their observations, implying that the model EROs indeed are too blue. It seems likely that the truncation process has removed a large proportion of potentially dusty objects with large amounts of extinction present.

5.1.6 Ages of EROs

As we have seen in Figure 5.2, model EROs span a relatively wide range in redshift. EROs are expected to be relatively old systems, to allow long enough for the stellar populations to evolve towards the red. As in the previous chapter, I take the formation time of the first progenitor halo of an object as an estimate of the age. Results for the three models are shown in Figure 5.6. The median ages are $3.48 \pm 0.87, 2.97 \pm 0.71$ and 3.57 ± 0.95 Gyr in models 1, 2 and 3 respectively, where the error bars are the standard deviations. EROs are systematically younger in model 2, due to the longer star formation timescale. How do these results compare with observations? McCarthy et al. (2004) provide a summary of numerous authors' attempts at deriving an age for the

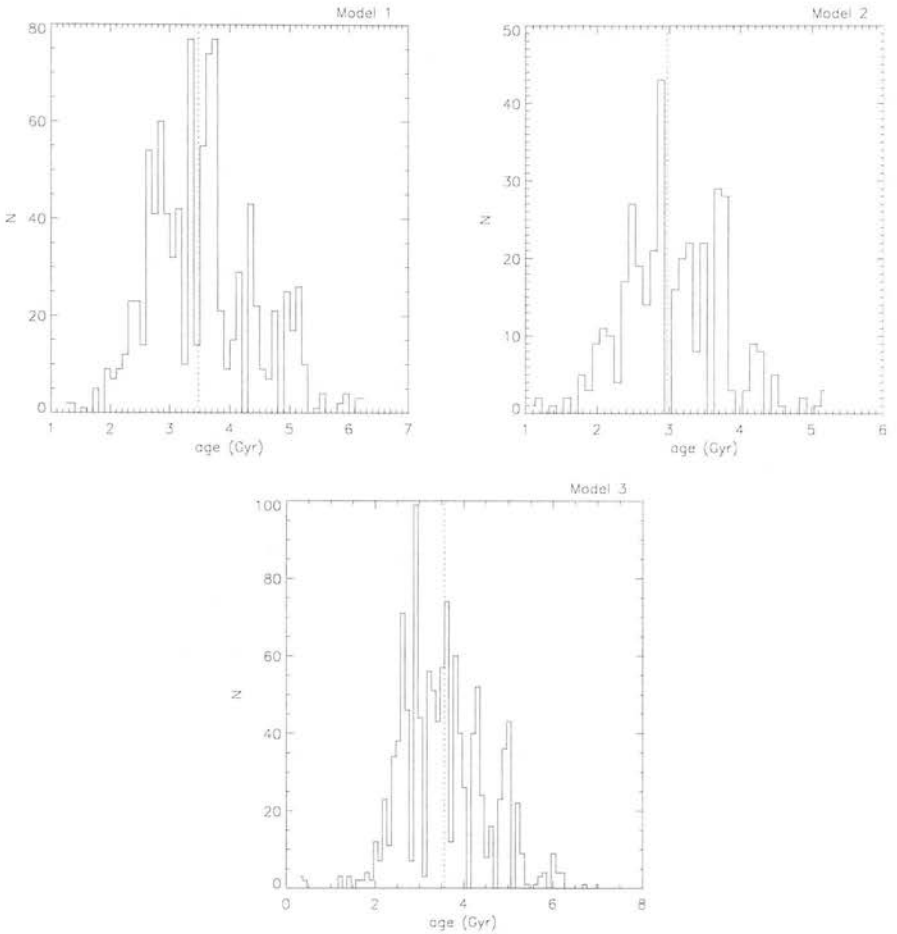

Figure 5.6: Ages of EROs in the three models. The dotted line in each panel gives the median value in each case.

archetypal red galaxy 53W091. Values of $1-2$ Gyr or ~ 3 Gyr are inferred by different groups, using various combinations of photometric measurements and SSP models. Caputi et al. (2005) find that their observed EROs are well fitted by passively-evolving galaxies formed at $z \sim 5$: for the peak in the ERO distribution at $z \sim 1.5$ this gives an age of ~ 3 Gyr. Longhetti et al. (2005) analyse 10 EROs at $z \sim 1.5$, and a combination of spectroscopic and photometric measurements with stellar population models give ages in the range $1-5$ Gyr, with the majority in the range $3-5$ Gyr. The model results seem to tie in nicely with the observations, implying that although they severely underpredict the number of such objects, their internal properties are at least consistent with reality.

model	all EROs ($10^{10}L_{\odot}$)	EROs ($M_{\rm gas} > 0$) ($10^{10}L_{\odot}$)	($M_{\rm gas} = 0$) ($10^{8}L_{\odot}$)
1	1.50(4.30)	2.84(4.83)	3.74(3.06)
2	1.20(3.42)	3.11(3.70)	4.74(3.54)
3	1.75(6.50)	3.15(7.50)	3.75(3.09)

Table 5.2: Median far-IR luminosities of EROs in the three models, categorised by their gas content. Standard deviations are given in brackets.

5.1.7 IR properties of EROs

Given that a good fraction of EROs appear to be dusty, star forming young galaxies, one would expect them to have high far-IR luminosities. As in the previous chapter, I define the far IR-luminosity as the integral over the SED of the galaxy in the range $8 - 1100$ μm. In Table 5.2 I give the mean far-IR luminosities of all EROs in a 1 deg^2 survey for the three models. As a number of objects in each survey have exceeded the truncation limit and hence lack gas, I give median values for all EROs, those with cold gas and those without. In Figure 5.7 I show the distribution of luminosities in model 3 for those with cold gas (for brevity, I only show results for this, the best model). The most surprising result is the relative lack of far-IR emission in those objects with cold gas present. HR10, the archetypal ERO has an inferred far-IR luminosity of $L_{\rm FIR} \sim 9 \times 10^{12} L_{\odot}$ (Greve, Ivison and Papadopoulos 2003). Given that this object is also luminous in the submillimetre, it might be argued that this particular galaxy is rather extreme, and may not be representative of the population as a whole. Based on radio observations of 11 dusty EROs, Smail et al. (2002b) derive a median value of $L_{\rm FIR} = 10^{11.9\pm0.3}$ $L_{\odot}$, assuming that the far-IR/radio correlation holds at high redshift. Based on this, it then seems that the model EROs are systematically too faint in the IR. As can be seen in Figure 5.7, few galaxies have luminosities in excess of 10^{11} $L_{\odot}$. This discrepancy is again likely due to the truncation process. Two factors are at play here: the gas reservoir not only provides the fuel for star formation, it is the source of the dust that produces the FIR emission. It seems probable that massive, dusty galaxies are being preferentially removed from the simulations.

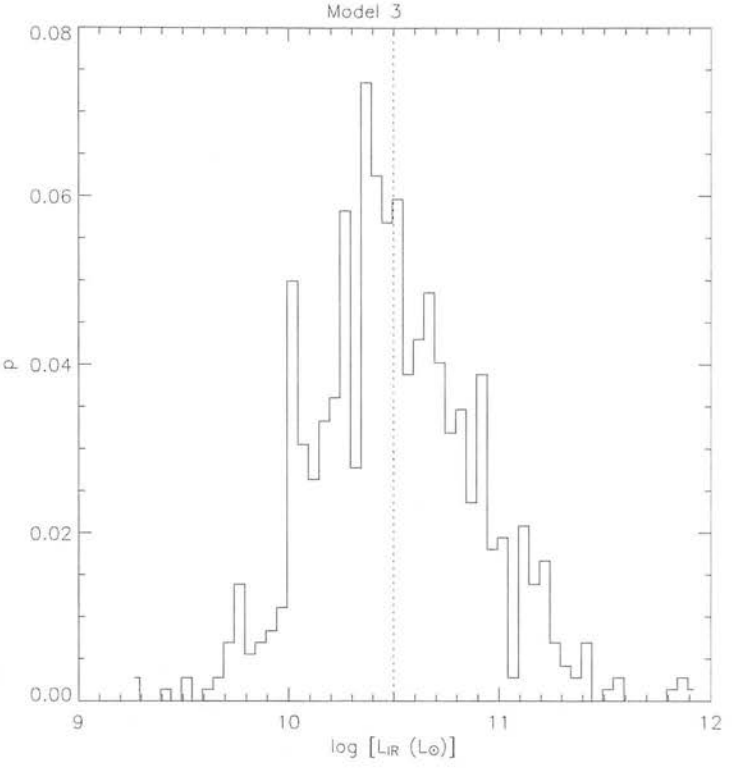

Figure 5.7: Far-IR luminosities of EROs (with cold gas reservoirs) in model 3. The dotted line gives the median value for this subset of objects.

5.1.8 What is the eventual fate of EROs?

As in the last chapter, I now discuss the descendants of EROs, using the full simulation box at $z = 0$. Median values of the rest-frame K-band magnitude and stellar masses are given in Table 5.3, and distributions of the magnitude, stellar mass and bulge-to total ratio are shown in Figure 5.8. A reasonably large proportion are now $L > L_*$ galaxies, and have correspondingly large stellar masses. Although discs again predominate, a reasonable number are elliptical in nature, and given the overall small fraction of ellipticals, this is gratifying. Model 2 predicts the most 'extreme' ERO descendant properties, but given that they are so rare in this model, I do not take this as a vindication for that particular model. It seems that any discrepancies between model EROs and the predicted properties of their descendants (ie. massive ellipticals) is not only due to the lack of such objects at high redshift, but shortcomings of the model in the local universe as well. Figure 5.9 shows

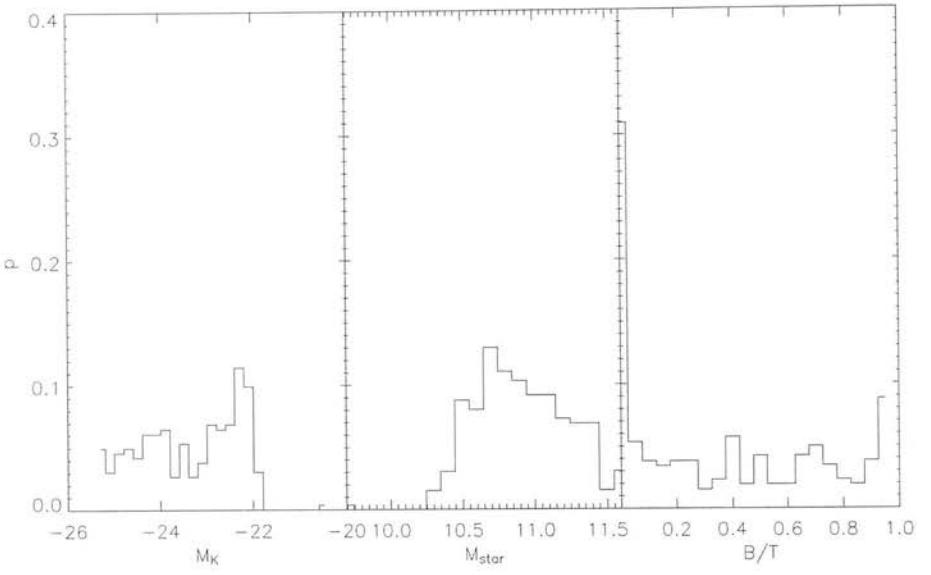

Figure 5.8: Properties of ERO descendants in model 3. Left-hand panel: distribution of rest frame K-band magnitudes. Middle panel: Distribution of stellar masses. Right-hand panel: distribution of bulge to total light ratio.

model	M_K	$M_{\rm star}(10^{10}\ M_\odot)$
1	−23.4(1.0)	9.4(9.5)
2	−23.8(0.9)	11.2(9.1)
3	−23.2(1.0)	8.8(9.5)

Table 5.3: Properties of ERO descendants in the three models. Median values are given together with the standard deviations in brackets.

an example merger tree of the descendant of an ERO, with the red dotted line showing the time of observation as an ERO. The galaxy has undergone a complicated merging history, with the vast majority of the halo mass already in place before $z = 1$.

5.1.9 Distant Red Galaxies (DRGs)

A subclass of EROs are the distant red galaxies (DRGs, eg. Papovich et al. 2006, Webb et al. 2006, van Dokkum et al. (2006). Lying at higher redshifts than the main population of red objects ($2 \simeq z \simeq 3$), they tend to be selected on

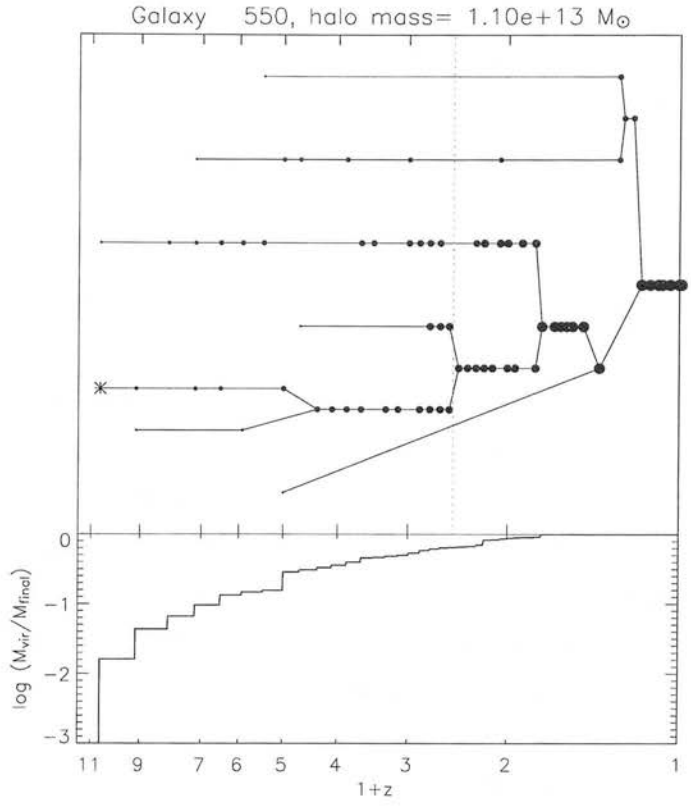

Figure 5.9: Example ERO merger tree from model 3. In the top panel, each circle represents a merging event, with the size of the symbol proportional to the mass of the halo. The cross shows the most massive progenitor. In the bottom panel I show the fraction of the final mass assembled in all progenitor haloes as a function of redshift.

the basis of their near-IR colours, with $(J-K)_{\rm Vega} > 2.3$ being a popular choice of colour cut. This corresponds to red rest-frame optical colours, implying old stellar populations and/or a large degree of dust extinction present in the galaxies. They tend to be massive ($> 10^{11}\ M_{\odot}$), and their ubiquity at such high redshifts (along with less red galaxies of similar K-band magnitude) presents problems for most semi-analytic models of galaxy formation (eg. Fontana et al. 2003, Daddi et al. 2004). Unsurprisingly, such massive galaxies at high-z are strongly clustered, with correlation lengths in the region $r_0 \sim 9{-}17\ h^{-1}$ Mpc (Daddi et al. 2004).

As I have shown, my model sorely underpredicts the number of massive objects at high redshift, so reproducing the properties of DRGs is likely to be

	N (arcmin^{-2})	$\langle \mathscr{R} \rangle$ (mag)	$\langle (J-K)_{\rm obs} \rangle$ (mag)	$\langle (U-V)_{\rm rest} \rangle$ (mag)	% ERG	% LBG
vD06	0.735	25.9	2.2	0.41	23	9
model 1	0.083	24.66	1.98	0.24	15	16
model 2	0.057	24.53	2.02	0.21	11	13
model 3	0.079	24.81	2.07	0.23	24	12

Table 5.4: Comparison between models and van Dokkum et al. (2006)

difficult. Nevertheless, it will be useful to see if such objects are predicted at all, irrespective of their relative abundances.

van Dokkum et al. (2006, vD06) present a study of 294 galaxies with inferred masses in excess of $10^{11}\ M_{\odot}$ in the redshift range $2 < z < 3$ over four independent fields with a total area of ~ 400 arcmin^2. The mean number density is thus 0.71 arcmin^{-2}, but with significant field-to-field variations (highlighting the effects of cosmic variance in small-scale regions of sky). As a comparision, I select galaxies in the same manner from a mock 1 deg^2 survey (choosing the large survey size to get a statistical number of rare high-mass objects). The predicted number densities are roughly an order of magnitude less than expected, with model 3 again faring the best. Table 5.4 presents a comparison of model results for these galaxies with the findings of vD06.

Not only are massive galaxies at high redshift lacking in the models, they are bluer in both observed frame near-IR and rest-frame UV-optical. They are also slightly underluminous in the far IR: Knudsen et al. (2005) estimate a median FIR luminosity of $\sim 10^{12}\ L_{\odot}$ for DRGs; the model predictions are $6.69 \times 10^{11}, 6.81 \times 10^{11}$ and $6.98 \times 10^{12} L_{\odot}$ for models 1, 2 and 3 respectively. Due to their comparitively high redshifts, only ~ 1 % of the galaxies reside in haloes with $V_c > 300$ kms^{-1}, so truncation and the associated loss of gas is not to blame here. The models find far smaller fractions being classified as DRGs, yet roughly the correct proportion of LBG detections. It seems that the models systematically underpredict both the numbers and properties of distant red galaxies.

Webb et al. (2005) present a survey of DRGs with $K_{\rm AB} < 23.2$ ($K_{\rm Vega} < 21.29$) in the redshift range $1.5 < z < 2.5$. They find 79 sources in the extended Hubble Deep Field South, an area of 100 arcmin^2, giving a number density of 0.79 arcmin^{-2}. The models predict number densities of $0.024, 0.018$ and

0.025 arcmin^{-2}, falling short of reality by a factor ~ 30. Using *Spitzer* observations they find that 65 % of the sources are detected at $S_{24\mu m} \simeq 40$ μJy. Note that in this redshift range rest-frame polychromatic aromatic hydrocarbon (PAH) features are shifted into the range of the filter. My galaxy models do not calculate emission from PAH features at present (although their inclusion is possible), and thus I do not expect to detect the model galaxies at a similar level. Indeed, the mean fluxes are $\langle S_{24\mu m} \rangle = 0.99, 1.05$ and 1.11 μJy for models 1, 2 and 3 respectively. It is clear that if future studies are going to include comparisons with *Spitzer* data at high redshift, the inclusion of PAH features in the models is a must.

5.2 Submillimetre sources

I now go on to study the submillimetre emission of galaxies at high redshift. The results presented so far are not encouraging: the models clearly lack massive galaxies at early times, and since the light cones are created entirely from relatively small 'fair samples' of the universe they will lack any of the large overdensities that SMGs and EROs are presumed to inhabit, given their either inferred or measured strong clustering. Nevertheless, I will proceed as before and present global properites of SMGs in the models before moving on to more detailed studies of the galaxies themselves.

5.2.1 Submillimetre number counts

As in the previous two sections, my first test of the models involves comparing the predicted number counts with observational results. For each model I create 20 mock 1 deg^2 surveys. For each, the cumulative number count in flux bins (ie. the number of galaxies brighter than the flux in question) is calculated. The results are shown in Figure 5.10. The solid red line shows the median at each flux value over the 20 mock surveys, and the black lines show the standard deviation at each value. References for the datasets can be found in Figure 1.4.

Every model drastically underpredicts the number of bright submillimetre sources at every flux band where data is available. The slope steepens with brightness in every case, a clear signature of small number statistics. This is observed in the data: Eales et al. (2000) and Barger et al. (2000) find a

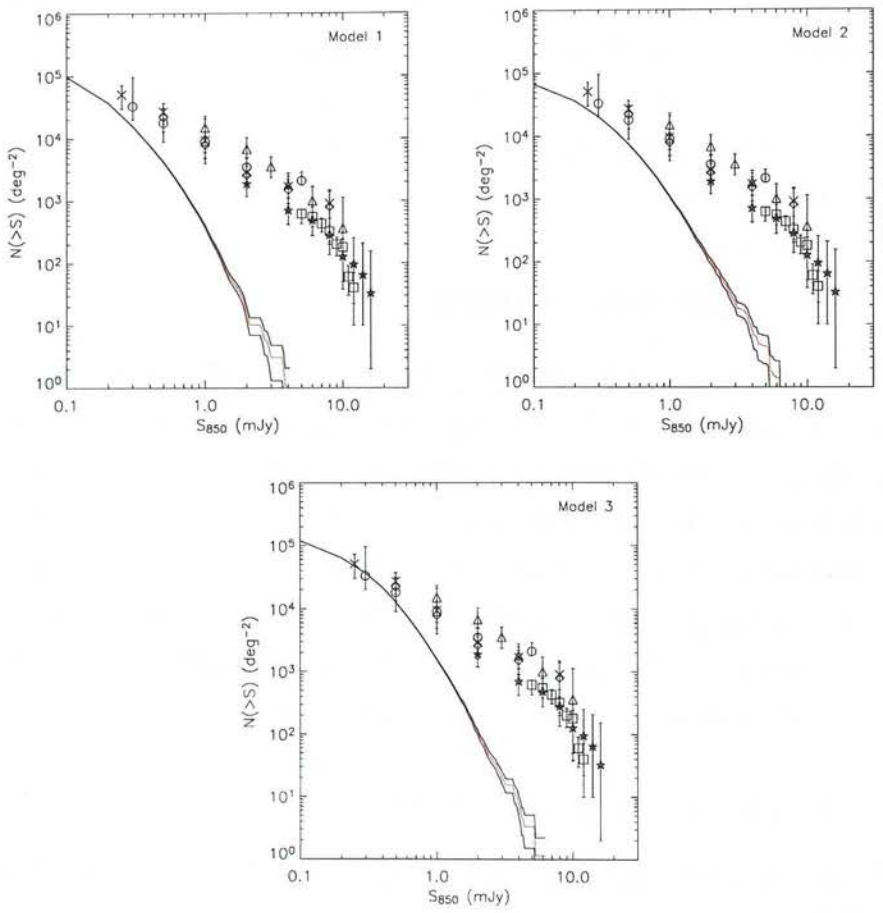

Figure 5.10: Cumulative submillimetere number counts for models 1, 2 and 3, compared with a variety of observational datasets. See figure (1.4) for symbol references. In each panel the red line represents the median count (over 20 mock surveys) in each flux bin, and the solid black lines give the standard deviation in each bin.

steepening of the source counts at bright flux levels, due to the small survey areas. Of course, the models are based on surveys some orders of magnitude larger than most of those presented in the literature, but the lack of significantly overdense regions in my simulation box could manifest itself in much the same way: the brightest sources are presumably located in the densest regions at a given epoch, which the models completely miss.

The number counts of model 1 are particularly poor, over an order of magnitude lower than expected at 1 mJy and around *three* orders of magnitude lower at 2 and 4 mJy, where I run out of bright sources. Note the large variation at the 'bright' end of the model number counts, a manifestation of the scarcity of the sources.

Recall that models 2 and 3 both include a modification to the dust emissivity beyond 100 μm. Baugh et al (2005) found that such a scheme gave a better fit to their model submillimetre number counts, and the same is true for my models (although 'better' is definitely a relative term here!). At 1 mJy model 2 has around an order of magnitude less sources than predicted, and this falls to two orders of magnitude by 3 mJy. The brightest sources in model 2 are ~ 6 mJy, an improvement on model 1 but still a good deal fainter than many of the brightest observations, not withstanding their extreme scarcity. Nevertheless, it is worth proceeding with the study, to quantify whether the objects are simply too rare, or whether their physical properties are inconsistent with 'real' SMGs.

As before, it is again worth emphasising the lack of overdense regions in the mock surveys. Although an unambiguous measure of SMG clustering is not yet available, it seems likely that it is strong (eg. Scott et al. 2002, Webb et al. 2003). The surveys again may be lacking the regions in which SMGs are most likely to be found, and this must be borne in mind when interpreting the number counts presented here.

5.2.2 The redshift distribution of SMGs

Given results for the model number counts, I now quantify exactly *where* the sources in question lie. In Figure 5.11 I show the redshift distributions for the three models. In each plot, the top panel shows all galaxies with $S_{850} \geq 0.1$ mJy, and the bottom panel shows the subset of sources with 'bright'

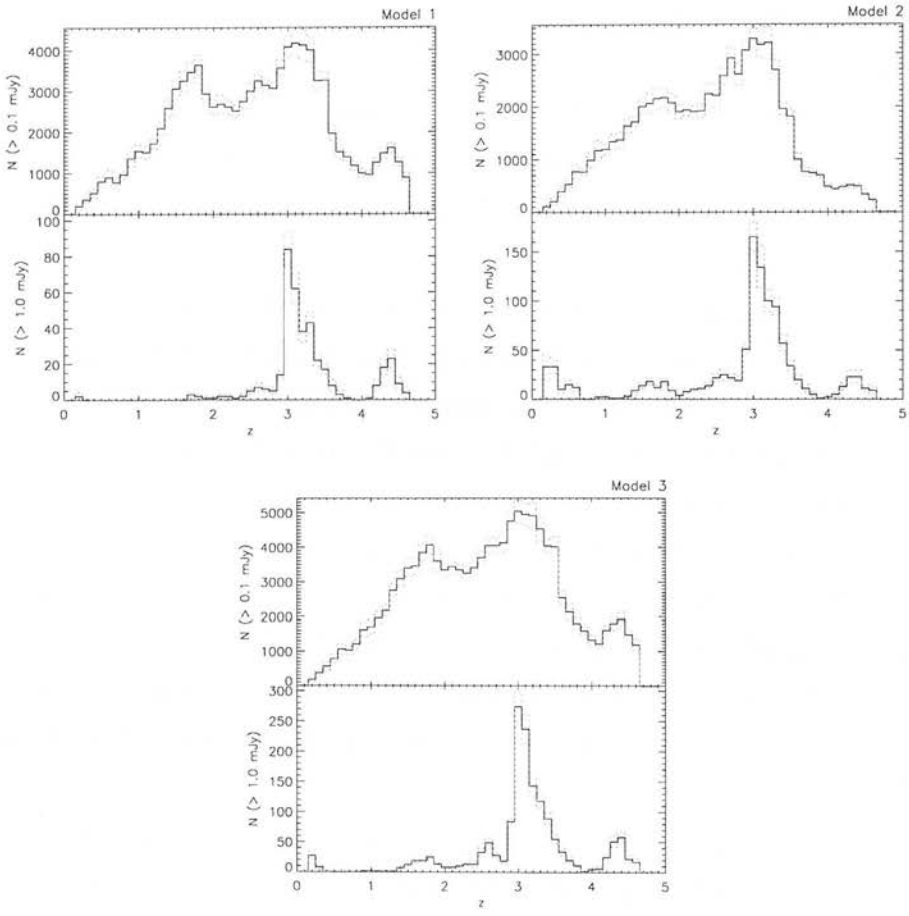

Figure 5.11: Redshift distributions of SMGs in model 1 (top-left), model 2 (top-right) and model 3 (bottom). In each case, the top panel includes all sources with $S_{850} \geq 0.1$ mJy, and the bottom panel only those with $S_{850} \geq 1$ mJy. The solid histogram gives the median number in each redshift bin, and the dotted histograms the median+standard deviation in each bin.

fluxes ($S_{850} \geq 1$ mJy). Considering the top panels first, it is obvious that faint sources can be found over a very wide redshift range, eventually peaking at $z \sim 3$. More interesting is the redshift distribution of the bright SMGs, which show a prominent peak at $z \sim 3$ in all the models. Note that a small number of very local, overly-bright (see Figure 2.12) submillimetre sources have been removed from the analysis, to avoid skewing the number counts. Although all the models lack very bright SMGs in the usual sense, it is nevertheless clear that they are extreme objects *in the context of the models*. With this in mind, it is tempting to associate these objects with the SMGs of the real world. Gratifyingly, the models predict a peak in the redshift distribution not too dissimilar to the observed peak at $z \simeq 2.4$ (Chapman 2003a).

5.2.3 The parent haloes of SMGs

In Figure 5.12 I show the properties of haloes housing bright ($S_{850} \geq 1$ mJy) SMGs. The median and standard deviations for the mass and circular velocity in each model are available in Table 5.5. The median halo mass is close to $10^{12} M_{\odot}$ for all the models, reasonably massive given the peak in the redshift distribution at $z \sim 3$.

Somerville (2004) finds that the number densities of SMGs can easily be accommodated by $10^{13} M_{\odot}$ haloes. My median halo mass is a factor 10 smaller than this, but one must bear in mind that the model SMGs are not as extreme as those observed in reality (we shall see in due course that they are considerably less massive than expected), and so could be housed in small haloes. The virialisation criterion for haloes in the model will also reduce the median halo mass by splitting large structures into sub-components if required.

Notice that the circular velocity of the haloes are below 300 kms^{-1} in all cases, below the crucial truncation limit. If they exceeded this value, the gas would be stripped from the galaxy and the source for the submillimetre emission would vanish. This should be seen as a major shortcoming of the model: the method of truncation required to curb the excess of bright galaxies at low redshift is severely hampering any given model's ability to produce similarly massive galaxies at high redshift. There is absolutely no reason to suppose that SMGs do not inhabit haloes with circular velocities in excess of 300 kms^{-1}; indeed it seems likely that such massive haloes (the most overdense regions

of the universe at such early times) will house these extreme objects. Using observationally-constrained analytic simulations, Shu, Mao and Mo (2001) predict that the mean circular velocity of haloes housing SMGs is ~ 350 kms^{-1}, well in excess of what the models predict. Of course, there are two caveats here: the model predictions for SMGs are severely lacking in terms of number counts and individual source brightness, so the comparison may not be a fair one. The other concerns the way haloes are treated in my models: Large, unrelaxed haloes are split up into individual overdense, relaxed subhaloes. Thus the given halo V_c and hence mass housing a given object may be expected to be smaller in the models than predicted.

5.2.4 Properties of SMGs

Despite the clear failure of the models to account for the number counts of SMGs, I now go on to study the brighter sources predicted by the models. Despite the shortcomings of the model, these sources are 'extreme' in comparison with the majority of galaxies in the simulations, and it is worthwhile comparing these with classical SMGs: they may well be equivalent objects, just far rarer and fainter than expected. From now on, in context to model results I use the term SMG to mean all those with $S_{850} \geq 1$ mJy.

Observed K band magnitudes

In Figure 5.10 I plot the observed K-band magnitudes of all SMGs in models 1, 2 and 3. Each galaxy is colour-coded by redshift: black for those at $z < 1$, green for those in the range $1 < z < 2$, blue for those with $2 < z < 3$ and red for sources lying beyond $z > 3$. There is the slightest hint of increasing submillimetre flux with K-band luminosity, but the scatter is very large. Model 2 shows the population of low redshift, K and submillimetre luminous galaxies seen in Figure 5.11. The longer star formation timescale allows significant star formation at later times due to the larger gas fractions, which through extinction contributes to the far-IR flux.

The spread of observed magnitudes corresponds reasonably well to those found for optical/near-IR counterparts of SMGs (eg. Fox et al. 2002, Ivison et al. 2002). Note however that a good proportion of the model galaxies (those with $K < 22$) would be hard to detect in reality.

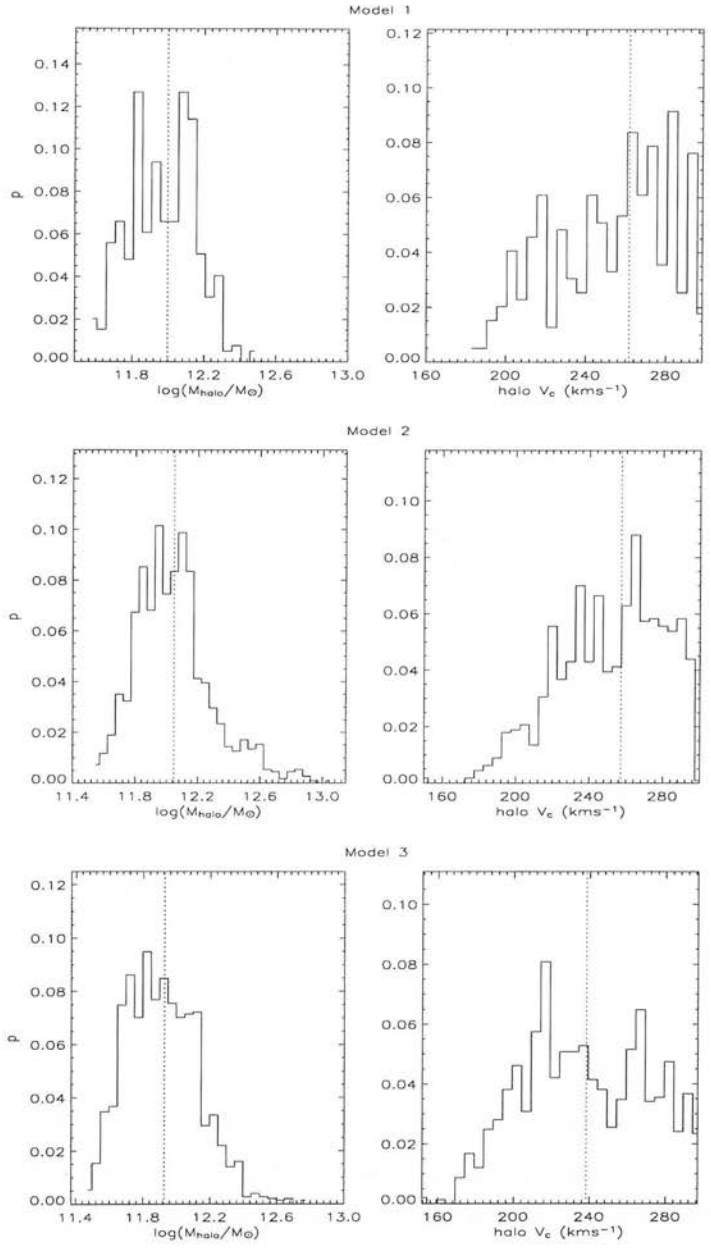

Figure 5.12: Parent halo properties for SMGs in models, 1 (top), 2 (middle) and 3 (bottom plot). Left hand panel: histogram of halo masses. The dotted line gives the median value. Right hand panel: histogram of halo circular velocities. Again, the dotted line gives the median value.

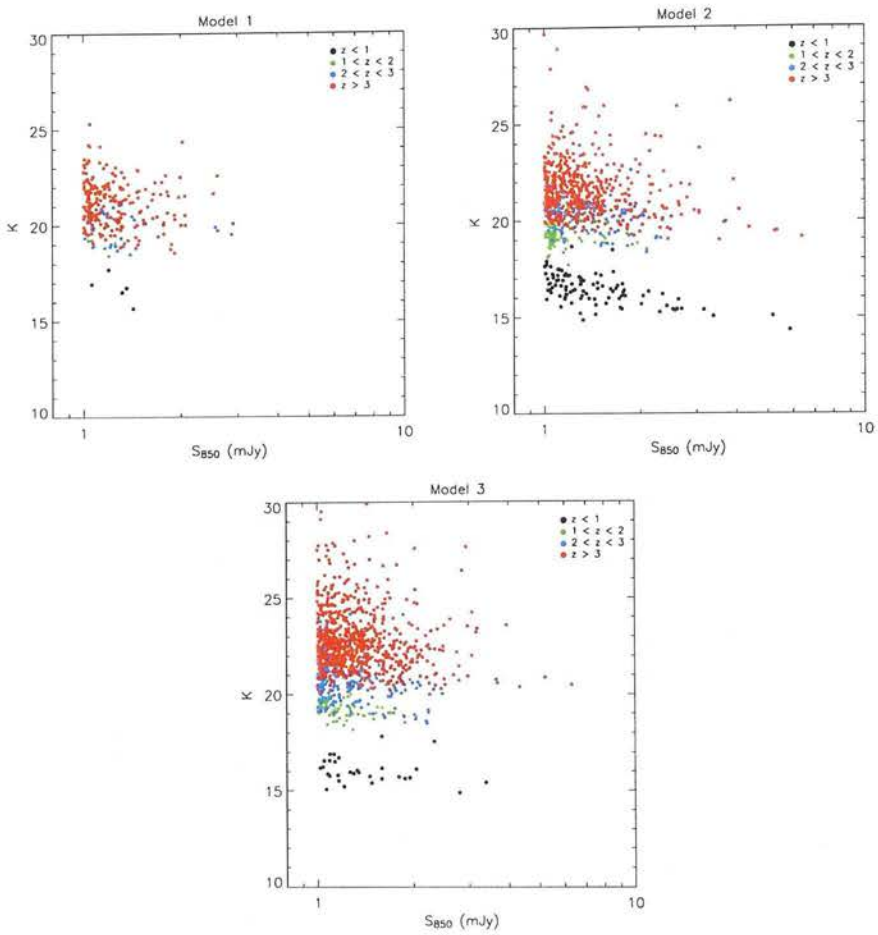

Figure 5.13: K-band magnitudes of SMGs in the models. The galaxies are colour-coded by redshift.

Stellar masses of SMGs

In the top panels of Figure 5.14 I show the predicted stellar masses for SMGs in models 1, 2 and 3 respectively . The majority of galaxies are in the range $0.3 - 10 \times 10^{11} M_{\odot}$, among the most massive galaxies for a mean redshift of 3 (see Figure 4.6). There is a small tail of low-mass sources in two of the models. How does this compare with observations? Using the IRAM Plateau de Bure Interferometer (PdBI), Genzel et al. (2003) infer a dynamical mass of $\geq 3 \times 10^{11} \sin^{-2} i h^{-1} M_{\odot}$ for the bright submillimetre galaxy SMMJ02399-0136 by virtue of its CO emission, the majority of which is expected to be stars. Genzel et al. (2004) observed CO emission in a sample of 7 SMGs using the IRAM Plateau de Bure Interferometer. The median redshift of the sources

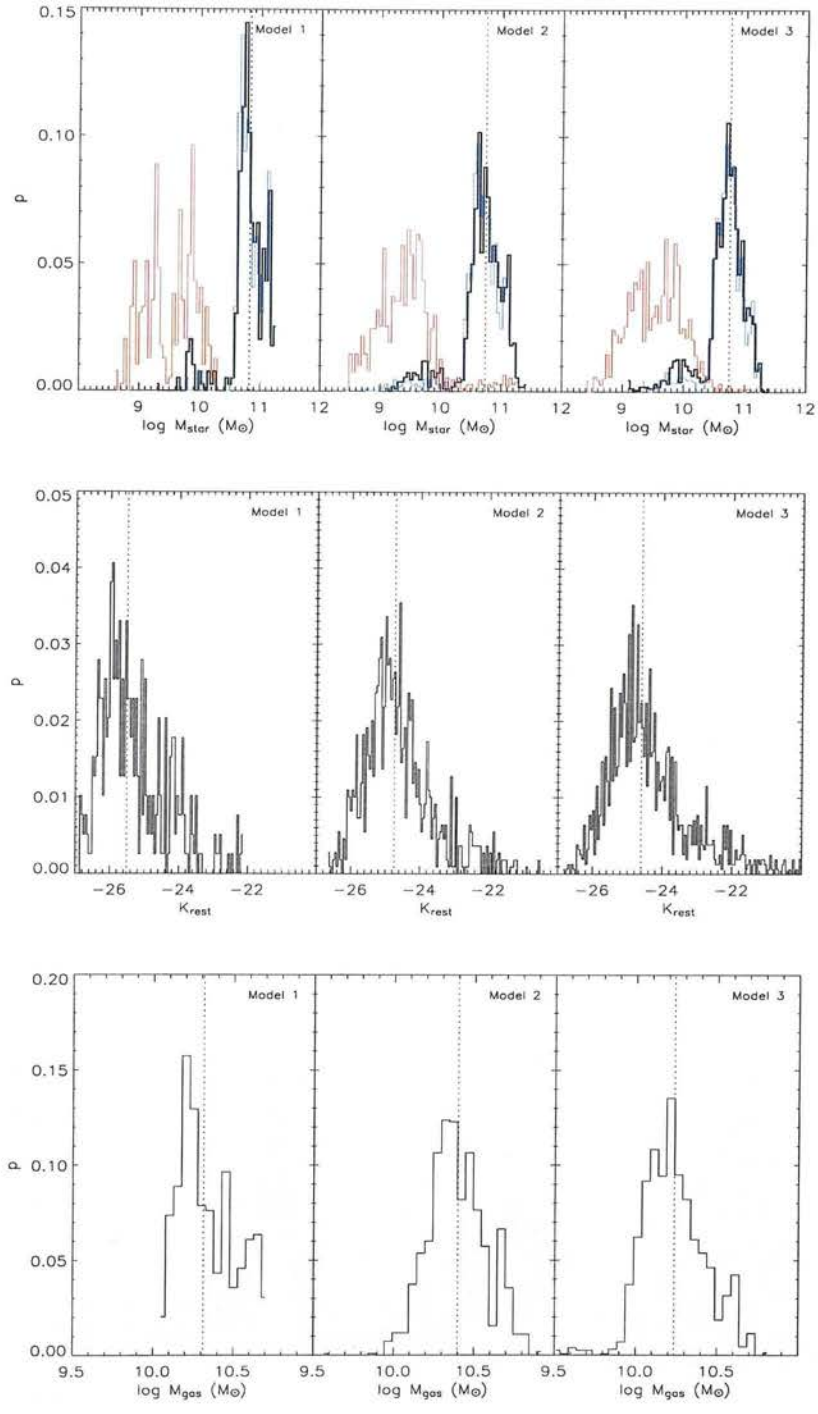

Figure 5.14: SMG properties in the three models. Top panels: the stellar mass of SMGs in models 1, 2 and 3. The black histogram gives the total mass, and the blue and red histograms give the masses of the disk and bulge components respectively. Middle panels: rest frame K-band magnitudes. Bottom panels: cold gas masses. Median values are available in Table 5.5.

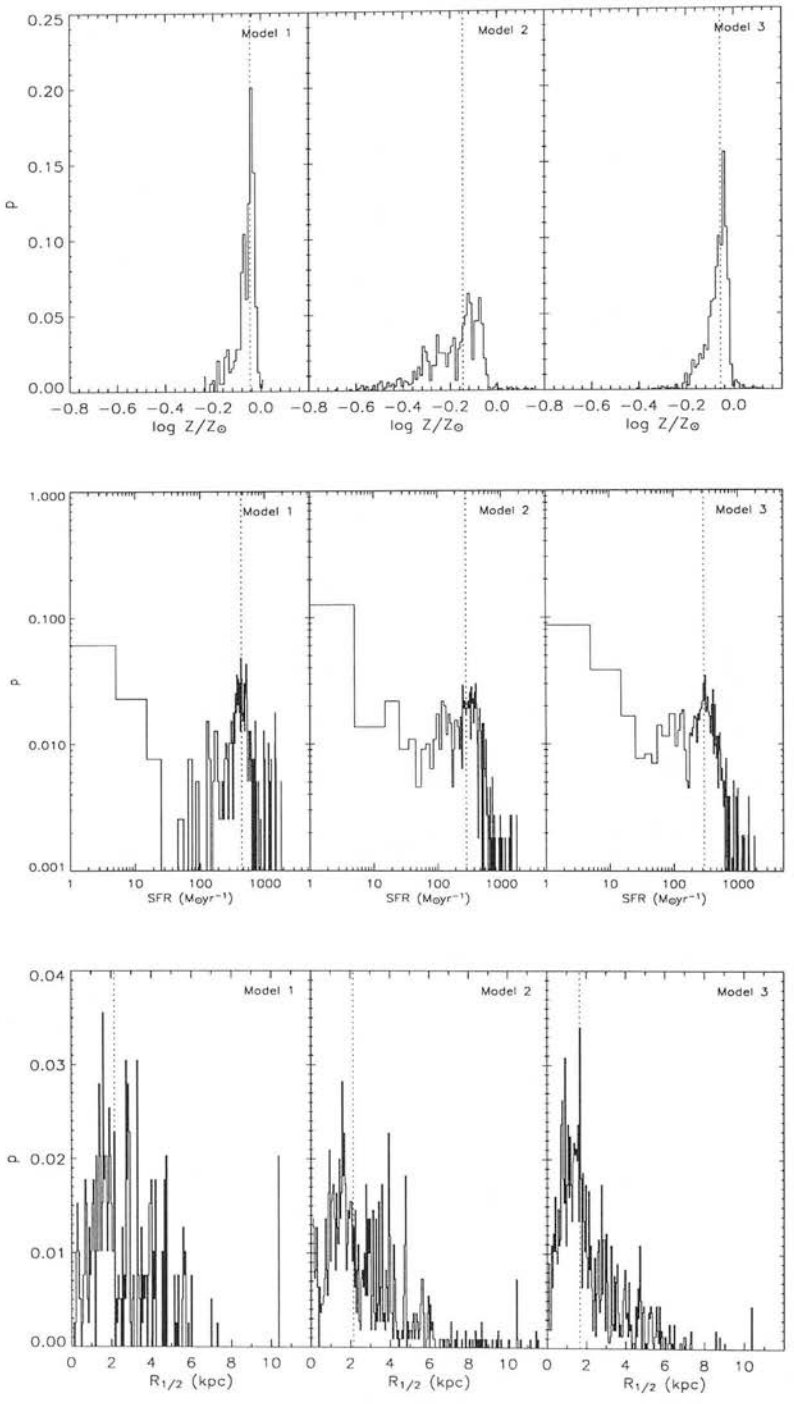

Figure 5.15: Further SMG properties in the three models. Top panels: the cold gas metallicity of SMGs in models 1, 2 and 3. Middle panels: Star formation rates (averaged over the last 100 Myr). Bottom panels: mass-weighted half-mass radii. Median values are available in Table 5.5.

is $z \sim 2.4$, and the observed high median velocity dispersions correspond to dynamical masses of $\sim 1-3\times10^{11}M_{\odot}$. In contrast, one of the SMGs observed by Genzel et al. (2003) has an inferred dynamical mass of $4.5\times10^{9}\sin^{-2}iM_{\odot}$, showing that low-mass SMGs can and do exist.

The majority of the stars in the models are locked up in disks, implying that the SMGs as a whole have undergone little in the way of *major* merging. Nevertheless, in all cases virtually all of the sources have undergone some king of merger event in the past Gyr, so this does not necessarily mean that a merger origin for SMGs is not compatible with the models. It appears that the majority of mergers in the simulation boxes are in fact classified as minor (using a standard value for the major/minor merger threshold), and this is a problem that needs to be examined in future work. Morphological studies of SMGs show many irregular, highly structured objects, clear indications of recent merger activity (eg Ivison et al. 2002, Conselice et al. 2003, Smail et al. 2004).

Recall that the typical stellar mass of an L_* galaxy today is $\sim 8\times10^{10}M_{\odot}$ (Cole et al. 2001). The fraction of SMGs with stellar masses in excess of this is $80.0, 56.3$ and 59.1 % for models 1, 2 and 3. This implies that a significant proportion of the model SMGs will end up as $L \geq L_*$ galaxies by the present day.

Rest frame K-band luminosities

In the middle panels of Figure 5.14 I present the rest-frame K-band luminosities for models 1, 2 and 3. The median magnitude for model 2 is significantly less than that of model 1 (and 3), reflecting the relative lack of stars in the galaxies. For model 1, the median magnitude corresponds to a galaxy of $L \sim 4L_*$ (although bear in mind that galaxies dim with time). Smail et al. (2002) find evidence for so-called class II SMGs (those with obvious optical and near-IR counterparts) having colours and brightnesses consistent with $\sim 5L_{K,*}$ ULIRGs.

Cold gas in SMGs

In the bottom panels of Figure 5.14 I show the predicted cold gas masses for SMGs in models 1, 2 and 3. Median values are in the region of $\sim 2\times10^{10}M_{\odot}$ in

all the models, indicating that model SMGs are gas-rich systems. Unsuprisingly, sources in model 2 harbour more gas, due to the relative suppression of star formation. The results compare well with observations: Smail et al. (2002a) infer molecular gas masses of $\sim 10^{11} M_{\odot}$ in a number of SMGs, and Neri et al. (2003) estimate that radio-selected SMGs are gas rich systems, with gas to dynamical masses as high as ~ 0.5. For dynamical masses of $\sim 10^{11} M_{\odot}$, this matches the model results reasonably well. Greve et al. (2004) use PdBI to infer a median molecular gas mass of $\sim 3 \times 10^{10} M_{\odot}$ for a sample of 12 CO-detected SMGs. Although the models are reasonably consistent with observations, the galaxies do seem to be slightly gas-deficient. Larger amounts of gas would lead to greater dust extinction and hence a brighter submillimetre flux. It is likely that if truncation was not an issue, SMGs in large haloes would have larger gas reservoirs and be significantly brighter.

Metallicity of the ISM

Having seen the gas masses present in model SMGs, I now explore the metallicity of the gas. In the top panels of Figure 5.15 I show the predicted cold gas metallicities of SMGs in models 1, 2 and 3. Observations indicate that SMGs have metallicities of $\sim 1-2 Z_{\odot}$ (Bouche et al. 2005 and references therein). The median values are close to solar metallicity in all the models (again slightly less in the case of model 2), reasonably consistent with the admittedly meagre observational constraints.

Star formation rates

The most striking feature of SMGs is their extremely large star formation rates, implied by their extremely high IR luminosities $(10^{12} - 10^{13} L_{\odot}$. Scott et al. (2002) use the far-IR SEDs to estimate SFRs of $> 1000 M_{\odot} \mathrm{yr}^{-1}$ in the brightest SMGs, confirmed in turn by a number of authors (eg Fox et al. 2002, Ivison et al. 2002, Chapman et al. 2004). Traditional estimates of dust-corrected UV luminosity (closely linked to the SFR) significantly underestimates the IR luminosity (eg Chapman et al. 2000, 2005), implying that UV-based SFR estimates are not reliable indicators of the conditions present in SMGs. Neither are optical emission line estimates; Simpson et al. (2004) estimate that up to $90\ \%$ of the star formation in SMGs is rendered completely

invisible by dust. Radio observations can also be used to determine the SFR, yielding similar results to estimates employing the far-IR SED (Ivision et al. 2002).

In the middle panels of Figure 5.15 I show the predicted star formation rates of SMGs in models 1, 2 and 3. Median and mean values are available in Table 5.5). Although the models do predict high star formation rates, in general they are not as high as the observations seem to suggest, although many galaxies do have SFRs in excess of $1000 M_{\odot} \mathrm{yr}^{-1}$. Of course, it must be borne in mind that the model SMGs are fainter and less numerous than their counterparts in reality. If there is a correlation between SFR and submillimetre flux, then the model SMGs will be naturally fainter on the whole.

The radii of SMGs

In the bottom panels of Figure 5.15 I show the mass-weighted half-mass radii (over the disk and bulge component) of SMGs in models 1, 2 and 3. They are expected to be reasonably large systems, with radii similar to that of model LBGs but with a significantly larger spread in the range of possible values. This is consistent with the results of Conselice et al. (2004), who find evidence for starburst activity over large regions (the radio-emitting regions span $\sim$ 10 kpc), and Pope et al. (2005), who derive Petrosian radii for SMGs of order 1 arcsec, giving a physical size of ~ 8 kpc for the cosmology used in this thesis.

Dust extinction in SMGs

As before, I use the quantity $E(B-V)$ to quantify how much dust has an effect on the model SMGs. It seems unlikely that the models will match the observations here: the submillimetre fluxes are too low, implying a lesser degree of extinciton than observed in reality. This may be due to the underabundance of gas in the SMGs, and it is likely that the truncation process is removing a number of potentially dusty and massive SMGs from the simulation boxes. Nevertheless, it is useful to calculate the extinction explicitly and see if this informed guess is correct.

The median rest and observed frame extinctions are given in Table 5.5, along with the standard deviations. SMGs are redder than LBGs on average (Table 4.2), in tune with observations (LBGs are less massive and hasve

	z	$\langle M_{\rm star}\rangle$ ($10^{10}M_\odot$)	$\langle M_{\rm halo}\rangle$ ($10^{11}M_\odot$)	$\langle M_{\rm gas}\rangle$ ($10^{10}M_\odot$)	$\langle Z_{\rm gas}\rangle$ ($Z_\odot$)	SFR ($M_\odot$ yr^{-1})
1	3.23(0.65)	6.70(4.24)	9.93(4.65)	2.05(1.14)	0.018(0.002)	433.7/468.7
2	3.01(0.99)	5.76(4.29)	11.1(11.1)	2.60(1.24)	0.014(0.004)	272.5/298.5
3	3.13(0.75)	5.50(3.80)	8.38(6.02)	1.74(0.98)	0.018(0.002)	286.7/297.8

	$\langle r_{1/2}\rangle$ (kpc)	M_K (rest)	V_c (halo) (kms^{-1})	$E(B-V)$ (obs)	$E(B-V)$ (rest)
1	2.15(1.84)	−25.6(1.0)	262.0(30.0)	0.32(0.23)	0.21(0.06)
2	2.38(2.11)	−24.8(1.1)	257.0(28.0)	0.31(0.40)	0.20(0.10)
3	1.63(1.82)	−24.6(1.9)	238.0(34.0)	0.51(0.52)	0.26(0.35)

Table 5.5: SMG properties for the three models

smaller gas reservoirs). But are they red enough? Smail et al. (2004) present rest-frame optical properties for a sample of 96 far-IR luminous galaxies (78 of which are detected in the submillimetre) with a median redshift of $\langle z\rangle = 2.2$. By combining the photometry of the sources with their redshifts, best fit model SEDs are derived for each source, yielding a mean rest-frame extinction of $A_V = 1.70 \pm 0.14$. Given that $A_V \simeq 3E(B-V)$, the model SMGs are clearly not red enough. It seems that a more sophisticated method of truncation will be required to match the reddening properties of the SMG population.

5.2.5 Ages of SMGs

Given their high median redshift, SMGs are expected to be young, active systems. As before, I estimate the age of a galaxy as the time interval between the collapse of the first progenitor halo and the time of observation. The median ages of SMGs are then 1.22, 1.26 and 1.21 Gyr in models 1, 2 and 3, slightly older than the haloes housing LBGs at roughly the same redshift. This should ensure that the SMGs are relatively free of any age-related uncertainties in their properties, although this should only be a significant problem at the mass resolution limit.

5.2.6 IR properties of SMGs

SMGs are among the most luminous objects observed in the universe, and the vast majority of their output is in the far-IR. The models fail to account for the

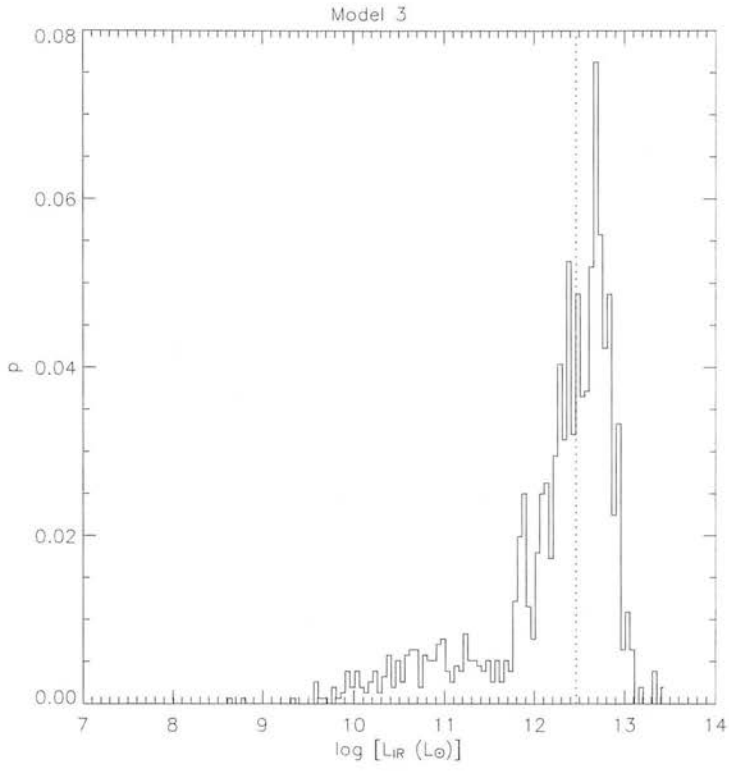

Figure 5.16: Total far-IR luminosities of SMGs in model 3. The dotted line gives the median value.

number of such extreme galaxies found at high redshift, but the properties of the few that do appear seem reasonably consistent with reality. Nevertheless, they tend to be too blue and perhaps lack large enough reservoirs of gas, and this inferred relative lack of dust extinction should also be reflected in lower far-IR luminosities than seen in reality. As before, I define the rest-frame IR luminosity as the integral over the galaxy SED in the range $8 - 1100$ μm. The median values are $4.68, 2.73$ and 2.90×10^{12} $L_{\odot}$ for models 1, 2 and 3 (for completeness, the standard deviations are $4.36, 3.32$ and 3.31×10^{12} $L_{\odot}$). SMGs in models 2 and 3 are fainter due to the different slope for dust emissivity, which boosts the flux beyond 100μm, allowing comparitively less-luminous galaxies to have a high submillimetre flux. In Figure 5.16 I show the distribution of fluxes for model 3 only, given that this appears to give the best results at high redshift.

How do the predictions compare with observations? Smail et al. (1999)

infer $L_{\rm IR} = 10^{12} - 10^{13}\ L_{\odot}$ for the SMGs found in the SCUBA Lens survey. Ivision et al. (2002) do not quote $L_{\rm IR}$ explicitly but their inferred SFRs (actually calculated using the far-IR flux) are consistent with $L_{\rm IR} = 10^{12} - 10^{13}\ L_{\odot}$ as well. More recently, Chapman et al. (2005) estimate a median IR luminosity of $8.5^{+7.4}_{-4.6} \times 10^{12}\ L_{\odot}$ for their sample of 73 SMGs. The model SMGs are thus underluminous in the IR, reflecting their bluer colours and (relatively) small gas masses. Although a large number of sources have $L_{IR} \sim 10^{12}\ L_{\odot}$, there are a number of galaxies with much smaller IR luminosities. The majority of these sources are located at relatively low redshift.

5.2.7 The submillimetre background

The submillimetre background can be quantified by deriving the specific intensity at 850 μm, ie. the total amount of flux recieved per unit area. Smail, Ivison and Blain (1997) derive a lower limit of $\nu I_{\nu} = 20.71$ Jy deg^{-2} down to a limit of 3 mJy. Knudsen et al. (2005) quote a value of 26 Jydeg^{-2} in the range $0.5 < S_{850} < 5$ mJy.

Clearly, the models fall far short of this target: models 1, 2 and 3 yield specific intensities of 0, 0.07 and 0.08 Jydeg^{-2} for $S_{850} \geq 3$ mJy, and 3.06, 5.84 and 9.82 Jydeg^{-2} in the range $0.5 < S_{850} < 5$ mJy. For reference, the entire background (all sources with $S_{850} > 0.1$ mJy) is 21.41, 19.49 and 33.09 mJy for models 1, 2 and 3. Despite the presence of brighter sources in model 2, the specific intensity is less than that of model 1 due to the smaller number of faint sources.

5.2.8 Are SMGs the progenitors of modern-day massive ellipticals?

The phenomenal star formation rates observed in SMGs are sufficent to assemble a massive galaxy in roughly a gigayear, leading to the belief that they are in fact the progenitors of today's massive ellipticals, which display colours consistent with a single, massive burst of star formation in the distant past. As before, I study the descendants of SMGs in the models, and see whether they can shed any light on this hypothesis. Median values of the rest-frame K-band magnitudes and stellar masses are given in Table 5.6, and the distribution of descendant properties in model 3 are shown in Figure 5.17.

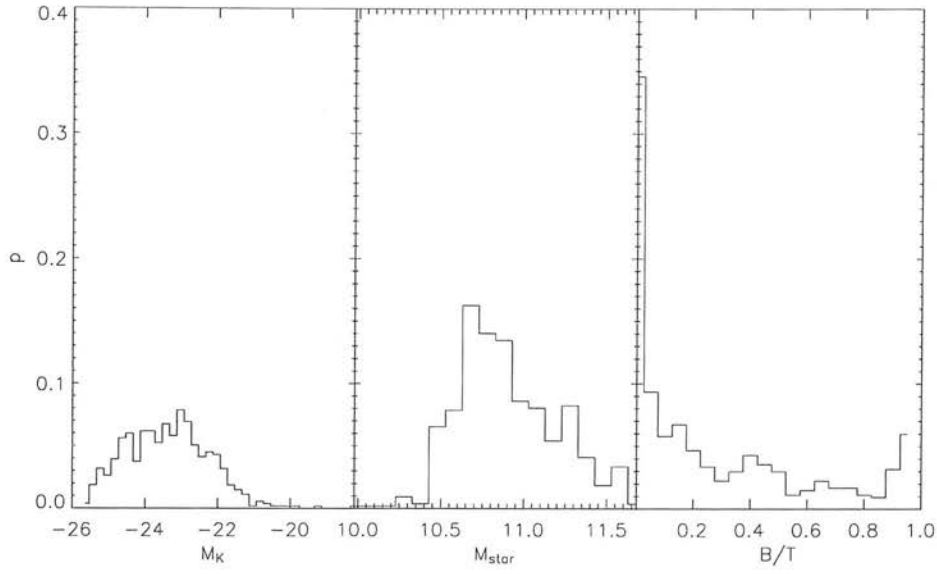

Figure 5.17: Properties of SMG descendants in model 3. Left-hand panel: Distribution of rest frame K-band magnitudes. Middle panel: distribution of stellar masses. Right-hand panel: distribution of bulge to total light ratios.

The eventual fate of SMGs seems roughly similar to that of the EROs, although there is a surprising trend towards slightly fainter, less massive galaxies. Nevertheless, many of the most massive galaxies at $z = 0$ were SMGs at some early time in their life, and many would now be considered ellipticals by virtue of their relative disk and bulge luminosities. Figure 5.18 shows an example merger tree of an SMG, with the dotted line giving its redshift of observation, with a flux of $S_{850} = 2.78$ mJy. The large flux appears to be the result of a large merger event, in which a significant proportion of the final halo mass came together.

Given the lack of both SMGs and local elliptical galaxies in the models, it is clearly too early to come to any conclusion regarding the two populations as different stages in a common evolutionary history. The hypothesis is by no means ruled out, but significant improvements to the model will be necessary to accurately determine whether it is the case.

model	M_K	$M_{\rm star}(10^{10}\ M_\odot)$
1	−23.1(1.1)	8.8(8.8)
2	−23.3(1.1)	6.9(8.1)
3	−23.3(1.1)	7.9(9.4)

Table 5.6: Properties of SMG descendants

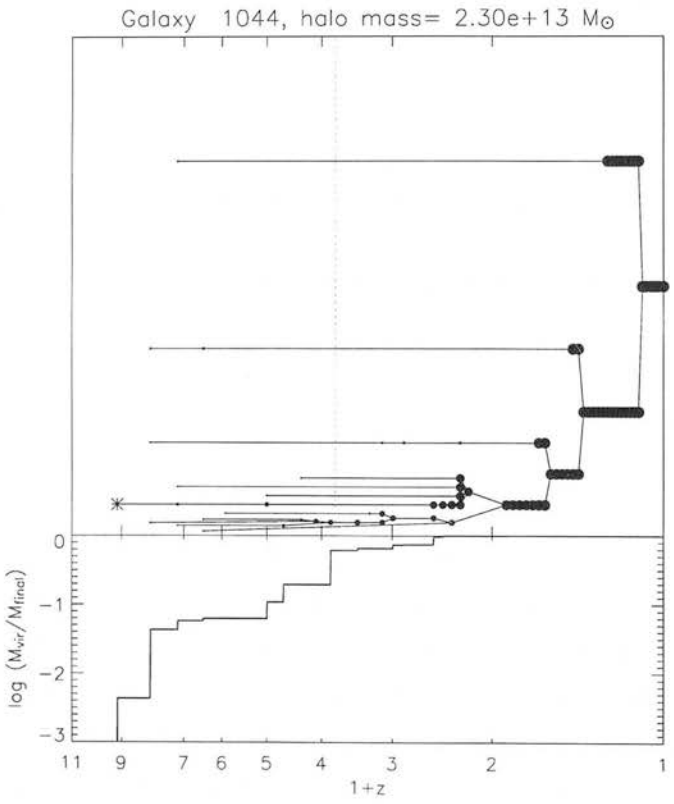

Figure 5.18: Example SMG merger tree from model 3. In the top panel, each circle represents a merging event, with the size of the symbol proportional to the mass of the halo. The cross shows the most massive progenitor. In the bottom panel I show the fraction of the final mass assembled in all progenitor haloes as a function of redshift.

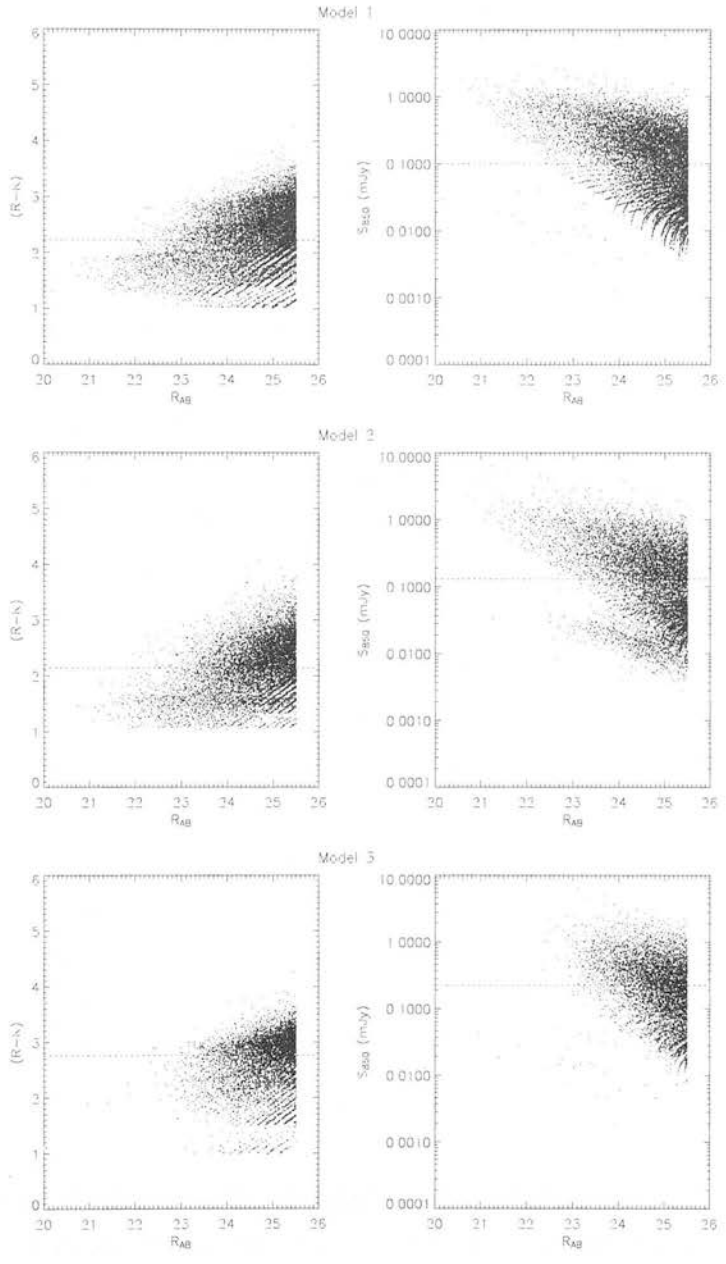

Figure 5.19: Left hand panel: $(R-K)$ colours as a function of $\mathscr{R}$ for LBGs in the three models. Right hand panel: 850 μm fluxes of LBGs in the three models. The dotted lines show the median values.

5.3 Overlaps between high redshift galaxy populations

As we have seen, the early universe is a diverse and interesting place. Given that LBGs appear to be the high-z analogue of 'normal' galaxies, it is natural to wonder if there is any overlap between them and more exotic members of the high redshift zoo, such as SMGs or EROs.

5.3.1 The LBG-SMG connection

A number of studies have been undertaken to try and determine the contribution LBGs make to the far-infrared background, and whether there is any overlap between LBGs and the bright end of the SMG distribution. Peacock et al. (2000) statistically detect the submillimetre fluxes of the bright optical sources in the HDF, yielding a flux of $S_{850} = 0.2 \pm 0.04$ mJy for a source SFR of $1\ h^{-2} M_{\odot}\ \mathrm{yr}^{-1}$. In contrast, Chapman et al. (2000a) study a sample of 16 LBGs with high UV-derived star formation rates ($> 360\ M_{\odot}\ \mathrm{yr}^{-1}$), and detect only one out of 16 sources at an rms level of 0.5 mJy. With an assumed dust model, submillimetre fluxes inferred from the the UV properties of the galaxy overpredict actual S_{850} fluxes by at least a factor 2. Further study on a larger sample by the same authors (Chapman et al. 2000b) yields a mean submillimetre flux of $S_{850} = 0.6 \pm 0.2$ mJy for bright LBGs, implying that they contribute only to the faint end of the submillimetre number counts (< 2 mJy). A few LBGs have moderately bright submillimetre fluxes: Westphal-MMD 11, has $S_{850} = 5.5 \pm 1.4$ mJy and appears to be a system of three distinct objects at the same redshift (Chapman et al. 2002b). In a survey of three seperate deep fields, Webb et al. (2003b) find four LBGs brighter than $S_{850} > 3$ mJy, but derive a mean LBG submillimetre fluxes of 0.382 ± 0.206, 0.414 ± 0.263 and 0 mJy in the three fields.

My results agree well with this conclusion. The mean submillimetre flux of LBGs is $\langle S_{850} \rangle = 0.10, 0.13$ and 0.23 mJy. The right-hand panel of Figure (5.19) shows the submillimetre flux of LBGs as a function of $\mathscr{R}$. There is a clear trend towards bright galaxies having larger S_{850} fluxes, although the scatter is large. A few LBGs have fluxes in excess of 1 mJy, as seen in reality. This also implies that on the whole, the IR fluxes derived for LBGs (section 4.3.6) are also reasonably accurate.

It is clear then that the majority of LBGs are not also masquerading as

bright SCUBA sources. Nevertheless, LBGs may well contribute to the overall submillimetre background. It is estimated that bright SMGs contribute to around $20 - 30\%$ of the S_{850} background (eg. Cowie, Barger and Kneib 2002, Smail et al. 2002), and if there is an overlap between faint (< 0.1 mJy) SCUBA sources and LBGs they may well make up the dominant component of the submillimetre. Adelberger and Steidel (2000) argue that faint LBGs can account for much of the background, assuming a $L_{\rm bol,dust}/L_{\rm UV}$ typical of local starbursts. Observations are generally not deep enough to probe this: Chapman et al. (2000) estimate that bright LBGs contribute to ~ 0.2 % of the submillimetre background, and Webb et al. (2003b) find contributions of $< 20, 16$ and 14 % for their three fields, assuming an even distribution of LBGs in the redshift range $1 < z < 5$. How do the models compare? Altogether, LBGs are responsible for 24.0, 25.4 and 12.2 % of the total ($S_{850} > 0.1$ mJy) submillimetre background in models 1, 2 and 3 respectively. If I move to brighter fluxes, I find a contribution of 61.1, 42.6 and 22.2 % to the background between $0.5 < S_{850} < 5$ mJy. This anomalously large contribution is due to the scarcity of SMGs in the models, and the large variation between models can be attributed to the relative numbers of bright SMGs (more in models 2 and 3) and LBGs (far too many in models 1 and 2). It seems that although the mean flux of model LBGs is roughly correct, there is too large an overlap between the populations, although given the failure at predicting the number counts of SMGs, this is not a surprise.

5.3.2 Are any LBGs red enough to be classed as EROs?

The left-hand panels of Figure 5.19 show the $(R - K)$ colours of LBGs in the three models. It is immediately obvious that none of the candidate LBGs are red enough to be also classed as EROs, irrespective of their K- band magnitude. This is unsurprising: LBGs seem to be galaxies undergoing rapid bursts of star formation near the start of their life, and thus should not have a dominant component of evolved red stars.

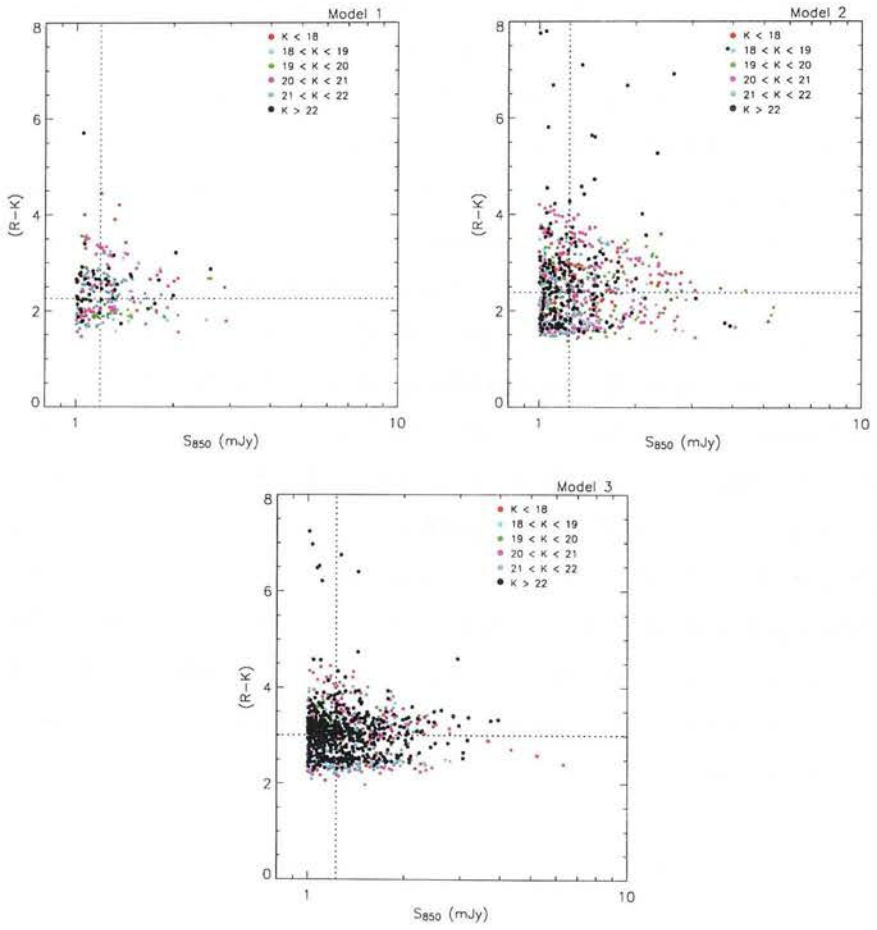

Figure 5.20: $(R-K)$ colours of SMGs in the three models. Galaxies are colour-coded by their (observed) K-band magnitude. The dotted lines give the median submillimetre flux and $(R-K)$ for the sample.

5.3.3 Connections between red objects and submillimetre sources?

Webb et al. (2003) study a sample of EROs ($K < 20.7$, $R - K > 5.3$) with SCUBA and find a mean flux of $\bar{S_{850}} = 0.40 \pm 0.07$ mJy. Selected in the same manner, models 1, 2 and 3 yield mean S_{850} fluxes of $0.06(0.10)$, $0.04(0.07)$ and 0.08 ± 0.34 mJy, with the standard deviations in brackets. This result is strongly affected by the truncation limit: many of the candidates lie in high-V_c haloes and have been stripped of their gas, leaving them with negligible flux in the submillimetre. I can examine this from the other point of view: in Figure 5.20 I plot the $(R - K)$ colours of all bright (> 1 mJy) in the three models. The dashed lines give the median submillimetre flux and $(R - K)$ for the sample. Each galaxy is colour-coded by their K-band magnitude. It is apparent that for the few sources that lie above the threshold for being classed as an ERO, their faint magnitudes render them invisible to the present generation of K-band surveys. This again is at odds with the observations: Ivison et al. (2002) find that roughly 1/3 of SMGs have ERO counterparts with $K < 21$, and Smail et al. find that 43 % of SMGs with $K < 21$ have colours redder than $(I - K) > 4$ (recall that this is roughly equivalent to $(R - K) > 5$).

Given the tiny overlap between the populations, it is no surprise to find that EROs contribute little to the submillimetre background: 0.3, 0.1 and 0.4 % for models 1, 2 and 3 respectively. Given that the ERO contribution to the *bright* end of the SMG number counts is estimated as somewhere between $\sim 10 - 50$ % (eg. Webb et al. 2003a), it is clear that the models fail spectacularly in matching even the lower observational estimates.

Knudsen et al. (2005) image a sample of 18 DRGs in the redshift range $2 < z < 3.5$ from a (usable) 12.8 arcmin^2 region of sky with SCUBA, in an attempt to quantify the submillimetre properties of DRGs. By stacking analysis they obtain a statistical S_{850} detection, yielding a median DRG flux of $\langle S_{850} \rangle = 1.1 \pm 0.28$ mJy. Selecting DRGs in the same manner from a mock 1 deg^2 survey, and find 1917, 717 and 2495 DRGs in models 1 and 2, an order of magnitude less sources per unit area. The median submillimetre flux of the sources are $\langle S_{850} \rangle = 0.12(0.14), 0.13(0.21)$ and $0.18(0.30)$ mJy for models 1, 2 and 3, where the brackets give the standard deviations. The small number

of DRGs predicted by the model are thus too faint in the submillimetre, in many cases due to a lack of gas caused by the truncation procedure.

Although the *direct* overlap between SMGs and EROs is negligible in the models, there is still the possibility that the two classes of object represent different stages in the evolution of a galaxy. With this in mind, I calculate the proportion of SMGs that are identified as $K < 21$ EROs *at lower redshift*, long after the submillimetre-bright phase of their life is over. 33.5, 2.3 and 9.3 % of SMGs are selected in this manner, indicating that for at least some of the model galaxies, bright submillimetere emission and consequent red colours represent two stages in the evolution of that particular source. Given the lack of both SMGs and EROs in the model, this result is encouraging: given proper proportions of the two populations unaffected by the truncation procedure, it is reasonable to hope that this fraction would rise. In Figure 5.21 I show three example merger trees of galaxies with both SMG and ERO phases in their past. Relatively recent merger events seem to be at the root of the bright submillmetre emission, and the later ERO phase occurs when the vast majority of the halo mass has already been assembled, despite the high redshift: evidence of long-standing passive evolution.

5.4 Conclusions

Sadly, the models fare rather badly when trying to account for the more unusual galaxies observed in the high redshift universe, although this is a long-standing problem with many other semi-analytic models in the literature.

It seems likely that the truncation process must shoulder much of the blame here. EROs and SMGs are thought to be amongst the most massive galaxies at a given epoch, and as such should reside in the most massive (high circular velocity) DM haloes. The truncation process as it stands halts star formation in such objects, and is likely depriving the models of a population of extreme objects necessary to flesh out the number counts. Both stellar and gas masses are lower than expected for EROs and SMGs, indicating that a high-tail population of sources is artificially absent. The IR fluxes are surprisingly low too in both classes of object: truncation also removes the cold gas from the galaxy, removing the main source of IR and submillimetre

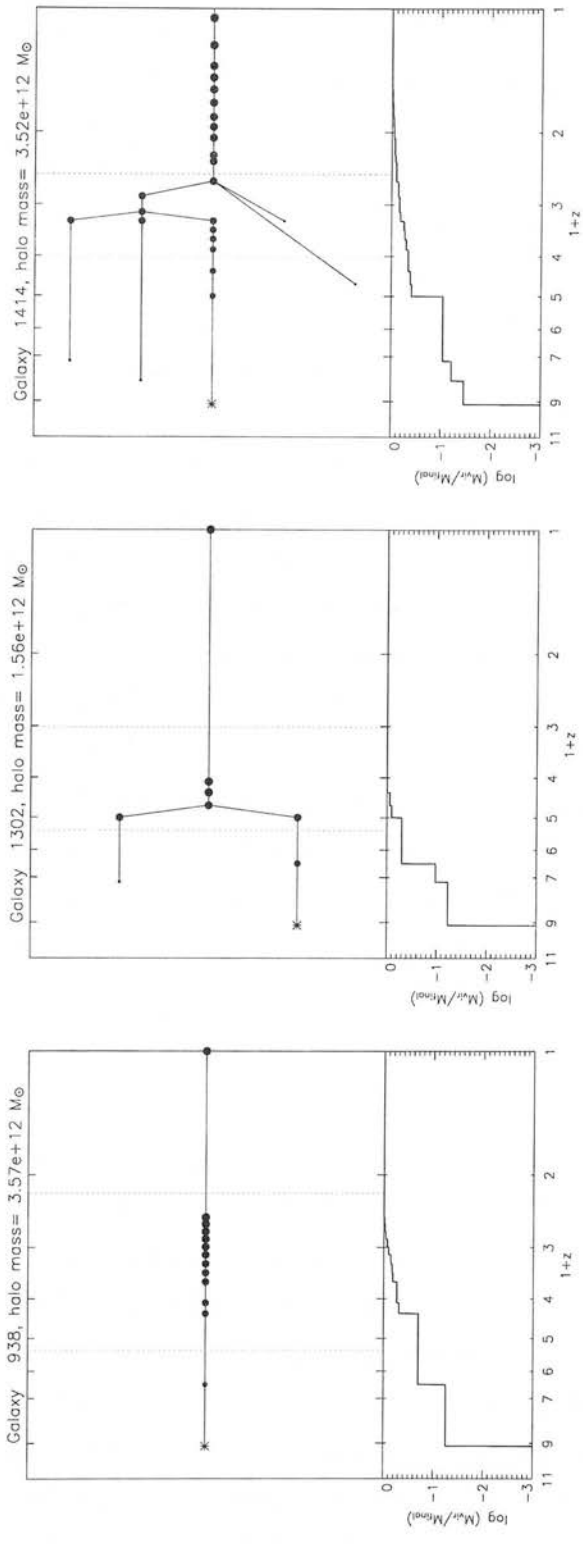

Figure 5.21: Example merger trees of galaxies with both SMG and ERO phases. In the top panel, each circle represents a merging event, with the size of the symbol proportional to the mass of the halo. The cross shows the most massive progenitor. In the bottom panel I show the fraction of the final mass assembled in all progenitor haloes as a function of redshift. The dotted blue line shows the redshift of observation as an SMG, and the red line shows the redshift of observation as an ERO.

emission as well as eradicating the fuel for star formation.

Of course, other factors may be at play as well. The magnitude of dust extinction (modulated by $t_{\rm esc}$) may still be too small: even though a sgnificantly larger value of t_{esc} is used in model 3, this still may not be enough to account for the ERO number counts (since R is probed by the rest-frame UV at the redshifts in consideration). Given that there is still an overabundance of LBGS even in model 3, upping $t_{\rm esc}$ again may be an option. Tuning of other dust-related free parameters may help here as well (eg. $M_{\rm cloud}$, $R_{\rm cloud}$). However, in the next chapter I will show that such adjustments cannot help rectify the discrepancy in the submillimetre.

Finally, it seems overwhelmingly likely that the nature of the simulation box used to construct the light cones is also an important factor in determining the numbers of EROs and SMGs. Both classes of galaxy are thought to be strongly clustered (proven in the case of EROs), implying that they preferentially inhabit overdense regions of the universe. Since the simulation box is designed to yield a 'fair sample' of the universe, a much larger volume will be required to include such statistically rare overdensities. Although mentioned before, it is important to bear this in mind when interpreting the number counts presented in this chapter: it is likely that the models would fare much better if a proto-cluster was present somewhere in the simulation volume. This possibility will be investigated briefly in the next chapter.

CHAPTER 6

Discussion and conclusions

In this chapter I summarise the results presented in this thesis, and outline some improvements that could be made in the future in order to help improve the modelling and hopefully our understanding of the high redshift universe.

6.1 Successes and failures of the model

In chapter 3 I presented the local properties of the universe as derived by the model. I derive good fits to the B and K-band luminosity functions, although I fare rather less well in the IR. The numbers of spirals are overpredicted at the expense of late-type galaxies. Colours as a function of morphology and mass tend to be too red, although the discrepancies are lessened when only the brighter galaxies in the simulation are considered. The star formation history of the universe is consistent with observational results.

In chapter 4 I extended the model to the high redshift universe. The models lack massive and bright galaxies at early times, in common with many other semi-analytic models. Many of the properties of LBGs can be adequately reproduced by the model. Model 3 in particular does reasonably well at predicting the physical properties and number counts of LBGs. An overabundance of faint LBGs is likely down to resolution issues, and a simulation with better mass resolution may help reduce the discrepancy.

In chapter 5 the model is used to predict properties of more extreme objects

at high redshift: EROs and SMGs. Here the models are shown to be inadequate: The number counts of EROs and SMGs are grossly deficient compared to reality. A major problem here is the lack of massive galaxies, likely due to the method of truncation involved. Nevertheless, the few objects that do exist are broadly similar to those seen in reality, although systematically less massive and lacking sufficent dust extinction. Again, model 3 performs the best in this chapter, and could in fact be considered an alternative fiducial model.

6.1.1 The overcooling problem

Perhaps the most acute flaw in the galaxy formation model set out in this thesis is the truncation required to match the local B and K luminosity functions. The simpler models of van Kampen, Jimenez and Peacock (1999) found that resolving halo substructure alone was sufficient to solve overcooling of gas in massive galaxies. Sadly, this is no longer the case in this more complicated refinement of the basic model (in part due to the value of $\Omega_B = 0.06$ used in the paper). As shown in chapter 3, without some method of preventing star formation in the largest haloes the models overpredict the number of bright galaxies observed at $z = 0$ by a considerable margin. Yet this appears to hinder the formation of massive, dusty galaxies at high redshift, and thus fails to produce sufficient numbers EROs and SMGs. As alluded to before, this is not a problem confined to my own models: Benson et al. (2003) among others have shown that when values of Ω_B consistent with the latest results are used, then overcooling becomes a severe problem, and a persistent excess of bright galaxies is produced. They invoked a number of physical mechanisms designed to prevent the formation of these unwanted objects: reheating of cold gas to the hot halo temperature, expansion of the hot gas reservoir (leading to longer cooling times) and expulsion of gas from the halo by 'superwinds'. None of these methods (taken alone or in tandem) are entirely satisfactory at solving the overcooling problem, and it seems that new physics will be neccessary to explain the break at the bright end of the LFs.

A number of authors have suggested that AGN might play an important role in the suppression of cooling in massive haloes, in the form of energy injection into the gas via radio jets (eg. Quilis et al. 2001, Churasov et al. 2002,

Bohringer et al. 2002, Binney 2004), and they are now being incorporated into semi-analytic models.

6.2 The role of Active Galactic Nuclei in semi-analytic modelling

It is now well known that a supermassive black hole resides at the centre of most galaxies with a spheroidal component (eg. Kormendy and Richstone 1995, Richstone et al. 1998). Nuclear activity (both quasar and AGN) is ascribed to the interaction between the central black hole and infalling matter. The observed correlation betweeen black hole mass and the velocity dispersion and mass of its parent spheroid (eg. Magorrian et al. 1998, McLure and Dunlop 2002) implies that the evolution of these distinct classes of object are in some way intimately linked (eg. Haehnelt, Natarajan and Rees 1998). This raises the question: has every galaxy housed an active nucleus at some point in its history? It is known that active nuclei were far more prevalent in the high-redshift universe, and that the cosmic star formation history peaks in tandem with the space density of quasars and starbursts (Boyle and Terlevich 1998, Dickinson 1998). In addition, we have seen earlier that AGN are thought to reside at the centre of a significant fraction of SMGs. It seems natural to assume that most galaxies have undergone a phase of increased nuclear activity at some point in history.

It is clear that AGN play a crucial role in the evolution of the galaxy population, and should be taken into account when constructing realistic models for galaxy formation. Until recently, AGN have been neglected in semi-analytic modelling, in the last few years a number of authors have included preliminary schemes for AGN activity and their environmental influence on their host galaxies.

Kaufmann and Haehnelt (2000) describes the first attempt at including the effects of active nuclei into a semi-analytic model. They suggest that major merger events fuel the growth of black holes, through accretion of gas and mergers of the holes themselves, and a certain amount of the energy involved is reradiated as light. A reasonable fit to the space density and luminosity functions of quasars is derived. They made no attempt to model

feedback resulting from nuclear activity, and had to introduce a rather *ad hoc* cutoff designed to prevent gas cooling in the largest haloes and hence an excess of bright galaxies.

Granato et al. (2004) present an alternative scenario for the formation of SMGs, as an evolutionary stage of quasars and their host galaxies. In their model, standard methods of gas cooling and star formation in DM haloes (drawn from the analytic distribution given by Sheth and Tormen 2002) are augmented by a prescription of black hole growth at the centre of the galaxy. Feedback from supernovae and the central active nucleus heats the interstellar medium, expelling a fraction from the halo and effectively truncating star formation. Radiation drag on the ISM (grains absorbing incident light, causing a force against the particle's orbital motion) causes gas to spiral into the nucleus through viscous drag, powering the central engine.

Supernovae feedback is more efficent at expelling gas in shallow potential wells. Thus the low-mass and late-forming haloes (as the potential well for a halo of given mass scales with its redshift of virialisation) lose the most gas, cutting off star formation. Radiation drag is most efficient in large haloes, resulting in a higher accretion of matter onto the central engine. Thus, high star formation rates and quasar activity are intimately linked, and massive high-redshift galaxies form in an anti-hierarchial manner, as intense bursts of star formation in the most massive haloes. This gives the outward appearance of monolithic collapse, agreeing with observations, while remaining perfectly consistent with the standard hierarchial assemblage of matter in ΛCDM. Combining star formation histories with a self-consistent treatment of dust (GRASIL, Silva 1998) yields successful predictions for K-band luminosity functions, ERO properties and submillimetre number counts. However, no predictions for the local universe are given.

Croton et al. (2006, C06) apply semi-analytic models to the Millenium Simulation, including a two-phase prescription for black hole growth. Of paramount importance is their characterisation of haloes by their cooling properties: *hot static halo* systems and *rapidly cooling* systems. When the mass of hot halo gas exceeds that of the cold gas disk, a static hot halo exists, and material can accrete onto the central object via a cooling flow. This

effect is most pronounced in massive haloes at late times, and is the root of the overcooling problem inherent in most semi-analytic models. Rapidly cooling systems arise when the cooling time is short, causing rapid infall of gas onto the central object, most pronounced in small objects and early times.

In their 'quasar mode', black holes grow through merger events in a similar manner to Kaufmann and Haehnelt (2000). No feedback from this process is modelled. In their 'radio mode', black holes also continously accrete matter from a static hot halo, assuming one exists. The energy created by accretion is a source of feedback, reheating infalling gas and hence depleting the cooling flow by some amount. The strength of the feedback scales with black hole mass, hot gas fraction and circular velocity. The efficiency of this process peaks at the present day, and naturally accounts for the cutoff at the bright end of the local luminosity function: gas cannot cool efficiently in the most massive haloes due to the energy injection from the AGN This renders the most massive galaxies red enough to match observational data (by cutting off star formation at late times). The correlations between black hole mass and host spheroid are well matched. Two physical models for AGN feedback are presented in addition to the phenomenological method, yielding similar results.

Bower et al. (2005) present their own semi-analytic model *avec* AGN treatment, and also apply their models to the Millenium Simulation (with independent and distinct derivations of the halo merger trees). As in C05, feedback only occurs in situations where a static hot halo is present, with gas accreting on the central object via a cooling flow. However, in contrast to C05, feedback does not scale with local conditions, but instead completely cuts off the cooling flow if the energy output of the AGN is sufficent to balance the energy radiated by the infalling gas. Local properties of the universe are well-reproduced by their model, and they also match the evolution of the K-band luminosity function out to $z \sim 2.5$. This is a significant success, producing for the first time sufficent massive galaxies at high redshift, something semi-analytic models struggle to achieve, including the model presented in this thesis. However, the stellar feedback they require is perhaps unphysically strong, in that the energy injection from feedback is in fact higher than that produced by supernovae.

In a similar vein, Cattaneo et al. (2006) implement AGN physics in GALICS, the semi-analytic model of Hatton et al. (2003). They allow star formation efficiency to vary with redshift, and assume that above a certain halo mass shock heating and subsequent heating of the gas by AGN prevents the formation of stars and accretion of gas. This transition occurs only after a given redshift, before which gas can cool and stars can form even in haloes above the critical mass limit. Both the critical mass limit and the transition redshift are free parameters, and they find that $M \sim 10^{12}\ M_{\odot}$ and $z \sim 3$ gives good matches to local luminosity functions and reproduces the bimodality seen in colour magnitude diagrams of early and late-type galaxies.

6.3 Improvements to the galaxy formation model

6.3.1 Truncation

Given the results of this thesis, the ubiquity of supermassive black holes in the universe, and promising results from other authors, it appears that the inclusion of AGN physics is the next major step for the work presented here. This would render the modelling more realistic from a purely aesthetic point of view (ignoring such an important feature of the galaxy population is rather unsettling), but would also give a natural, redshift dependent method of truncation rooted in physical reality and hopefully capable of resolving many of the issues raised in this thesis. In particular, removing the artificial cessation of star formation in massive haloes in favour of a physically motivated, self-regulating feedback mechanism may allow massive galaxy formation at high redshift without the subsequent runaway star formation that can taint the present-day luminosity functions. It seems that the era of hiding one's head in the sand when faced with AGN is drawing to a close: it is a reality that must be embraced.

6.3.2 Halo lifetimes

In its present state, the simulation calculates galaxy properties over the lifetimes of each individual halo. In essence, each galaxy evolves on its own grid of timesteps. It is possible that the properties of a galaxy are thus influenced slightly by the time at which a simulation ends. Consider the observation of a

galaxy at the end of a simulation at some time t_0, and some later time t_1. If the halo in which the galaxy resides in has not merged in the time between the two observations, then it has a longer lifetime. The cooling properties of the halo and hence the star formation history of the daughter galaxy may therefore change, such that the properties of the galaxy as t_0 *looking back* from time t_1 may not be the same as if the galaxy was observed at t_0. A way around this would be to evolve all haloes simultaneously on a fixed grid of timesteps.

6.3.3 Choice of IMF

One potential free parameter I have ignored up until now is the choice of initial mass function. The Salpeter IMF has fallen out of favour in recent years, and latest observational results seem to imply an IMF with a log-normal form (eg. Chabrier 2003). This is deficient in low-mass stars as compared to more traditional IMFs, and thus show a more pronounced dimming with time, as a larger proportion of the stars evolve and die within a Hubble time or so. Another possibility is following the lead of Baugh et al. (2005) and introducing a top-heavy IMF for bursts. This was the only way they could reproduce the submillimetre number counts, and such a choice would certainly boost the submillimetre flux in the model presented in this thesis. There is little theoretical justification for a top-heavy IMF over a standard choice, and little evidence suggesting that there are such large variations in the slope of the IMF (eg. Kroupa 2001). In any case, it remains to be seen whether an improvement in the submillimetre regime would simultaneously degrade the results in other wavebands, especially the rest-frame UV.

6.3.4 An improved treatment of disks

The treatment of disks in the model is very simplistic and could be improved considerably. One might ask whether more realistic modelling of individual facets of the model is necessary when there are more fundamental problems present that influence the results in a profound manner. Nevertheless, it should be argued that more realistic treatments are desirable whenever possible, especially where the extra computational expense involved is minimal. As alluded to earlier, an attempt at modelling a Kennicutt threshold for star formation degraded the model results significantly: although the overall mor-

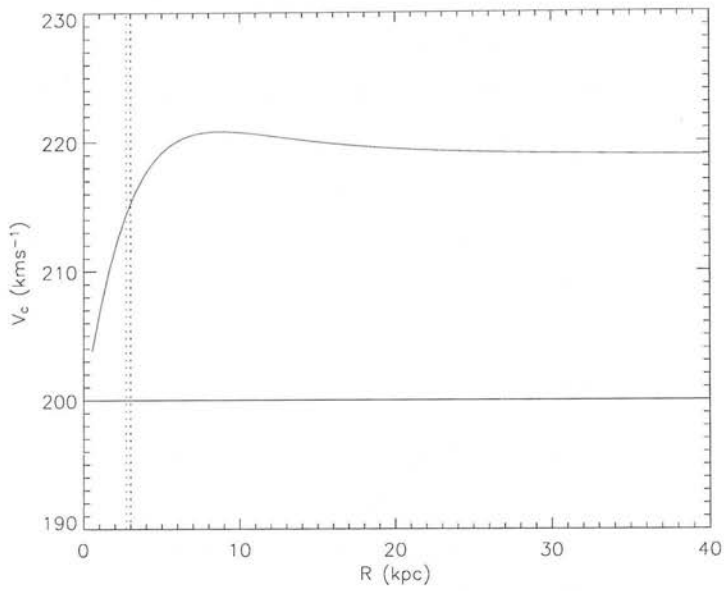

Figure 6.1: The effects of self-gravity on a disk. The black solid line shows the flat rotation curve (equivalent to the circular velocity of the halo) when the self-gravity of the disk is ignored. The solid red line shows the rotation curve of the disk when self-gravity is taken into account. The right-hand vertical dashed line is the original R_d, and the left-hand vertical dashed line is the iterated value of R_d consistent with the new rotation curve.

phological mixture of galaxies improved slightly, a reasonable match to the K-band LF was lost, showing that there was too much suppression of star formation.

Assuming that the self-gravity of a disk can be ignored is unrealistic, and including this will result in a non-flat rotation curve (eg. Mo, Mao and White 1998). Adding in the effect of the gravitational potential of the disk will also reduce its scalelength if the exponential profile still holds. The peak circular velocity of the disk (ie. that used in determining the Tully-Fisher relation) will also change. But by how much?

Consider a pure, self-gravitating disk system in a halo. For a general rotation curve, the value at each radius is given by a sum in quadrature of the circular velocity of the disk and dark matter halo components (Mo, Mao and White 1998):

$$V_c^2(R) = V_{c,\mathrm{disk}}^2(R) + V_{c,\mathrm{halo}}^2(R). \tag{6.1}$$

For haloes modelled by a singular isothermal sphere, the circular velocity of the halo is constant, and we need only worry about the disk component, which is given by (Binney and Tremaine 1987?)

$$V^2_{c,\mathrm{disc}}(y) = \frac{2GM}{R_d} y^2 [I_0(y)K_0(y) - I_1(y)K_1(y)], \tag{6.2}$$

where M_{disk} is the combined mass of stars and cold gas, $y = R/2R_d$ and $I_i(y)$, $K_i(y)$ are modfied Bessel functions.

Finding the correct scalelength is an iterative procedure: following Mo, Mao and White (1998) and Rimes (2003), as a first guess the scalelength of the disk is calculated for a flat rotation curve using (whatever). The rotation curve is calculated from equation (6.1) (using equation 6.2). Then, a new scalelength is chosen, such that the angular momentum of the disk is conserved ie.

$$j_{disc} = \int_0^\infty \Sigma_0 \exp(R/R_d) V_c(R) R^2 \mathrm{d}R, \tag{6.3}$$

does not change, and then the procedure is repeated until the value of R_d converges.

As an example, I consider a pure disk located in a halo with circular velocity $V_c = 200$ kms^{-1}, a scalelength (as computed from equation 2.23) of $R_d = 3$ kpc and a total mass of $10^{10} M_\odot$. I follow the procedure outlined above until convergence of the scalelength is achieved, which only requires a few iterations in most cases. The results are shown in Figure 6.1. the black line gives the old rotation curve, and the red line the more realistic curve once self-gravity is accounted for. The vertical dotted lines show the old and new scalelengths: the converged value consistent with the rotation curve is 2.74 kpc, slightly smaller than before. The rotation curve shows a rise, peak at $\sim 3R_d$ as expected (cf. Mo, Mao and White 1998) and flattens off. Note that the peak is considerably higher than the flat rotation curve of the halo: 220.8 kms^{-1} in this case. This would in fact have a detrimental effect on the models, as evidenced by the poor fit to the Tully-Fisher relation. Galaxies are already rotating too fast (or are too faint in I), and adding self-gravity would exacerbate the discrepancy between model predictions and data.

6.3.5 Disk instabilities

In my model, bulges form from mergers of existing disks. In reality, this transformation can also occur for isolated disks, if the self-gravity of such systems

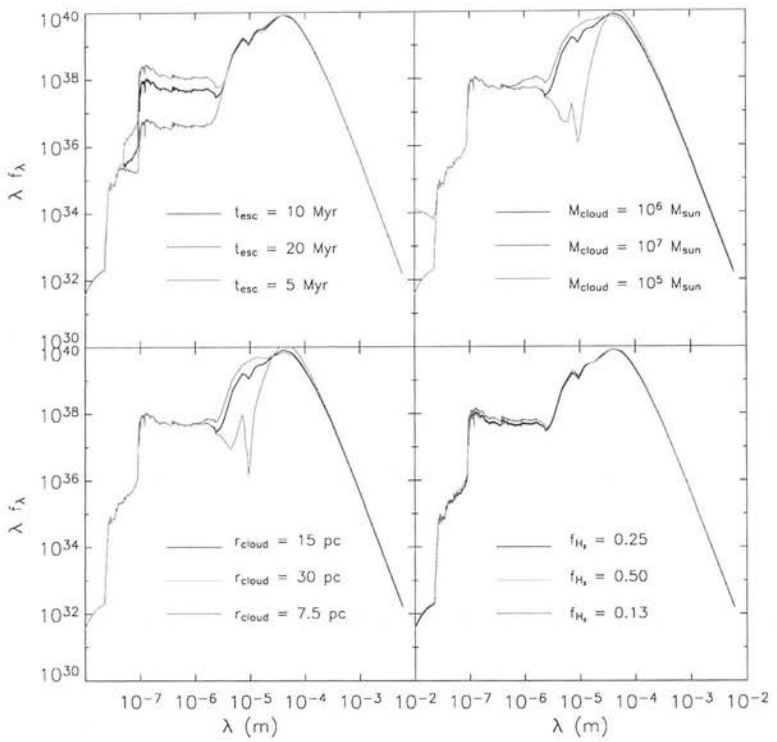

Figure 6.2: The effects of changing some free parameters in the dust model. In each panel the black line shows the rest-frame SED of the most submillimetre-luminous galaxy in the model 3 mock survey (ie. with $t_{\rm esc} = 10$ Myr as standard. The red and blue lines show the effects of varying some of the free parameters. Top-left: escape time of stars from molecular clouds. Top-right: Molecular cloud mass. Bottom-left: Molecular cloud radius. Bottom-right: molecular gas fraction.

is important. Efsathiou, Lake and Negroponte (1982) used N-body simulations to show that disks are unstable to bar formation when the following criterion is met

$$\epsilon \equiv \frac{V_{max}}{(GM_d/R_d)^{1/2}} \leq 1.1. \tag{6.4}$$

In this situation, the self-gravity of the disk is sufficient to warp the structure, form a bar and perhaps settle down into a lenticular or elliptical configuration, given a big enough instability.

6.3.6 Varying the free parameters

On the whole, I deliberately chose to use the same GRASIL parameter choices as Granato et al. (2000) and Baugh et al. (2005). Nevertheless, is there a different set of dust parameters that would yield better results, particularly in the submillimetre regime? In Figure 6.2 I show the effects of changing some of the free parameters in the dust model, using the brightest SMG in model 3 as the test subject. Varying $t_{\rm esc}$ has a dramatic effect on the rest-frame optical SED, and varying the molecular cloud mass and radius has a profound influence on the mid-IR region of the SED. Nevertheless, the sub-millimetre range of the SED is completely insensitive to variations in the free parameters, showing that this alone is not a viable route to a more accuarate determination of the submillimetre number counts.

6.3.7 Dust temperatures

It is possible that the poor fit to the submillimetre counts are due to large dust temperatures. Figure 1.3 shows the strong dependence of submillimetre flux on the dust temperature (calculated using equation 1.4): for a given dust luminosity, the flux can vary by as much as two magnitudes for a modest change in $T_{\rm dust}$. This plot implies that empirical fitting of the submillimetre number counts should be easy by minimal adjustments of $T_{\rm dust}$, but this is not physically consistent: the dust temperature derives from the thermal equilibrium of dust grains between cooling and heating. Treatment of dust in GRASIL is computed so that this condition holds, and so I can *infer* an 'average' dust temperature by fitting a grey-body approximation to the sub-millimetre region of a galaxy SED, given again here for completeness:

$$f_\nu \propto [\nu(1+z)]^{3+\beta} \left[\exp\left(\frac{h\nu(1+z)}{kT} \right) - 1 \right]^{-1}. \tag{6.5}$$

With this in mind, I take the bright SMGs in model 3 ($\geq$ 1 mJy), and use the IDL curve-fitting routine `MPFITFUN` (see `http://cow.physics.wisc.edu/ craigm/idl/mpfittut.html` for the documentation and source code) to derive values of β and $T_{\rm dust}$ in the (rest-frame) submillimetre regime.

For this sample of SMGs, the mean dust emissivity slope is $\beta = 1.37 \pm 0.11$, and the mean dust temperature is $T_d = 59.9 \pm 12.9$ K. The slope is not too

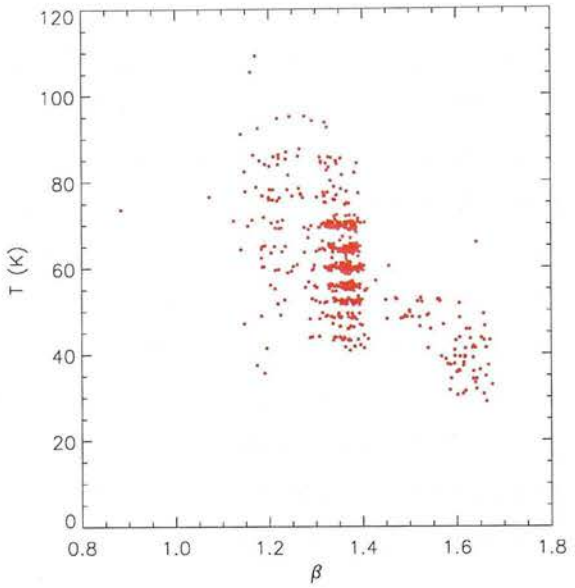

Figure 6.3: Scatter plot of inferred dust slopes and temperatures for the SMGs in model 3. The dust temperatures are higher on the whole than expected.

dissimilar to $\beta = 1.3 \pm 0.2$ found in local submillimetre sources by Dunne et al. (2000), but the dust temperature is significantly higher than expected: Dunne et al. (2000) derive $T_{\rm dust} = 36 \pm 4.9$ K, and Chapman et al. (2005) find $T_{\rm dust} = 36 \pm 7$ K in their sample of 73 high redshift submillimetre sources.

6.3.8 Galaxy geometry: its influence on the submillimetre flux

Another possible avenue for extracting larger submillimetre fluxes at high redshift is altering the geometry of the galaxies. With this in mind, I take the ten brightest SMGs from the simulation volume at $z = 3$ (using model 3) and artificially alter the half-mass radii of the disk and bulge, and then process the artificial galaxies. The changes this induces on the submillimetre flux is summarised in Table 6.1.

From the results, it is clear that in virtually all cases reducing the physical extent of the disk will increase the flux of the galaxy. Altering the scale of the bulge has little effect simply due to their relative unimportance at this stage in the evolutionary history of the galaxies, as seen in the top panels of Figure 5.17. This behaviour is simple to understand: confining the same amount

galaxy	standard	$R_d = 2R_d$	$R_d = R_d/2$	$R_b = 2R_b$	$R_b = R_b/2$
750	2.89	2.53	3.24	2.89	2.89
919	2.76	2.41	3.04	2.76	2.76
1007	2.50	2.25	2.87	2.50	2.50
2263	6.48	5.71	7.38	6.48	6.48
2509	2.42	2.22	2.72	2.42	2.42
2873	3.14	2.73	3.49	3.14	3.14
3995	5.34	2.21	6.06	5.27	5.34
4831	2.41	2.21	2.75	2.41	2.41
6117	5.37	4.86	6.18	5.37	5.37
6536	3.16	3.26	2.66	3.16	3.16

Table 6.1: The influence of galaxy geometry on submillimetre flux in model 3. For each galaxy (the ten brightest SMGs in the $z = 3$ simulation box) I show the change in flux when the sizes of the disk and the bulge are changed by factors of 2. Second column: original flux. Third column: R_d increased by a factor 2. Fourth column: R_d reduced by a factor 2. Fifth column: R_b increased by a factor 2. Sixth column: R_b reduced by a factor 2 (all are half-mass radii).

of dust into a smaller area will increase the number of photons incident per unit area, and increase the luminosity. Although one might expect the dust temperature to rise in turn, it seems that the increased dust luminosity is more than sufficent to balance this. Altering the sizes of disks can be achieved by tuning $\mathscr{J}$, but it is unclear whether varying the fraction of halo angular momentum transferred to the disk is a physically reasonable assumption.

6.3.9 Larger simulation volumes

Using a larger box size would clearly be advantageous in future studies of the high redshift universe. The effects of cosmic variance would diminish, and perhaps more crucially, the simulation volume would include more massive, rare structures. Given that both EROs and SMGs are either found or inferred to be strongly clustered, one would expect them to be preferentially found in regions of significant overdensity. The more active cluster environment may induce more merger-induced bursts of star formation, hopefully helping to improve the SMG number counts.

With this in mind, I have a preliminary simulation of a cluster system, designed to reproduce the A901/A902 system (E. van Kampen, priv. comm.).

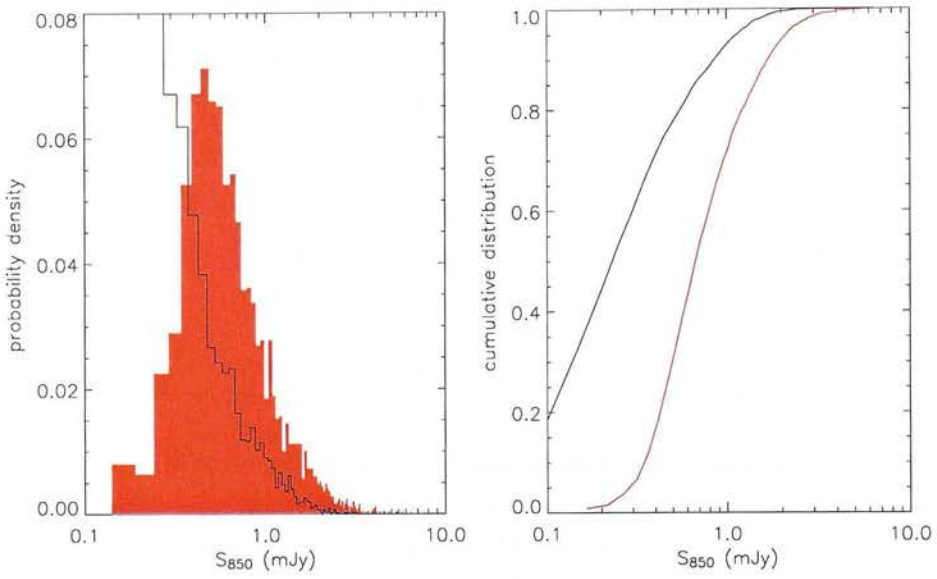

Figure 6.4: A comparison of submillimetre fluxes in a cluster and the field (both using model 3). Left hand panel: distribution of fluxes. The black histogram in the unconstrained simulation volume (black histogram), and in the cluster (solid red histogram). Right hand panel: cumulative flux distribution. The black histogram is the unconstrained box, and the solid red histogram is the cluster.

The initial conditions are constrained such that two overdensities are present in the box, separated by 10 h^{-1} Mpc (the box has side length 60 h^{-1}Mpc). Very briefly, potential overdensities are defined as peaks in the initial density field after smoothing with a gaussian window function. The rms density fluctuation of the smoothed field is then (van Kampen 1995)

$$\sigma_0(R_s) = \sqrt{\int \frac{k^2}{2\pi^2} \exp\left(-R_s^2 k^2\right) \mathrm{d}k}, \tag{6.6}$$

where R_s is the smoothing length chosen in the gaussian kernel. The simulation thus houses a broad $2.8\sigma_0$ and a $3.2\sigma_0$ overdensity, both smoothed on a scale 4 Mpc. The total halo mass and stellar mass in the volume is 1.6×10^{16} $M_\odot$ and 5.0×10^{14} $M_\odot$ respectively, compared with 9.9×10^{15} $M_\odot$ and 2.5×10^{14} $M_\odot$ in the unconstrained volume.

In Figure 6.4 I show the probability distribution of submillimetre fluxes of galaxies in the cluster simulation at $z = 3$, and compare with the unconstrained simulation. Although the brightest source is only slightly more lu-

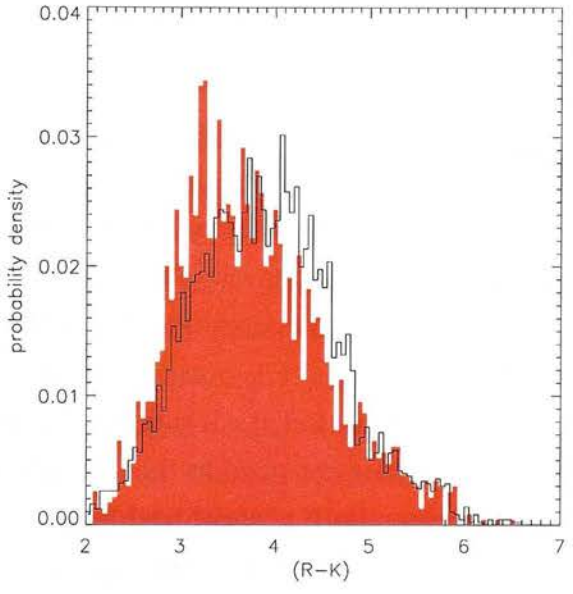

Figure 6.5: A comparison of $(R-K)$ colours in an unconstrained simulation box (black histogram) and a box destined to house a large cluster (solid red histogram).

minous compared with the brightest in the unconstrained run, on the whole galaxies are far more submillimetre luminous in the cluster (right-hand panel of 6.4), due to the enhanced merging and relatively early accumulation of mass in such dense environments.

In contrast, Figure 6.5 gives the probability distributions of $(R-K)$ in both the cluster and the field at $z = 1.5$. There is little difference between the two, although galaxies tend to be bluer in the cluster, a result of the enhanced merging atmosphere causing more frequent bursts of star formation. The abundances of EROs is similar in both cases, suggesting that although more massive galaxies will be present in the cluster, they are not necessarily red enough to be classed as EROs. Of course, the adverse effects of truncation are still at play here, and a more realistic method of curbing star formation in large haloes at late times will be of even more importance if dense environments are to be properly simulated.

There is little more one can do with this cluster simulation at present; I certainly cannot attempt to include it in the light-cone building process. I have merely attempted to show that a larger simulation volume may house a large cluster at the present day, and including such dense regions should im-

prove the chances of matching of matching the submillimetre number counts at high redshift.

6.4 The future

Despite the weaknesses of the galaxy formation model presented in this thesis, it is nevertheless clear that it is capable of probing the high redshift universe with some accuracy. The highlighted problems have given some insight into the methodology required to accurately reproduce the more extreme facets of the galaxy population at early times. Inclusion of PAH features in the dust model (available but not used in this thesis) will help interpret the wealth of *Spitzer* observations both present and future. The inclusion of AGN physics will be an exciting major leap forwards in the predictive power of the model, and with larger simulation volumes the mock-survey technique described in chapter 4 will be an invaluable tool in helping design, quantify and interpret future wide-field surveys.

A wealth of new instrumentation will be coming online over the next five or so years. SCUBA-2 is scheduled for delivery to the JCMT in August 2006. This CCD-style instrument will image the sky some 1000 times faster than SCUBA down to the same signal-to-noise (eg. Holland et al. 2003), allowing wide-field surveys down to the confusion limit to be completed in *hours* rather than years. This will finally allow unabmiguous measures of the SMG clustering strength, and may well unveil rare, extremely bright SMGs that have gone undetected up until now.

Herschel, a 3.5m diameter space telescope for far-IR and submillimetre imaging, is due to fly in July 2007 (see `http://sci.esa.int/science-e/www/area/index.cfm?fareaid=16` for a mission overview). Operating in an L2 orbit, *Herschel* will image the sky between $60 - 670$ μm. Without the varying opacity of the atmosphere to contend with, this instrument will allow deep observations of high-redshift dusty galaxies, and the range of IR data points will allow more precise redshift estimates. The mid-IR data will help determine the nature of the emission in such extreme objects, and will quantify the energy contribution of AGN in the early universe.

The Atacama Large Millimetre Array (ALMA) is being constructed

at Llano de Chajnantor in Chile. Some 5000m above sea-level, the exceptionally dry conditions are perfect for precision (sub)millimetre imaging (see www.eso.org/projects/alma/ for an overview of the project). Fifty movable antennae will be able to image the millimetre sky at sub-arcsecond resolution. The remarkable potential for this instrument spans all of astronomy. Of particular interest (see www.eso.org/projects/alma/publications/papers/blainalma.ppt for an overview of the potential extragalactic science available with ALMA) is the detection and *precise pinpointing* of galaxies out to $z \sim 10$. Detailed morphological studies of SMGs will shed light on their nature and their place in the evolutionary history of galaxies. Average galaxies like the Milky Way will be detectable out to $z \sim 3$, allowing precise, unbiased measurements of the star formation history of the universe.

The high redshift universe is about to be opened up for detailed scrutiny like never before, and hopefully the work presented here will help with the understanding of this varied, confusing and complex universe we occupy.

Bibliography

Abadi M.G., Moore B., Bower R.G., 1999, MNRAS, 308, 947

Adelberger K.L., Steidel C.C., 2000, ApJ, 544, 218

Adelberger K.L., Steidel C.C., Giavalisco M., Dickinson M., Pettini M., Kellogg M., 1998, ApJ, 505, 18

Adelberger K.L., Steidel C.C., Pettini M., Shapley A.E., Reddy N.A., Erb D.K., 2005, ApJ, 619, 697

Alexander D., 2004, In Multiwavelength AGN Surveys, pp. 129–+

Alexander D.M., et al., 2003, AJ, 125, 383

Almaini O., et al., 2003, MNRAS, 338, 303

Baldry I.K., Balogh M.L., Bower R., Glazebrook K., Nichol R.C., 2004, In Allen R.E., Nanopoulos D.V., Pope C.N., eds., AIP Conf. Proc. 743: The New Cosmology: Conference on Strings and Cosmology, pp. 106–119

Balogh M.L., Baldry I.K., Nichol R., Miller C., Bower R., Glazebrook K., 2004, ApJ, 615, L101

Barger A.J., Cowie L.L., Trentham N., Fulton E., Hu E.M., Songaila A., Hall D., 1999, AJ, 117, 102

Barger A.J., Cowie L.L., Richards E.A., 2000, AJ, 119, 2092

Barnes J., Hut P., 1986, Nature, 324, 446

Barnes J.E., Hernquist L.E., 1991, ApJ, 370, L65

Baugh C.M., Cole S., Frenk C.S., 1996a, MNRAS, 282, L27

Baugh C.M., Cole S., Frenk C.S., 1996b, MNRAS, 283, 1361

Baugh C.M., Cole S., Frenk C.S., Lacey C.G., 1998, ApJ, 498, 504

Baugh C.M., Lacey C.G., Frenk C.S., Benson A.J., Cole S., Granato G.L., Silva L., Bressan A., 2004, New Astronomy Review, 48, 1239

Baugh C.M., Lacey C.G., Frenk C.S., Granato G.L., Silva L., Bressan A., Benson A.J., Cole S., 2005, MNRAS, 356, 1191

Beichmann C.A., 1985, Infrared Astronomical Satellite (IRAS) catalogs and atlases. Explanatory supplement. Pasadena: Jet Propulsion Laboratory, 1985, edited by Beichmann, C.A.

Bell E.F., McIntosh D.H., Katz N., Weinberg M.D., 2003, ApJS, 149, 289

Bell E.F., et al., 2004, ApJ, 608, 752

Benson A., 2000, Ph.D. Thesis

Benson A.J., Frenk C.S., Lacey C.G., Baugh C.M., Cole S., 2002a, MNRAS, 333, 177

Benson A.J., Lacey C.G., Baugh C.M., Cole S., Frenk C.S., 2002b, MNRAS, 333, 156

Benson A.J., Bower R.G., Frenk C.S., Lacey C.G., Baugh C.M., Cole S., 2003, ApJ, 599, 38

Bentz M.C., Osmer P.S., Weinberg D.H., 2004, ApJ, 600, L19

Bertelli G., Bressan A., Chiosi C., Fagotto F., Nasi E., 1994, A&AS, 106, 275

Bertschinger E., 1998, ARA&A, 36, 599

Binney J., Tremaine S., 1987, Galactic dynamics. Princeton, NJ, Princeton University Press, 1987, 747 p.

Binney J.J., Evans N.W., 2001, MNRAS, 327, L27

Blain A.W., Smail I., Ivison R.J., Kneib J.P., 1999, MNRAS, 302, 632

Blain A.W., Smail I., Ivison R.J., Kneib J.P., Frayer D.T., 2002, Phys. Rep., 369, 111

Blaizot J., Guiderdoni B., Devriendt J.E.G., Bouchet F.R., Hatton S.J., Stoehr F., 2004, MNRAS, 352, 571

Blanton M.R., et al., 2001, AJ, 121, 2358

Bond J.R., Cole S., Efstathiou G., Kaiser N., 1991, ApJ, 379, 440

Borys C., Chapman S., Halpern M., Scott D., 2003, MNRAS, 344, 385

Borys C., Scott D., Chapman S., Halpern M., Nandra K., Pope A., 2004, MNRAS, 355, 485

Bothun G.D., Impey C.D., Malin D.F., 1991, ApJ, 376, 404

Bouché N., Lehnert M.D., Péroux C., 2005, MNRAS, 364, 319

Bower R.G., et al., 2005, astro-ph/0511338

Boyle B.J., Terlevich R.J., 1998, MNRAS, 293, L49

Bremer M.N., Jensen J.B., Lehnert M.D., Schreiber N.M.F., Douglas L., 2004, ApJ, 615, L1

Brusa M., et al., 2005, A&A, 432, 69

Bruzual A. G., 1983, ApJ, 273, 105

Buta R., Mitra S., de Vaucouleurs G., Corwin H.G., 1994, AJ, 107, 118

Butcher H., Oemler A., 1978, ApJ, 219, 18

Caputi K.I., Dunlop J.S., McLure R.J., Roche N.D., 2004, MNRAS, 353, 30

Caputi K.I., Dunlop J.S., McLure R.J., Roche N.D., 2005, MNRAS, 361, 607

Carlberg R.G., 1994, ApJ, 433, 468

Carroll S.M., Press W.H., Turner E.L., 1992, ARA&A, 30, 499

Chapman S.C., Scott D., Borys C., Fahlman G.G., 2002a, MNRAS, 330, 92

Chapman S.C., Shapley A., Steidel C., Windhorst R., 2002b, ApJ, 572, L1

Chapman S.C., Blain A.W., Ivison R.J., Smail I.R., 2003a, Nature, 422, 695

Chapman S.C., Windhorst R., Odewahn S., Yan H., Conselice C., 2003b, ApJ, 599, 92

Chapman S.C., Smail I., Windhorst R., Muxlow T., Ivison R.J., 2004, ApJ, 611, 732

Chapman S.C., Blain A.W., Smail I., Ivison R.J., 2005, ApJ, 622, 772

Chapman S.C., et al., 2000, MNRAS, 319, 318

Cimatti A., et al., 2002, A&A, 392, 395

Cimatti A., et al., 2004, Nature, 430, 184

Clements D., et al., 2004, MNRAS, 351, 447

Cole S., Kaiser N., 1988, MNRAS, 233, 637

Cole S., Aragon-Salamanca A., Frenk C.S., Navarro J.F., Zepf S.E., 1994, MNRAS, 271, 781

Cole S., Lacey C.G., Baugh C.M., Frenk C.S., 2000, MNRAS, 319, 168

Cole S., et al., 2001, MNRAS, 326, 255

Collison A.J., Fix J.D., 1991, ApJ, 368, 545

Conselice C.J., Chapman S.C., Windhorst R.A., 2003, ApJ, 596, L5

Cowie L.L., Gardner J.P., Hu E.M., Songaila A., Hodapp K.W., Wainscoat R.J., 1994, ApJ, 434, 114

Cowie L.L., Barger A.J., Kneib J.P., 2002a, AJ, 123, 2197

Cowie L.L., Barger A.J., Kneib J.P., 2002b, AJ, 123, 2197

Daddi E., Cimatti A., Pozzetti L., Hoekstra H., Röttgering H.J.A., Renzini A., Zamorani G., Mannucci F., 2000, A&A, 361, 535

Daddi E., et al., 2004, ApJ, 600, L127

de Jong R., 1995, Ph.D. Thesis

Devriendt J.E.G., Guiderdoni B., Sadat R., 1999, A&A, 350, 381

Dickinson M., 1998, In The Hubble Deep Field, pp. 219–+

Draine B.T., 2003, ARA&A, 41, 241

Draine B.T., Lee H.M., 1984, ApJ, 285, 89

Drory N., Salvato M., Gabasch A., Bender R., Hopp U., Feulner G., Pannella M., 2005, ApJ, 619, L131

Dunlop J., Peacock J., Spinrad H., Dey A., Jimenez R., Stern D., Windhorst R., 1996, Nature, 381, 581

Dunlop J.S., 2005, astro-ph/0501429

Dunne L., Eales S., Edmunds M., Ivison R., Alexander P., Clements D.L., 2000, MNRAS, 315, 115

Eales S., Lilly S., Webb T., Dunne L., Gear W., Clements D., Yun M., 2000, AJ, 120, 2244

Efstathiou A., Rowan-Robinson M., 2003, MNRAS, 343, 322

Efstathiou G., Lake G., Negroponte J., 1982, MNRAS, 199, 1069

Eke V.R., Cole S., Frenk C.S., 1996, MNRAS, 282, 263

Evrard A.E., 1991, MNRAS, 248, 8P

Fabian A.C., et al., 2000, MNRAS, 315, L8

Ferrara A., Bianchi S., Cimatti A., Giovanardi C., 1999, ApJS, 123, 437

Fixsen D.J., Dwek E., Mather J.C., Bennett C.L., Shafer R.A., 1998, ApJ, 508, 123

Fontana A., et al., 2004, A&A, 424, 23

Fox M.J., et al., 2002, MNRAS, 331, 839

Freedman W.L., et al., 2001, ApJ, 553, 47

Gear W.K., Lilly S.J., Stevens J.A., Clements D.L., Webb T.M., Eales S.A., Dunne L., 2000, MNRAS, 316, L51

Genzel R., Baker A.J., Tacconi L.J., Lutz D., Cox P., Guilloteau S., Omont A., 2003, ApJ, 584, 633

Genzel R., et al., 2004, astro-ph/0403183

Georgakakis A., Hopkins A.M., Afonso J., Sullivan M., Mobasher B., Cram L.E., 2006, MNRAS, pp. 140–+

Ghigna S., Moore B., Governato F., Lake G., Quinn T., Stadel J., 1998, MNRAS, 300, 146

Giavalisco M., 2002, ARA&A, 40, 579

Giavalisco M., Dickinson M., 2001, ApJ, 550, 177

Giavalisco M., Steidel C.C., Macchetto F.D., 1996, ApJ, 470, 189

Giavalisco M., Steidel C.C., Adelberger K.L., Dickinson M.E., Pettini M., Kellogg M., 1998, ApJ, 503, 543

Gilbank D.G., Smail I., Ivison R.J., Packham C., 2003, MNRAS, 346, 1125

Gingold R.A., Monaghan J.J., 1977, MNRAS, 181, 375

Giovanelli R., Haynes M.P., da Costa L.N., Freudling W., Salzer J.J., Wegner G., 1997, ApJ, 477, L1+

Granato G.L., Danese L., 1994, MNRAS, 268, 235

Granato G.L., Danese L., Franceschini A., 1996, ApJ, 460, L11+

Granato G.L., Lacey C.G., Silva L., Bressan A., Baugh C.M., Cole S., Frenk C.S., 2000, ApJ, 542, 710

Granato G.L., De Zotti G., Silva L., Bressan A., Danese L., 2004, ApJ, 600, 580

Greve T.R., Ivison R.J., Papadopoulos P.P., 2003, ApJ, 599, 839

Groth E.J., Peebles P.J.E., 1977, ApJ, 217, 385

Guiderdoni B., Hivon E., Bouchet F.R., Maffei B., 1998, MNRAS, 295, 877

Haehnelt M.G., Natarajan P., Rees M.J., 1998, MNRAS, 300, 817

Hatton S., Devriendt J.E.G., Ninin S., Bouchet F.R., Guiderdoni B., Vibert D., 2003, MNRAS, 343, 75

Helly J.C., Cole S., Frenk C.S., Baugh C.M., Benson A., Lacey C., 2003a, MNRAS, 338, 903

Helly J.C., Cole S., Frenk C.S., Baugh C.M., Benson A., Lacey C., Pearce F.R., 2003b, MNRAS, 338, 913

Hoffman Y., Ribak E., 1991, ApJ, 380, L5

Holland W.S., Duncan W., Kelly B.D., Irwin K.D., Walton A.J., Ade P.A.R., Robson E.I., 2003, In Phillips T.G., Zmuidzinas J., eds., Millimeter and Submillimeter Detectors for Astronomy. Edited by Phillips, Thomas G.; Zmuidzinas, Jonas. Proceedings of the SPIE, Volume 4855, pp. 1-18 (2003)., pp. 1–18

Holland W.S., et al., 1999, MNRAS, 303, 659

Hopkins A.M., 2004, ApJ, 615, 209

Hornschemeier A.E., et al., 2000, ApJ, 541, 49

Hu E.M., Ridgway S.E., 1994, AJ, 107, 1303

Huang J.S., Glazebrook K., Cowie L.L., Tinney C., 2003, ApJ, 584, 203

Huang J.S., et al., 2005, ApJ, 634, 137

Huchtmeier W.K., Richter O.G., 1988, A&A, 203, 237

Hughes D.H., et al., 1998, Nature, 394, 241

Ivison R.J., et al., 2002, MNRAS, 337, 1

Iwata I., Inoue A.K., Burgarella D., 2005, A&A, 440, 881

Jenkins A., Frenk C.S., White S.D.M., Colberg J.M., Cole S., Evrard A.E., Couchman H.M.P., Yoshida N., 2001, MNRAS, 321, 372

Kauffmann G., 1995a, MNRAS, 274, 153

Kauffmann G., 1995b, MNRAS, 274, 161

Kauffmann G., Haehnelt M., 2000, MNRAS, 311, 576

Kauffmann G., White S.D.M., 1993, MNRAS, 261, 921

Kauffmann G., White S.D.M., Guiderdoni B., 1993, MNRAS, 264, 201

Kauffmann G., Guiderdoni B., White S.D.M., 1994, MNRAS, 267, 981

Kauffmann G., Colberg J.M., Diaferio A., White S.D.M., 1999a, MNRAS, 303, 188

Kauffmann G., Colberg J.M., Diaferio A., White S.D.M., 1999b, MNRAS, 307, 529

Kaviani A., Haehnelt M.G., Kauffmann G., 2003, MNRAS, 340, 739

Kennicutt R.C., 1983, ApJ, 272, 54

Kennicutt R.C., 1989, ApJ, 344, 685

Knudsen K.K., et al., 2005a, ApJ, 632, L9

Knudsen K.K., et al., 2005b, ApJ, 632, L9

Kochanek C.S., et al., 2001, ApJ, 560, 566

Kolatt T.S., et al., 1999, ApJ, 523, L109

Kormendy J., Richstone D., 1995, ARA&A, 33, 581

Lacey C., Cole S., 1993, MNRAS, 262, 627

Lacey C., Cole S., 1994, MNRAS, 271, 676

Lahav O., Liddle A.R., 2006, astro-ph/0601168

Landy S.D., Szalay A.S., 1993, ApJ, 412, 64

Lanzoni B., Guiderdoni B., Mamon G.A., Devriendt J., Hatton S., 2005, MNRAS, 361, 369

Laor A., Draine B.T., 1993, ApJ, 402, 441

Lawrence A., 2001, MNRAS, 323, 147

Le Delliou M., Lacey C., Baugh C.M., Guiderdoni B., Bacon R., Courtois H., Sousbie T., Morris S.L., 2005, MNRAS, 357, L11

Lilly S.J., Longair M.S., 1984, MNRAS, 211, 833

Lilly S.J., Le Fevre O., Hammer F., Crampton D., 1996, ApJ, 460, L1+

Liu M.C., Dey A., Graham J.R., Bundy K.A., Steidel C.C., Adelberger K., Dickinson M.E., 2000, AJ, 119, 2556

Longhetti M., et al., 2005, MNRAS, 361, 897

Lotz J.M., Madau P., Giavalisco M., Primack J., 2004, American Astronomical Society Meeting Abstracts, 205,

Loveday J., 1996, MNRAS, 278, 1025

Loveday J., Peterson B.A., Maddox S.J., Efstathiou G., 1996, ApJS, 107, 201

Madau P., Ferguson H.C., Dickinson M.E., Giavalisco M., Steidel C.C., Fruchter A., 1996, MNRAS, 283, 1388

Madau P., Pozzetti L., Dickinson M., 1998, ApJ, 498, 106

Madgwick D.S., et al., 2002, MNRAS, 333, 133

Magorrian J., et al., 1998, AJ, 115, 2285

Mannucci F., Pozzetti L., Thompson D., Oliva E., Baffa C., Comoretto G., Gennari S., Lisi F., 2002, MNRAS, 329, L57

Maraston C., Thomas D., 2000, ApJ, 541, 126

Mathewson D.S., Ford V.L., Buchhorn M., 1992, ApJS, 81, 413

Mayer L., Governato F., Colpi M., Moore B., Quinn T., Wadsley J., Stadel J., Lake G., 2001, ApJ, 559, 754

McCarthy P.J., 2004, ARA&A, 42, 477

McLure R.J., Dunlop J.S., 2002, MNRAS, 331, 795

Menci N., Cavaliere A., Fontana A., Giallongo E., Poli F., 2002, ApJ, 575, 18

Menci N., Fontana A., Giallongo E., Salimbeni S., 2005, ApJ, 632, 49

Mihos J.C., Hernquist L., 1994, ApJ, 425, L13

Miller G.E., Scalo J.M., 1979, ApJS, 41, 513

Mo H.J., Mao S., White S.D.M., 1998, MNRAS, 295, 319

Mo H.J., Mao S., White S.D.M., 1999, MNRAS, 304, 175

Moore B., Katz N., Lake G., 1996, ApJ, 457, 455

Moore B., Governato F., Quinn T., Stadel J., Lake G., 1998a, ApJ, 499, L5+

Moore B., Lake G., Katz N., 1998b, ApJ, 495, 139

Moore B., Lake G., Quinn T., Stadel J., 1999, MNRAS, 304, 465

Mortier A.M.J., et al., 2005, MNRAS, 363, 563

Mould J.R., Akeson R.L., Bothun G.D., Han M., Huchra J.P., Roth J., Schommer R.A., 1993, ApJ, 409, 14

Nagamine K., 2002, ApJ, 564, 73

Nagamine K., Springel V., Hernquist L., Machacek M., 2004, MNRAS, 350, 385

Nagamine K., Cen R., Hernquist L., Ostriker J.P., Springel V., 2005, ApJ, 627, 608

Nagashima M., Lacey C.G., Baugh C.M., Frenk C.S., Cole S., 2005, MNRAS, pp. 244–+

Navarro J.F., White S.D.M., 1993, MNRAS, 265, 271

Navarro J.F., White S.D.M., 1994, MNRAS, 267, 401

Navarro J.F., Frenk C.S., White S.D.M., 1995, MNRAS, 275, 56

Neri R., et al., 2003, ApJ, 597, L113

Norberg P., et al., 2002, MNRAS, 332, 827

Oke J.B., Gunn J.E., 1983, ApJ, 266, 713

Oliver S., et al., 2000, MNRAS, 316, 749

Panter B., Heavens A.F., Jimenez R., 2003, MNRAS, 343, 1145

Papovich C., Dickinson M., Ferguson H.C., 2001a, ApJ, 559, 620

Papovich C., Dickinson M., Ferguson H.C., 2001b, ApJ, 559, 620

Papovich C., et al., 2006, ApJ, 640, 92

Peacock J.A., 1999, Cosmological physics. Cosmological physics. Publisher: Cambridge, UK: Cambridge University Press, 1999. ISBN: 0521422701

Peacock J.A., et al., 2000, MNRAS, 318, 535

Peebles P.J.E., 1980, The large-scale structure of the universe. Research supported by the National Science Foundation. Princeton, N.J., Princeton University Press, 1980. 435 p.

Percival W., Miller L., 1999, MNRAS, 309, 823

Perlmutter S., et al., 1998, Nature, 391, 51

Pettini M., Shapley A.E., Steidel C.C., Cuby J., Dickinson M., Moorwood A.F.M., Adelberger K.L., Giavalisco M., 2001a, ApJ, 554, 981

Pettini M., Shapley A.E., Steidel C.C., Cuby J.G., Dickinson M., Moorwood A.F.M., Adelberger K.L., Giavalisco M., 2001b, ApJ, 554, 981

Pierce M.J., Tully R.B., 1992, ApJ, 387, 47

Pope A., Borys C., Scott D., Conselice C., Dickinson M., Mobasher B., 2005, MNRAS, 358, 149

Pozzetti L., et al., 2003, A&A, 402, 837

Press W.H., Schechter P., 1974, ApJ, 187, 425

Primack J.R., Wechsler R.H., Somerville R.S., 2003, In Bender R., Renzini A., eds., The Mass of Galaxies at Low and High Redshift, pp. 284–+

Richstone D., et al., 1998, Nature, 395, A14+

Rimes C.D., 2003, Ph.D. Thesis

Roche N.D., Almaini O., Dunlop J., Ivison R.J., Willott C.J., 2002, MNRAS, 337, 1282

Roche N.D., Dunlop J., Almaini O., 2003, MNRAS, 346, 803

Rowan-Robinson M., 2001, ApJ, 549, 745

Rowan-Robinson M., et al., 1991, Nature, 351, 719

Sage L.J., 1993, A&AS, 100, 537

Sanders D.B., Mirabel I.F., 1996, ARA&A, 34, 749

Saracco P., et al., 2006, MNRAS, 367, 349

Scalo J.M., 1986, Fundamentals of Cosmic Physics, 11, 1

Schechter P., 1976, ApJ, 203, 297

Sciama D.W., 2000, MNRAS, 312, 33

Scott S.E., et al., 2002, MNRAS, 331, 817

Serjeant S., Farrah D., Geach J., Takagi T., Verma A., Kaviani A., Fox M., 2003a, MNRAS, 346, L51

Serjeant S., et al., 2003b, MNRAS, 344, 887

Severgnini P., et al., 2000, A&A, 360, 457

Shapley A.E., Steidel C.C., Adelberger K.L., Dickinson M., Giavalisco M., Pettini M., 2001, ApJ, 562, 95

Shapley A.E., Erb D.K., Pettini M., Steidel C.C., Adelberger K.L., 2004, ApJ, 612, 108

Sheth R.K., Tormen G., 1999, MNRAS, 308, 119

Sheth R.K., Tormen G., 2002, MNRAS, 329, 61

Shu C., Mao S., Mo H.J., 2001, MNRAS, 327, 895

Silva L., 1999, Ph.D. Thesis

Silva L., Granato G.L., Bressan A., Danese L., 1998, ApJ, 509, 103

Simien F., de Vaucouleurs G., 1986, ApJ, 302, 564

Simpson C., Dunlop J.S., Eales S.A., Ivison R.J., Scott S.E., Lilly S.J., Webb T.M.A., 2004, MNRAS, 353, 179

Smail I., Ivison R.J., Blain A.W., 1997, ApJ, 490, L5+

Smail I., Ivison R.J., Kneib J.P., Cowie L.L., Blain A.W., Barger A.J., Owen F.N., Morrison G., 1999, MNRAS, 308, 1061

Smail I., Ivison R.J., Owen F.N., Blain A.W., Kneib J.P., 2000, ApJ, 528, 612

Smail I., Ivison R.J., Blain A.W., Kneib J.P., 2002a, MNRAS, 331, 495

Smail I., Owen F.N., Morrison G.E., Keel W.C., Ivison R.J., Ledlow M.J., 2002b, ApJ, 581, 844

Smail I., Chapman S.C., Blain A.W., Ivison R.J., 2004, ApJ, 616, 71

Soifer B.T., Neugebauer G., 1991, AJ, 101, 354

Soifer B.T., Boehmer L., Neugebauer G., Sanders D.B., 1989, AJ, 98, 766

Somerville R.S., 2004, astro-ph/0401570

Somerville R.S., Primack J.R., 1999, MNRAS, 310, 1087

Somerville R.S., Primack J.R., Faber S.M., 2001a, MNRAS, 320, 504

Somerville R.S., Primack J.R., Faber S.M., 2001b, MNRAS, 320, 504

Somerville R.S., Lee K., Ferguson H.C., Gardner J.P., Moustakas L.A., Giavalisco M., 2004, ApJ, 600, L171

Spergel D.N., et al., 2003, ApJS, 148, 175

Spitzer L.J., 1969, ApJ, 158, L139+

Springel V., Hernquist L., 2005, ApJ, 622, L9

Springel V., Yoshida N., White S.D.M., 2001, New Astronomy, 6, 79

Springel V., et al., 2005, Nature, 435, 629

Stanway E.R., Bunker A.J., McMahon R.G., Ellis R.S., Treu T., McCarthy P.J., 2004, ApJ, 607, 704

Steidel C.C., Hamilton D., 1993, AJ, 105, 2017

Steidel C.C., Pettini M., Hamilton D., 1995, AJ, 110, 2519

Steidel C.C., Giavalisco M., Dickinson M., Adelberger K.L., 1996, AJ, 112, 352

Steidel C.C., Adelberger K.L., Dickinson M., Giavalisco M., Pettini M., Kellogg M., 1998, ApJ, 492, 428

Steidel C.C., Adelberger K.L., Giavalisco M., Dickinson M., Pettini M., 1999, ApJ, 519, 1

Steidel C.C., Adelberger K.L., Shapley A.E., Pettini M., Dickinson M., Giavalisco M., 2003, ApJ, 592, 728

Stevens J.A., et al., 2003, Nature, 425, 264

Sutherland R.S., Dopita M.A., 1993, ApJS, 88, 253

Swinbank A.M., Smail I., Chapman S.C., Blain A.W., Ivison R.J., Keel W.C., 2004, ApJ, 617, 64

Thompson D., et al., 1999, ApJ, 523, 100

Toomre A., 1964, ApJ, 139, 1217

Tully R.B., Fisher J.R., 1977, A&A, 54, 661

Tully R.B., Mould J.R., Aaronson M., 1982, ApJ, 257, 527

van Dokkum P.G., et al., 2006, ApJ, 638, L59

van Kampen E., 1995, MNRAS, 273, 295

van Kampen E., 2000, astro-ph/0002027

van Kampen E., Jimenez R., Peacock J.A., 1999, MNRAS, 310, 43

van Kampen E., et al., 2005, MNRAS, 359, 469

Weatherley S.J., Warren S.J., 2005, MNRAS, 363, L6

Webb T.M., et al., 2003a, ApJ, 587, 41

Webb T.M., et al., 2003b, ApJ, 582, 6

Webb T.M.A., Brodwin M., Eales S., Lilly S.J., 2004, ApJ, 605, 645

Webb T.M.A., et al., 2006, ApJ, 636, L17

Wechsler R.H., Somerville R.S., Bullock J.S., Kolatt T.S., Primack J.R., Blumenthal G.R., Dekel A., 2001, ApJ, 554, 85

Wehner E.H., Barger A.J., Kneib J.P., 2002, ApJ, 577, L83

Weinberg D.H., Hernquist L., Katz N., 2002, ApJ, 571, 15

White S.D.M., 1996, In Cosmology and Large Scale Structure, pp. 349–+

White S.D.M., Frenk C.S., 1991, ApJ, 379, 52

White S.D.M., Rees M.J., 1978, MNRAS, 183, 341

White S.D.M., Efstathiou G., Frenk C.S., 1993, MNRAS, 262, 1023

Wilson G., et al., 2004, ApJS, 154, 107

Yan L., Thompson D., 2003, ApJ, 586, 765

Zel'Dovich Y.B., 1970, A&A, 5, 84